Diffusion et propagation des enzymes lignocellulolytiques dans leur substrat polymérique : impact de la concentration en polymère et de leur activité

Maike Petermann

THÈSE

En vue de l'obtention du

DOCTORAT DE L'UNIVERSITÉ DE TOULOUSE

Délivré par :

Institut National Polytechnique de Toulouse (Toulouse INP)

Discipline ou spécialité :

Ingénieries Microbienne et Enzymatique

Présentée et soutenue par :

Mme MAIKE PETERMANN

le lundi 10 juillet 2023

Titre :

Diffusion et propagation des enzymes lignocellulolytiques dans leur substrat polymérique : impact de la concentration en polymère et de leur activité

École doctorale :

Sciences Écologiques, Vétérinaires, Agronomiques et Bioingénieries (SEVAB)

Unité de recherche :

Toulouse Biotechnology Institute, Bio & Chemical Engineering (TBI - INSA)

Directeurs de Thèse :

M. ANTOINE BOUCHOUX

MME CLAIRE DUMON

Rapporteurs :

M. LUC SAULNIER, INRA NANTES

MME FRANÇOISE NAU, INSTITUT AGRO RENNES

M. THIERRY ASTRUC, INRA CLERMONT FERRAND

Membres du jury :

M. PATRICE BACCHIN, UNIVERSITE TOULOUSE 3, Président

M. ANTOINE BOUCHOUX, INSA TOULOUSE, Membre

MME CLAIRE DUMON, INSA TOULOUSE, Membre

Associated work

Publications

Submitted

1. Maike Petermann, Lucie Dianteill, Amal Zeidi, Roméo Vaha Ouloassekpa, Paul Budisavljevic, Claude Le Men, Cédric Y. Montanier, Pierre Roblin, Bernard Cabane, Ralf Schweins, Claire Dumon, Antoine Bouchoux
   "Arabinoxylan in Water Through SANS: Single Chain Conformation, Chain Overlap and Clustering" Biomacromolecules (2023)

International conferences

1. *"Enzymatic degradation of semi dilute polymer solutions: coupling between enzyme mobility and activity"*
   M. Petermann, A. Bouchoux, C. Dumon
   ECIS conference, 05.-10.09.2021 Athens (online poster)

2. *"Small-Angle scattering characterization of dilute to semi-dilute arabinoxylan polysaccharide solutions in water"*
   M. Petermann, L. Dianteill, P. Budisavljevic, C. Montanier, C. le Men, P. Roblin, R. Schweins, B. Cabane, C. Dumon, A. Bouchoux
   EPNOE conference, 11.-15.10.2021 Nantes (presentation)

National conferences

1. *"Transport et diffusion d'enzymes dans les matériaux qu'elles dégradent"*
   M. Petermann, A. Bouchoux, C. Dumon
   GDR SLAMM, 18-21.11.2019 Roscoff (poster presentation)

2. *"Enzymatic degradation of semi dilute polymer solutions: coupling between enzyme mobility and activity"*
   M. Petermann, A. Bouchoux, C. Dumon
   GDR SLAMM, 02.-05.11.2021 Biarritz (poster presentation)

3. *"Small-Angle scattering characterization of dilute to semi-dilute arabinoxylan polysaccharide solutions in water"*
   M. Petermann, L. Dianteill, P. Budisavljevic, C. Montanier, C. le Men, P. Roblin, R. Schweins, B. Cabane, C. Dumon, A. Bouchoux
   GDR SLAMM, 02.-05.11.2021 Biarritz (presentation)

Seminars

1. *"Diffusion et propagation des enzymes lignocellulolytiques dans leur substrat polymérique"*
   M. Petermann, A. Bouchoux, C. Dumon
   TIM team seminar, 17.09.2020 Toulouse (presentation)

2. *"Diffusion and propagation of enzymes in confined substrates"*
   M. Petermann, A. Bouchoux, C. Dumon
   CIMEs team seminar, 03.12.2020 Toulouse (presentation)

3. *"Diffusion des enzymes lignocellulolytiques dans leur substrat polymérique"*
   M. Petermann, A. Bouchoux, C. Dumon
   FERMaT seminar, 12.02.2021 Toulouse (presentation)

Remerciements

Tout d'abord, je tiens à remercier sincèrement mes encadrants, Antoine et Claire, qui m'ont appris tant de choses. Parfois, le fait d'avoir plusieurs encadrants, et surtout des encadrants de différents domaines scientifiques, peut être compliqué. Et parfois, quand il y a du respect et de l'appréciation, on a la chance de voir une formidable synergie, comme celle qui a créé un environnement harmonieux et fructueux pour moi et mon travail. Antoine et Claire, merci pour tous ces 150+ jeudi matins que vous avez réservés pour discuter enzymes, diffusion et phénomènes fluorescents mystérieux. Merci pour votre soutien, votre encouragement et votre profonde gentillesse. Merci pour cette belle aventure scientifique et humaine, je n'aurais pas pu avoir des meilleurs encadrants.

Je voudrais ensuite remercier les membres du jury Patrice Bacchin, Françoise Nau, Luc Saulnier et Thierry Astruc d'avoir accepté d'évaluer ce travail, d'avoir consacré du temps à lire ce manuscrit et à me suggérer des pistes d'amélioration. Je souhaiterais aussi vous remercier pour la richesse des discussions menées lors de la soutenance de thèse.

Je voudrais aussi remercier toutes les personnes ayant collaborés et aidés à ce projet. En premier, Claude Le Men, le magicien qui a monté le microscope et a prêté beaucoup de son expertise à ce projet. Un grand merci aussi à Cédric Montanier, qui m'a montré comment produire des enzymes et mesurer leur activité, et à Paul Budisavljevic, qui a contribué à cette thèse lors de son stage. Puis les RMNistes de TBI, Guy Lippens et Cyril Charlier, pour les tests de RMN, et Mateo Milani et Laurence Ramos pour les tests d'imagerie Speckle au LCC à Montpellier. Je remercie également Pascale Laborie pour les analyses SEC-MALS aux IMRCP et Carine Froment pour les analyses de spectrométrie de masse à l'IPBS.

Ensuite je remercie les membres des équipes 1 et 7 de TBI qui m'ont accueillie et soutenue le long de ma thèse, particulièrement Arnaud Cockx, Luc Fillaudeau, Nathalie Clergerie, et bien-sûr la bande des « jeunes » qui ont embelli chacun de mes jours à TBI : les docteurs Gaëlle, Eliot, Vincent, Irem, Alex, Carlos et Ryma et les futurs docteurs Ahmed, Gina, Ernest et Camilo.

Ein großes Dankeschön gilt auch meinen Liebsten, nah und fern : Michi, was hätte ich nur ohne dich getan, Nadine und mein Lieblingspatenkind, immer an meiner Seite, ma Marion, mi querida Connie, Kilian, Dr. Niclas, Dr. Konstantin, Dr. Anna und natürlich Ela und Franzi ; danke, dass ihr immer für mich da seid.

Das größte Dankeschön gilt meiner Familie, die mich immer unterstützt hat und mir den Mut und die Sicherheit gegeben hat, so lange und an so vielen verschiedenen Orten auf der Welt meiner Ausbildung nachzugehen. Und Amine, ich bin gespannt auf unsere Zukunft.

Abstract

The valorisation of lignocellulosic plant biomass plays an important role in the transition towards a more sustainable economy. Due to the complexity of this material, its valorisation is challenging and needs a pre-treatment that is expensive. One way to reduce the costs of this step, is to use it in combination with a biological treatment. Here, specific enzymes are used in 'soft' conditions to hydrolyse the polysaccharides that constitute the biomass. This step is promising, but it lacks in efficiency. One approach for its optimisation is to better understand what happens during the enzymatic degradation of a polymer and then use this information to improve it. During the degradation, the enzyme is confronted with high concentrations of polymer and has to navigate a dense and complex environment to access its target sites. However, enzymes are poorly characterised at high substrate concentration and crucial questions need to be addressed. How does the presence of the polymer impact the mobility of the enzyme inside this structure? Does the activity of the enzyme impact its mobility? And is its activity in turn impacted by the high concentrations of polymer?

These are the questions that guided this PhD project and were studied using an experimental approach that combines enzymology, physics and imaging. At first, we characterised our polymer, wheat arabinoxylan, using small-angle neutron scattering to determine its structure and network characteristics at different polymer concentrations. The latter is a key information for the diffusivity of the polymer solution and our later diffusion experiments. Then, we studied the enzymatic degradation of the polysaccharide by a xylanase at different substrate concentrations up to 50 $g.L^{-1}$ using a colorimetric activity assay and size-exclusion chromatography with multi-angle light scattering. While we did not see an effect of the polymer concentration on the initial reaction rate, we saw some indications that a higher polymer concentration led to the creation of smaller degradation products. Finally, we used fluorescence microscopy and imaging to study the diffusion of the active and inactive xylanase in the polymer solutions up to 90 $g.L^{-1}$. We found that the diffusion of the enzyme did not follow the Stokes-Einstein relation but was governed by an effective viscosity, in-between the pure solvent and the polymer solution viscosity, and decreased with increasing polymer concentration. To address the link between the mobility and activity of the enzyme, we compared the diffusion of active and inactive xylanase. In the case of the active enzyme, the diffusion was accelerated, showing the link between enzymatic activity and mobility.

All in all, these results increase our knowledge on enzymatic degradation of concentrated polymers. In addition, preliminary experiments pave the way for other physico-chemical techniques that can be used to further unravel the link between an enzyme's activity and mobility.

Résumé

La valorisation de la biomasse lignocellulosique fait partie des solutions envisageables pour la transition vers une économie durable. La complexité de cette biomasse nécessite un pré-traitement coûteux pour sa valorisation. Pour réduire les couts, il est possible de le combiner avec un traitement biologique. Pour cela, des enzymes spécifiques au substrat catalysent la déconstruction des polysaccharides de la biomasse sous conditions 'douces'. Néanmoins, les pré-traitements biologiques sont peu efficaces. Pour les optimiser, il est important de comprendre ce qui se passe lors de la dégradation enzymatique d'un polymère et ensuite trouver des approches pour l'améliorer. Lors de la dégradation, l'enzyme est confrontée à une concentration élevée en polymère et doit se propager dans une structure dense et complexe. En général, les enzymes sont peu caractérisées à fortes concentrations en substrat, et plusieurs questions cruciales doivent être abordées. Comment est-ce que la présence du polymère impacte cette propagation ? Est-ce que l'activité de l'enzyme impacte sa mobilité ? Et cette activité, est-elle aussi impactée par la concentration élevée en polymère ?

Ce sont les questions qui ont guidé ce projet de thèse, qui se fonde sur une approche expérimentale qui combine l'enzymologie, la physique et l'imagerie. Dans un premier temps, nous avons caractérisé le polymère, arabinoxylane extrait du blé, pour déterminer sa structure et les caractéristiques du réseau formé par ses chaînes à différentes concentrations en polymère. Ces caractéristiques sont des informations importantes pour les expériences de diffusion dans les solutions de polymère. Ensuite, nous avons étudié la dégradation enzymatique du polysaccharide à différentes concentrations par une xylanase, avec des mesures de vitesse de réaction et de la taille des produits. Nous n'avons pas constaté d'impact de la concentration en polymère sur la vitesse de réaction, mais nos résultats suggèrent qu'une forte concentration en polymère entraînerait des produits de réaction plus petits. Finalement, nous avons utilisé la microscopie à fluorescence pour étudier la diffusion de la xylanase active et inactive dans les solutions de polymère jusqu'à 90 $g.L^{-1}$. Les résultats ont montré que la diffusion de l'enzyme ne suit pas la relation de Stokes-Einstein, mais qu'elle est déterminée par une viscosité effective, entre la viscosité du solvant et celle des solutions du polymère, et que la diffusion diminue avec la concentration en polymère. Pour étudier le lien entre l'activité et la mobilité de l'enzyme, nous avons comparé la diffusion de la xylanase active et inactive. Dans le cas de l'enzyme active, la diffusion était accélérée, ce qui montre un couplage entre l'activité et la mobilité de l'enzyme.

Résumé

Au total, ces résultats améliorent notre compréhension de la dégradation enzymatique des polymères concentrés. En complément, des expériences préliminaires ouvrent la voie à d'autres techniques physico-chimiques, qui peuvent être utilisées pour poursuivre l'étude du couplage entre l'activité et la mobilité d'une enzyme.

Table of contents

CHAPTER I : Introduction 1

CHAPTER II : Context, Questions and Strategy 9

i. Context: Valorisation of Lignocellulosic Plant Biomass 10

a. Plant cell wall structure and composition 10

b. Valorisation processes 14

c. Enzymatic deconstruction of lignocellulose 18

ii. Specific Questions 25

a. Can high polymer concentrations affect enzymatic deconstruction? 25

b. What determines the propagation of the enzyme in its polymeric substrate? 27

iii. Strategy 37

a. Model system 38

b. Study of the impact of the polymer concentration 43

c. Tracking of enzymatic mobility using fluorescence microscopy 44

d. Other techniques to follow enzymatic action 49

CHAPTER III : Characterisation of Arabinoxylan 51

i. Preamble 52

ii. Article 53

iii. Supporting Information 90

CHAPTER IV : Enzymatic Hydrolysis 103

i. Preamble 104

ii. Introduction 105

iii. Materials and Methods 107

a. Expression and purification of the enzyme 107

b. Preparation of the polymer solution.....109

c. Enzymatic activity.....111

d. SEC-MALS analysis.....114

iv. Results and Discussion 115

a. Characterisation of short-term reaction kinetics: Michaelis-Menten parameters 116

b. Characterisation of long-term kinetics 119

c. Characterisation of the size of the degradation products 122

v. Conclusion 137

vi. Supporting Information..... 139

CHAPTER V : Enzyme Propagation and Diffusion..... 145

i. Preamble 146

ii. Introduction 147

iii. Materials and Methods..... 149

a. Polymer solution.....149

b. Enzyme labelling 149

c. Experimental set-up.....150

d. Diffusion experiments.....152

e. Image treatment 154

f. Determination of the diffusion coefficient 155

iv. Results and Discussion 157

a. Typical workflow for image treatment and analysis.....157

b. Diffusion of the inactive enzyme 160

c. Active enzyme 166

v. Conclusion *175*

vi. Supporting information *177*

CHAPTER VI : Following the *In-Situ* Degradation of AX..... 193

i. Preamble *194*

ii. Nuclear magnetic resonance sprectroscopy *195*

a. Materials and methods 196

b. Results and discussion 196

c. Conclusion 200

iii. Photon Correlation Imaging *201*

a. Materials and methods 201

b. Results and discussion 202

c. Conclusion 204

CHAPTER VII : General Conclusion and Perspectives 207

References 213

CHAPTER I

Introduction

i. Context

A crucial step in our fight against climate change and for the transition to a sustainable economy is the substitution of fossil carbon with a renewable source. One promising candidate is lignocellulosic plant biomass, that can be valorised into biofuel, bioplastics or other platform molecules for the industry [1]. Lignocellulose makes up the secondary cell walls of plants and is especially abundant in wood and grasses, which are non-food substrates and often by-products of the agroindustry [2]. Before lignocellulose can be valorised, it has to be broken down into its basic sugars. This is difficult, because it is chemically and structurally very complex: Its three main components cellulose, hemicellulose and lignin form a very tight and interconnected network, that causes a high resistance towards degradation [3]. In nature, organisms like fungi have evolved to hydrolyse lignocellulose over time using a combination of different enzymes [4]. In industrial processes however, time and efficiency are of the essence, and even though enzymatic degradation is already used in some processes, it is usually preceded by a physico-chemical pre-treatment to increase efficiency [5]. These pre-treatments often need high temperatures or large volumes of dilute acids, which costs a lot of energy and resources. If the enzymatic hydrolysis of lignocellulose was more efficient, additional pre-treatments could be reduced or even neglected. One way to optimise the hydrolysis would be to find more efficient enzymes or better enzymatic cocktails. Another way would be to have a closer look at what happens during hydrolysis and to improve our understanding of it first. What happens when the enzyme is confronted with such a complex environment? How does it navigate this dense, polymeric network to access its substrate? Does the polymer impact its activity? And what determines its mobility?

These are very particular questions that are at the intersection of physics and biology. In terms of activity, enzymes are very rarely characterised at high concentrations of polymeric substrate. One study by Cheng et al. [6] on this subject found a decrease in the reaction rate of the enzyme at high polymer concentrations, caused by diffusion limitation. This suggests a possible impact of the polymer concentration on the degradation, and the relevance of further investigations.

The subject of enzymatic diffusion on the other hand has captured the interest of the physics community: Over the last years, the controversial phenomenon of enhance diffusion of an enzyme in presence of its molecular substrate has emerged [7]–[10], in one case also for a polymeric substrate [11].

All in all, very little is known about the activity or the mobility of enzymes in concentrated polymeric substrates, hence the relevance of this PhD project.

ii. Strategy

We studied the diffusion of enzymes in their polymeric substrate and the impact of their activity on mobility using a model system of an enzyme (xylanase) and a soluble polysaccharide (wheat arabinoxylan). Our experimental approach combines physics, enzymology and imaging to (i) characterise the polymer (**chapter III**), (ii) study the effect of polymer concentration on enzymatic activity in homogeneous conditions (**chapter IV**) and (iii) study the effect of the polymer concentration on the mobility of the active and inactive enzyme and investigate the link between the enzyme's activity and mobility (**chapter V**).

The experimental approach consisted of several steps:

1) Experimental set-up of the custom fluorescence microscope

The team's engineer Claude Le Men designed and built a custom fluorescence microscope for this PhD. The excitation and emission filters were adapted to the used fluorophore and the images were captured by a camera. The circular microscopy chamber was designed by him as well. It allowed the introduction of a localised enzyme source into the polymer solution and observe how it spread radially.

2) Production of the polymer solutions

The preparation protocol for the wheat arabinoxylan solutions was chosen with respects to optimum hydration of the polymer chains, which was confirmed using small-angle neutron scattering (SANS) and size-exclusion chromatography with multi-angle light scattering (SEC-MALS).

3) Characterisation of the polymer

We studied the structure and network characteristics of wheat arabinoxylan in water using SANS. Aside from valuable information like the persistence length and the Flory exponent, the key information was the mesh size of the polymer in solution and how it evolves with polymer concentration.

4) Production of the active enzyme

The recombinant fungal xylanase *Np*Xyn11A from *Neocallimastix patriciarum* was produced using *E.*coli and a well-established protocol. The presence of a C-terminal histidine-tag enabled a purification using immobilised metal ion affinity chromatography.

5) Characterisation of the enzymatic activity in homogeneous polymer solutions

First, we determined the evolution of the initial reaction rate of the enzyme as a function of polymer concentrations. Then, we measured the impact of the hydrolysis on the structure of the polymer in terms of chain length (SEC-MALS).

6) Labelling of the enzyme

The enzyme was covalently labelled using TRITC (tetramethylrhodamine-5-(and-6)-isothiocyanate), a commercial rhodamine dye. Residual free fluorophore was removed by gel filtration. After a lot of trial and error, we could adapt and optimise the labelling protocol to achieved a good labelling efficiency, while preserving the activity of the enzyme.

7) Diffusion experiments

We studied the diffusion of the active and inactive labelled enzyme in 0, 16, 35, 50 and 90 $g.L^{-1}$ arabinoxylan using our custom microscope.

8) Image treatment and determination of the diffusion coefficient

The captured images of the diffusion experiment were treated using a custom script in Python and radial intensity profiles were extracted. By fitting a numerical solution of Fick's second law, the diffusion coefficient could be estimated.

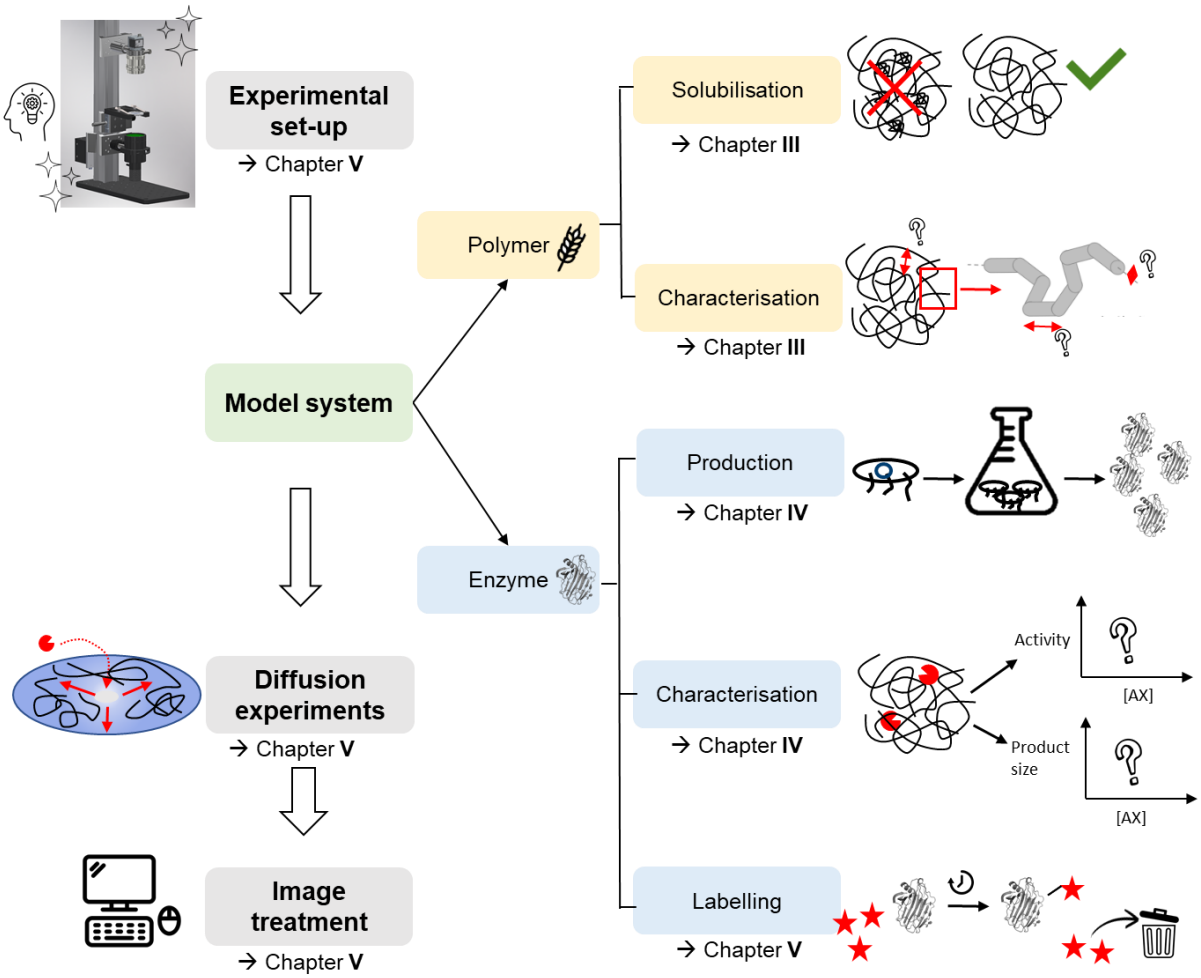

Figure 1: Strategy of the PhD and chapter references.

This manuscript consists of seven chapters, including one submitted article and one in preparation.

Chapter I (introduction) explains the context and strategy of this PhD.

Chapter II consists of three parts. First, the structure and composition of lignocellulosic biomass is reviewed, as well as the different processes for its valorisation with a special focus on enzymatic deconstruction. Then, we present the specific questions of this PhD and finally detail our strategy to investigate them.

Chapter III presents the characterisation of our model polymer arabinoxylan. Its structure, conformation and network properties in aqueous solution were studied at different concentrations using small-angle neutron scattering. This chapter has been recently submitted to the journal Biomacromolecules.

Chapter IV is the study of the enzymatic activity at different polymer concentrations under homogeneous conditions. We quantified the impact of the enzyme on the size polymer chains over the course of the degradation using SEC-MALS, and the impact of the polymer concentration

Chapter V presents the propagation and diffusion of the active and inactive enzyme in polymer solutions at different concentrations. It details the set-up, preparation and execution of the diffusion experiments using a custom fluorescence microscope. We found a difference in the mobility of active and inactive enzymes, which is discussed in the end of this chapter.

Chapter VI presents the preliminary results of two innovative techniques we used to follow the spatial progress of polymer deconstruction. For this, we used nuclear magnetic resonance spectroscopy imaging and photon correlation imaging to spatially visualise the change in the dynamics of the polymer chains under deconstruction. We were able to see the change in dynamics for both techniques. The localisation of the gradient needs more fine-tuning.

Chapter VII is the general conclusion that summarises our findings on the activity and mobility of enzymes in their polymeric substrates.

CHAPTER II

Context, Questions and Strategy

i. Context: Valorisation of Lignocellulosic Plant Biomass

a. Plant cell wall structure and composition

Over time, plant cell walls have evolved to withstand any kind of biotic and abiotic stress by developing a chemically and structurally highly complex and recalcitrant network [3]. These cell walls consist of different layers, depending on the species and developmental stage of the plant. One of these layers is the secondary cell wall (see Figure 2). It is formed after the plant cell finished expansion to give it mechanical support and reinforcement [12].

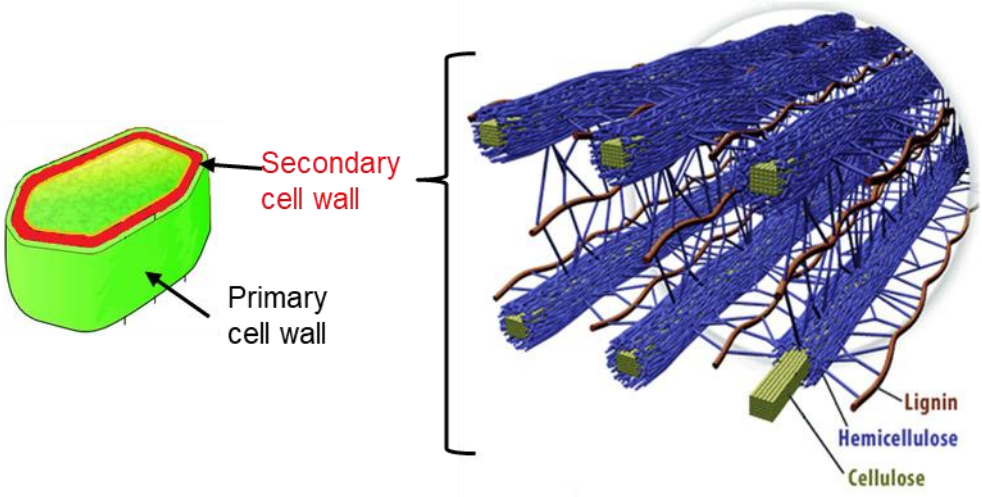

Figure 2: Source of lignocellulose and the network it forms. Cellulose chains stacked into microfibrils (yellow) are embedded into a matrix of hemicellulose (blue) and lignin (red) (adapted from [13]).

The composition of secondary cell wall is as diverse as the plants it makes up, and varies not only from plant to plant but also within the same plant in function of the tissue. In addition to proteins, it consists of three main components: Cellulose, making up 40-50 % of the dry weight, hemicellulose, making up 25-30 % and lignin with 15-20 % [1] (see Table 1). This composition gives it the name lignocellulose or lignocellulosic biomass.

Table 1: Composition of secondary cell wall [1].

	Cellulose (% dry weight)	Hemicellulose (% dry weight)	Lignin (% dry weight)
Wheat (straw)	35-39	22-30	12-16
Wheat (bran)	11-15	36-39	8-13
Pine	42-49	13-25	23-29
Cotton	85-95	5-15	0

Cellulose is a linear polysaccharide that consists of D-glucose monomers linked by ß-(1→4)-glycosidic bonds. The chains are of different lengths and can contain tens of thousands of glucose monomers. They are unbranched and tightly assemble themselves into microfibrils stabilized by hydrogen bonds.

This assembly leads to regular, crystalline regions that are interrupted by unordered, amorphous ones [14] (see Figure 3).

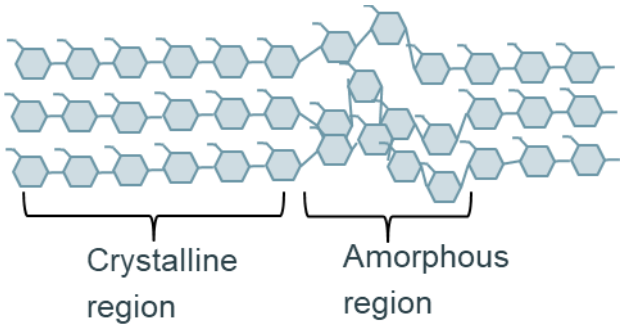

Figure 3: Schematic representation of the crystalline and amorphous regions of cellulose.

Unlike cellulose, hemicellulose is not crystalline and more varied in its structure and composition. Scheller *et al.* define hemicelluloses as polysaccharides with a ß-(1→4)-linked backbone, that consist of D-xylose, D-mannose, L-arabinose, D-galactose and D-glucuronic acid units (see Figure 4).

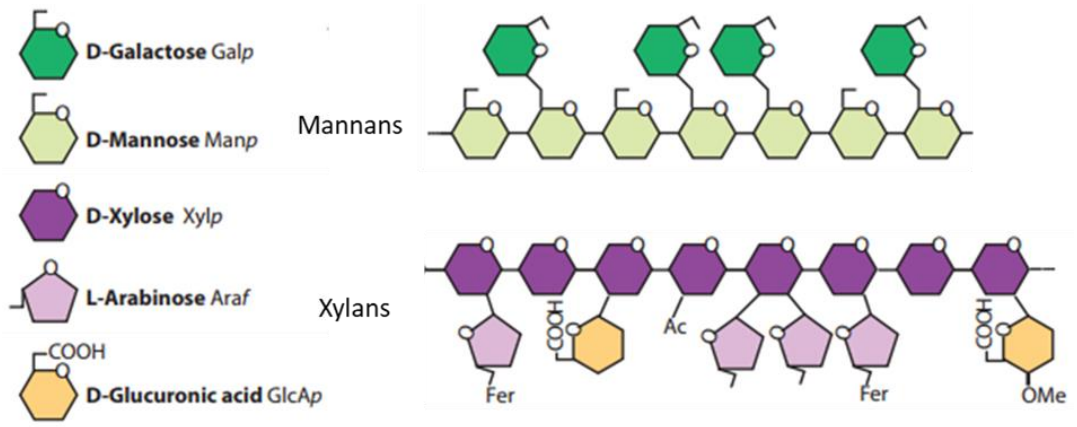

Figure 4: Schematic representation of the main hemicellulose polysaccharides found in secondary cell walls of plants. Fer represents esterification with ferulic acid (adapted from [15]).

While glucomannans and galactomannans are very abundant in the secondary plant walls of conifers (10-30 % w/w), glucuronoxylans mainly occur in hardwoods (20-30 % w/w). In grasses such as cereals, the main hemicellulose is arabinoxylan (40-50 % w/w), which makes it an abundant agricultural residue (see Table 2). Due to hydrogen bonding, hemicellulose has a high affinity to cellulose and non-covalently binds to the surface of the cellulose microfibrils [16]. Müller *et al.* showed that xylan for example, folds around the microfibrils in a twofold helical screw conformation [17]. Since xylan is especially important for this PhD, its structure will be further detailed later (section iii.a).

Table 2: Composition of hemicellulose [15].

	Hardwoods		**Grasses**		**Conifers**	
Polysaccharide (% w/w)	Prim.	Sec.	Prim.	Sec.	Prim.	Sec.
Xyloglucan	20-25	minor	2-5	minor	10	Abs/few
Glucuronoxylan	Abs/few	20-30	Abs/few	Abs/few	Abs/few	Abs/few
Arabinoxylan (AX)	5	Abs/few	20-40	40-50	2	5-15
(Galacto)gluco-mannan	3-5	0-3	2	0-5	Abs/few	10-30

The last component, lignin, is a complex, cross-linked polyphenolic polymer that consists of three main units: guaiacyl, syringyl and p-hydroxyphenyl. It is highly branched and has a randomly arranged structure that is often covalently linked to hemicellulose via ferulic acid for instance [18]. Lignin is often considered as the major contributor to biomass recalcitrance [19]. This recalcitrance has to be overcome for the valorisation of plant biomass, which will be discussed in the following section.

b. Valorisation processes

Over time, valorisation processes for plant biomass have evolved to use more and more complex substrates. In the beginning, most efforts were concentrated on starch- and sugar-rich or oily parts of plants (so-called first-generation substrates). With the advances in technology, processes evolved to unlock the valorisation potential of more complex biomass such as lignocellulose or the by-products of first-generation valorisation [2], [20]. These second-generation substrates are not in competition with food and feed applications and an important step towards an 'industrial metabolism', where all parts of the plant are valorised [21].

The valorisation process of plant biomass can be roughly divided into two steps that are 1) the deconstruction of complex plant polymers, especially polysaccharides, into simple sugars or other small molecules using a variety of physico-chemical and biological (pre-) treatments, and 2) the transformation of these sugars and molecules into more complex compounds using chemical or biological processes (Figure 5).

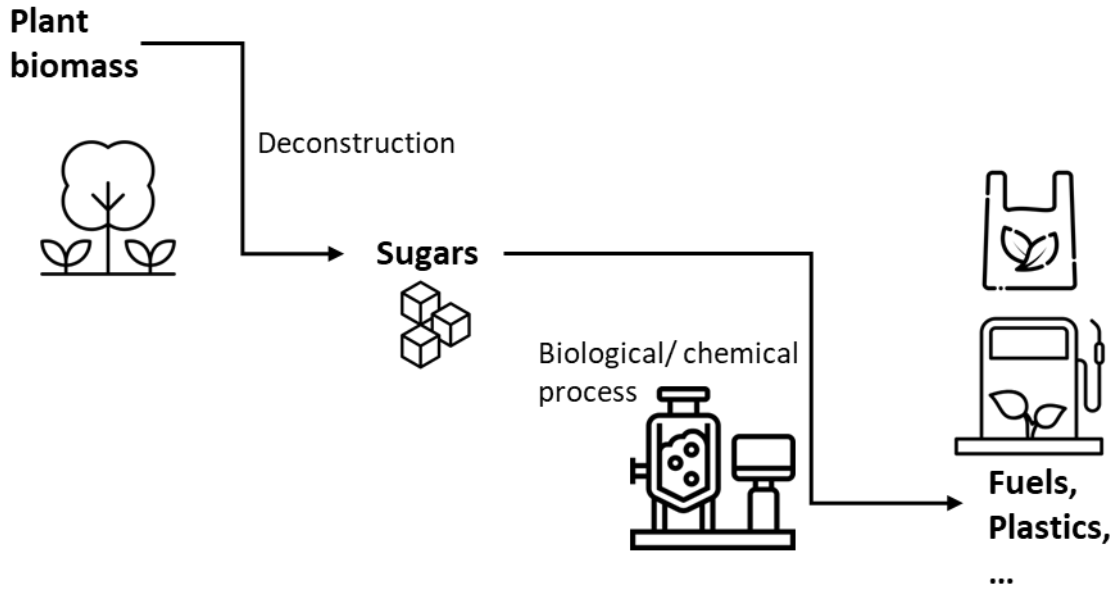

Figure 5: Simplified schema of the valorisation of plant biomass.

Depending on the kind of biomass that is used, the process is more or less difficult. Biomass like fruit, that is initially already very rich in sugars, can be directly used as a substrate for microorganisms for fermentations such as wine making. Lignocellulosic biomass on the other hand is a lot more difficult to process. Its structure is very complex and needs a pre-treatment to simplify it first and increase valorisation efficiency. Pre-treatments can be physical, chemical, to a lesser extent biological, and frequently a combination.

Physical pre-treatments like milling or grinding decrease the particle size and increase the surface area and accessibility for coupled chemical treatments. The objective of chemical pre-treatments is to weaken the lignocellulosic network by restructuring or removing one or several of its components, particularly lignins. Examples for chemical pre-treatments are the use of acids to remove hemicellulose by hydrolysation, the use of bases to attack lignin and hemicellulose, and the use of ionic liquids to increase porosity [1], [5]. Biological degradation involves the use of enzymes and will be detailed in **section c**.

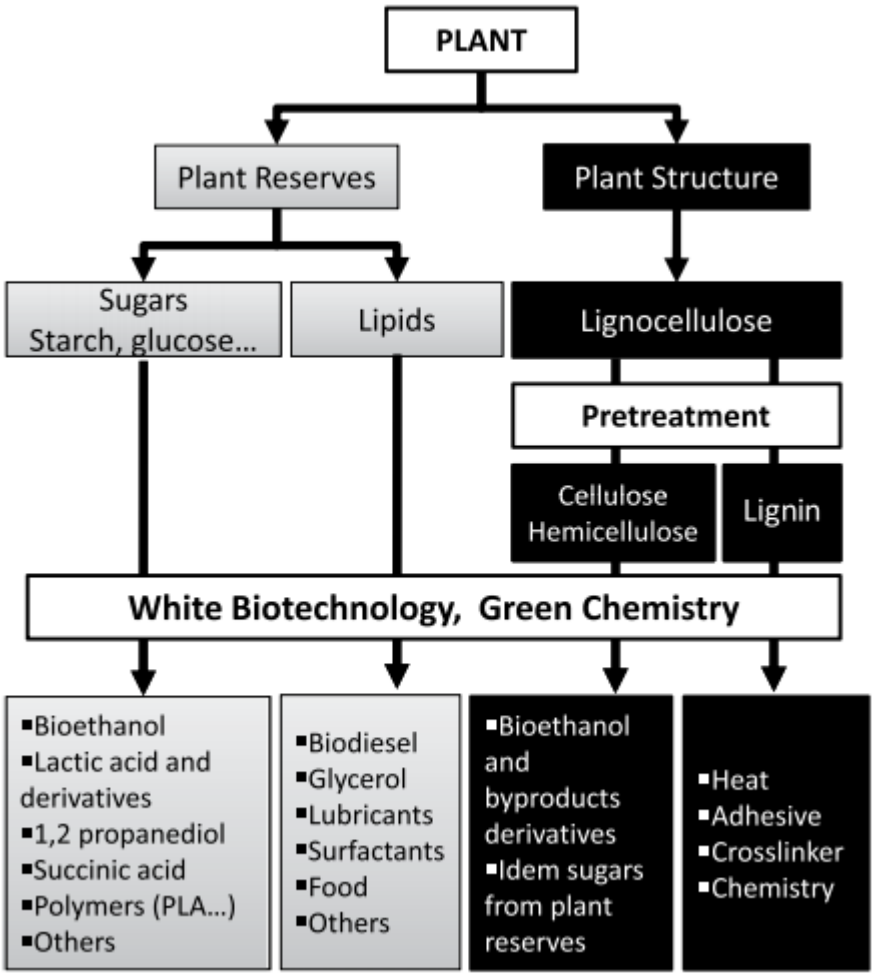

Figure 6: Whole plant valorisation using White Biology (enzymes and microorganisms) and Green Chemistry (chemical reactions that prioritise sustainability and environmental friendliness) [21].

After the pre-treatment, lignocellulose can be fractioned and the individual compounds can be further valorised.

The valorisation of cellulose has for a long time been the centre of research efforts, because it is very abundant and its monomer, glucose, a welcome substrate for many established industrial fermentations [22]. The use of cellulose or starch from plants like sugar cane or corn for the production of ethanol ('bio ethanol') as fuel is probably the best-known biotechnological process. After a mechanical and acidic pre-treatment, cellulose or starch are recovered and enzymatically hydrolysed to obtain glucose (saccharification). Glucose is in turn fermented into alcohol using yeasts [23]. Using different microorganisms, glucose can be used for the production of many more

compounds like polylactic acid for bioplastic [24], or glutamate and succinate as additives for the food industry [1]. In addition, cellulose can be chemically modified and used as emulsifiers or thickening agents in the food industry [25].

The valorisation of lignin is more challenging, because it is very heterogeneous and complex to depolymerise. However, it can be used to chemically produce high-value products like vanillin or solvents like benzene and toluene [26]. Azadi *et al.* used a solvent derived from lignin for the chemical down streaming of glucose and other biomass products [27].

Hemicellulose can make up to 30 % of lignocellulosic plant biomass, which makes its utilisation very interesting and important for the economic efficiency and feasibility of lignocellulosic biomass valorisation [1]. It mainly consists of hexose and pentose sugars that can be extracted from lignocellulose using a chemical pre-treatment and enzymatic hydrolysis. In general, hemicellulose can be used to produce a variety of chemical platform molecules such as ethanol, furfural, acetone or glycerol [28], materials such as bioplastics and other polymers or food and feed ingredients [29], [30]. One main sugar of hemicellulose is xylose, which can be used to produce fuel, prebiotics, bioplastic and other platform molecules using biological or chemical processes [22], [28].

We can see that there is a large potential in the valorisation of each compound of lignocellulose and that a lot of processes are in place. Nevertheless, all these processes rely on the efficiency of the deconstruction of the biomass for their yield. In turn, the deconstruction usually relies on expensive and resource intensive physico-chemical methods, because most demand high temperatures or pressure and large quantities of solvents [5]. This could be improved by including biological treatments. Here, enzymes are used to deconstruct lignocellulose under soft conditions in very targeted reactions. These enzymes can be found in nature, where microorganisms like mushrooms and termites produce them to decompose plants and trees every day.

Which and how enzymes can deconstruct lignocellulose is discussed in the next section.

c. Enzymatic deconstruction of lignocellulose

Enzymes are substrate-specific proteins with a catalytic activity. Lignocellulolytic enzymes can be divided into cellulose degrading enzymes, hemicellulose degrading enzymes and lignin degrading enzymes according to their substrate.

Enzymes that deconstruct lignocellulose can be found in nature, where they are secreted by fungi like *Aspergillus*, *Penicillium*, and *Trichoderma* or bacteria like *Bacillus* and *Clostridium* [31]. One major group of lignocellulolytic enzymes are enzymes that catalyse the hydrolysis of glycosidic bonds, the bonds that make up the polysaccharides. These enzymes are called glycoside hydrolases (GH) and are classified into different families according to their primary sequence (see CAZy database [32]).

The degradation of cellulose into its glucose monomers requires three main enzymatic activities: endo-1,4-ß-glucanases, exo-1,4-ß-glucanases, and ß-glucosidases (Figure 7). The first one hydrolyses in the middle of the cellulose chain, while the others hydrolyse it from the reductive or non-reductive ends. The last step, the hydrolysis of cellobiose to glucose, is catalysed by glucosidase [33]–[35]. The activity of these enzymes leads to an erosion and defibrillation of the cellulose fibres until they are fully hydrolysed [36].

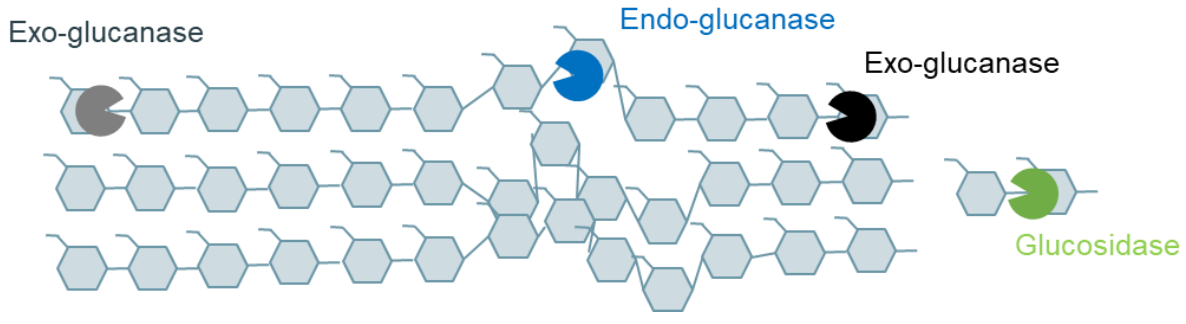

Figure 7: Schema of the enzymatic deconstruction of cellulose.

To degrade hemicellulose, a branched polymer, enzymes cleaving the backbone as well as enzymes cutting the branches are needed (Figure 8). Depending on the type of hemicellulose, countless different enzymes such as mannanases or xylanases are involved in the deconstruction. In the case of arabinoxylan, endo-1,4-ß-xylanase randomly cleaves the xylan backbone into oligomers, followed by the action of exo-1,4-ß-xylosidase that can hydrolyse the xylose oligomers into monomers. Their action relies greatly on the accessibility of the backbone- and therefore on the action of α-L-arabinofuranosidase, that removes arabinose branches. Other hemicelluloses need equivalent enzymes depending on their sugar composition, such as ß-mannase for a mannose backbone. Additional enzymes to remove further decorations are carbohydrate esterases and α-glucuronidases [22], [37].

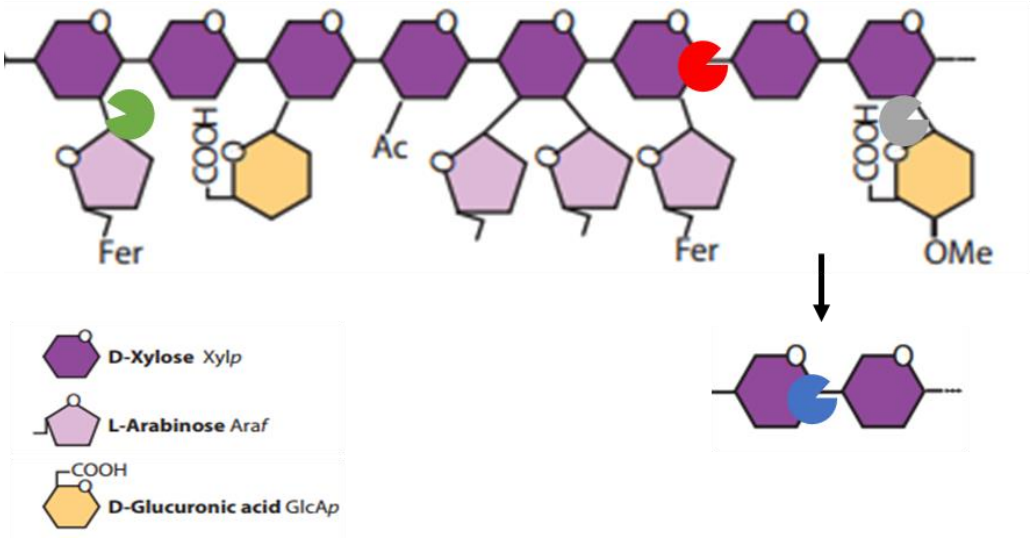

Figure 8: Schema of the enzymatic deconstruction of decorated xylan endo-xylanase (red symbols), exo-xylanase (blue symbols), arabinofuranosidase (green symbols) and glocuronidase (grey symbols). Adapted from [15].

For the degradation of lignin, laccase, lignin peroxidase and manganese peroxidase play an important role [38].

Another group of enzymes involved in the degradation of polysaccharides are lytic polysaccharide monooxygenases (LPMO). Contrary to the action of glycoside hydrolases, they do not hydrolyse the glycosidic linkage of polysaccharides, but they catalyse their oxidative cleavage. Due to the fact that they can oxidize recalcitrant internal bonds of the chain, they can facilitate the access for other endoenzymes [39].

Most of those enzymes work together in synergy [33], meaning that the action of several enzymes together is higher than the sum of the respective activities when the enzyme works alone. For example, hemicellulases cleave the matrix, granting cellulases access to cellulose [40]. Or endo-xylanases, hydrolysing long chains into shorter ones, thus creating more chain ends for the action of xylosidases. The extent of this synergy becomes very evident in nature, where some anaerobic bacteria even produce very efficient multi-enzyme complexes, so called cellulosomes, where cellulases and other carbohydrate active enzymes are physically linked together [41], [42].

Another special feature of many lignocellulolytic enzymes are carbohydrate binding modules (CBMs) [34], [43]–[45]. They are a part of the multi-modular structure of the enzyme and possess a special fold that has no catalytic activity. This fold binds to the substrate itself or to another substrate in close proximity, consequently enhancing substrate-enzyme affinity. The exact mechanism of the action of CBMs is still in debate, but it is well admitted that CBMs bring their appended enzymes in close proximity to the target substrate leading to an increase in activity (see Figure 9) [43].

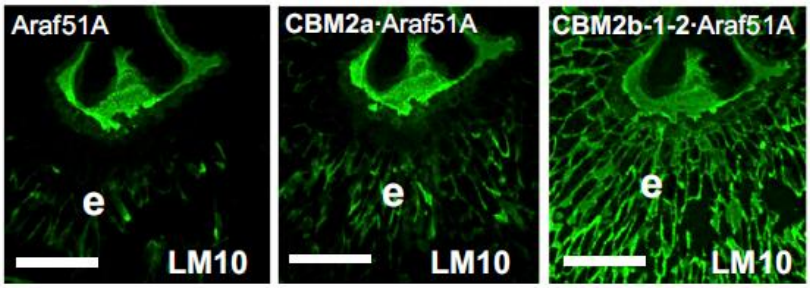

Figure 9: Indirect immunofluorescence microscopy pictures of a wheat grain endosperm cell wall. The enzyme (Araf51A) targets arabinoxylan and strips the arabinose residues off the xylan backbone. By doing so, it makes the xylan accessible for the fluorescent antibody (LM10). The presence of CBMs (middle and right picture) shows an increase in fluorescence compared to their absence (left picture), indicating more accessible xylan for the fluorophore and consequently more effective enzymatic action. CBM2a binds to cellulose whereas CBM2b binds to xylan, making it more effective [43].

We can see that in nature, the complexity of lignocellulose is met with an equally complex mixture of enzymes that work together for degradation. Therefore, a first strategy for the development of more eco-friendly industrial processes is to go look for new enzymes in nature, for example in termite hindguts [46], [47], bovine rumen [48], or in soil [49]. Another possibility is the use of molecular engineering to create more efficient enzymes by directed evolution [50], site directed mutagenesis [51], through structural changes [52], or to create new multifunctional enzymes [53].

Instead of looking at only one enzyme, interactions and synergies between different enzymes can be exploited as well by using enzymatic cocktails [54] and synthetic cellulosomes [55].

Enzymatic deconstruction is often characterised using 'simple' substrates like purified polysaccharides or oligosaccharides in dilute solution [56]–[58], and determining the rate at which the enzyme cleaves or otherwise modifies this substrate. For this, the product that is created over time is either directly quantified or indirectly quantified, where it is revealed through a reaction that leads to a change in colour, pH or other. Traditionally, enzymes are characterised by the initial reaction rate, which is the rate directly upon contact with their substrate. Usually, this initial reaction rate increases with the substrate concentration, following the Michaelis-Menten kinetics model (see Figure 10) [59]. For low substrate concentrations, the substrate is the limiting factor and the reaction rate increases with increasing concentration. As soon as all enzymes are saturated with substrate and working at full capacity, the reaction rate reaches a plateau and shifts from substrate-limited to enzyme-limited. The plateau represents the maximal reaction rate, V_{max} and the substrate concentration that corresponds to half its value is the Michaelis-Menten constant K_M. The smaller this constant, the higher the affinity of the substrate. K_M and the initial enzyme concentration allow the calculation of the catalytic constant k_{cat}.

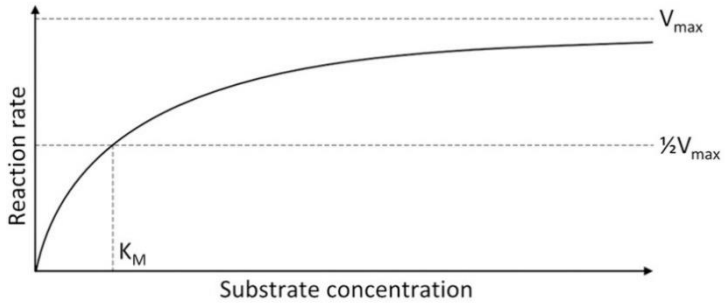

Figure 10: Evolution of the initial reaction rate of an enzyme in dependence of substrate concentration [60].

The deconstruction of natural substrates on the other hand is mainly characterised by observing the structure of the biomass and its changes during enzymatic attack. This can be done using techniques like scanning electron microscopy [61] and optical microscopy coupled with staining [62], atomic force microscopy [63], fluorescence microscopy [64], [65] and X-ray microtomography [66] (see Figure 11).

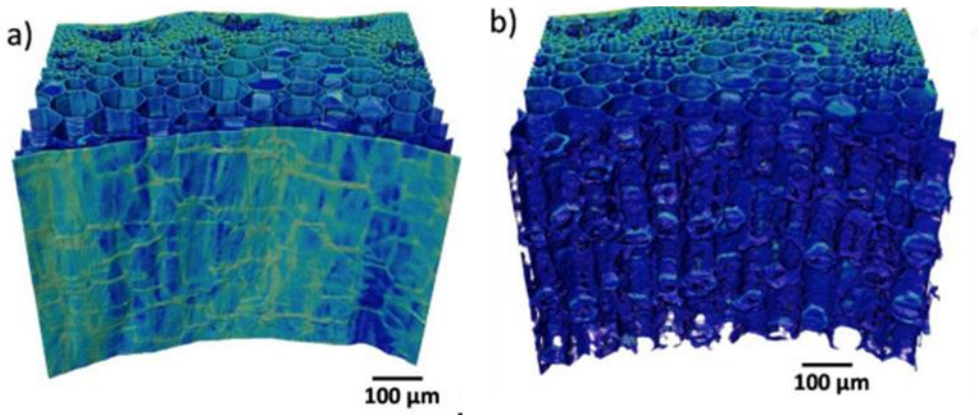

Figure 11: Example of the use of X-ray microtomography to study the enzymatic deconstruction of a wheat straw. The reconstructed 3D structure before (a) and after 72 h of enzymatic degradation (b) shows the impact of the enzymatic action [66].

The characterisation using natural substrates is complicated, but it respects the real working conditions of the enzymes and consequently gives a more accurate picture of the degradation. For one, the consideration of the chemical structure and composition is important, because not only the substrate can determine the affinity and activity of the enzyme, but also its environment [67]. Another important factor is the physical structure, which is characterised by a heterogeneous and potentially very high polymer concentration. This results in a porous network, which impacts substrate accessibility and therefore deconstruction [68], [69].

In this PhD project, we consider the factor of polymer concentration for our characterisation and study the propagation of the enzyme as they navigate and degrade this polymeric substrate.

iii. Specific Questions

a. Can high polymer concentrations affect enzymatic deconstruction?

For the degradation to occur, the enzyme has to access its target substrate and bind to it, forming an enzyme-substrate complex. At high polymer concentrations however, the accessibility of the substrate can be limited. For one, the high concentration could prevent the enzyme from penetrating into fibrous substrates due to obstruction effects [70]. Inside the concentrated substrate, the polymer chains can trap the enzyme and thus limit its movement and the access to the target site. This was observed by Cheng *et al.* for the degradation of guar by mannase [6]. They observed that for high guar concentrations, the reaction rate deviated from the Michaelis-Menten predictions and decreased due to diffusion limitation (see Figure 12). This diffusion limitation also plays a role in the degradation of gels [71], [72].

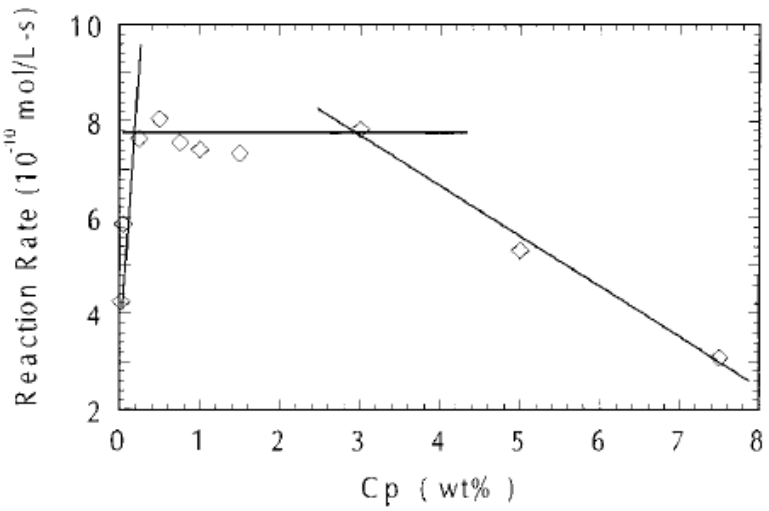

Figure 12: Reaction rate of ß-mannase in its polymeric substrate (guar) as a function of the substrate concentration [6].

Another phenomenon that can impact the degradation is the inhibition caused by the presence and accumulation of the products of the reaction. This long-term effect (hence not visible in the previous graphs dealing with initial reaction rates) makes the enzyme work less and less efficiently with time, because the enzyme encounters an increasing number of reaction products which occupy the active site and block the access for larger molecules [73]. In the case of lignocellulose degradation, enzymes can in additon be inhibited by unspecific binding to lignin [74]–[76].

b. What determines the propagation of the enzyme in its polymeric substrate?

Studies on the diffusion of enzymes in complex structures, like a polymeric substrate, are scarce, and especially studies that consider the impact of the enzymatic activity [11], [77]. In simpler environments, like aqueous solutions, the propagation of the enzyme is diffusive and follows the principles of a three-dimensional random walk like any small particle [78]. This means that every step is independent of the previous one and that at every step, all directions are equally probable. Looking at this as a one-dimensional problem, a particle can move either back or forth with each displacement. Therefore, the position x of a particle at any given step n can be described as its previous position (n – 1), plus or minus a step length δ:

$$x\,(n) = x\,(n-1) \pm \delta \quad (Equ.\,1)$$

Due to the randomness of the displacement, half of the particles will go forward (+ δ) and half of them backward (- δ), eliminating the last term in the equation. Consequently, the average displacement of a particle does not change from step to step. The particles do however spread out around their origin, leading to a Gaussian distribution (Figure 13). Their spreading can be described by the mean square displacement, obtained after squaring Equ. 1:

$$\langle x^2(n)\rangle = n\delta^2 \quad (Equ.\,2)$$

As the time of the displacement is the product of the number of steps n and the step duration τ, n can be substituted in Equ. 2:

$$\langle x^2(t)\rangle = \frac{\delta^2}{\tau}\,t \quad (Equ.\,3)$$

The term $\frac{\delta^2}{2\tau}$ is defined as the diffusion coefficient D, leading to a final expression of the mean square displacement as

$$\langle x^2(t)\rangle = 2Dt \ \ (\text{one} - \text{dimensional}) \ \ (Equ. 4)$$

The mean square displacement increases with time, leading to an increase in the standard deviation of the distribution and a spreading of the peak in Figure 13.

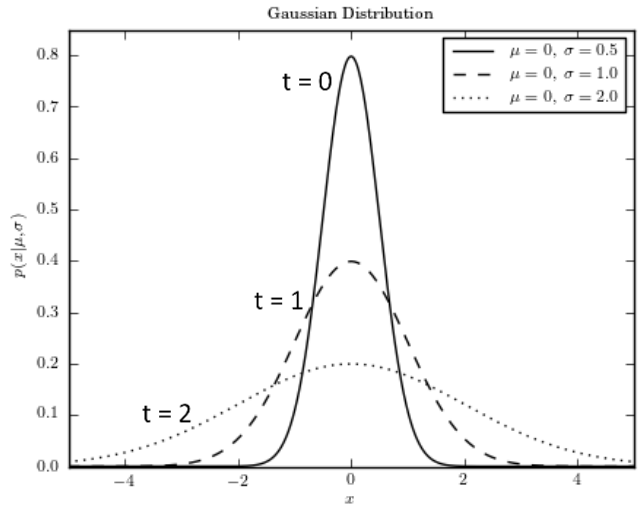

Figure 13: One-dimensional diffusion: A schematic of the probability of finding particles at different points x. The probability follows a Gaussian distribution, spreading out over time (solid to dashed line)[78] .

Similarly, when the movement in all three dimensions is considered, the expression for the mean square displacement is

$$\langle x^2(t)\rangle = 6Dt \ (\text{three} - \text{dimensional}) \ \ (Equ. 5)$$

In an aqueous solution, the diffusion of a particle can be considered as 'free' and is only influenced by its hydrodynamic radius r_h, the temperature T and the viscosity η of the solution. This is described by the well-known Stokes-Einstein relationship [79] for the diffusion coefficient, including the Boltzmann constant k_B:

$$D = \frac{k_B T}{6\pi\eta r_h} \quad (Equ. 6)$$

While this equation describes the diffusion of a single particle, the diffusion flux J_u of many particles can be described using Fick's first law [80]. This law states that the flux of particles is proportional to their local density gradient $\frac{\partial\rho}{\partial u}$ at a given location r, linked by the diffusion coefficient D.

$$J_u(r,t) = -D\,\frac{\partial\rho\,(r,t)}{\partial u} \qquad (u = x,y,z)\ \ (Equ. 7)$$

The flux goes from regions of high concentration to regions of low concentration, following the gradient.

At high polymer concentrations however, the diffusion of small particles is slowed down, resulting in an effective diffusion coefficient D_{eff} that is smaller than the diffusion coefficient in pure solvent (D_0). Curiously, while D_{eff} is found to be smaller than D_0, it is still faster than predicted by the Stokes-Einstein equation using the viscosity of the polymer solution (Equ. 6) [81]–[83]. This could be explained by the fact that the nanoparticles' diffusion is much faster than the dynamics of the polymer chains. Therefore, the chains remain almost static, limiting the effect of their viscosity on the nanoparticle diffusion. Or it could be a matter of size, and the nanoparticles are simply too small to feel the 'full' solution viscosity but rather a 'microscopic' or effective viscosity, somewhere between the viscosity of the pure solvent ant the solution viscosity [82].

Quite obviously, diffusion was found to decrease with increasing polymer concentration [81]–[83]. This can be explained by the network formed by the polymer chains in solution and its evolution with polymer concentration. At high concentrations, the polymer chains overlap and form a network (Figure 14). This network can be characterized using two length scales, the correlation length ξ and the pore size a [84]. The correlation length is defined as the average distance between the two nearest monomers of different polymer chains and is typically 5 times smaller than the pore size (a ≈ 5*ξ).

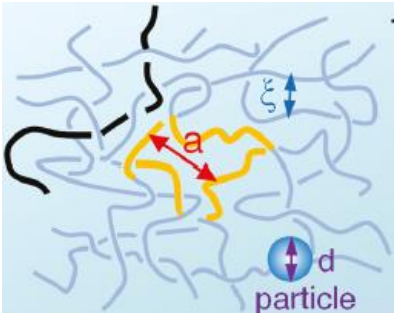

Figure 14: The schema of a concentrated polymer network. It can be characterised using the correlation length ξ and the pore size a [84].

With increasing polymer concentration, the mesh tightens and its size (correlation length) decreases [85], [86]:

$$\xi\,(c) \propto R_g\,(\frac{c}{c^*})^{-0{,}76} \quad (equ.8)$$

Where M_w is the molecular weight of the polymer, N_A Avogadro's constant, c* the overlap concentration and R_g the gyration radius.

Depending on the size of the particle, or rather the size of the particle relative to the mesh size, the particle will be more or less confined within the polymer network. Accordingly, the particle size (d) to mesh size ratio (ξ) is a key parameter for the diffusion of nanoparticles in polymers and can be used to define different mobility regimes, as done in an extensive theoretical study by Rubinstein *et al* [84] .

We can see the complexity of the diffusion of particles in polymer solutions and the impact of the polymer concentration and mesh size. What about more enzyme-specific factors, such as the structural impact of its activity on the diffusion?

In the previously mentioned study by Rubinstein *et al.* [84], the impact of the length of the polymer chains at constant volume fraction on the diffusion of nanoparticles was considered as well. So, even though it is not the particle itself that changes the size of the polymer as an enzyme would do, the effect on the polymer is the same, and it is possible to relate these findings to the case of enzymatic diffusion.

Figure 15 traces the diffusion coefficient in function of the polymer length N. Reading N from right to left, so in the sense of a degradation, it starts with chains so long they entangle ($N > N_e$). Then, as N decreases, the solution passes by the unentangled, overlap, semi-dilute regime ($N_e > N > N_d$), and finally the dilute concentration regime ($N_\xi > N$). Reading this figure from right to left, meaning with decreasing N, we can describe the behaviour of the particles according to their size as briefly explained below:

(i) If the particle is smaller than the correlation length of the network, its diffusion corresponds to the diffusion in pure solvent, no matter the length of the polymer chains (dashed line, read from right to left with decreasing N).

(ii) For particles larger than the correlation length but smaller than the pore size $a \approx 5\,\xi$ (dash-dotted line), Rubinstein shows that they have a constant diffusion coefficient in the regime where $N > N_d$, i.e. until the size of the chains gets close to the size of the particle. Then, when the size of the particle gets larger than the polymer ($N < N_d$), there is a regime where the particles 'feel' the viscosity of the polymer, such as their relative diffusivity increases linearly with N. Then, there is a degree of polymerisation N_ξ, starting from which the particles do not 'feel' the presence of the polymer anymore ($N < N_\xi$). Therefore the diffusion, as in case (i), corresponds to the diffusion in pure solvent.

(iii) In the entangled regime ($N > N_e$), the diffusion coefficient of large particles (full line) is highly impacted by the polymer. The relative diffusivity increases as a power of 3 with the degree of polymerisation. Then, once the chains are too short to

entangle, the diffusivity increases sharply and then follows the behaviour of intermediate particles.

This recent -and quite complex- theory, from the group of one the most influential researcher in the polymer community, is a 'scaling' theory; meaning it has not the ambition to predict quantitatively the diffusion coefficient of a specific tracer in a polymer solution. However, it has the merit to give an explicit picture of what we could expect for the diffusion on a particle in a polymer solution where N is changing.

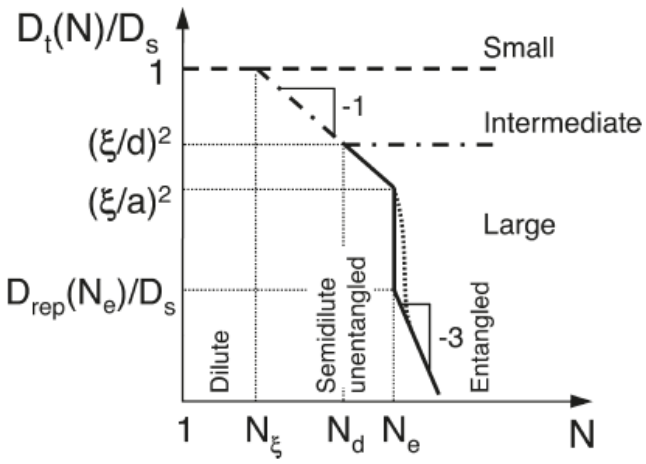

Figure 15: The development of the normalized terminal diffusion D_t coefficient in dependence of the chain length N of the polymer (degree of polymerisation). D_s is the diffusion coefficient in absence of polymer. The concentration of the polymer is constant, however the changes in its length lead to different concentration regimes (dilute, semi-dilute unentangled, entangled). Different particle sizes are considered: particles smaller than the correlation length ξ (small, dashed line), particles larger than ξ but smaller than the pore size a ≈ 5ξ (intermediate, dash dotted line) and particles larger than the pore size (large, solid line) [84]. We refer the reader to article [84] for the detailed definition of N_e, N_d, and N_ξ.

One peculiar phenomenon of enzymatic diffusion that has captured attention in recent years is the so-called 'enhanced enzymatic diffusion', or EED. EED is a potential increase in the diffusion coefficient of the enzyme in presence of its substrate. It was observed for enzymes like urease [7], [10], [87]–[89], aldolase [89]–[91] and catalase [10], [88]. Muddana *et al.* [10] found that the diffusion coefficient of urease increased by almost 30 % in presence of its substrate (Figure 16).

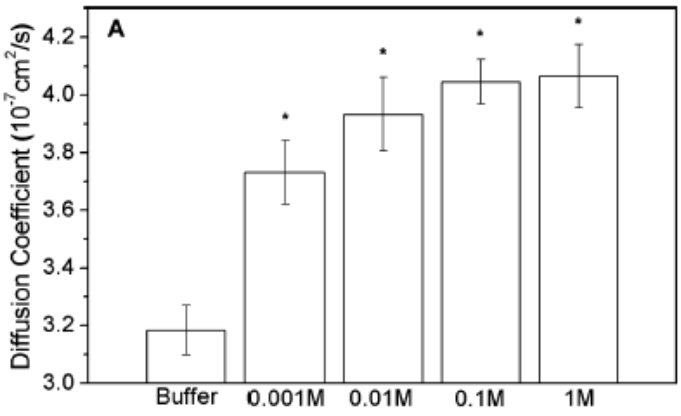

Figure 16: Diffusion coefficient of urease plotted against buffer or urea concentration determined using fluorescence correlation spectroscopy [10].

There are several theories that were proposed to explain this possible EED [9], [92]. In the case of urease, the reaction creates ammonium and bicarbonate ions that could create a local electric field that impacts the enzyme. Moreover, during substrate binding and unbinding, the size of the enzyme can decrease as it gets more compact. It is however in doubt whether this change is large enough to explain EED. Thermal effects, such as the exothermicity of a lot of the reactions catalyzed by the studied enzymes, could also lead to local changes in the diffusion coefficient.

Granick *et al.* [8] did an extensive study including ten catalytic enzymes with a wide range of catalytic turnover rates and using two independent measurements of mobility, FCS and dynamic light scattering. In this study, they found that the boosted diffusion is directly proportional to the product of the reaction rate and the Gibbs free energy of the system, the 'free energy release rate' (see Figure 17).

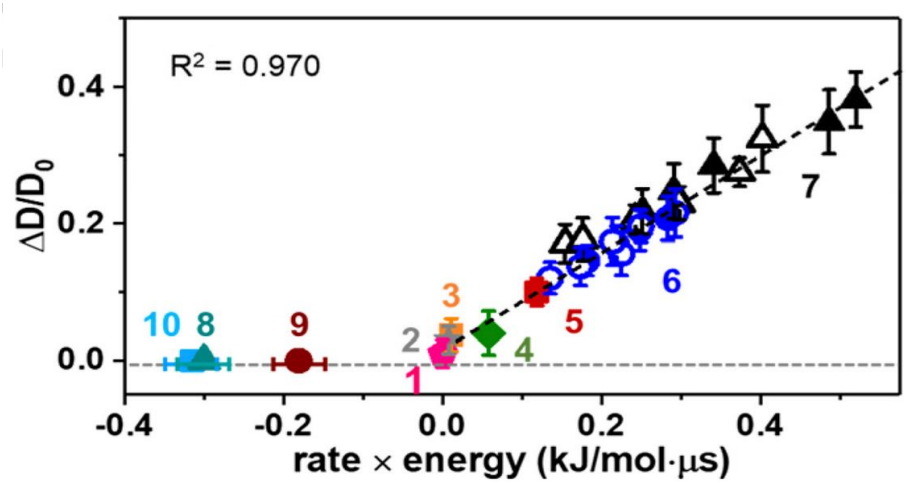

Figure 17: Plot of the normalized diffusion coefficient as a function of the free energy release rate. $\Delta D = D\text{-}D_0$ (measured diffusion coefficient D minus the diffusion coefficient in pure solvent D_0). Enzymes are fructose bisphosphate aldolase (1), phosphofructokinase (2), pyruvate kinase (3), hexokinase (4), phosphoglucoisomerase (5), acetylcholinesterase (6), urease (7), phosphoglycerate kinase (8), triosephosphate isomerase (9)*, alkaline phosphatase (10)*. Filled symbols correspond to DLS measurements, empty ones to FCS. Enzyme 6 and 7 include auxiliary measurements at different temperatures and pH to study their impact on EED. *endotherm [8]*

Very recently, Bonnin *et al.* [11] found the diffusion of pectin methylesterase in a polymer matrix enhanced in the presence of substrate, transferring this phenomenon from monomer to polymer systems.

v. Strategy

Based on the previous exposition, we can see that the knowledge concerning the mechanisms involved in the diffusion and activity of enzymes in a polymeric substrate remains fragmentary. Two important questions are the impact of the polymer on the activity of the enzyme, as well as the effect of the polymer and the activity of the enzyme on its mobility. The investigation of these questions is the fundamental objective of this work.

Due to the complexity of the questions, the model system used was kept as simple and controllable as possible: Only one hemicellulose polymer (arabinoxylan) was used as substrate that was degraded by one type of hemicellulase (xylanase).

In the following chapter, we will go over the different aspects of this strategy. At first, the two components of the model system are presented: the polysaccharide arabinoxylan and the xylanase (**section a**). Then, we will give details on the approach used to study the effect of polymer concentration (**section b**) and to study the diffusion of the enzyme (**section c**).

a. Model system

Arabinoxylan is a very common hemicellulose, especially in non-food crops and by-products like grasses, where it can make up to 50 % of cell wall content [15]. Its abundance and the fact that it is a non-food substrate makes it a very interesting candidate for valorisation and consequently for this study [93]–[95].

Arabinoxylan is a linear polysaccharide with a backbone of ß-(1,4) linked D-xylopyranose units, randomly carrying L-arabinofuranose constituents on the oxygens in position O2 and/or O3 [96] (see Figure 18). Other possible constituents are acetyl groups or methyl glucuronic acid, and arabinose substituents can carry ferulic acid groups. The degree of substitution varies within plant species, stage of development and type of tissue, and impacts the interactions of arabinoxylan with cellulose and lignin. While ferulic acid can be a covalent link to lignin [18], the degree of substitution and even the substitution pattern of arabinoses on the xylan backbone modulate the adsorption of arabinoxylan on cellulosic surfaces [97].

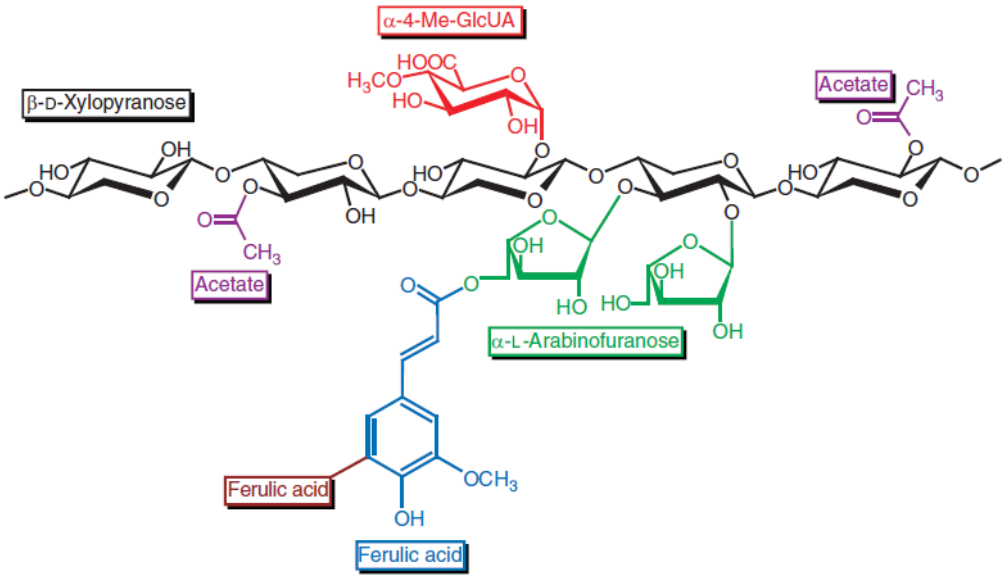

Figure 18: General structure of arabinoxylan [96].

The arabinoxylan used in this study is a commercially available water-soluble polysaccharide extracted from wheat flour. Its solubility allows the production of homogeneous solutions, which is an advantage for characterisation. While its specific extraction and purification protocol is unknown, it generally includes the removal of starch and proteins using enzymes, followed by an alkali treatment to remove ferulic acids and a recovery with ethanol precipitation [98]. Consequently, the structure of the arabinoxylane used here is a lot simpler and is principally composed only of xylose and arabinose (see Figure 19). Due to the absence of charged substitutions like ferulic or glucuronic acid, the polymer is globally neutral and does not have electrostatic interactions with its surroundings, which helps to keep the model system as simple as possible.

Arabinoxylan solutions were used at different concentrations, up until concentrations where the chains of the polymer theoretically start to obstruct the enzyme. The choice of the preparation for these concentrated polymer solutions as well as their characterisation is an important part of this PhD project and the subject of **Chapter III** (submitted article). In that chapter, we identified a preparation protocol that leads to a good solubilisation at high polymer concentrations. We also determined local and intermediate dimensions of the polymer chains like its size, cross-section and stiffness. Finally, we studied the organisation of the polymer chains in solution. We determined the overlap concentration c*, at which the chains start to form a network and then how this network evolved with polymer concentration.

The endo-xylanase for this study is called *Np*Xyn11A, from the fungi *Neocallimastix patriciarum.* We chose this enzyme, because it cleaves the ß-(1,4) glycosidic bond of the backbone of arabinoxylan (Figure 19) and consequently has an obvious impact on the structure of the polymer. Its optimum temperature and pH are 37 °C and 6 respectively. According to its primary amino-acid sequence, it is classified into the glycoside-hydrolase family 11 (GH11) of the CAZy database.

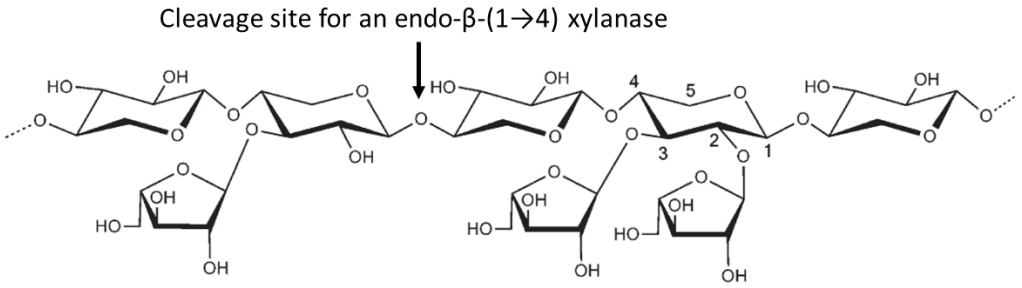

Figure 19: Schema of an arabinoxylan showing the cleavage site for an endo-xylanase belonging to the glycoside hydrolase family 11 (adapted from Köhnke et al.[97])

Since there is a close relation between primary sequence and structure of an enzyme, *Np*Xyn11A and all xylanases in the GH-11 family have two structural characteristics in common. The first one is the conserved catalytic domain forming a so-called jelly-roll, a barrel-like architecture that consists of eight beta strands. The second one is a characteristic long loop located between strands B7 and B8 (Figure 20) [99]. Because of these characteristics, the overall structure of *Np*Xyn11A resembles a partially folded right hand, with the long loop representing the thumb. It is a globular enzyme of approximately 6 nm in size estimated using DLS, and a molecular mass of 26 kDa.

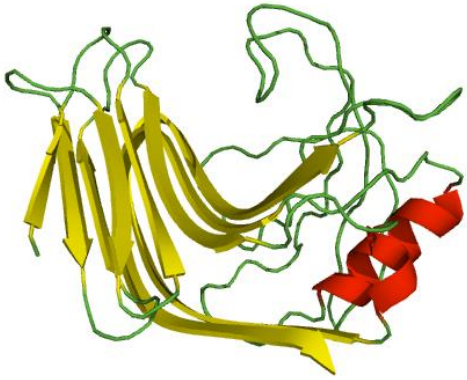

Figure 20: The three-dimensional structure of NpXyn 11A with β sheets (yellow,) α-helices (red) and loops (green) [99].

The substrate is hydrolysed by a double displacement acid-base assisted mechanism inside the catalytic site. The catalytic site of the enzyme has the shape of a long open cleft that interacts with the polymer in several locations, so called subsites (Figure 21). Each one of these subsites can bind to one, possibly decorated, sugar unit through hydrogen bonding interactions. They are numbered from +1 to +n for the reducing end moieties and -1 to -n for the non-reducing end moieties. The catalytic site lies between subsites 1 and -1, that cannot accommodate a decorated sugar unit. *Np*Xyn11A can recognize and accommodate up to six xylose residues with identified subsites from -3 to +3 on both sides of the catalytic site [100]. According to Montanier *et al.* [101], the optimum temperature and pH of the enzyme are 37 °C and 6-7 respectively. For the degradation of our substrate, an optimum pH of 6 was found (results not shown).

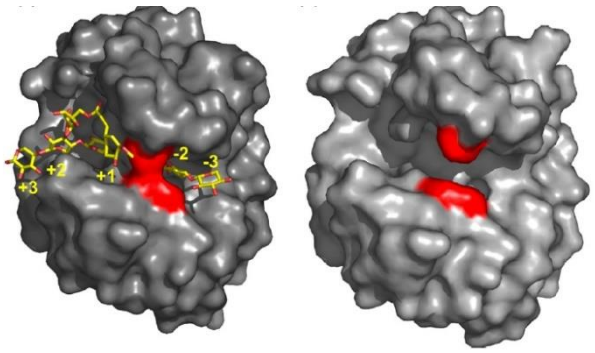

Figure 21: The surface of EyXyn, homologue to NpXyn11A, showing the cleft of the active site closed (left) and open (right), clasping its substrate[100]. Subsites +1 to + 3 accommodate the reducing end moiety and negative subsite accommodate the non-reducing end moiety.

In case of the inactive enzyme, the nucleophile catalytic amino acid E113 is mutated to alanine, which quenches its activity without impact on the enzyme's size.

b. Study of the impact of the polymer concentration

Here, we are in the case where the enzymes are considered to be dispersed homogeneously in the polymer solution before their activity is triggered (an ideal case which – as explained later - we tried to reproduce in our experiments).With increasing polymer concentration, the network formed by the chains of the polymer tighten and, sooner or later, affect the mobility of the enzyme. Can this in turn affect its activity? To study possible effects of the polymer concentration on the deconstruction, we considered the initial activity of the enzyme as well as the size of the degradation products.

The activity was measured using a colorimetric activity assay that quantifies the number of catalytic events. Does a high polymer concentration lead to a diffusion limitation of the reaction and decrease the activity? If yes, can this be linked to the network characteristics, such as the mesh size?

The size of the degradation products is measured using size-exclusion chromatography coupled with multi-angle light scattering (SEC-MALS). Does a locally ‘confined’ enzyme work differently than a ‘free’ enzyme? Will the local confinement of the enzyme lead to a more thorough, repeated attack on the surrounding chains, creating smaller degradation products?

These questions will be addressed in **Chapter IV**.

c. Tracking of enzymatic mobility using fluorescence microscopy

Here, we are in the case where a localised source of enzymes gets into contact with the polymer solution, and then propagates into this substrate (no homogeneous dispersion). In this case, there is the important notion of *directionality* of the enzymatic attack, that we proposed to address by following the concentration gradient of the enzymes while they enter their substrate.

For that, we used fluorescence, which is a common technique for particle tracking, especially in biological systems. It relies on the detection of fluorescence, a photoluminescence phenomenon where molecules, so called fluorophores, that are brought into an electronically excited state emit light as they return to their ground state. This phenomenon can be divided into three steps (see Figure 22). In the first step, excitation, an electron on the ground state level absorbs light at a specific wavelength. The absorbed light will boost the electron into a higher energy state that consists of several levels. Once in the excited state, the electron will lose some of its energy as it falls back to the lowest level of the excited state through a process called vibrational relaxation. Then, in the final step of emission, the electron returns to its ground state by emitting a photon. Emission generally occurs almost instantly at lower energy than excitation, so at a longer wavelength [102].

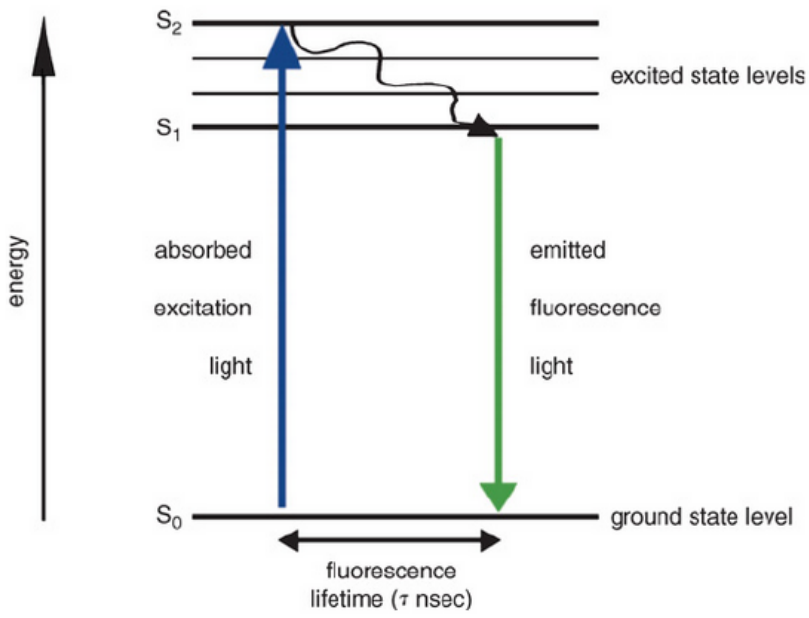

Figure 22: Jablonski diagram displaying the different energy levels of an electron in terms of fluorescence. Absorption of light excites the electron from ground state level (S_0) to excited state level (S, blue arrow). Then, the electron transitions to the lowest level of the excited state by vibrational relaxation (black arrow), before dropping back to the ground state level by emitting fluorescence light (green arrow) [103].

Usually, a molecule cannot undergo this process indefinitely. After a certain time, the molecule undergoes photon-induced damage and loses its ability to fluoresce (photobleaching). While photobleaching reduces the fluorescence of a molecule irreversibly, quenching is reversible. Quenching is concentration dependent and due to the re-absorption of the emitted fluorescence by the solution [102]. This leads to a non-linear relationship between polymer concentration and fluorescence intensity at high concentrations (see Figure 23).

Fluorescence is closely linked to absorption, because the light emitted by a fluorophore (I_f) is proportional to the absorbed light (I_a):

$$I_f = \Phi_f * I_a \quad (Equ. 9)$$

Where ϕ_f is called the quantum yield that describes the efficiency of the fluorescence emission as the ratio of photons emitted to photons absorbed, ranging from one to zero [102].

The intensity absorbed by the fluorophore can be expressed as the difference between the initial and transmitted intensity:

$$I_a = I_0 - I_t \quad (Equ. 10)$$

Furthermore, the transmitted intensity is defined as:

$$I_t = I_0 * 10^{-\varepsilon lc} \quad (Equ. 11)$$

Substituting equ. 9 using equ. 10 and 11, we obtain

$$I_f = \Phi_f * \left[I_0 - \left(I_0 * 10^{-\varepsilon lc}\right)\right]$$

$$I_f = I_0 * \Phi_f * [1 - 10^{-\varepsilon lc}] \quad (Equ. 12)$$

With ε the molecular extinction coefficient, l the length of the optic path and c the concentration of the fluorophore.

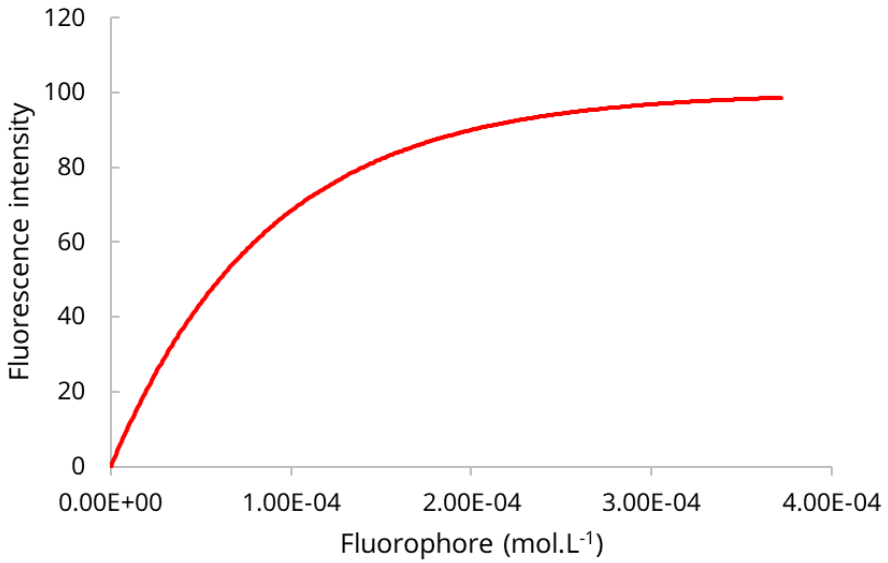

Figure 23: Exemplary evolution of the fluorescence intensity as a function of fluorophore concentration (Equ. 12). For small concentrations, a linear approximation can be used. For high concentrations, a plateau is reached as the fluorescence is more and more reduced by re-absorption (quenching).

The tracking of particles using fluorescence can be categorized into two groups: single particle tracking or ensemble motion tracking [104]. Single particle tracking localizes individual particles and identifies their trajectories. Ensemble motion tracking such as fluorescence recovery after photobleaching (FRAP), fluorescence correlation spectroscopy (FCS) or fluorescence microscopy is a more global approach where temporal and local changes in fluorescence intensity are observed and analysed.

These techniques however are used to observe enzymes that are homogeneously dispersed, which means that their mobility is measured within a substrate that is already under deconstruction. To get an accurate idea of the coupling between the enzyme's activity and mobility however, the diffusion of the enzyme into non-degraded, native polymer has to be studied. For this, the enzyme cannot be dispersed but instead, the diffusion of an enzymatic front or gradient has to be tracked. This can be done by using fluorescence microscopy, which is the only technique that allows the direct imaging of the directional bulk mobility, i.e. the gradient of the enzyme concentration. Usually, the enzymes are labelled with a fluorophore that can be visualised using light in the visible spectrum and the fluorescent signal is captured using a camera. However, it is also possible to exploit the auto-fluorescence of enzymes which requires the use of ultra-violet light [11], [105].

In this study, the conventional approach was used and the enzyme was labelled using the commercially available fluorophore TRITC (tetramethylrhodamine-6-isothiocyanate, see Figure 24). TRITC is a green fluorophore that reacts covalently with primary amines of proteins, such as accessible lysine residues.

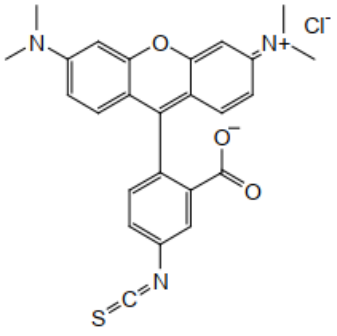

Figure 24: Structure of TRITC [106].

To follow the mobility of the enzyme, we used a custom set-up that had been designed and built by the team's engineer, Claude Le Men. This ensemble consists of a fluorescence microscope that captures images of the sample, and a circular sample cell. The design of the sample cell allows the introduction of a small, localised enzyme source into a thin layer of polymer solution (see Figure 25). Over time, the enzyme spreads out radially, creating a gradient that is captured by the camera of the microscope. The diffusion can then be quantified by image treatment and analysis using a custom program in Python (**details in Chapter V**).

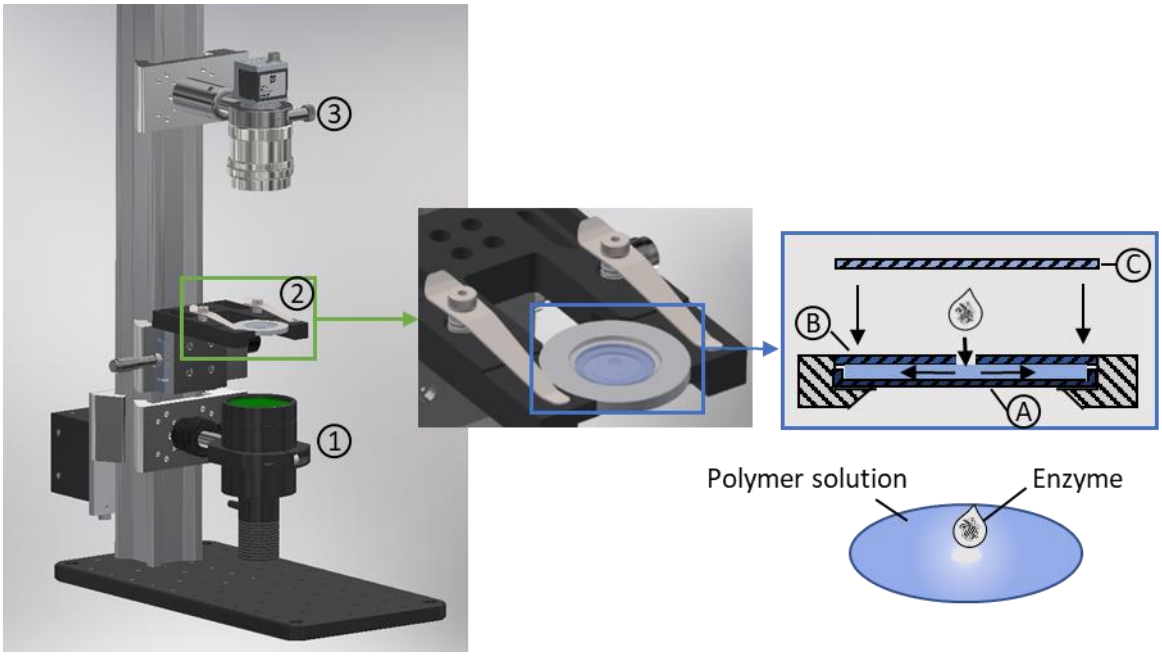

Figure 25: Experimental set-up. Left-hand side: Custom fluorescence microscope consisting of (1) a LED + excitation filter, (2) sample holder and (3) camera + emission filter. Middle: Sample holder. Right-hand side: The circular microscopy chamber made up of a bottom layer (A) holding the polymer solution (light blue layer), a middle layer with a hole for the deposit of the enzyme solution (B) and a top layer (C) to close the chamber.

Most studies on the diffusion of enzymes are under homogeneous conditions, so-called self-diffusion [8], [87], [107], [108] and only some rare studies use a heterogeneous system like ours to study directional diffusion and, most importantly, the impact of enzymatic activity on its mobility [11], [77].

d. Other techniques to follow enzymatic action

In the framework of this PhD, we also considered two other techniques to potentially follow the activity of enzymes in concentrated substrate solution – although they were never used for that purpose (to our knowledge). In **Chapter VI**, we explore these techniques and their preliminary, yet very promising, results:

1. Nuclear magnetic resonance spectroscopy (NMR),

2. Photon correlation imaging (PCI)

Technically speaking, both techniques can be used to follow the evolution of the dynamics of the polymer over time: The reduction of the size of the polymer chains by the enzyme leads to an increase in their dynamics. In addition, both techniques could be used for imaging, which therefore opens the possibility to follow a degradation front (= enzyme front).

CHAPTER III

Characterisation of Arabinoxylan in Water using SANS (Article)

i. Preamble

In this chapter, we present the characterisation of arabinoxylan in water. The results of this study complete the rather scarce information found in literature, and help us understand the structure and organisation of the polymer in water. We aimed for a comprehensive characterisation, moving from the single-chain to the solution characteristics. For the context of this PhD work, important results were:

1. A preparation protocol starting with a very dilute stock solution followed by the gradual removal of water to concentrate the polymer leads to a good solubilisation even for high polymer concentrations

2. The general properties of the single chain: Its average size (M_n of 73.5 kDa, M_w of 168.9 kDa), cross-section (11-12 Å), radius of gyration (51.5 nm) and length of a chain segment (~17 xylose units), representing its stiffness.

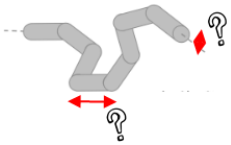

3. The concentration at which the polymer chains start to form a network (overlap concentration c*): approximately 3.3 $g.L^{-1}$

4. The evolution of the mesh size with polymer concentration. This information is crucial to understand the diffusional properties of arabinoxylan solutions, which plays a central role in this PhD work.

This article has been submitted to the journal *Biomacromolecules* on April 12th.

ii. Article

Arabinoxylan in Water Through SANS: Single Chain Conformation, Chain Overlap and Clustering

Maike Petermann,[†,1] *Lucie Dianteill,*[†,1] *Amal Zeidi,*[†] *Roméo Vaha Ouloassekpa,*[†] *Paul Budisavljevic,*[†] *Claude Le Men,*[†] *Cédric Y. Montanier,*[†] *Pierre Roblin,*[‡] *Bernard Cabane,*[#] *Ralf Schweins,*[‖] *Claire Dumon,*[†] *Antoine Bouchoux*[*,†]

[†]TBI, Université de Toulouse, CNRS, INRAE, INSA, Toulouse, France

[‡]Laboratoire de Génie Chimique, Université de Toulouse, CNRS, INPT, UPS, Toulouse, France

[#]LCMD, CBI, ESPCI - Paris Tech, 75231 Paris, France

[‖]Institut Laue-Langevin, DS/LSS, 71 Avenue des Martyrs, CS-20156, 38042 Grenoble, France

[1]Both authors contributed equally to the work

ABSTRACT

Using small-angle neutron scattering (SANS), we examine the structure and conformational behavior of wheat arabinoxylan (AX) in aqueous solutions prepared at various concentrations. As for another major hemicellulose, xyloglucan, we observe a small number of large clusters, surrounded by AX chains that behave exactly as a polymer in good solvent with a Flory exponent ν = 0.588. The fit of the data at high q-values to a standard worm-like chain model gives the persistence length l_p = 45 Å, and cross-section of the chains, $2R_c$ = 11-12 Å. In addition, using a dedicated modeling approach, we extract from the SANS data at intermediate q-range the correlation length ξ of the solutions in the semidilute regime. The decay of ξ with concentration follows a scaling law that further confirms the self-avoiding statistical behavior of the AX chains. This first comprehensive study about the properties of water-soluble AX at different length scales may certainly help in the development of products and/or processes involving AX as a substitute to fossil carbon molecules.

GRAPHICAL ABSTRACT

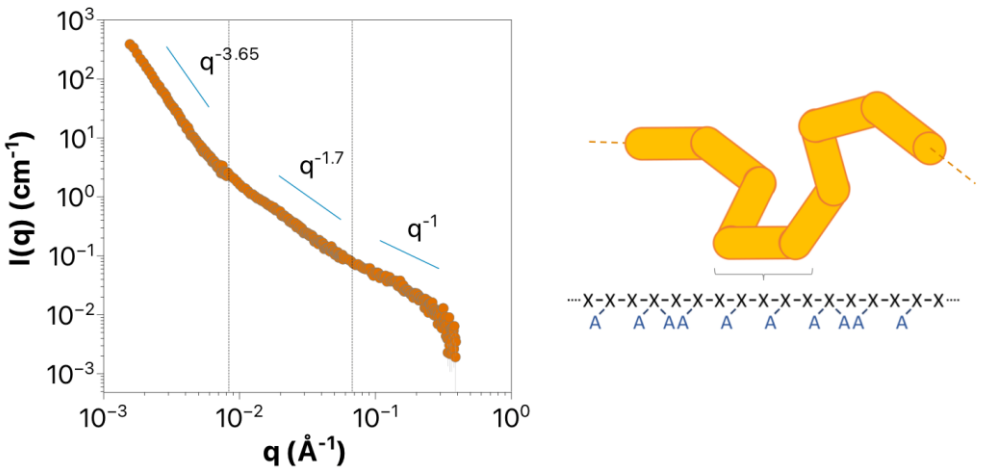

INTRODUCTION

During evolution, plants have gained an outstanding diversity of structures and chemical compositions.[1] De facto, many of the biomolecules found in plant cell walls are interesting alternatives to fossil carbon molecules for producing fuels, plastics, or other value chemicals.[2] Arabinoxylan (AX), a polysaccharide, is one of these promising biopolymers. AX is the main hemicellulose in grasses such as wheat and rye. It is the second-most abundant polysaccharide -after cellulose- in these species, and it is readily available as by-product of the corresponding agro-industrial processes.[3] AX is a linear chain that consists in a (1,4)-β-D-linked xylose (X) backbone decorated with arabinose (A) substitutions on the second and/or third carbon. Additional occasional substitutions are acetate or glucuronic acid decorations, which are found to be involved in the interaction between AX and cellulose microfibrils *in planta*.[4] Ferulic acid residues can also be found on the arabinose side chain, and in this case are involved in the covalent binding of AX with lignin in the plant cell wall.[5]

Historically, AXs extracted from plant biomass were first used for their viscous nature, improving the property of dough in bread-making for instance.[6] Nowadays, their use as thickeners or emulsifiers becomes increasingly common in the food industry,[7] with recent researches that even suggest a positive health effect of AX addition.[8] Other applications are based on the film-forming properties of AXs,[9] or their ability to form gels through interchain covalent linkage between ferulic acid residues.[10] The natural propensity of AX to interact with cellulose also makes it a natural candidate for coating dedicated surfaces and/or designing composite objects for specific applications.[11–14]

Depending on the plant source and/or extraction process, AXs have diverse chemical compositions with respect to their A/X number ratio, and the presence or not of additional substitutions, i.e. acetate, glucuronic, ferulic. Accordingly, a fair number of research works deals with the chemical characterization of AXs from different sources,[6,15–17] with some attempts to link the chemical composition of the biopolymer to its macroscopic physicochemical properties such as solubility,[12] or rheology.[18] Here we focus on a simple version of AX extracted from wheat, which is a water-soluble AX that lacks any substitutions other than arabinose residues. One important reason for this choice is that the solubility in water is a crucial parameter with respect to applications, where it is much more practicable to use solutions of a polymer in processes and operations that must be reproducible. As demonstrated by Köhnke et al.,[12] solubility in water is ensured when the A/X number ratio is high, typically > 0.5. At such degree of substitution, the A residues are sufficiently evenly distributed on the chain to prevent associative interactions between unsubstituted X residues (presumably *via* hydrogen-bonds).[19]

Surprisingly, the question of the conformation and organization of AX chains when dispersed in water is still not clear, whereas this information is essential for the applications cited above and for developing new ones. To our knowledge, the most complete dataset is the one provided by Dervilly-Pinel et al. in the early 2000's, where water-soluble AX are characterized using rheology, size exclusion chromatography (SEC) and multi-angle laser light scattering (MALS).[20] However, as pointed out later on by Picout et al.,[21] those results only lead to an indirect and questionable quantification of some polymer parameters, namely the polymer-solvent interactions (Flory exponent

v) and the chain flexibility (persistence length l_p). Interestingly, small-angle scattering techniques (X-rays, SAXS, or neutrons, SANS) are able to directly quantify those values, as it was nicely demonstrated by Muller et al. in their pioneering work on xyloglucan (XG), another hemicellulose.[22]

The first objective of this work consists in accurately determining the properties of a *single chain* of AX when the polymer is dispersed in water, as it is done in Muller's study on XG.[22] For that, we focus on SANS data obtained in a *q*-range that informs about the conformational statistics at intermediate (coil) scale, down to the persistence length and the equivalent cross-section of the chain. We discuss the results in light of the chemical structure of the AX source, and in comparison with recent SANS results on non-soluble AX polymers.[18]

Our second objective is to focus on the AX chain behavior at high concentration, namely in the *semidilute regime* where the AX concentration C is higher than the overlap concentration C^*; the latter being determined precisely through viscosity measurement. The main question is how the characteristic length scale of the polymer solution, i.e., the correlation length ξ, evolves with C. This question is clearly of fundamental interest, with still a limited number of experimental works that measure ξ and confront these measurements with theoretical scaling predictions,[23,24] especially for polysaccharides. On the other hand, the general behavior of AX chains in the semidilute regime, and the change in ξ as a function of C, are also crucial information for applications where the concentration of polymer in solution has to be maximized and/or where the diffusional properties of the polymer solution must be controlled.[25]

EXPERIMENTAL SECTION

Material and Sample Preparation. AX, extracted and purified from wheat flour, was purchased from Megazyme (Wicklow, Ireland). The same lot, reference P-WAXYL n°120601, was used for preparing all the samples. The product is a slightly yellowish powder that contains ~95% AX in mass. The AX chains have a A/X molar ratio of 38/62. According to previous HPLC and NMR analyses,[12,26] this arabinoxylan source is free from traces of ferulic or glucuronic acid so that the AX chains are fully neutral. In these works and others, AX solutions of 5 to 10 $g.L^{-1}$ are prepared by vigorously mixing the powder with water at high temperature (40-100 °C) for a given time (from 10 minutes to a few hours).[12,20,26] The AX chains are in all cases considered as completely dissolved, as in the work of Köhnke et al.[12] for instance, where a 10 $g.L^{-1}$ AX solution prepared in such a way has no measurable turbidity at 700 nm.[12] However, as described in the Supporting Information, we find from SAXS experiments that, even if the solutions indeed appear translucid, aggregates are still present and prevent a proper analysis of the solution structure (Figure S1). These aggregates presumably originate from strong and pre-existing interactions between AX chains in the powder. One way to dissolve such aggregates is to lower the AX concentration to 1 $g.L^{-1}$ during the solubilization at high temperature. For reaching higher AX concentrations, we then extract water from the solution using the osmotic stress technique, as detailed hereafter. In the SAXS and SANS spectra of concentrated AX solutions prepared in that way, the presence of aggregates is greatly reduced, and the signature of individual AX chains is then clearly visible (Figure S1 and Figure 2). Note however that there is still an intensity upturn at low q-values ($< 7 \times 10^{-3}$ $Å^{-1}$) in all our samples, which suggests that it is not possible to

get rid of all associative interactions between the AX chains. We discuss this feature in the text in light of the works of Muller et al.[27] and Yu et al.[18] on XG and AX from *Plantago ovata*, respectively.

Unless noted otherwise, all samples were thus prepared starting from a low-concentration, 1 g.L^{-1}, AX solution. This very solution was itself prepared by mixing for 2 h at 90 °C the AX powder in a volume of a 50 mM sodium phosphate aqueous buffer at pH 6. We chose to use a buffer rather than MilliQ water to ensure that the physicochemical conditions are the same in all cases. Also, this buffer is the one that we use in a further study that aims at investigating the degradation of AX by enzymes that are active in these buffer conditions (ongoing experiments). As the AX is fully neutral, electrostatic interactions should not have any effect on its conformational properties at the different length scales. This contrasts with charged polymers for which the persistence length l_p (stiffness), for instance, depends on the ionic strength and/or pH of the buffer. Consequently, we believe that the structural features of the AX chains, as reported in this work, should not be significantly different from the ones that would be measured in pure water.

After cooling to room temperature, the 1 g.L^{-1} AX solution was simply diluted in buffer for preparing solutions at C < 1 g.L^{-1}. On the other hand, and as already mentioned, solutions at C > 1 g.L^{-1} were prepared by concentrating 1 g.L^{-1} AX solutions using osmotic stress, still at room temperature. Osmotic stress is based on water exchange between the sample and a reservoir of controlled osmotic pressure, generally a polyethylene glycol (PEG) solution.[28,29] Briefly, 1 g.L^{-1} AX solutions were placed in 6000-8000 g.mol^{-1} cutoff dialysis bags (Spectra/Por 1 RC, Spectrum, US) that were immersed in a 100-fold

volume of PEG solutions prepared in the same buffer at known concentrations. We used PEG20000 (Sigma-Aldrich, US) at concentrations from 50 to 250 $g.L^{-1}$, which corresponds to osmotic pressures between 2.5 kPa and 1 MPa.[30,31] The difference in osmotic pressure between the sample and the reservoir causes the buffer (water and ions) to flow out of the sample, while the AX and PEG cannot pass through the dialysis membrane. This leads to a slow and gentle concentration (from one day to one week, with regular refills of the bags with fresh AX solution) of the AX samples at different levels as a function of the PEG concentration. Note that our intention was not to actually measure the osmotic pressure of the AX solutions using the osmotic stress technique, which is beyond the scope of this paper as it would require dedicated and even more delicate experiments.[28,31,32] Therefore we did not wait for the thermodynamic equilibrium between the bags and the PEG solutions. We rather simply followed the concentration process in real-time using refractometry (see next section), until a desired concentration was reached in the bags.

For SANS experiments, one sample was prepared at 0.9 $g.L^{-1}$ AX in a deuterated sodium phosphate buffer at pD 6 using the same protocol, i.e., 90 °C and 2 h. In the case of low concentration and consequently low scattered intensity, we used D_2O instead of H_2O to take advantage of the small incoherent scattering from D_2O.[33]

Polymer concentration. For practical and cost-effective reasons, we prepared only small volumes of sample using the osmotic stress technique. As a result, the AX concentration could not be determined accurately through drying as the remaining mass was generally too small. We therefore used refractometry for measuring the AX concentration in those samples. We used a standalone refractometer (Mettler Toledo

RM50, CH) that only requires 500 µL of sample per measurement. The increment in refractive index d*n* relative to pure buffer was measured at 25 °C and converted into AX concentration using d*n*/d*C* = 0.146 mL.g^{-1}.[20] We double-checked this d*n*/d*C* value using the refractometer of the SEC-MALS chain (Size exclusion chromatography coupled to multi-angle light scattering, next section) and standard AX samples prepared at 1-5 g.L^{-1} (Figure S2). We were also able to both measure d*n* and determine the AX concentration through drying for two concentrated samples for which we had enough volume (25 and 30 g.L^{-1}). Again, a d*n*/d*C* value 0.146 mL.g^{-1} was found (Figure S2). For higher d*n* values, we considered that the linear relationship between *n* and *C* is conserved, as for simple monosaccharide solutions in a similar range of concentration.[34]

Size exclusion chromatography coupled to multi-angle light scattering (SEC-MALS). The SEC-MALS analysis was performed with a setup composed of three SEC columns connected in series (Shodex OH-Pak SB-805 HQ, SB-803 HQ, SB-802.5 HQ, Showa Denko, JP), a differential refractometer, and a DAWN HELEOS light scattering detector (Wyatt Technology, US). The mobile phase was 50 mM sodium phosphate buffer in MilliQ water, pH 6, with a flow rate of 0.8 mL.min^{-1}. A 1 g.L^{-1} AX sample was prepared in the same buffer and filtered through a 0.22 µm syringe filter (Sartorius, DE). 50 µL of this sample was injected in the system, the elution and detection temperatures being set to 25 °C. The refractive index (RI) and light scattering data (LS) data were analyzed using the ASTRA software (version 7) from Wyatt Technology. A d*n*/d*C* of 0.146 mL.g^{-1} was used for the data treatment.

Rheology. The rheology measurements were performed with a HAAKE MARS III (Thermo Scientific, US) using a cone and plate geometry of diameter 60 mm and angle 1°. The viscosity was measured at 25 °C, as a function of shear rate in the range 0.1-100 s^{-1}. All the samples investigated, from 0.2 to 30 $g.L^{-1}$ in AX, behave as Newtonian fluids over this range, leading to one average value of the dynamic viscosity η. The viscosity of pure buffer at 25 °C was measured in the same way and found to be η_0 = 8.774 x 10^{-4} Pa.s. This allowed to calculate the so-called specific viscosity, η_{sp} which gives the additional contribution of the polymer to the solution viscosity as compared to the buffer only

$$\eta_{\mathrm{sp}} = \left(\frac{\eta-\eta_0}{\eta_0}\right) \quad (1)$$

For concentrations < 4 $g.L^{-1}$, the reduced and inherent viscosities, η_{red} and η_i were calculated according to

$$\eta_{\mathrm{red}} = \left(\frac{\eta-\eta_0}{\eta_0}\right)/C \quad (2)$$

and

$$\eta_{\mathrm{i}} = \ln\left(\frac{\eta}{\eta_0}\right)/C \quad (3)$$

The intrinsic viscosity [η] was determined by plotting either η_{red} or η_i as a function of C (Huggins' and Kraemer's plot, respectively) and extrapolating to zero concentration.[35]

Small-angle Neutron Scattering. The SANS experiments were performed on the D11 instrument, Institut Laue-Langevin (ILL, Grenoble, France) during the experiment numbered 9-13-718 (https://doi.org/10.5291/ILL-DATA.9-13-718). We present the results for samples prepared at four AX concentrations: 0.9 (in D_2O buffer), 14, 56 and 135 $g.L^{-1}$. The 0.9 and 14 $g.L^{-1}$ samples were placed in 5- and 1-mm path length quartz cells (Hellma Analytics, DE), respectively. The 56 and 135 $g.L^{-1}$ were much more viscous and placed in specific sandwich cells of 1 mm path length, closed by two quartz windows (Hellma Analytics, DE). The sample cells were positioned in a rack that was thermostatically controlled at 37 °C, a slightly higher temperature than the one used for the SEC-MALS and viscosity measurements. The neutron scattering intensities were collected at neutron wavelength 6 Å and at three sample-to-detector distances: 1.4, 8 and 39 m. The intensities were radially averaged, merged and arranged as a function of scattering vector q in the range $q \approx 1.5\times10^{-3}$ - 3.9×10^{-1} $Å^{-1}$. The corrections for instrumental background, empty cell, and transmission, as well as the normalization to absolute intensities, were achieved following the standard procedures of D11. The sample background was determined from the intensity signal of pure buffer solutions in H_2O and D_2O. It was then subtracted from the intensity scattered from the samples to obtain the intensity from the solute only.

RESULTS AND DISCUSSION

In the following, we first present and discuss some general features and properties of the AX chains and AX solutions, as obtained using SEC-MALS and viscosity measurements. In a second section, we give a general description of the SANS profiles obtained at the different AX concentrations. The third section focuses on the single-chain properties of AX as determined by modeling the SANS data at intermediate and high q-values. The final section is dedicated to the behavior of the AX polymer solution at concentrations > C^* and the determination of the correlation length ξ as a function of C.

Size distribution and overlap concentration.

Table 1. SEC-MALS analysis of the arabinoxylan (AX) chains

Sample	M_n[a] (10^3 g.mol^{-1})	M_w[b] (10^3 g.mol^{-1})	M_w/M_n[c]	R_g[d] (Å)
Wheat arabinoxylan Megazyme P-WAXYL lot 120601	73.5 ± 15%	168.9 ± 8%	2.3 ± 16%	515 ± 18%

[a]Number-averaged molecular weight, [b]weight-averaged molecular weight, [c]polydispersity index, [d]radius of gyration, which is the mass-averaged root mean square radius obtained from the SEC-MALS data. The mass recovery was 96.3%. The RI and LS profiles are given in the Supporting Information (Figure S3).

Table 1 gives the results obtained using SEC-MALS with an AX solution of 1 g.L^{-1} prepared using the previously described solubilization protocol. Here, the sample was further filtered through a syringe filter with a 0.22 µm molecular weight cut-off. The first important pieces of information are the mass recovery which is > 95%, and the absence of any large objects in the SEC profile (Figure S3). This clearly indicates that the solution is free of the large and strong aggregates observed in SAXS with solutions

prepared using less cautious protocols (Figure S1), and confirms that the polymer chains are in a well hydrated state when following our solubilization protocol.[22] However, in SAXS (Figure S1, compressed sample at 8.3 $g.L^{-1}$) and in the following SANS results (Figure 2), we note that large objects are still visible a low *q*-values. Such objects were also observed in XG solutions,[22,27] and with AX extracted from *Plantago ovata* seed mucilage that form gels in water but that is in a fully hydrated state in 0.7 M KOD solution.[18] As concluded in those previous works, these are most probably weak aggregates or clusters, presumably made from the H-bonded mediated association of a few AX chains. As they form spontaneously, these associative entities cannot be removed from the bulk and are inevitably present in solution. However, they are probably weak enough to be broken by the high shear experienced in the SEC columns, which would explain why they are not detected using SEC-MALS (see the description of Figure S3).[22]

Overall, the data in Table 1 shows that the AX chains are quite polydisperse, with $M_w/M_n >> 1$. Considering the average number of arabinose decorations per xylose, the obtained weight averaged molecular weight M_w corresponds to a chain backbone of ~800 xylose monomers, while the M_n value gives ~350 xylose monomers.

The viscosities of AX solutions at concentrations ranging from 0.2 to 30 $g.L^{-1}$ are given in Figure 1. The inset shows the plots of the reduced (η_{red}, eq 2) and inherent (η_i, eq 3) viscosities which, extrapolated to zero concentration, give an estimation of the intrinsic viscosity [η] of the polymer.[35] Both extrapolations give the same value of [η] ≈ 3 $g.dL^{-1}$.

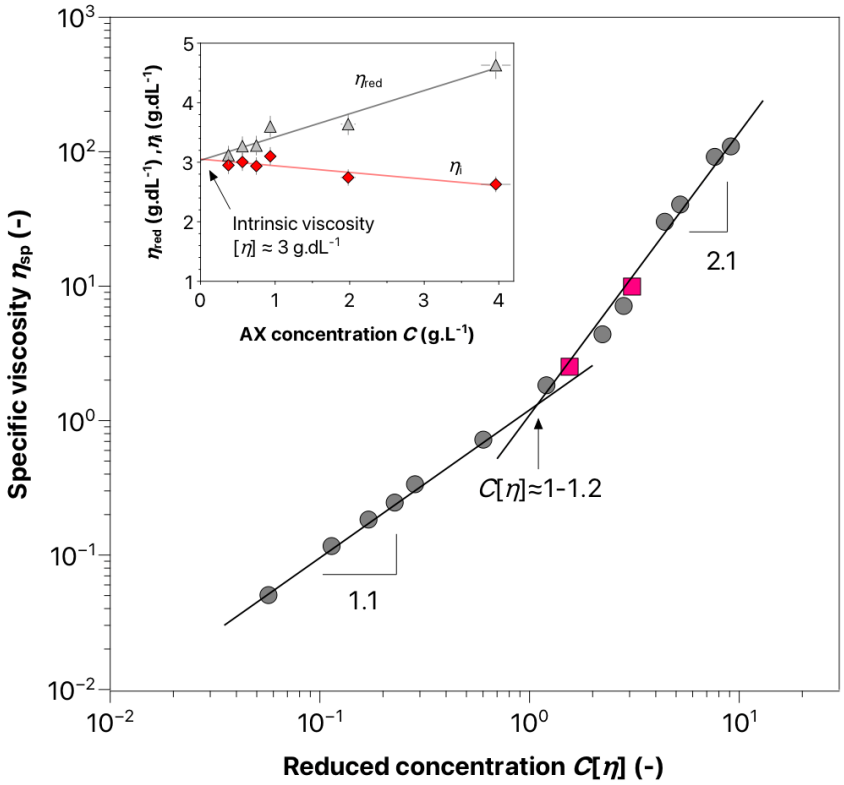

Figure 1. Specific viscosity η_{sp} as a function of AX reduced concentration $C[\eta]$ for AX solutions prepared at low concentration (C < 1 g.L^{-1}) and then compressed using the osmotic stress technique (gray circles). We also show results obtained with AX solutions directly prepared at concentration 10 g.L^{-1} and 5 g.L^{-1} at 90 °c for 2 h (purple squares). The inset gives the so-called Huggins' and Kraemer's plots of the reduced (η_{red}) and inherent (η_i) viscosities, respectively, for $C \leq 4$ g.L^{-1}.

Figure 1 displays the variation of the specific viscosity (η_{sp}, eq 1) as a function of $C[\eta]$. On such a log-log representation, the change of slope indicates the crossover from the dilute regime, where the AX chains are independent and do not interact with each other, to the semidilute unentangled regimes where the chains overlap. This crossover takes place at $C[\eta] \approx$ 1-1.2, which is consistent with the theoretical value for linear

chains, $C[\eta] = 1$.[27] This gives an overlap AX concentration $C^* \approx 3.3\text{-}3.9$ g.L^{-1}. Also the slopes of ~1.1 and ~2.1 in the dilute and semidilute regimes, respectively, are in very good agreement with the values reported for XG (another linear neutral polymer) in good solvent,[27] and also with the values for a linear polyelectrolyte in an excess of salt, which in this case behaves like neutral polymers as electrostatic interactions are entirely screened.[36]

Accordingly, the large clusters that we know are present in the AX solutions do not seem to have any visible impact on the viscosity of the solutions. This is a point that has already been discussed by Muller et al. for XG solutions, where the authors explain that only a few links are possible per XG chain, leading to clusters that have a structure "not far from a linear chain" and thus a viscosity behavior that is similar to a linear chain.[27] An additional explanation would be that the relative number of these clusters is too low for contributing substantially to the viscosity of the solutions. The two square points in Figure 1 are the viscosities measured for AX solutions directly prepared at 5 and 10 g.L^{-1}, i.e., without using osmotic compression. In such solutions, we know from our preliminary SAXS results (Figure S1) that AX aggregates are much more present than in solutions prepared through osmotic stress. The fact that the viscosities measured for these two samples fall in line with the other points further suggests that the quantity of AX associative entities is in all cases negligible with regard to the viscosity of the AX solutions.

SANS / General features. We now move on to the SANS characterization of the AX chains, with a first general analysis of the scattering curves obtained at different concentrations (Figure 2). The 0.9 $g.L^{-1}$ solution was prepared in a D_2O buffer solution to maximize the signal-to-background ratio at such a low concentration. The other solutions (14-135 $g.L^{-1}$) were prepared in a H_2O buffer, using the osmotic stress technique. Note the high quality of those SANS data in terms of statistics (small error bars) and *q*-values that are explored (from 1.5×10^{-3} $Å^{-1}$ to 3.9×10^{-1} $Å^{-1}$).

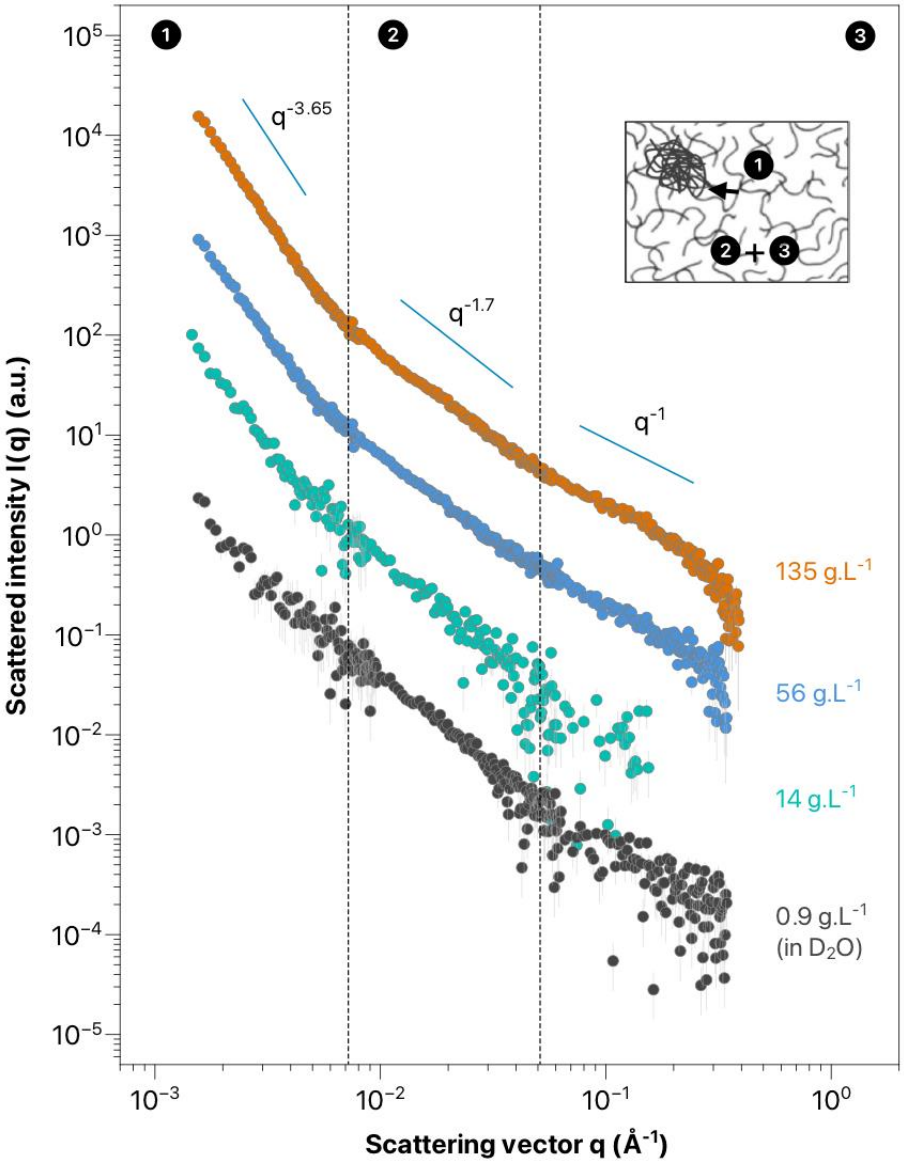

Figure 2. The SANS intensities of AX solutions from 0.9 to 135 g.L^{-1}. The data have been shifted along the *y*-axis for clarity. For all concentrations, the SANS profiles can be divided into three distinct *q*-regions where different length scales are explored (see the inset and the discussion below).

For the naked eye, the general shape of the scattering curves appears quite similar at all concentrations (Figure 2). On all curves, we clearly identify three distinct *q*-regions, noted 1, 2, and 3, which correspond to structural information at different length scales,

i.e., from large (few hundreds of nanometers) to local dimensions (Ångströms), respectively:

. **Region 1** (q < 7.5×10^{-3} Å^{-1}) shows a sharp rise in intensity towards low q-values which is the signature of the clusters that we discuss earlier. These clusters are also observed in XG solutions using static light scattering (SLS),[27] and using SANS in solutions of gel-forming AX extracted from *Plantago ovata* but in non-gelled, highly basic conditions.[18] We observe the same power-law behavior over the entire q-range of region 1, which indicates that the size of these objects is most likely > $2\pi/q_{min} \approx 400$ nm. The slope of the signal, estimated from the data with the best statistics (135 g.L^{-1}), is about $q^{-3.65}$. This suggests that the clusters are rough 3D entities,[18] with a surface fractal dimension D_s given by $I_c(q) \sim q^{(6-D_s)}$, i.e., D_s = 2.35.[37] As discussed in the previous section, we can reasonably consider that the mass concentration of those objects is low compared to the concentration of the free AX chains in solution. Furthermore, the fact that the shape of the SANS profile does not change much with concentration suggests that the relative number of clusters (scattered intensity in region 1) does not change either with the total number of AX chains (intensity in regions 2 and 3). However, the analysis becomes speculative at this point as we do not know if the cluster size changes with AX concentration. Also, we will not go further into this discussion as the purpose of this work is to examine the characteristics of the free AX chains in solution, i.e., using the SANS information in regions 2 and 3.

. **Region 2** (7.5×10^{-3} Å^{-1} < q < 5.5x 10^{-2} Å^{-1}) corresponds to the solution structure at intermediate scale, i.e., ~10-100 nm. On a log-log scale, the scattering curves all appear as quasi-linear in this region (Figure 2), with a power law ~$q^{-1.7}$. This exponent value is

characteristic of a polymer chain in good solvent; meaning the AX chain adopts the conformation of a real, self-avoiding chain with excluded volume effects.[22,38,39] The 1.7 value corresponds to the theoretical Flory exponent ν = 1/1.7 = 0.588 for such a situation; where ν describes the relation between the size of a single, free polymer coil (R_g) and the number N of repetition units that compose the chain, i.e., $R_g \sim N^{\nu}$. To our knowledge, it is the first time that a Flory parameter of 0.588 -and the underlying self-avoiding statistic- is unambiguously determined for water-soluble AX. As discussed by Picout et al., it is indeed not possible to obtain a good approximation of that parameter using the former SEC-MALS results of Dervilly-Pinel on similar AX polymers.[20,21] On the other hand, the recent SANS results of Yu with AX from *Plantago ovata* seed mucilage also shows a $q^{-1.7}$ decay of the scattered intensity in a similar q-range.[18] But in this case the AX is non-soluble in water, and the solubilization of the chains is forced by using 0.7 M KOD as solvent. The raw material and the experimental conditions are thus very different from those of the present work, which makes a direct comparison impossible (at least there is no contradiction between the two results). Finally, the self-avoiding statistical behavior of water-soluble AX chains is strongly reminiscent of the SANS work of Muller et al., who find the exact same behavior for XG solubilized in water.[22] This resemblance is noteworthy, and is certainly due to similarities between the properties and chemical nature of the two hemicelluloses: XG being also a neutral and linear water-soluble polysaccharide, made of a glucose backbone decorated with xylose residues.

. **Region 3** (q > 5.5x 10^{-2} Å^{-1}) contains structural information at small length scale, i.e., from ~10 nm to a few Å. It starts with a clear inflexion of the scattering profile from ~$q^{-1.7}$ to a ~q^{-1} dependency (Figure 2). The q^{-1} scaling law is characteristic of a 3D object with a mass fractal D_m = 1, meaning the chain behaves as a rod at this length scale. This indicates that the AX polymer can be pictured as a semiflexible chain, made of N connected rods/segments of a given length, the Kuhn length l_K.[39] The Kuhn length l_K, or perhaps the more commonly used persistence length $l_p = l_K/2$, gives a direct indication of the chain stiffness: a higher persistence length indicates a stiffer chain. In the SANS profiles, the persistence length is related to $I(q)$ at the transition from ~$q^{-1.7}$ to ~q^{-1}. In the next section, we determine precisely l_p by modeling the SANS data in this zone. At still higher q-values (from $q \approx 0.2$ Å^{-1}), the scattered intensity deviates from the q^{-1} power law, with a progressive and sharper decrease in I with q. This is the signature of thick rods, where the deviation from the q^{-1} exponent gives an indication on the radius of gyration of the cross section of the rods, R_c. Again, we show in the following section how to quantify precisely R_c using an adequate model.

SANS / Single chain. Here the objective is to quantify precisely the two parameters of the AX chain at the local scale which are its stiffness, i.e., the persistence length l_p, and its cross-section R_c. The approach consists in fitting the data to a model that considers these two parameters, plus the fact that the chain is in good solvent condition, i.e., with excluded volume effects. An analytical expression for such a worm-like chain (WLC) model has been proposed recently by Boze et al.,[40] based on the earlier work of Sharp and Bloomfeld.[41]

$$I_{\mathrm{WLC}}(q) = I_0\left[\frac{2(e^{-x}+x-1)}{x^2} + \frac{2l_p}{L}\left[\frac{4}{15} + \frac{7}{15x} - \left(\frac{11}{15} + \frac{7}{15x}\right)e^{-x}\right]\right] exp\left(\frac{-q^2R_c^2}{2}\right) \quad (4)$$

where $x = q^2\frac{Ll_p}{3}$, I_0 is the intensity scattered at $q \to 0$, L is the contour length of the chain (i.e., the length at maximal extension), l_p its persistence length, and R_c the polymer equivalent cross-section radius. This model is clearly equivalent to the one used by Muller et al. for XG chains,[22] and that is implemented in the SASfit software.[42]

For the fit, we use the SANS profile at 135 g.L^{-1} as it shows the best statistics at high q-values (more data points, small error bars). Also, it is safe to assume that the local chain dimensions l_p and R_c do not change with C and -more importantly- are contained in the SANS profile at 135 g.L^{-1} as it shows both the transition from a $q^{-1.7}$ to a q^{-1} power law and the further decrease in intensity that corresponds to the Guinier's law of the chain cross-section. However, 135 g.L^{-1} is way over the overlap concentration C^* ≈ 3.3-3.9 g.L^{-1}. Therefore, the WLC model, that gives the form factor of a single chain, cannot be used on the whole available q-range. Consequently, we do not consider in the fit the data at $q < 2\times10^{-2}$ Å^{-1}, i.e., the q-value where the slope of the intensity starts to deviate from the $q^{-1.7}$ dependency (Figure 3). Also, at $C > C^*$, the chains overlap, and the L parameter has no physical meaning in the WLC form factor model. L is then fixed to an arbitrary large

value (1 µm), so that it does not intervene in the fit in the chosen q-region. The I_0 value, which depends on the L parameter, has no direct physical meaning either and is not discussed in the following.

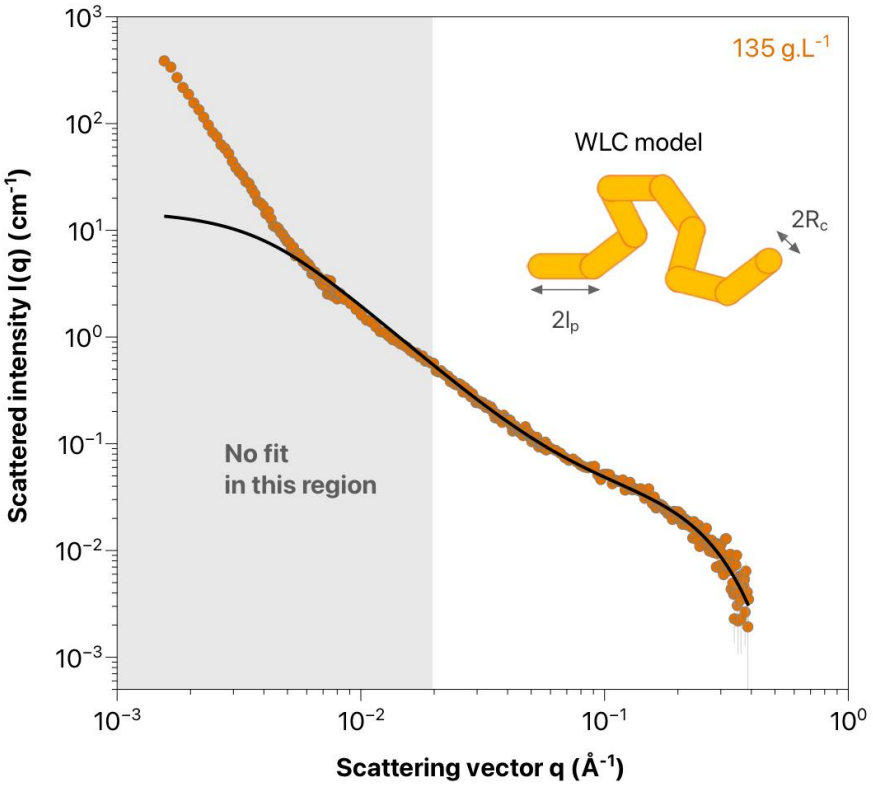

Figure 3. The fit of the experimental data at 135 g.L^{-1} AX (orange) to the WLC model described in the text (black line).

The fit consists in varying I_0, l_p and R_c to minimize the distance between the model and the experimental data at $q > 2\times10^{-2}$ Å^{-1}. The result is clearly excellent, as shown in Figure 3, with the best fit giving l_p = 45.0 Å and R_c = 5.8 Å. The value of the persistence length is characteristic of a semiflexible, relatively stiff polymer, as compared to much more flexible polymers like PEG for instance (l_p = 3.8 Å[43]). The obtained value contrasts with the 86 Å value estimated from SEC-MALS data obtained with a similar AX by

Dervilly-Pinel et al.[20] However it is consistent with the 30 Å average value estimated by Picout et al. from the same SEC-MALS data but using calculations based on different theoretical considerations.[21] Clearly, the SANS technique gives a much more precise quantification of the AX persistence length. The value of 45.0 Å corresponds to an elementary Kuhn segment of ~17 xylose units ($l_K=2l_p$, Figure 4).[17] In comparison, the SANS-measured persistence length of water-soluble XG from tamarind seeds is about twice this size, i.e., 80 Å.[22] The reason for that is not straightforward but is probably a combination between the difference in chemical nature of the backbone (glucose vs. xylose), and the fact that XG has a different substitution pattern than AX, with more side chain residues and in some cases galactose substitutions on the decorating xyloses.[22] The comparison is probably more direct with the SAXS experiments performed by Yu et al. with AX from *Plantago ovata* seed.[18] In that case, the measured persistence length of AX solubilized in 0.7 M KOD solution is 45-47 Å, which is very similar to our result. Regarding the cross-section of the equivalent polymer segment, the value that we obtain, i.e., $2R_c$ = 11.6 Å, is about twice the average size of one xylose or arabinose residue (5-6 Å),[17] which is fully consistent with the AX chain structure and composition (Figure 4). Interestingly, the cross-sections reported by Yu et al. for the *Plantago ovata* AX polymer are much larger, with $2R_c \approx$ 18-22 Å. It is probably because this peculiar, gel-forming, AX (i) has presumably a higher number of arabinose side-chain residues than the AX used in the present study,[18] (ii) has a less linear backbone structure that contains some atypical β-1,3 linked xylose residues.[44]

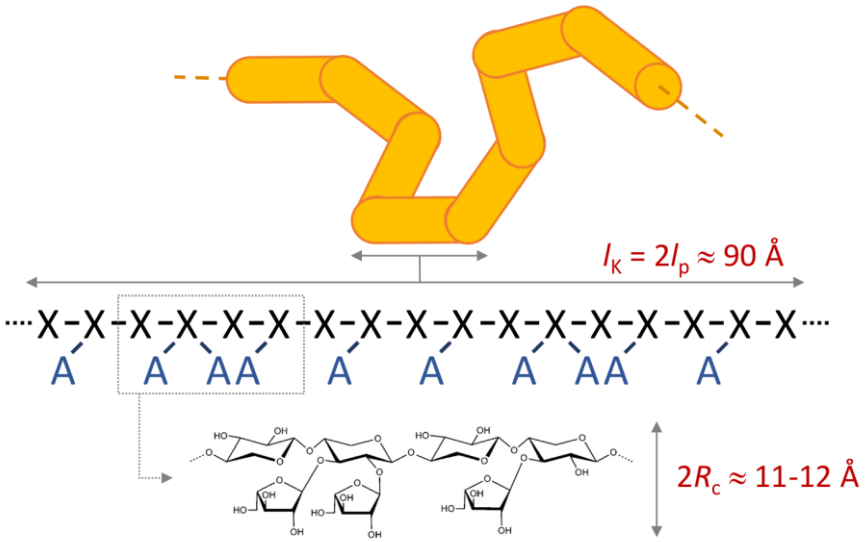

Figure 4. A schematic representation of the WLC structure of the water-soluble AX used in the present study, together with the local parameter l_p and R_c obtained from the model.

SANS / Semidilute solutions. In the semidilute regime, i.e., when the AX concentration exceeds C^*, the polymer chains get closer together and start to overlap. When this happens, a characteristic distance emerges which is the correlation length ξ of the polymer solution. ξ is the average distance from one monomer of one chain to the nearest monomer of another chain.[25,45] It is a parameter of fundamental importance, as it controls -for instance- the diffusivity of particles in the polymer solution. In a common polymer solution, ξ is directly linked to the q-value at which a plateau appears in the SAXS or SANS intensity at low q.[38,46] In our case, the analysis is complicated by the presence of large objects in this q-range, which literally hides such a plateau behavior at low and intermediate length scale (regions 1 and 2). To leverage this difficulty, we fit our data to a simple model that considers the scattered intensity as resulting from two independent contributions:

. $I_c(q)$, the contribution of the associative clusters at low q. We do not know their size neither their internal organization, but they have a surface fractal dimension $D_s \approx 2.35$, so that, in the explored q-range,

$$I_c(q) = A\, q^{-(6-D_s)} = \mathrm{A}\, q^{-3.65} \quad (5)$$

with A a scaling factor

. $I_s(q)$, the contribution of the AX solution of correlation length ξ. We use the expression of Falcao et al., since it predicts accurately the $q^{-1.7}$ dependency at intermediate q-values (end of region 2 here)[46]

$$I_s(q) = B\, \frac{(1+q\xi)^{1/3}}{1+q^2\xi^2} \quad (6)$$

with B a second scaling factor

The total intensity is then obtained by adding up the two contributions

$$I_s(q) = I_c(q) + I_s(q) \quad (7)$$

And the only adjustable parameters of the model are A, B and ξ.

Note that this basic model does not describe the semidilute solution at small scale, i.e., where the SANS profile is related to the local properties of the chain (l_p and R_c, see previous section). Therefore, we exclude this length scale from the fitting procedure and only use the experimental data obtained at $q > 5 \times 10^{-2}$ Å^{-1}. The results of the fits are given in Figures 5-7.

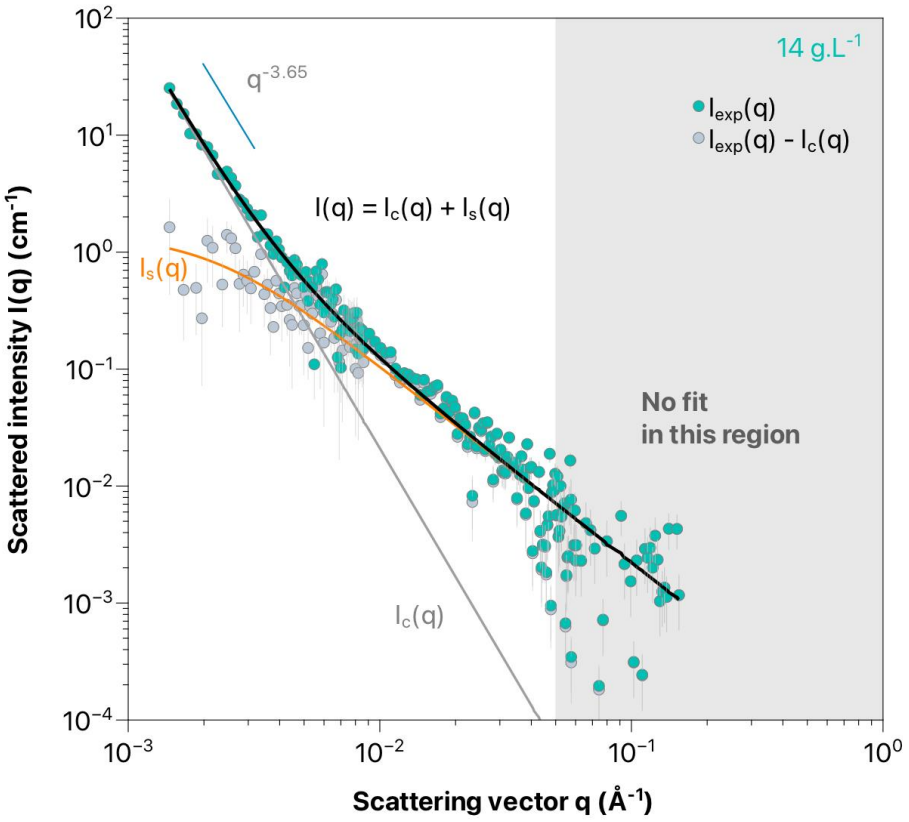

Figure 5. The SANS profile of the 14 g.L^{-1} AX sample (green circles, $I_{exp}(q)$), with the fit of the experimental data to the composite model described in the text (black line, $I(q)$).

The gray line, $I_c(q)$, is the contribution of the clusters to the scattered intensity calculated from the model, while the orange line, $I_s(q)$, is the contribution of the dissolved AX chains. The light gray circles are the experimental intensities after subtraction of the cluster contribution $I_c(q)$ obtained from the fit of the model.

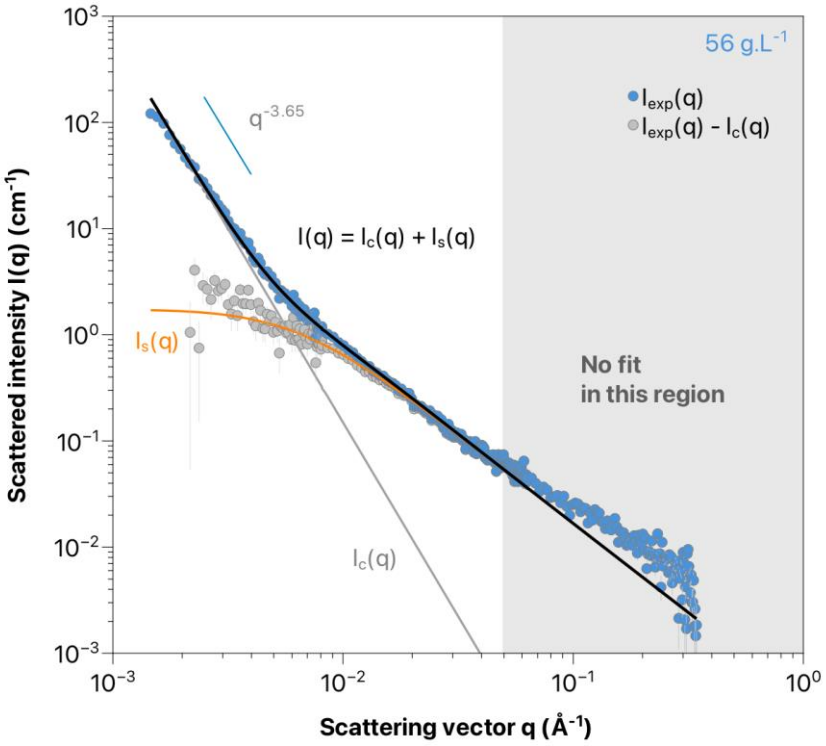

Figure 6. The SANS profile of the 56 g.L^{-1} AX sample (blue circles, $I_{exp}(q)$), with the fit of the experimental data to the model described in the text (black line, $I(q)$).

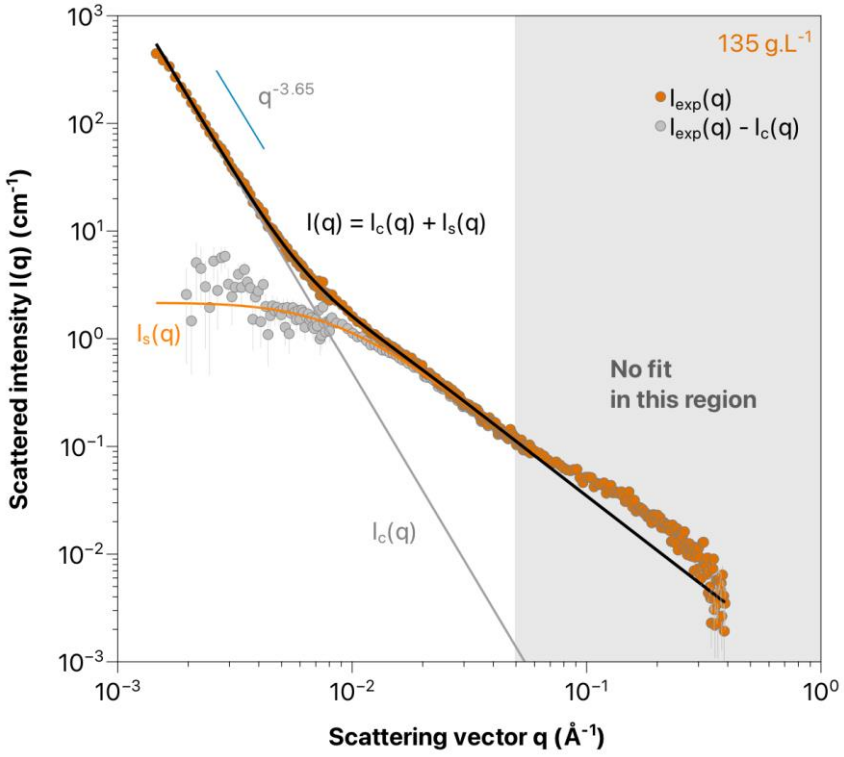

Figure 7. The SANS profile of the 135 g.L^{-1} AX sample (orange circles, $I_{exp}(q)$), with the fit of the experimental data to the model described in the text (black line, $I(q)$).

The fits (black lines) are very satisfactory for all the concentrations investigated. For clarity, Figures 5-7 also give the two individual contributions $I_c(q)$ and $I_s(q)$ to the total scattering, as given by eqs 5 and 6. $I_s(q)$ has this characteristic shape with a plateau at low q and the transition to a progressive decay in $q^{-1.7}$ when the explored length scale approaches the correlation length ξ. Knowing the contribution of the clusters $I_c(q)$, it is also possible to calculate the difference $I_{exp}(q)$-$I_c(q)$ between the experimentally measured scattered intensities and the cluster contribution as obtained from the fit (gray circles). In all cases, and especially when the statistics is good (135 and 56 g.L^{-1}), we see that the obtained data nicely align with the theoretical polymer intensities within the inflexion zone, i.e., from 4×10^{-3} - 2×10^{-2} Å^{-1}. This suggests that our modelling approach, despite its relative simplicity, is quite consistent. Note that the

correspondence between I_{exp}(q)-$I_c(q)$ and $I_s(q)$ is less marked at lower q-values. This is because the contribution of the clusters is dominant in this region, leading to less reliable values for I_{exp}(q)-$I_c(q)$.

Figure 8 gives the correlation lengths ξ obtained from the fits at concentrations 14, 56 and 135 g.L^{-1}. In addition, we give the ξ value obtained from a fit to the SANS data measured in D_2O at 0.9 g.L^{-1} (see Figure S4). By definition, ξ is the length beyond which interchain correlations overtake intrachain correlations. When C < C*, as it is the case at 0.9 g.L^{-1}, interchain correlations are negligible. Therefore ξ should corresponds to the space occupied by one single chain in solution, meaning $\xi \approx R_g$. The R_g value obtained by SEC-MALS at 1 g.L^{-1} is reported in Figure 8. As expected, ξ and R_g are indeed very close. As C then increases and exceeds C^*, the chains progressively overlap and interchain correlations gradually overtake intrachain correlations. This results in the decrease of the correlation length ξ with C. As shown experimentally with several polymer systems,[46,47] the crossover from dilute to semidilute solutions can occur over about one decade in concentration, which appears to be the case for our system as well (~2-20 g.L^{-1}). At further higher concentrations, interchain correlations must dominate so that the correlation length ξ should decrease according to the scaling theory for semidilute polymer solution in good solvent, i.e., $\xi \sim C^{-\nu/(3\nu-1)} = C^{-0.77}$.[25,38] Figure 8 gives the comparison between our data and the theory, showing a very good agreement between the two. Clearly, this result further confirms that the AX chains can be considered as polymer chains in good solvent, as already stated from the general shape of the SANS profiles at intermediate length scale (Figures 2 and 3).

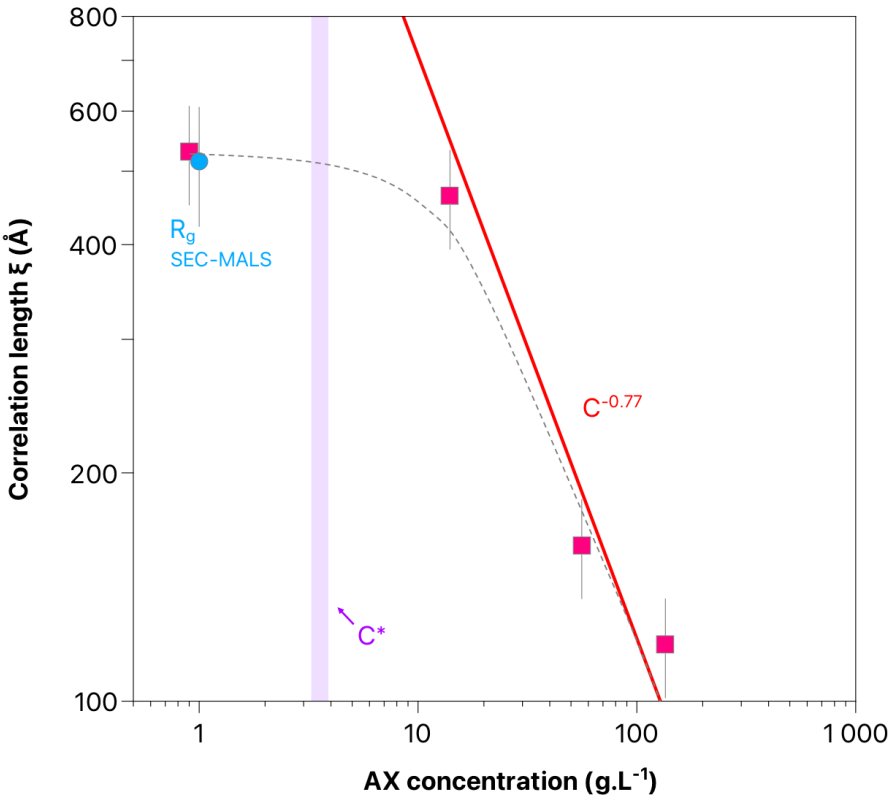

Figure 8. Crossover from dilute to semidilute solutions of AX.Variation of the correlation length ξ obtained from the fits of our model as a function of AX concentration. The straight line gives the $C^{-0.77}$ dependence that is expected for semidilute solutions of polymer chains in good solvent.[25,46] The vertical thick line corresponds to the C^* values obtained from rheology. For comparison, we give the R_g value obtained from SEC-MALS at 1 g.L^{-1} AX. The dashed line is a guide for the eye.

CONCLUSIONS

Using SANS, complemented with SEC-MALS and viscosity measurements, we were able to obtain a complete characterization of the structure and conformational behavior of a generic arabinoxylan (AX, extracted from wheat-flour) when dispersed in water. Our first finding, that is consistent with observations made with another major hemicellulose (xyloglucan XG),[22,27] is the fact that despite the large solubility of AX in water, it is not possible to fully get rid of the associative interactions between some AX chains. This results in the presence of some large objects (> 500 nm), that we call clusters in the present study, but at a concentration that is too small for having an effect on the viscosity of the AX solutions. In a second step, we examine closely the SANS profile of AX solutions in the intermediate and high q-ranges. This allows us to unambiguously determine that the AX chains behave as a polymer in good solvent, adopting the statistical conformation of a self-avoiding chain with excluded effects. A worm-like chain model fits the data nicely at these length scales, allowing us to quantify accurately the stiffness of the polymer, l_p = 45 Å, and its average cross-section size, $2R_c$ = 11-12 Å. Finally, we focus on the SANS data at low and intermediate q-ranges, with the aim of understanding how the chains behave when entering the semidilute concentration regime, i.e., $C > C^*$. For that, we follow a simple modeling approach that allows us to extract the correlation length ξ of the polymer solution from the SANS profiles, in conditions spanning more than two decades of concentrations (~1-135 g.L^{-1}). The change in ξ as the macromolecules get closer together with concentration is fully consistent with the behavior of a polymer in good solvent, especially in the high concentration regime where the data closely follow the scaling theory that is expected in that case.

We believe that such a thorough and unprecedented characterization of AX in water, from low to high concentrations, provides a variety of information that are both of fundamental and practical interests: (i) fundamental as our work gives a unique complement to the -still scarce- SAXS and SANS studies dedicated to the conformational behavior of hemicellulosic polymers in solution,[18,22] (ii) practical as AX can potentially be used as a substitute to oil-based molecules in many applications that our results may contribute to develop and/or control.

ASSOCIATED CONTENT

Supporting Information.

The Supporting Information is available free of charge on the ACS publication website at DOI: SAXS preliminary experiments for the determination of the best solubilization process, determination of the increment of refractive index for arabinoxylan, SEC-MALS results, fit of the correlation length ξ model to the SANS data obtained at 0.9 g.L-1 (PDF)

AUTHOR INFORMATION

Corresponding Author

*E-mail antoine.bouchoux@insa-toulouse.fr

Author Contributions

All authors have given approval to the final version of the manuscript. MP and LD contributed equally to the work.

Notes

The authors declare no competing financial interest

ACKNOWLEDGMENTS

We thank Pascale Laborie for her technical assistance on the SEC-MALS experiments (Technopolym analysis platform, Université de Toulouse, CNRS, Toulouse), as well as the research federation FERMaT (Université de Toulouse, CNRS, INSA Toulouse, Toulouse INP) for providing access to the SAXS instrument. We also thank L. Ramos from Laboratoire Charles Coulomb (Université de Montpellier, CNRS, Montpellier) for fruitful discussions.

ABBREVIATIONS

AX, arabinoxylan; A, arabinose; X, xylose; SEC, size exclusion chromatography; MALS, multi-angle laser light scattering; SAXS, small angle X-ray scattering; SANS, small angle neutron scattering; XG, xyloglucan; NMR, nuclear magnetic resonance; HPLC, high performance liquid chromatography; RI, refractive index; light scattering, LS

REFERENCES

(1) Sarkar, P.; Bosneaga, E.; Auer, M. Plant Cell Walls throughout Evolution: Towards a Molecular Understanding of Their Design Principles. *Journal of Experimental Botany* **2009**, *60* (13), 3615–3635. https://doi.org/10.1093/jxb/erp245.

(2) Gao, S.; Song, W.; Guo, M. The Integral Role of Bioproducts in the Growing Bioeconomy. *Industrial Biotechnology* **2020**, *16* (1), 13–25. https://doi.org/10.1089/ind.2019.0033.

(3) Smith, P. J.; Wang, H.-T.; York, W. S.; Peña, M. J.; Urbanowicz, B. R. Designer Biomass for Next-Generation Biorefineries: Leveraging Recent Insights into Xylan Structure and Biosynthesis. *Biotechnology for Biofuels* **2017**, *10* (1), 286. https://doi.org/10.1186/s13068-017-0973-z.

(4) Grantham, N. J.; Wurman-Rodrich, J.; Terrett, O. M.; Lyczakowski, J. J.; Stott, K.; Iuga, D.; Simmons, T. J.; Durand-Tardif, M.; Brown, S. P.; Dupree, R.; Busse-Wicher, M.; Dupree, P. An Even Pattern of Xylan Substitution Is Critical for Interaction with Cellulose in Plant Cell Walls. *Nature Plants* **2017**, *3* (11), 859–865. https://doi.org/10.1038/s41477-017-0030-8.

(5) de O. Buanafina, M. M. Feruloylation in Grasses: Current and Future Perspectives. *Molecular Plant* **2009**, *2* (5), 861–872. https://doi.org/10.1093/mp/ssp067.

(6) Izydorczyk, M. S.; Biliaderis, C. G. Cereal Arabinoxylans: Advances in Structure and Physicochemical Properties. *Carbohydrate Polymers* **1995**, *28* (1), 33–48. https://doi.org/10.1016/0144-8617(95)00077-1.

(7) Yan, J.; Jia, X.; Feng, L.; Yadav, M.; Li, X.; Yin, L. Rheological and Emulsifying Properties of Arabinoxylans from Various Cereal Brans. *Journal of Cereal Science* **2019**, *90*, 102844. https://doi.org/10.1016/j.jcs.2019.102844.

(8) Chen, Z.; Li, S.; Fu, Y.; Li, C.; Chen, D.; Chen, H. Arabinoxylan Structural Characteristics, Interaction with Gut Microbiota and Potential Health Functions. *Journal of Functional Foods* **2019**, *54*, 536–551. https://doi.org/10.1016/j.jff.2019.02.007.

(9) Höije, A.; Sternemalm, E.; Heikkinen, S.; Tenkanen, M.; Gatenholm, P. Material Properties of Films from Enzymatically Tailored Arabinoxylans. *Biomacromolecules* **2008**, *9* (7), 2042–2047. https://doi.org/10.1021/bm800290m.

(10) Carvajal-Millan, E.; Landillon, V.; Morel, M.-H.; Rouau, X.; Doublier, J.-L.; Micard, V. Arabinoxylan Gels: Impact of the Feruloylation Degree on Their Structure and Properties. *Biomacromolecules* **2005**, *6* (1), 309–317. https://doi.org/10.1021/bm049629a.

(11) Mikkelsen, D.; Flanagan, B. M.; Wilson, S. M.; Bacic, A.; Gidley, M. J. Interactions of Arabinoxylan and (1,3)(1,4)-β-Glucan with Cellulose Networks. *Biomacromolecules* **2015**, *16* (4), 1232–1239. https://doi.org/10.1021/acs.biomac.5b00009.

(12) Köhnke, T.; Östlund, Å.; Brelid, H. Adsorption of Arabinoxylan on Cellulosic Surfaces: Influence of Degree of Substitution and Substitution Pattern on Adsorption Characteristics. *Biomacromolecules* **2011**, *12* (7), 2633–2641. https://doi.org/10.1021/bm200437m.

(13) Köhnke, T.; Lin, A.; Elder, T.; Theliander, H.; Ragauskas, A. J. Nanoreinforced Xylan–Cellulose Composite Foams by Freeze-Casting. *Green Chem.* **2012**, *14* (7), 1864–1869. https://doi.org/10.1039/C2GC35413F.
(14) Talantikite, M.; Beury, N.; Moreau, C.; Cathala, B. Arabinoxylan/Cellulose Nanocrystal Hydrogels with Tunable Mechanical Properties. *Langmuir* **2019**, *35* (41), 13427–13434. https://doi.org/10.1021/acs.langmuir.9b02080.
(15) Warrand, J.; Michaud, P.; Picton, L.; Muller, G.; Courtois, B.; Ralainirina, R.; Courtois, J. Contributions of Intermolecular Interactions between Constitutive Arabinoxylans to the Flaxseeds Mucilage Properties. *Biomacromolecules* **2005**, *6* (4), 1871–1876. https://doi.org/10.1021/bm049249p.
(16) Dervilly, G. Isolation and Characterization of High Molar Mass Water-Soluble Arabinoxylans from Barley and Barley Malt. *Carbohydrate Polymers* **2002**, *47* (2), 143–149. https://doi.org/10.1016/S0144-8617(01)00172-2.
(17) Dervilly, G.; Saulnier, L.; Roger, P.; Thibault, J.-F. Isolation of Homogeneous Fractions from Wheat Water-Soluble Arabinoxylans. Influence of the Structure on Their Macromolecular Characteristics. *J. Agric. Food Chem.* **2000**, *48* (2), 270–278. https://doi.org/10.1021/jf990222k.
(18) Yu, L.; Yakubov, G. E.; Martínez-Sanz, M.; Gilbert, E. P.; Stokes, J. R. Rheological and Structural Properties of Complex Arabinoxylans from Plantago Ovata Seed Mucilage under Non-Gelled Conditions. *Carbohydrate Polymers* **2018**, *193*, 179–188. https://doi.org/10.1016/j.carbpol.2018.03.096.
(19) Andrewartha, K. A.; Phillips, D. R.; Stone, B. A. Solution Properties of Wheat-Flour Arabinoxylans and Enzymically Modified Arabinoxylans. *Carbohydrate Research* **1979**, *77* (1), 191–204. https://doi.org/10.1016/S0008-6215(00)83805-7.
(20) Dervilly-Pinel, G.; Thibault, J.-F.; Saulnier, L. Experimental Evidence for a Semi-Flexible Conformation for Arabinoxylans. *Carbohydrate Research* **2001**, *330* (3), 365–372. https://doi.org/10.1016/S0008-6215(00)00300-1.
(21) Picout, D. R.; Ross-Murphy, S. B. On the Chain FLexibility of Arabinoxylans and Other B-(1 “4) Polysaccharides. *Carbohydrate Research* **2002**, 4.
(22) Muller, F.; Manet, S.; Jean, B.; Chambat, G.; Boué, F.; Heux, L.; Cousin, F. SANS Measurements of Semiflexible Xyloglucan Polysaccharide Chains in Water Reveal Their Self-Avoiding Statistics. *Biomacromolecules* **2011**, *12* (9), 3330–3336. https://doi.org/10.1021/bm200881x.
(23) Tao, H.; Huang, C.; Lodge, T. P. Correlation Length and Entanglement Spacing in Concentrated Hydrogenated Polybutadiene Solutions. *Macromolecules* **1999**, *32* (4), 1212–1217. https://doi.org/10.1021/ma981468d.
(24) Lopez, C. G.; Horkay, F.; Mussel, M.; Jones, R. L.; Richtering, W. Screening Lengths and Osmotic Compressibility of Flexible Polyelectrolytes in Excess Salt Solutions. *Soft Matter* **2020**, *16* (31), 7289–7298. https://doi.org/10.1039/D0SM00464B.
(25) Cai, L.-H.; Panyukov, S.; Rubinstein, M. Mobility of Nonsticky Nanoparticles in Polymer Liquids. *Macromolecules* **2011**, *44* (19), 7853–7863. https://doi.org/10.1021/ma201583q.
(26) McCleary, B. V.; McKie, V. A.; Draga, A.; Rooney, E.; Mangan, D.; Larkin, J. Hydrolysis of Wheat Flour Arabinoxylan, Acid-Debranched Wheat Flour Arabinoxylan and Arabino-Xylo-Oligosaccharides by β-Xylanase, α-l-

Arabinofuranosidase and β-Xylosidase. *Carbohydrate Research* **2015**, *407*, 79–96. https://doi.org/10.1016/j.carres.2015.01.017.

(27) Muller, F.; Jean, B.; Perrin, P.; Heux, L.; Boué, F.; Cousin, F. Mechanism of Associations of Neutral Semiflexible Biopolymers in Water: The Xyloglucan Case Reveals Inherent Links. *Macromol. Chem. Phys.* **2013**, *214* (20), 2312–2323. https://doi.org/10.1002/macp.201300265.

(28) Bonnet-Gonnet, C.; Belloni, L.; Cabane, B. Osmotic Pressure of Latex Dispersions. *Langmuir* **1994**, *10* (11), 4012–4021. https://doi.org/10.1021/la00023a019.

(29) Parsegian, V. A.; Rand, R. P.; Fuller, N. L.; Rau, D. C. Osmotic Stress for the Direct Measurement of Intermolecular Forces. In *Methods in Enzymology*; Biomembranes Part O: Protons and Water: Structure and Translocation; Academic Press, 1986; Vol. 127, pp 400–416. https://doi.org/10.1016/0076-6879(86)27032-9.

(30) Cohen, J. A.; Podgornik, R.; Hansen, P. L.; Parsegian, V. A. A Phenomenological One-Parameter Equation of State for Osmotic Pressures of PEG and Other Neutral Flexible Polymers in Good Solvents. *J. Phys. Chem. B* **2009**, *113* (12), 3709–3714. https://doi.org/10.1021/jp806893a.

(31) Pasquier, C.; Beaufils, S.; Bouchoux, A.; Rigault, S.; Cabane, B.; Lund, M.; Lechevalier, V.; Le Floch-Fouéré, C.; Pasco, M.; Pabœuf, G.; Pérez, J.; Pezennec, S. Osmotic Pressures of Lysozyme Solutions from Gas-like to Crystal States. *Phys. Chem. Chem. Phys.* **2016**, *18* (41), 28458–28465. https://doi.org/10.1039/C6CP03867K.

(32) Bouchoux, A.; Cayemitte, P. E.; Jardin, J.; Gésan-Guiziou, G.; Cabane, B. Casein Micelle Dispersions under Osmotic Stress. *Biophys.J.* **2009**, *96* (2), 693–706.

(33) Jacrot, B.; Zaccai, G. Determination of Molecular Weight by Neutron Scattering. *Biopolymers* **1981**, *20*, 2413–2426.

(34) Yeh, Y.-L. Real-Time Measurement of Glucose Concentration and Average Refractive Index Using a Laser Interferometer. *Optics and Lasers in Engineering* **2008**, *46* (9), 666–670. https://doi.org/10.1016/j.optlaseng.2008.04.008.

(35) Cheng, Y.; Brown, K. M.; Prud'homme, R. K. Characterization and Intermolecular Interactions of Hydroxypropyl Guar Solutions. *Biomacromolecules* **2002**, *3* (3), 456–461. https://doi.org/10.1021/bm0156227.

(36) Krause, W. E.; Bellomo, E. G.; Colby, R. H. Rheology of Sodium Hyaluronate under Physiological Conditions. *Biomacromolecules* **2001**, *2* (1), 65–69. https://doi.org/10.1021/bm0055798.

(37) *Characterizing polymer structure with small-angle neutron scattering: A Tutorial: Journal of Applied Physics: Vol 129, No 17*. https://aip.scitation.org/doi/10.1063/5.0045841 (accessed 2023-03-10).

(38) Gennes, P. G. de. *Scaling Concepts in Polymer Physics*; Cornell University Press, 1979.

(39) Iwao, Teraoka. *Polymer Solutions: An Introduction to Physical Properties | Wiley*. Wiley.com. https://www.wiley.com/en-fr/Polymer+Solutions%3A+An+Introduction+to+Physical+Properties-p-9780471389293 (accessed 2023-03-13).

(40) Boze, H.; Marlin, T.; Durand, D.; Pérez, J.; Vernhet, A.; Canon, F.; Sarni-Manchado, P.; Cheynier, V.; Cabane, B. Proline-Rich Salivary Proteins Have Extended Conformations. *Biophysical Journal* **2010**, *99* (2), 656–665. https://doi.org/10.1016/j.bpj.2010.04.050.

(41) Sharp, P.; Bloomfield, V. A. Light Scattering from Wormlike Chains with Excluded Volume Effects. *Biopolymers* **1968**, *6* (8), 1201–1211. https://doi.org/10.1002/bip.1968.360060814.
(42) Breßler, I.; Kohlbrecher, J.; Thünemann, A. F. SASfit: A Tool for Small-Angle Scattering Data Analysis Using a Library of Analytical Expressions. *J Appl Cryst* **2015**, *48* (5), 1587–1598. https://doi.org/10.1107/S1600576715016544.
(43) Lee, H.; Venable, R. M.; MacKerell, A. D.; Pastor, R. W. Molecular Dynamics Studies of Polyethylene Oxide and Polyethylene Glycol: Hydrodynamic Radius and Shape Anisotropy. *Biophysical Journal* **2008**, *95* (4), 1590–1599. https://doi.org/10.1529/biophysj.108.133025.
(44) Yu, L.; Yakubov, G. E.; Zeng, W.; Xing, X.; Stenson, J.; Bulone, V.; Stokes, J. R. Multi-Layer Mucilage of Plantago Ovata Seeds: Rheological Differences Arise from Variations in Arabinoxylan Side Chains. *Carbohydrate Polymers* **2017**, *165*, 132–141. https://doi.org/10.1016/j.carbpol.2017.02.038.
(45) Sorichetti, V.; Hugouvieux, V.; Kob, W. Determining the Mesh Size of Polymer Solutions via the Pore Size Distribution. *Macromolecules* **2020**, *53* (7), 2568–2581. https://doi.org/10.1021/acs.macromol.9b02166.
(46) Falcao, A. N.; Pedersen, J. S.; Mortensen, K. Structure of Randomly Crosslinked Poly(Dimethylsiloxane) Networks Produced by Electron Irradiation. *Macromolecules* **1993**, *26* (20), 5350–5364. https://doi.org/10.1021/ma00072a011.
(47) Li, J.; Turesson, M.; Haglund, C. A.; Cabane, B.; Skepö, M. Equation of State of PEG/PEO in Good Solvent. Comparison between a One-Parameter EOS and Experiments. *Polymer* **2015**, *80*, 205–213. https://doi.org/10.1016/j.polymer.2015.10.056.

iii. Supporting Information

Supporting Information

Arabinoxylan in Water Through SANS: Single Chain Conformation, Chain Overlap and Clustering

Maike Petermann,[†,1] *Lucie Dianteill,*[†,1] *Amal Zeidi,*[†] *Roméo Vaha Ouloassekpa,*[†] *Paul Budisavljevic,*[†] *Claude Le Men,*[†] *Cédric Montanier,*[†] *Pierre Roblin,*[‡] *Bernard Cabane,*[#] *Ralf Schweins,*[‖] *Claire Dumon,*[†] *Antoine Bouchoux**[,†]

[†]TBI, Université de Toulouse, CNRS, INRAE, INSA, Toulouse, France
[‡]Laboratoire de Génie Chimique, Université de Toulouse, CNRS, INPT, UPS, Toulouse, France
[#]LCMD, CBI, ESPCI - Paris Tech, 75231 Paris, France
[‖]Institut Laue-Langevin, DS/LSS, 71 Avenue des Martyrs, CS-20156, 38042 Grenoble, France
[1]Both authors contributed equally to the work

SAXS preliminary experiments / Solubilization and sample preparation processes

The following SAXS data are from preliminary experiments performed to determine the solubilization state of the AX chains in different conditions of preparation. All experiments were conducted in the Laboratoire de Génie Chimique (LGC, Toulouse, France), on a SAXS XEUSS 2.0 instrument (Xenocs, FR) equipped with a copper internal source Genix3D and a Pilatus 1M (Dectris, CH) detector. The samples and their corresponding buffers were placed in 2 mm diameter glass capillaries (Glas, DE) sealed with wax. The data were collected at sample to detector distances of 2.5 m and 1 m, at room temperature. The 22.7 $g.L^{-1}$ and 8.3 $g.L^{-1}$ data are the average of 20 measurements, each collected over 600 s. The 10 $g.L^{-1}$ and 8.3 $g.L^{-1}$ data are the average of 10 measurements, each collected over 7200 s. Figure S1 gives the actual solute scattering intensities in the samples after having subtracted the signal of the background, i.e, capillary + buffer.

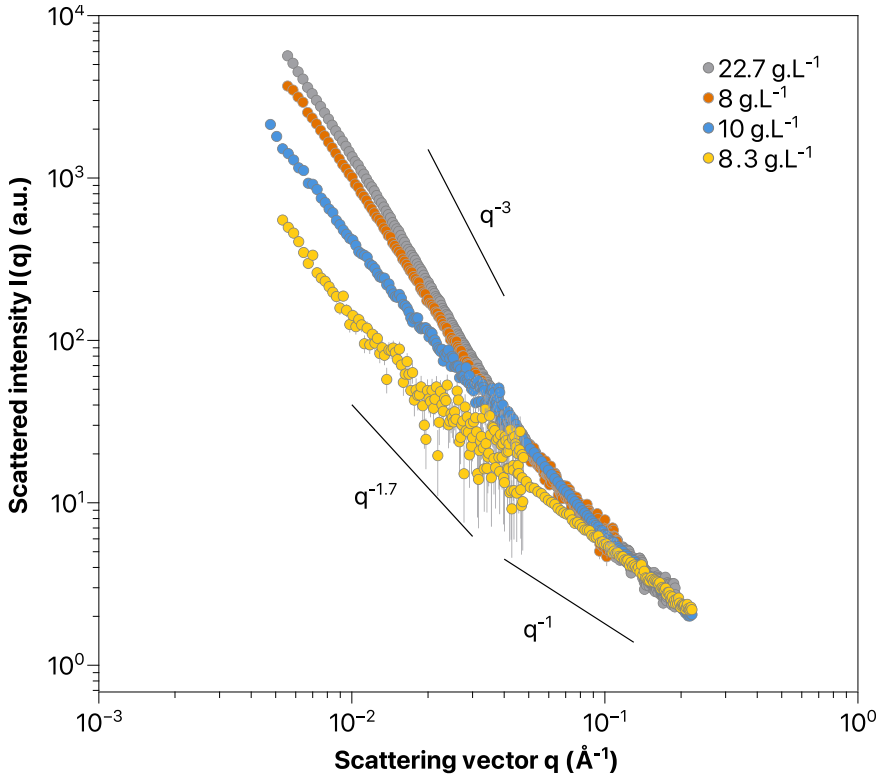

Figure S1. SAXS profiles for 8-20 g.L-1 AX solutions prepared following different protocols (see below for a full description). The intensities are in arbitrary units (a.u.); the data having been shifted along the y-axis to match the intensities at high *q* values.

22.7 g.L^{-1} (gray) - Direct preparation

The AX powder is directly dissolved in MilliQ water at a final concentration of 22.7 g.L^{-1}. Mixing is performed overnight (~15 h) at 70°C. Here the intensity decays approximately as q^{-3} over nearly the entire range of scattering vector, from $q = 5 \times 10^{-3}$ to 0.1 Å^{-1}. There is no plateau (Guinier Region) at low *q* values that would be linked to the size of the polymer, neither there is any $q^{-5/3}$ - q^{-2} dependence of the scattered intensity at intermediate *q* values, as expected for linear polymer chains in different solvent conditions.[1–3] The observed q^{-3} signature is most probably due to the presence of large objects, presumably AX aggregates that are not dissolved during the preparation due to strong remaining associative interactions. This difficulty to reach full solubilization is quite common for so-called "water-soluble" polysaccharide

powders. This is for instance the case for xyloglucan, another hemicellulose for which the presence of supramolecular aggregates in solution has been reported if relevant hydration strategies are not followed during solubilization.[2,4]

8 g.L^{-1} (orange) - Dilution

Water is simply added, at room temperature, to the 22.7 g.L^{-1} solution in order to reach an AX concentration of 8 g.L^{-1}. In Figure S1, the intensities are shifted along the *y*-axis to match the data of the 22.7 g.L^{-1} solution at high *q* values. It thus appears clearly that the shape of the SAXS spectra at 8 g.L^{-1} is virtually identical to the one obtained before dilution, with only slightly less scattering in the low- and intermediate-*q* regions. This suggests that only a marginal part of the AX aggregates is dissociated by adding water in the 22.7 g.L^{-1} solution. As a result, the SAXS intensity is still dominated by large objects and the signature of individual polymer chains is still not visible in the spectrum, whereas - as for its homologous at 22.7 g.L^{-1} - the 8 g.L^{-1} solution has no visible turbidity and appears totally transparent.

10 g.L^{-1} (blue) - Direct preparation

This time the solution is prepared directly at 10 g.L^{-1} rather than 22.7 g.L^{-1}. The same conditions for mixing are used (70°C overnight). Only the solvent is slightly different as we now switch from pure water to the 50 mM sodium phosphate buffer used in the experiments presented in the article. Here we see a clear difference with the previous SAXS data at 22.7 g.L^{-1} and 8 g.L^{-1}: (i) there is a clear drop in the scattered intensity at low and intermediate *q* values, (ii) the slope of the scattering decay is less than -3 but still differs from what is expected for fully hydrated polymer chains. This suggests that AX aggregates are still present in the solution but in much less quantity than previously. This can have two origins. The first one has to do with the nature of the solvent as a 50 mM sodium phosphate buffer is used instead of MilliQ water. However, this reason is quite unlikely as AX is a neutral polymer that should not be sensitive to the addition of a such small quantity of ionic strength (the pH is nearly the

same, i.e., about neutral, in pure water and in buffer). The second origin, which we believe is much more plausible, is that the quantity of AX aggregates depends on the actual concentration in AX chains during the solubilization step at high temperature.

8.3 g.L^{-1} (yellow) - Osmotic stress

Here the solution is prepared following a two-step process. First, we prepare an AX solution at low concentration, 1 g.L^{-1}, and high temperature (70°C mixing overnight), with the idea of limiting if not totally dissolving the large AX aggregates observed in the conditions described above. Second, we concentrate the solution up to 8.3 g.L^{-1} by extracting water from it using the osmotic stress technique (see the article for a full description). As shown in Figure S1, the SAXS profile is strikingly different from the others. First the signal is much less intense, which explains the noise at intermediate q values. Second, the dependence of the scattered intensity with q now matches the expected behavior of a polymer solution with a $q^{-5/3}$ scaling law at intermediate q values and q^{-1} scaling law at high q (see the article for details). Nevertheless, there is still an intensity upturn at low q values (< 7×10^{-3} Å^{-1}). As discussed in the article, and based on the works of Muller et al.[5] and Yu et al.[6], we assign this feature to weak clusters that form in situ in the AX solution rather than strong AX aggregates that persist from the powder state.

Arabinoxylan d*n*/d*C*

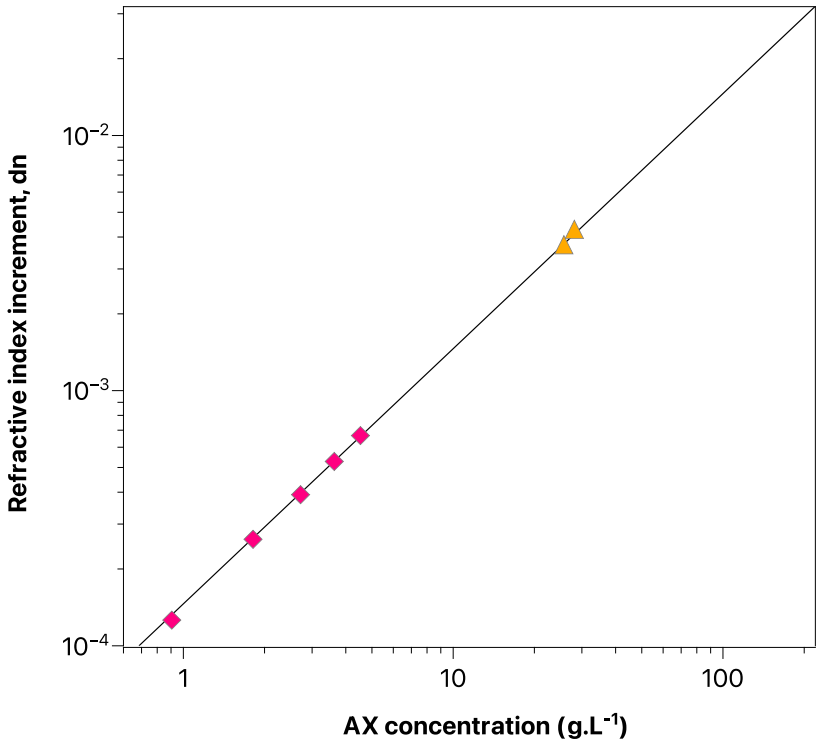

Figure S2. The increment of refractive index of AX solutions as a function of AX concentration.

The line in Figure S2 is the linear relationship using the value of d*n*/d*C* = 0,146 at 25° as reported by Dervilly-Pinel *et al.*[7] The diamonds are the refractive index increments measured at 25°C using the SEC-MALS differential refractometer and with AX solutions prepared by dispersing the AX powder in water for 2h at 90°C. The triangles are the refractive index increments measured at 25°C using a Mettler Toledo RM50 standalone refractometer and with solutions prepared through osmotic stress. For these two points, the volume prepared was enough for assessing the AX concentration by drying out the samples at 125°C for a few hours and measuring the resulting dry mass.

SEC-MALS analysis

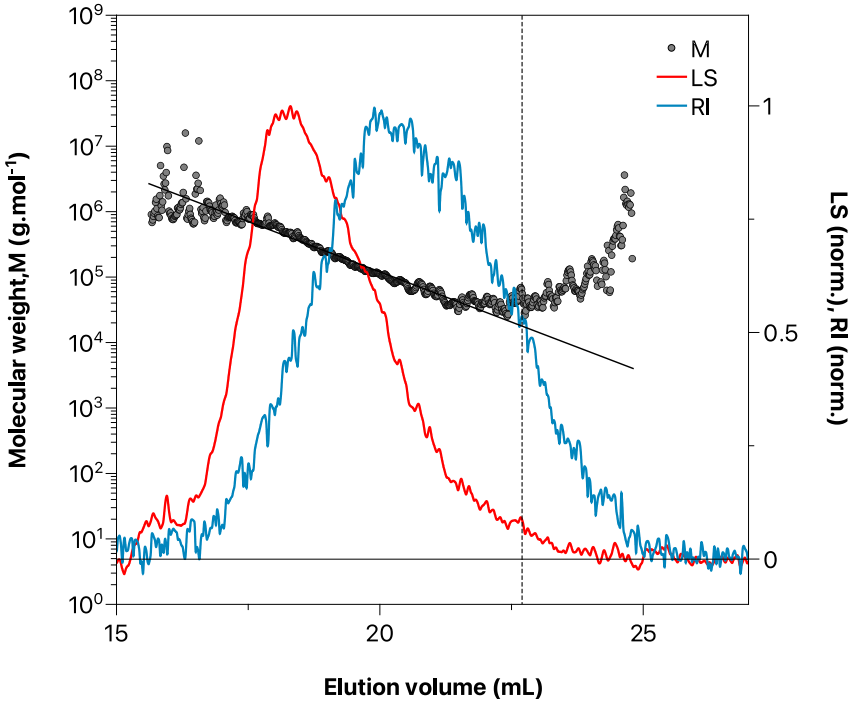

Figure S3. SEC-MALS profile of a 1 g.L^{-1} AX solution. The light scattering signal (LS, 90° angle, red), the refractive index (RI, blue), and the estimated molecular weight (M, gray circles) are given as a function of elution volume. The black line is one of the typical 'models' that is used in the treatment of SEC-MALS data when a correction of the *M* results appears necessary (see discussion below). The vertical dashed line gives the elution volume from which such a correction could be applied. The details about the experiment (columns, mobile phase, elution flow rate) are given in the article.

Figure S3 shows the SEC-MALS results obtained with a 1 g.L^{-1} AX solution. We are interested in this very concentration as it corresponds to the best conditions of solubilization for the AX chains. This is a chromatography result, meaning the data are plotted as a function of the elution volume. The refractive index signal (RI) is proportional to the mass concentration of the polymer, while the light scattering signal (LS, here at 90° angle) results both from the size and concentration of the chains. At a given elution time, the molecular weight *M* is estimated using the Zimm method and the LS intensities acquired at multiple angles. The number-averaged molecular weight

M_n and the weight-averaged molecular weight M_w are then calculated from the distribution of M as a function of the mass concentration, i.e., the RI signal.

In our case, from ~15 to 22.5 mL elution volume, M clearly decreases with the elution volume, which is what we expect in size-exclusion chromatography. However, starting from 22.5 mL of elution, M increases with concentration. This is an effect that occurs quite frequently in SEC and that is due to the retarded elution of some large chains because of attractive interactions with the columns' material. These large chains are surrounded by chains of much smaller size that elute 'normally' at these elution volumes. However, because of their size, the large chains scatter much more light than the small chains, which is why MALS tends to overestimate the actual M in this region. As we do not know the exact proportion of large versus small chains at these elution volumes, this phenomenon complicates the estimation of the averaged-values M_n and M_w. One first approach consists in using the raw results and ask the MALS software to compute M_n and M_w from the experimental M values in the whole range of elution volume (gray circles in Figure S3). The second approach consists in extrapolating the 'correct' decrease of M with the elution volume in the affected region, by considering that M follows the black line at the right-hand side of the dashed vertical line in Figure S3, for instance. Fortunately, the region of the chromatogram where such a correction may be necessary is quite limited (after 22.5 mL elution volume), and therefore concerns only a small fraction of the AX injected mass (i.e., the area below the blue curve). As a result, the M_n and M_w values obtained from approaches 1 and 2 are quite similar: M_n = 73.5×10^{-3} ± 15% vs 62.3×10^{-3} ± 25% g.mol^{-1} and M_w = 168.9×10^{-3} ± 8% vs 199.2×10^{-3} ± 5% g.mol^{-1}). In the present work, we decided to stick to the experimental values obtained from LS, and therefore to follow approach 1.

A second important remark about these SEC-MALS results is the fact that they do not show any evidence of the presence of AX clusters, although we know from SANS and SAXS that they form in-situ in the AX solutions. Such clusters would lead to much higher M values, most certainly at low elution volumes. We see two reasons why these

objects are not visible in Figure S3: (i) because their mass concentration is much lower than the one of the free AX chains, and/or (ii) they are probably too fragile to resist the high shear stress experienced in the SEC columns. This last explanation is also favored by Muller et al. in their recent work about xyloglucan.[2]

SANS modeling

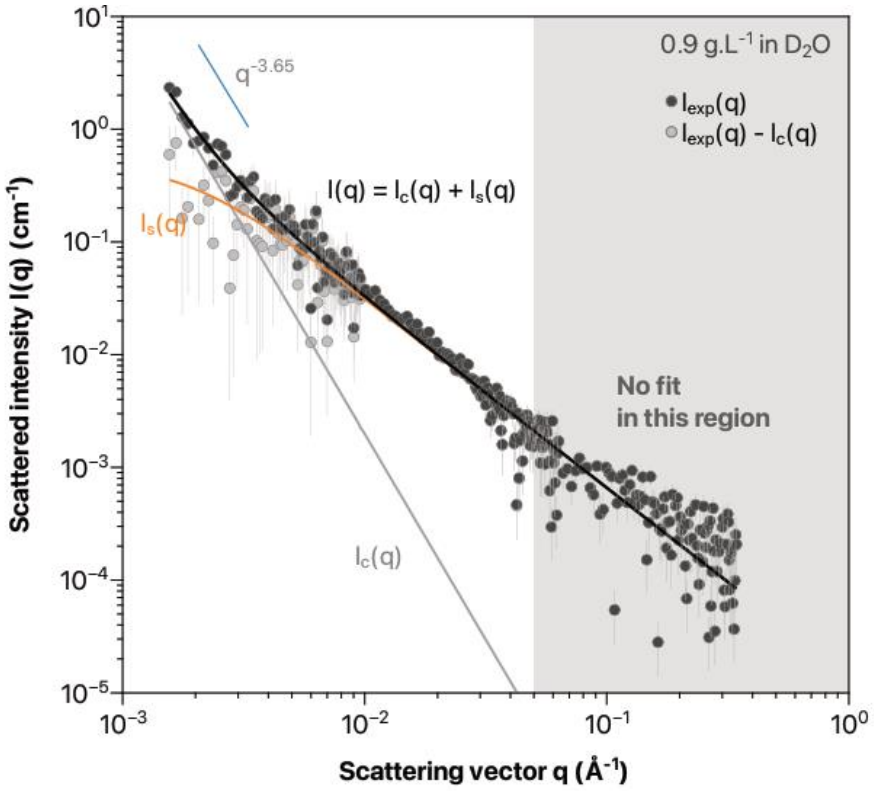

Figure S4. The SANS profile of the 0.9 g.L^{-1} AX sample (dark circles, $I_{exp}(q)$), with the fit of the experimental data to the model described in the text (black line, $I(q)$). The gray line, $I_c(q)$, is the contribution of the clusters to the scattered intensity calculated from the composite model, while the orange line, $I_s(q)$, is the contribution of the swollen AX chains. The light gray circles are the experimental intensities after subtraction of the clusters contribution $I_c(q)$ obtained from the fit of the model.

References

(1) Falcao, A. N.; Pedersen, J. S.; Mortensen, K. Structure of Randomly Crosslinked Poly(Dimethylsiloxane) Networks Produced by Electron Irradiation. *Macromolecules* **1993**, *26* (20), 5350–5364.

(2) Muller, F.; Manet, S.; Jean, B.; Chambat, G.; Boué, F.; Heux, L.; Cousin, F. SANS Measurements of Semiflexible Xyloglucan Polysaccharide Chains in Water Reveal Their Self-Avoiding Statistics. *Biomacromolecules* **2011**, *12* (9), 3330–3336.

(3) Pedersen, J. S.; Schurtenberger, P. Scattering Functions of Semiflexible Polymers with and without Excluded Volume Effects. *Macromolecules* **1996**, *29* (23), 7602–7612.

(4) Picout, D. R.; Ross-Murphy, S. B.; Errington, N.; Harding, S. E. Pressure Cell Assisted Solubilization of Xyloglucans: Tamarind Seed Polysaccharide and Detarium Gum. *Biomacromolecules* **2003**, *4* (3), 799–807.

(5) Muller, F.; Jean, B.; Perrin, P.; Heux, L.; Boué, F.; Cousin, F. Mechanism of Associations of Neutral Semiflexible Biopolymers in Water: The Xyloglucan Case Reveals Inherent Links. *Macromol. Chem. Phys.* **2013**, *214* (20), 2312–2323.

(6) Yu, L.; Yakubov, G. E.; Martínez-Sanz, M.; Gilbert, E. P.; Stokes, J. R. Rheological and Structural Properties of Complex Arabinoxylans from Plantago Ovata Seed Mucilage under Non-Gelled Conditions. *Carbohydrate Polymers* **2018**, *193*, 179–188.

(7) Dervilly-Pinel, G.; Thibault, J.-F.; Saulnier, L. Experimental Evidence for a Semi-Flexible Conformation for Arabinoxylans. *Carbohydrate Research* **2001**, *330* (3), 365–372.

CHAPTER IV

Enzymatic Hydrolysis in Homogeneous Conditions

i. Preamble

This chapter deals with the first major question of this PhD work, which is related to the activity of the enzyme and whether it is impacted by high concentrations of its polymeric substrate. Our questions are:

1. What are the Michaelis-Menten parameters of the degradation?

2. Does the polymer concentration impact the initial activity of the enzyme?

3. Can we see any effect of the polymer concentration on the long-term kinetics?

4. Is there an effect of the polymer concentration on the size of the degradation products?

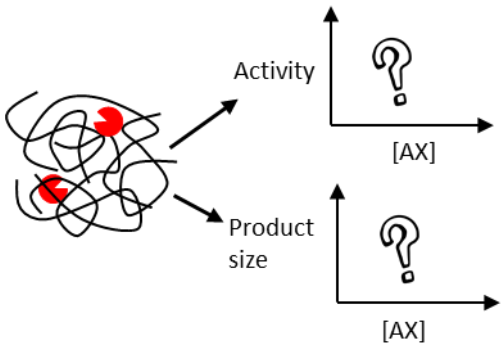

ii. Introduction

Enzymatic hydrolysis of molecular, homogeneous solutions is very well characterised and known to follow so-called Michaelis-Menten kinetics. The Michaelis-Menten model [59] is used to determine standard parameters like the apparent substrate affinity of the enzyme or the catalytic efficiency of the reaction. This model describes the enzymatic reaction in two steps. Firstly, the enzyme *E* reversibly binds (k_1) and unbinds (k'_1) to its substrate *S* forming a substrate-enzyme complex [*ES*]. Then, the reaction product *P* is released at the catalytic rate k_{cat}:

$$E + S \overset{k_1, k'_1}{\longleftrightarrow} [ES] \overset{k_{cat}}{\longrightarrow} E + P$$

From this, the following equation can be derived:

$$v_0 = k_{cat}[E_0] \frac{[S]}{K_m + [S]} \quad (Equ. 13)$$

Where v_0 is the initial reaction rate, $[E_0]$ and $[S]$ the concentration of enzyme and substrate respectively, k_{cat} the catalytic rate and K_m the ratio k_1/k'_1, called the Michaelis-Menten constant representing the substrate affinity.

For the experimental determination of the Michaelis-Menten parameters, the initial reaction rate for several substrate concentrations is determined and plotted, resulting in a characteristic saturation curve from which k_{cat} and K_m can be calculated using Equ. 13.

Like any model, the Michaelis-Menten model makes several assumptions that have to be taken into account for the correct application and interpretation of the model [109]. Among the general assumptions is the use of the initial velocity of the reaction at very short times (close to 0) and the excess of substrate over enzyme. The steady-state assumption describes the second state or part of the curve, the plateau, where, after the initial increase with substrate concentration, the concentration of enzyme-substrate complexes and therefore the reaction rate is constant.

Another assumption is that the catalytic step, the formation of the product, is the rate-limiting step of the reaction (rapid-equilibrium assumption).

Today, with an increasing interest in the valorisation of plant biomass [1], [110] and therefore enzymes that are active on polymers, the characterisation of (concentrated) polymer degradations gains importance. These reactions take place in dense and complex environments, which raises the question whether a characterisation that relies only on the initial reaction rate is sufficient.

Studies have shown that at high polymer concentrations, enzymes experienced steric hindrance from the polymer chains, resulting in a diffusion controlled degradation [6], [71], [72]. This effect however was observed over the course of hours or even days, which is very different to the time scale that is used for the determination of the initial reaction rate (usually minutes). Given the fact that the knowledge of a diffusion limitation is an important and interesting information for the characterisation of enzymatic deconstruction, a long-term study of the activity for polymeric substrates is relevant. And what if the polymer concentration does not only impact the degradation rate but also the degradation products? To investigate this, an additional characterisation of the size and composition of the products is necessary.

In the following, we will characterise the enzymatic hydrolysis of wheat arabinoxylan at different substrate concentrations. We will study the hydrolysis rate at short time scales for the traditional Michaelis-Menten approach as well as at long time scales. In addition, we will use size-exclusion chromatography with multi angle light scattering (SEC-MALS) to determine the size of the degradation products. After a brief look at the initial state of the prepared arabinoxylan solutions, the special focus will be on the impact of the polymer concentration on the activity of the enzyme.

iii. Materials and Methods

a. Expression and purification of the enzyme

The gene encoding the *Np*Xyn11A enzyme [100] with a C-terminal His6-tag was cloned in a pET22b plasmid inducible by the t7-RNA polymerase (DE3 system) and is resistant to ampicillin.

The enzyme was expressed using competent Escherichia coli BL21-DE3 cells. These cells were transformed using the heat shock method. For this, plasmids and cells were brought together and first kept on ice for 30 min, then at 42 °C for one minute before being transferred back on ice for 5 min. The transformed cells were mixed with 250 µL selective Luria-Bertani (LB) broth (containing 50 µg.mL^{-1} ampicillin) and plated on selective LB agar. The plates were incubated upside-down overnight at 37 °C. The next day, isolated colonies were selected and grown in 8 mL pre-cultures of selective LB-broth at 37 °C under agitation overnight. For the main culture, each pre-culture was transferred into a 2 L Erlenmeyer flask containing 800 mL selective LB broth and incubated at 37 °C under agitation. The growth of the cultures was monitored by spectrophotometer until mid-exponential phase (A_{600} nm = 0.4 - 0.6). At that point, recombinant protein expression was induced by adding 1 mM isopropyl 1-thio-B-D-galactopyranoside (IPTG) and incubation was continued for another 4 h. The cultures were centrifuged and the recovered cells were stored at -20 °C until purification.

To purify the enzymes, the thawed cells were lysed by sonication and centrifuged. The supernatant was filtered through a 22 µm membrane and then the enzymes were recovered by immobilized metal ion affinity chromatography (IMAC) using a cobalt resin. The resin was decanted, rinsed with deionized water and equilibrated with 50 mM sodium phosphate buffer at pH 7.4 containing 300 mM NaCl. Then, the cell-free extract was added, mixed and incubated for 10 min on ice. Once the flow-through was released, the resin was washed once with 50 mM sodium phosphate buffer at pH 7.4 containing 300 mM NaCl, and once with 50 mM sodium phosphate buffer at pH 7.4 containing 300 mM NaCl and 5 mM imidazole.

Finally, the enzymes were eluded twice using 50 mM sodium phosphate buffer at pH 7.4 containing 300 mM NaCl and 100 mM imidazole. Gel electrophoresis confirmed the presence of purified enzymes in both elution fractions, so they were combined and dialysed using membranes with 6-8 kDa molecular cut-off to remove the imidazole. Before use, the dialysis bags were rehydrated twice for 15 min in deionized water. The enzymes were dialysed against 2 L of 50 mM sodium phosphate buffer at pH 7.4 for 2 h at 4 °C and then in fresh buffer for another 16 h at 4 °C under light agitation.

The enzyme was recovered and the success of the purification was determined by gel electrophoresis and gel filtration using a Superdex75 16/60 column (Cytiva). Both confirmed a high purity (see Supplementary Information).

b. Preparation of the polymer solution

(i) Preparation using filtration/centrifugation

Low viscosity arabinoxylan (P-WAXYL, Megazyme) solutions were prepared in two steps. First, a diluted stock solution at 1 $g.L^{-1}$ was prepared in 50 mM sodium phosphate buffer at pH 6, stirred and heated to approximately 90 °C and kept at this temperature for 2 h. The second step is the concentration of this stock solution by gradually removing water. For this, the solution was filtered through a membrane with a molecular cut-off of 3 kDa using centrifugal filter devices (Amicon® Ultra -15 3 kDa). For each filtration step, the volume of the solution was reduced from 10 mL to approximately 5 mL. Before the next filtration step, the sample volume was readjusted to 10 mL using the stock solution. Centrifugations were performed at 4500 x g for 25 to 60 min for 1 to 4 days, depending on the target concentration and volume (Eppendorf 5804 R centrifuge). The concentration was verified by measuring the refractive index of the solution (Mettler Toledo RM50).

(ii) Preparation using osmotic compression

The initial stock solution at 1 $g.L^{-1}$ was prepared in the same way as the solution in (i). The solution was then transferred into a rehydrated semi-permeable membrane with a molecular cut-off of 5-8 kDa (Spectra/Por® 1 dialysis membrane) and plunged into 4 L of concentrated PEG solutions between 60 and 200 $g.L^{-1}$ under light agitation. The osmotic pressure gradient between the two solutions acts as the driving force that pushes the water from the sample into the surrounding PEG solution, increasing the sample concentration. The evolution of the concentration of the AX solution was followed by weighing the dialysis bag and measuring the refractive index regularly (Mettler Toledo RM50) until the desired concentration was reached. At some point during the osmotic compressions, we noticed the presence of PEG in some of the samples. The amount of the contamination was limited to a maximum of 15 % in volume and the concentration of AX could be corrected using the ratio of the initial and

final volume of the dialysis bag. The presence of PEG could be caused by a leak in the dialysis membrane or residual PEG that remained after the membrane was rinsed before use, it was however not possible to detect the precise reason in our case. To avoid any further risk of contaminations, osmotic compression was replaced by filtration/centrifugation preparation for future solutions (e.g. for the diffusion experiments in Chapter V).

(iii) Preparation using direct dissolution

After the exclusion of osmotic compression due to PEG contaminations, we needed a last-minute alternative to produce adequate volumes of more concentrated polymer solutions for SEC-MALS analysis. As a compromise, we chose the preparation of intermediate concentrations using direct dissolution. These solutions were prepared in only one step, as the stock solution was directly prepared at the final concentration and agitated at 90 °C for 2 h.

c. Enzymatic activity

Enzymatic activity was measured using the dinitrosalicylic acid (DNS) assay. This assay is a colorimetric method that measures the absorbance of the product of the reaction between 3,5-dinitrosalicylic acid (DNS acid) and the aldehyde or ketone group of a reducing sugar. In the case of wheat arabinoxylan (WAX) degradation, the reaction partner of the DNS acid is the free aldehyde group belonging to the xylose unit at the reducing end of the polymer chain. Over the course of the enzymatic hydrolysis, more and more reducing ends are created. Using a standard curve of xylose, the absorbance of the reaction product can be correlated to the concentration of the sugar and the degradation rate can be expressed as a liberation of xylose equivalents over time.

(i) Initial activities as a function of polymer concentration (Michaelis-Menten plot)

The polymer solutions were prepared using direct dissolution ($c < 5$ g.L^{-1}), osmotic compression (5 g.L^{-1} < c < 31 g.L^{-1}) and centrifugation ($c > 31$ g.L^{-1}) at concentrations ranging from 0.25 g.L^{-1} to 50 g.L^{-1}. The enzyme was diluted using 50 mM sodium phosphate buffer at pH 6 supplemented with 1 g.L^{-1} BSA (Sigma Aldrich). To start the degradation, 20 µL of enzyme solution was transferred into 980 µL polymer solution and a final enzyme concentration of 1.2 for small substrate concentrations (< 13 g.L^{-1}) to 4 nM (> 13 g.L^{-1}). The enzyme concentration was reduced for small substrate concentrations to slow the reaction down and increase the number of experimental points for a more accurate determination of v_i.

The enzymatic reactions were carried out in 1.5 mL Eppendorf tubes at 37 °C and 1200 rpm agitation (ThermoMixer© Eppendorf). At specific times between 0 and 15 min, samples of 100 µL were taken and mixed with 100 µL of DNS supplemented with 0.2 g.L^{-1} xylose. For the standard curve, xylose solutions from 0 to 5 g.L^{-1} were prepared in ultra-pure water and mixed with the supplemented DNS solution in the same way. For the DNS analysis, all the samples including the standards were incubated at 95 °C

for 10 min in a water bath. After cooling, 1 mL of deionized water was added to the samples to adjust the absorbance. 300 µL of each sample were displayed in a 96-wells plate and the absorbance was measured using a microplate spectrophotometer at 540 nm. With the help of the standard curve, absorbance was converted into xylose equivalents and plotted over time. To obtain the initial activity of the enzyme, the slope of the linear part of the plot was used.

(ii) Long-term activities and SEC-MALS samples

While the degradation of 5 and 10 $g.L^{-1}$ AX took place at 37 °C, the degradation of 35 $g.L^{-1}$ AX belonged to a different set of experiments and took place at 23 °C (PCI experiment in Chapter VI). Due to organisational difficulties, there was no time to repeat the experiment at 37 °C. The difference in temperature has to be considered for the results.

For the long-term activities, reactions were launched and sampled over a period of 24 h. In all cases, the substrates prepared by dissolution (5 and 10 $g.L^{-1}$) and centrifugation (35 $g.L^{-1}$) were pre-heated in a water bath at 37 °C for 5 and 10 $g.L^{-1}$ and at 23 °C for 35 $g.L^{-1}$. The enzyme was diluted in 50 mM sodium phosphate buffer at pH 6 supplemented with 1 $g.L^{-1}$ BSA and added at a final concentration of $1.2x10^{-9}$ M for all studied concentrations. For the reaction, the mix was incubated in the water bath at 37 °C for 5 and 10 $g.L^{-1}$ and 23 °C for 35 $g.L^{-1}$. Before taking each sample, the mix was thoroughly vortexed.

For SEC-MALS analysis, samples of 1 mL were pipetted into a 1.5 mL Eppendorf tube and immediately transferred into a water bath at 95 °C for 10 min to inactivate the enzyme. They were stored at -20 °C until further analysis.

For DNS assay, samples of 50 µL were pipetted into an equal volume of DNS solution supplemented with 0.2 $g.L^{-1}$ xylose and mixed to deactivate the enzyme. They were stocked at -20 °C until DNS analysis. The xylose samples for the standard curve were prepared in the same way and also stocked at -20 °C. For the DNS analysis, all samples were thawed and then incubated in a water bath at 95 °C for 10 min.

After cooling down, 1 mL of deionized water was added to adjust the absorbance. Then, 300 µL of each sample were displayed in a 96-wells plate and the absorbance was measured using a microplate spectrophotometer (TECAN sunrise) at 540 nm. With the help of the standard curve, absorbance was converted into xylose equivalents and plotted over time.

d. SEC-MALS analysis

Size exclusion chromatography was carried out using three Shodex columns in series (805, 803, 802.5) connected to three detectors: a differential refractometer (Agilent 1260 Affinity), a UV detector (254 nm, Varian) and a multi angle light scattering detector (18 angles, MALLS Wyatt Dawn Helios, laser @658 nm). The eluant was 50 mM sodium phosphate buffer at pH 6 and a flow rate of 0.8 $mL.min^{-1}$. All data were analysed using ASTRA VI software (Wyatt Technology).

Before the analysis, the samples were thawed on ice and then filtered through 0.45 µm pore size syringe filters.

iv. Results and Discussion

In the following section, we first look at the reaction rate of the enzyme and its evolution with polymer concentration at two different length scales (initial and long-term). Then, we move on to the characterisation of the size of the reaction products for the different substrate concentrations.

b. Characterisation of short-term reaction kinetics: Michaelis-Menten parameters

The objective of this section is to determine the evolution of the specific activity of the enzyme for dilute to high substrate concentrations. The specific activity is the millimolar concentration of liberated xylose equivalents per minute and per milligram of enzyme at initial times. Will the concentration of the polymeric structure affect the activity of the enzyme?

To answer this question, the evolution of the specific activity of the enzyme at 37 °C is plotted in function of the concentration of substrate (see Figure 26). We use the specific activity to consider the two different enzyme concentrations that we used for the reactions. For substrate concentrations of 13 $g.L^{-1}$ and beneath, the concentration of enzyme was reduced for experimental convenience (see experimental section c.(i)). The polymer solutions between 5 and 31 $g.L^{-1}$ were produced using osmotic compression and their concentrations had to be corrected due to a contamination with PEG (max 15% in volume, see experimental section b (ii)).

The evolution follows a typical Michaelis-Menten saturation kinetic [59]. The kinetic parameters V_{max} and K_m can be determined by fitting the model onto the experimental data. Because we plot the specific activity, V_{max} corresponds to the plateau of the curve, but normalised by the molar concentration instead of the mass concentration. Consequently, we first multiply the value of the fit by the mass concentration of the enzyme and then divide it by the molar concentration of the enzyme. We obtain a K_m of 0.66 $g.L^{-1}$ and a k_{cat} of 3.15 x 10^3 s^{-1}, resulting in a catalytic efficiency k_{cat}/K_m of 4.76 x 10^3 $s^{-1}.L.g^{-1}$ or 2.85 x 10^5 $min^{-1}.L.g^{-1}$. The catalytic efficiency reported by Vardakou *et al.* [100] for the same enzyme using oat spelt xylan was 8.4 x 10^4 $min^{-1}.L.g^{-1}$, and for beechwood xylan 3.2 x 10^4 $min^{-1}.L.g^{-1}$ [111]. In the case of oat spelt xylan, this is due to a lower apparent affinity (4.2 $g.L^{-1}$), while for beechwood xylan the lower catalytic efficiency indicates the impact of the glucuronic substitutions on the turnover of the enzyme. This suggests the dependence of these parameters on the specific enzyme-substrate combination, and not only on the type of catalysis. The fit

is a good quality, suggesting that the presence of the PEG contamination did not chemically or sterically interfere with the hydrolysis.

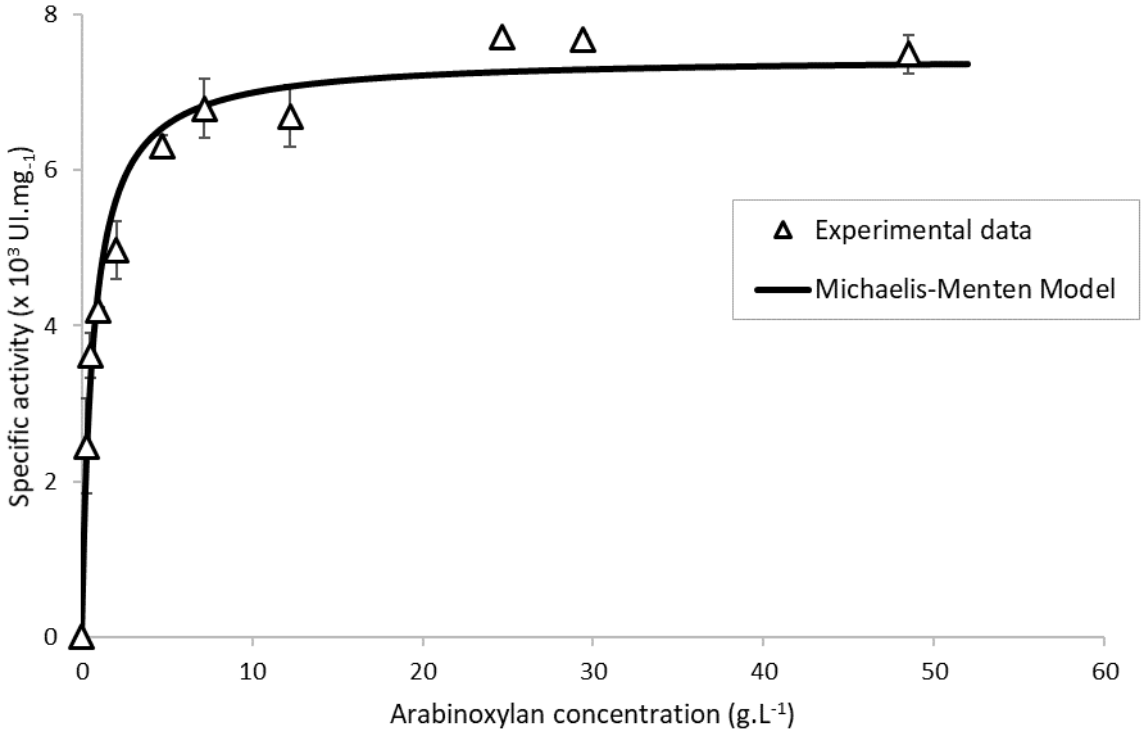

Figure 26: Specific activity of NpXyn 11A at 37 °C which in millimolar of liberated xylose equivalents per minute and per milligram of enzyme (UI/mg). Empty triangles: Experimental data. Line: fitted Michaelis-Menten model.

Since the plateau rate is maintained until the highest studied concentration, polymer concentrations up to 50 $g.L^{-1}$ do not impact the specific activity of the enzyme.

Prud'homme *et al.*, who studied the enzymatic degradation of guar, a galactomannan polysaccharide, found that the reaction rate of the enzyme decreased at high polymer concentrations due to diffusion limitations [6]. They observed the onset of this effect at polymer concentrations between 3 and 5 wt% (~30 and 50 g.L^{-1}), and linked it to the size of the correlation length ξ of the network that decreases with polymer concentration c by $\xi = R_g \left(\frac{c}{c^*}\right)^{-3/4}$. They calculated this using a radius of gyration R_g of 150 nm and an overlap concentration c^* of 0.1 %wt (~1 g.L^{-1}). Consequently, the theoretical mesh sizes are 12 and 8 nm for 3 and 5 %wt respectively, which is close enough to the size of the enzyme (6 nm) to block its mobility and provoke a diffusion limitation. In our case, the enzyme is estimated to be the same size (6 nm, determined by DLS) and the highest studied polymer concentration was 50 g.L^{-1}. According to previous experiments, the correlation length of a solution of 50 g.L^{-1} is approximately 15 nm (see Chapter III), which is larger than in the case of Prud'homme. However, the theoretical correlation length using R_g = 51.5 nm obtained from SEC-MALS and c^* = 3.6 g.L^{-1} obtained from the specific viscosity (see Chapter III for both) is only 7.2 nm, which would put the enzyme here in the same confined situation as for Prud'homme. The fact that we did not observe a decrease in the reaction rate could mean that in our case, the theoretical correlation length underestimates the mesh size, while in the case of Prud'homme it does not, therefore the enzyme was not on the same confinement level. The difference could also be due to the different structural properties of the two polymers: While AX has a ratio of xylose to arabinose of 1.6, the ratio of mannose to galactose for guar is 2. The higher level of substitution for the polymer used by Prud'homme *et al.* leads to different rheological and diffusional properties of the polymer and its degradation products. Or, we do not observe the same reaction rate and cannot compare them to each other. Indeed, the reaction rates used by Prud'homme are measured only indirectly and at rather long times: Using SEC-MALS, they followed the evolution of the size of the polymer chains over the course of the degradation and used it to calculate the degradation rate of the enzyme.

c. Characterisation of long-term kinetics

In the previous section we found that the polymer concentration did not impact the initial specific activity of the enzyme, but can we see an effect at longer degradation times? At very short times, the enzyme might always be able to find and hydrolyse a target site close by, even if it experiences some obstruction from the chains of the polymer. Maybe the diffusion limitation is not an immediate effect on the reaction rate, but becomes visible only over time. In the following, we will look at the long-term kinetics of the degradation of 5, 10 $g.L^{-1}$ and 35 $g.L^{-1}$ AX. It is important to note that the temperature of the reaction was 23 °C for 35 $g.L^{-1}$ instead of 37 °C for the others (see Materials and Methods section). To get an idea of the impact of the temperature difference on the degradation of 35 $g.L^{-1}$ AX, we additionally look at the short-time degradation of a sample at 30 $g.L^{-1}$ AX at 37 °C.

Figure 27 displays the results of the DNS assay for the different degradations. The number of liberated xylose equivalents is normalised by the total theoretical amount of xylose in the sample. This normalisation was chosen to visualise the degradation efficiency of the different reactions: The final theoretical reaction product of the endo-xylanase is xylobiose, so in theory a complete reaction would generate 50 % of possible reducing ends (= xylose units). To calculate the theoretical amount of xylose in the initial AX solution, we first calculated the concentration of xylose in the sample using the ratio A/X = 0.61 and the fact that their mass is identical, and then calculated the amount of xylose using its molar mass (150.13 Da).

For very early times, the evolution for the degradation of 5 and 10 $g.L^{-1}$ is similar (green and blue colour), indicating an identical degradation rate, independent of the polymer concentration. This is in good agreement with the previous results displayed in Figure 20, where the specific activity for 5 $g.L^{-1}$ marks the beginning of the plateau and therefore a constant reaction rate. The initial slope of the degradation of 35 $g.L^{-1}$ (yellow colour) is a lot smaller, which is mainly due to the lower temperature (23 °C, as opposed to 37 °C for 5 and 10 $g.L^{-1}$). To get an estimation on the impact of the temperature on the initial slope, we consult the deconstruction of a similar polymer concentration, but at 37 °C. We can see that for the degradation of 30 $g.L^{-1}$ at 37 °C (black colour), the initial slope is similar to the slope of the other degradations at 37 °C (see inlet Figure 27). This confirms that the reason for the considerably flatter slope in the case of 35 $g.L^{-1}$ is the difference in temperature, and not the higher substrate concentration.

What should however not be affected by temperature is the final product yield. In the case of the degradation of 5 and 10 $g.L^{-1}$, the liberation of degradation products reached a plateau after approximately 10 h, visually indicating the end of the degradation. The final amount of normalised xylose equivalents isabout 53 % in both cases, therefore the theoretical maximal yield for our reaction conditions was reached. In the case of the degradation of 35 $g.L^{-1}$ however, the liberation of xylose equivalents appears to plateau at a lower level, even if this plateau is not yet reached after 48 h. This low yield could be caused by a loss of enzymatic activity. In our case however, we can

confirm that the enzyme is stable at room temperature (which corresponds to the temperature used for this degradation) and conserves its activity for 72 h (see SI Chapter V). Another explanation for this low yield could be the effects of degradation products on the viscosity of the system. While the cleavage of the polymer chains leads to a decrease in the macroscopic solution viscosity, the increasing number of small molecules generated by the enzymatic activity could increase the local, microscopic viscosity of the system. This increase in microscopic or solvent viscosity happens on a scale that is small enough to impact the diffusion of the enzyme. Consequently, the low yield could be a sign of diffusion limitation caused by small reaction products at intermediate polymer concentrations. To confirm whether there really is a lower yield and to exclude the temperature as a reason, the experiment needs to be repeated at 37 °C.

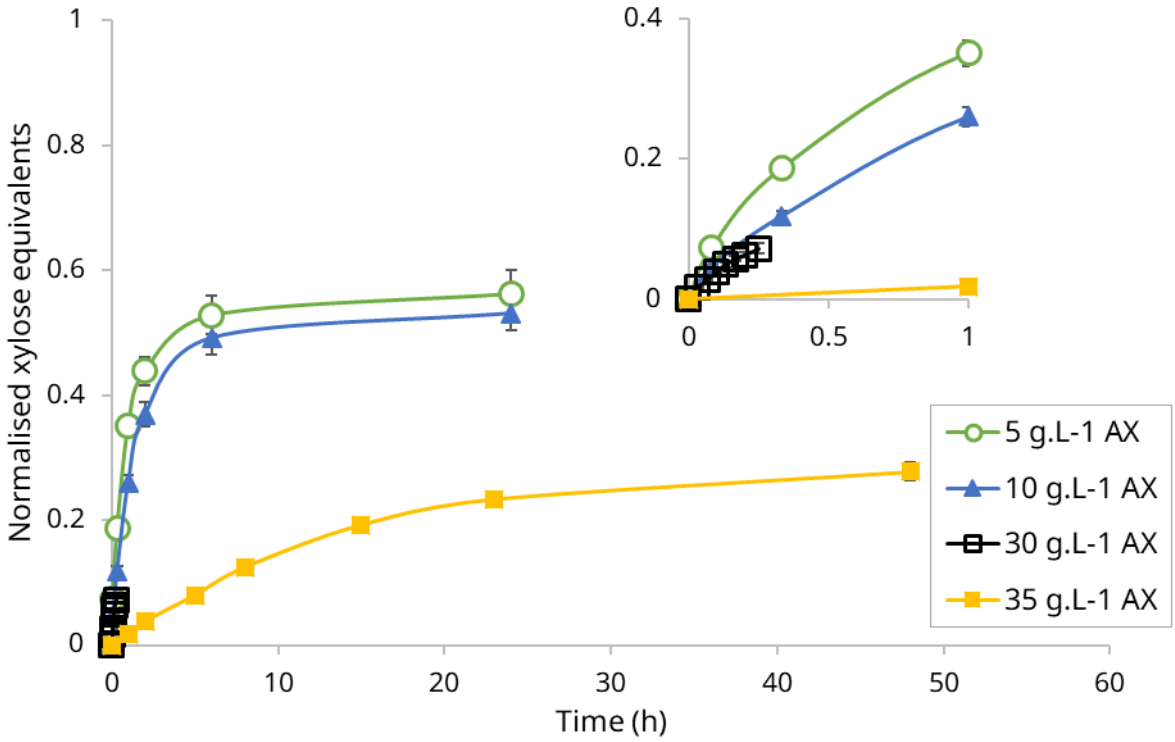

Figure 27: Normalised xylose equivalents over time for the degradation of 5, 10 and 35 g.L^{-1} AX dosed by DNS assay. Reactions using 5 (green colour), 10 (blue colour) and 30 (black colour) g.L^{-1} of AX were carried out at 37 °C, while the degradation of 35 g.L^{-1} occurred at 23 °C. Values were normalised by the total theoretical amount of xylose units in the initial solution. The inlet is a close-up view of times between 0 and 1 h. The lines serve as guide for the eye.

d. Characterisation of the size of the degradation products

In the previous sections, we saw that the polymer concentration did not have an impact on the reaction rate of the enzyme and therefore the number of catalytic events. What about the size of the released degradation products? If the enzyme is limited in its diffusion, its radius of action could be reduced, leading to a locally concentrated deconstruction and the formation of smaller degradation products. To study the size of the degradation products and its evolution over time, we analysed samples of the degradation of 5, 10 and 35 $g.L^{-1}$ using SEC-MALS. At first, we will look at the state of the intact polymer solution to compare the effect of the two different preparation protocols. Then, we move on to the effect of the deconstruction on the polymer solution in terms of quality (RI spectra) and quantity (evolution of the average molecular weight).

The polymer solutions of 5 and 10 $g.L^{-1}$ AX had been prepared using direct dissolution of the polymer powder in solvent. The consequent limited hydration of the polymer chains led to the formation of aggregates, even more so for the higher concentration of 10 $g.L^{-1}$ than for 5 $g.L^{-1}$. The aggregates can be seen on the light scattering spectra between 15 and 18 mL elution volume (Figure 28). The respective refractive index is very small in both cases, suggesting that these aggregates are few. The polymer solution of 35 $g.L^{-1}$ was prepared using a very dilute stock solution that was progressively concentrated using a filtration/centrifugation method. This preparation had a positive impact on the hydration of the polymer, and the light scattering signal showed less and/or smaller aggregates.

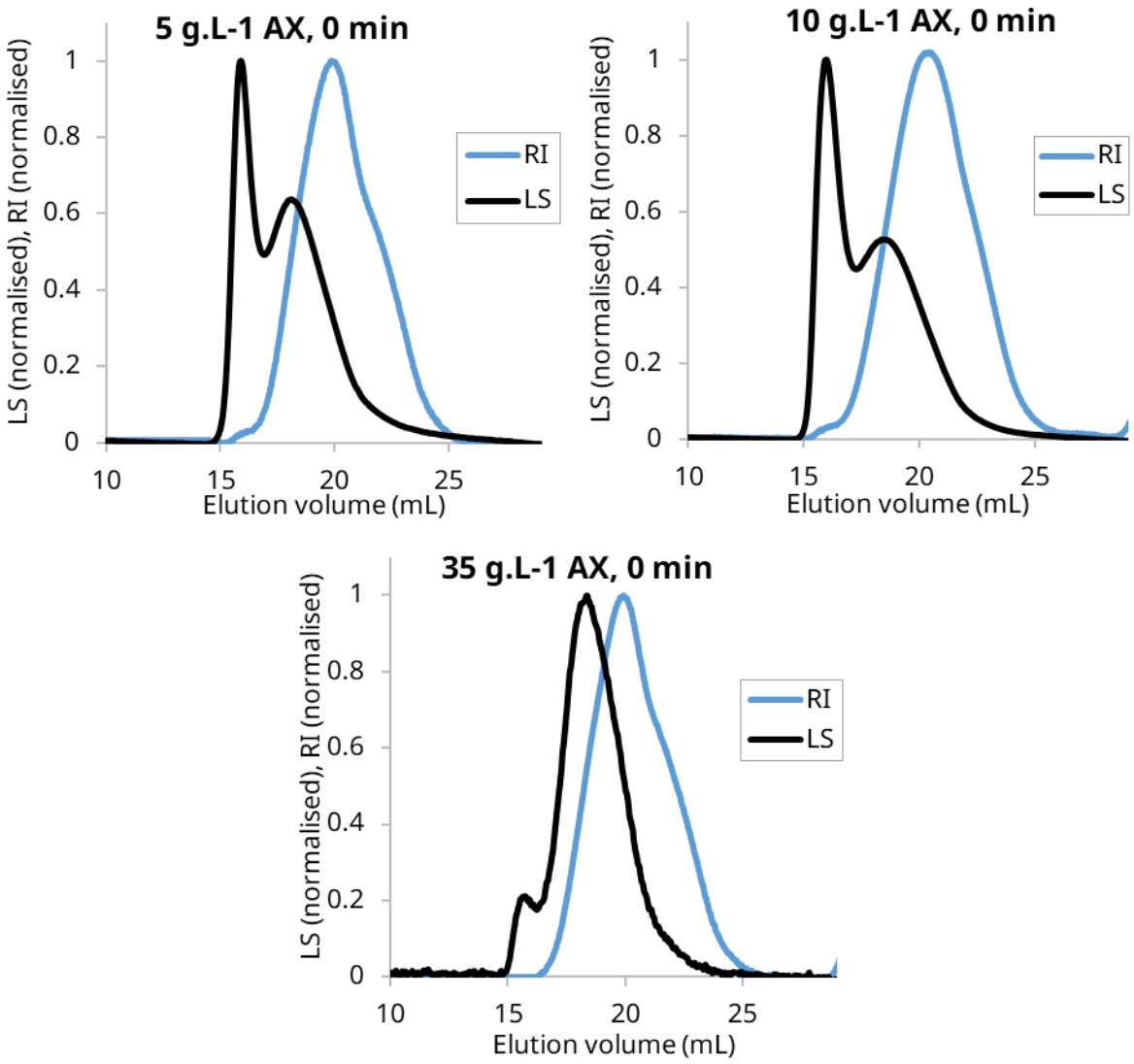

Figure 28: Light scattering signal (LS, 90° angle, black) and refractive index (RI, blue) of the intact AX concentrations (t0) in function of the elution volume. The polymer concentrations were 5, 10 and 35 g.L^{-1} as indicated. Solutions at 5 and 10 g.L^{-1} were prepared using direct dissolution of the powder in solvent, the solution of 35 g.L^{-1} was prepared at a stock solution of 1 g.L^{-1} and progressively concentrated using filtration/centrifugation.

To get an idea of the resistance of these aggregates, we considered the spectra of the samples after the beginning of the enzymatic hydrolysis to see if, and how fast, the light scattering peak of the aggregates decreased (Figure 29). In the case of 5 $g.L^{-1}$, after only 5 min the peak decreased to a small shoulder of the main peak. On the other hand, the aggregates in the solution prepared at 10 $g.L^{-1}$ took 1 h to decrease in a similar fashion. This resistance could be due to the larger size of these aggregates, which would need a progressive and slow erosion-like degradation. The light scattering spectrum for the solution of 35 $g.L^{-1}$ AX showed a two-fold decrease of the aggregate peak after 1 h of degradation.

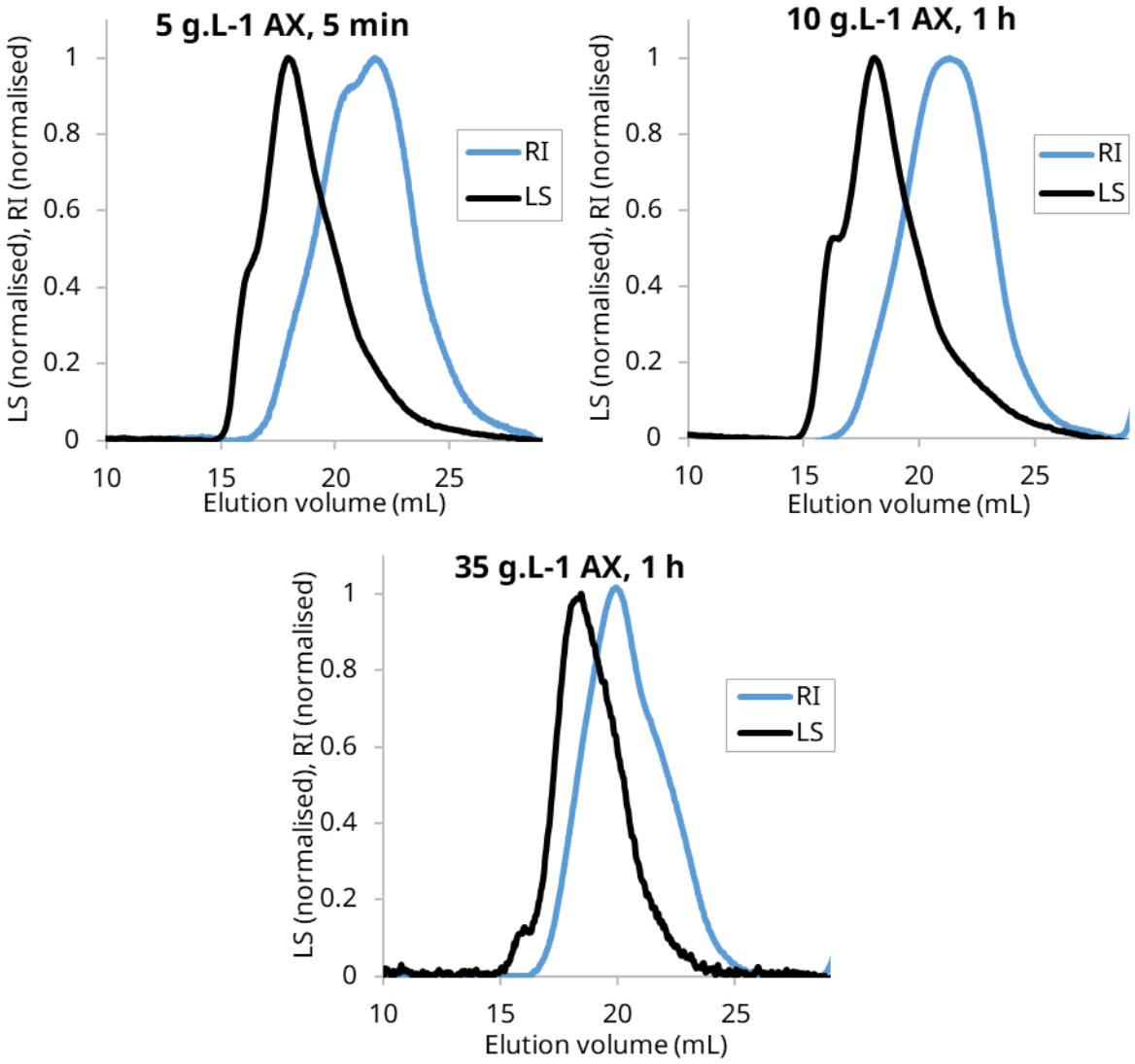

Figure 29: Light scattering signal (LS, 90° angle, black) and refractive index (RI, blue) of the AX concentrations after 5 min (for 5 $g.L^{-1}$ AX) or 1 h in function of the elution volume.

To observe the effect of enzymatic deconstruction on the polymer chains, we can look at the evolution of the refractive index over the course of enzymatic degradation. Figure 30 shows the refractive index for 5 (black), 10 (blue) and 35 $g.L^{-1}$ (yellow) before the enzymatic attack (0 h, full lines) and after 24 h (dashed lines) or 48 h (dotted line). For all three concentrations, the refractive index shifted towards smaller masses and its distribution broadened, indicating the creation of degradation products of different sizes. The spectra of 5 and 10 $g.L^{-1}$ evolved in a very similar fashion, which is in good agreement with the results of the long-term kinetics (Figure 27). The spectrum of 35 $g.L^{-1}$ after 24 h is different to the spectra of the other solutions after 24 h, it is rather the spectrum after 48 h that resembles them (dotted line). This shows the effect of the lower temperature (23 °C instead of 37 °C for the other reactions) on the advancement of the reaction. Interestingly, while these spectra are similar, the advancement of the reaction is not: The long-term kinetics had shown that the deconstruction in the case of 5 and 10 $g.L^{-1}$ has reached its theoretical limit (50 % of total xylose equivalents liberated), while the deconstruction of the 35 $g.L^{-1}$ solution has only reached 60 % of this theoretical limit (30 % of total xylose equivalents liberated).

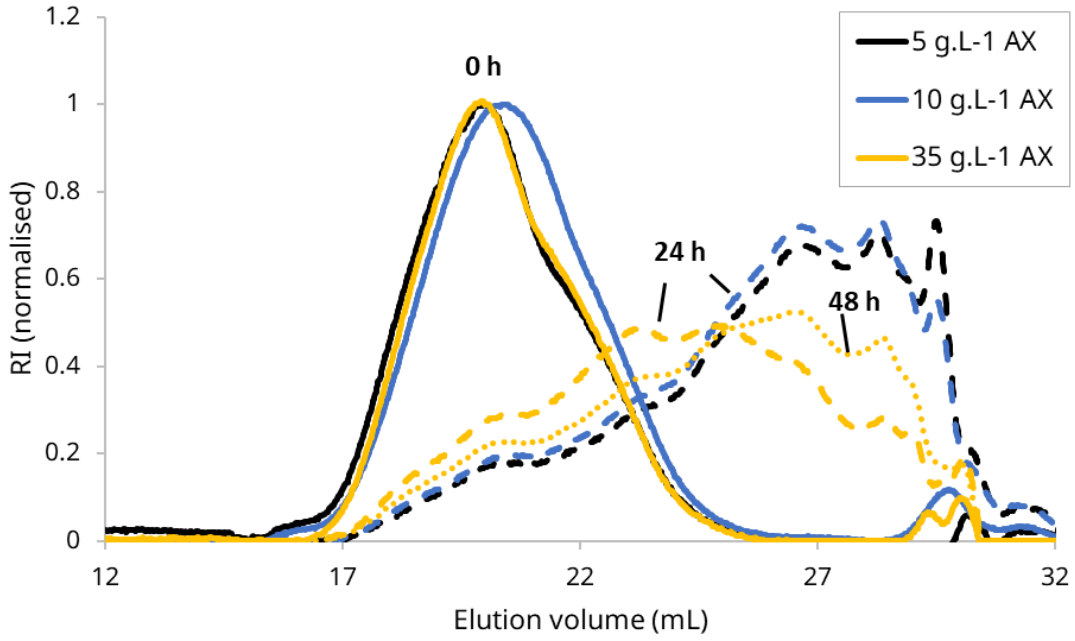

Figure 30: Refractive index plotted against elution volume after 0 (full lines) and 24 h (dashed lines) and 48 h (dotted line) of enzymatic degradation for 5 (black), 10 (blue) and 35 $g.L^{-1}$ (yellow).

We can also look at it the other way around, where we consider two spectra at the same theoretical reaction advancement. The advantage of this is that we observe the state of the reaction decoupled from time, and therefore free from the effects of temperature. Figure 31 displays the spectrum of 10 $g.L^{-1}$ after 1 h of degradation, where the degradation has liberated 26 % of xylose equivalents (black dashed line), and the spectrum of 35 $g.L^{-1}$ after 24 h of degradation, with 23 % of liberated xylose equivalents (blue dashed line). In both cases, the peak appeared in the same range of elution volume (17 to 30 mL). Its distribution however is not the same. The solution of 35 $g.L^{-1}$ contained, after the same number of catalytic events, more small molecules, because its intensity at large elution volumes is above the intensity of the 10 $g.L^{-1}$ solution (red arrow). This could confirm our hypothesis that the enzyme is active in a smaller radius, leading to a localised and more complete degradation of the surrounding polymer chains into smaller products. The reduction of the 'active' radius could either be due to the steric obstruction caused by the mesh of the polymer network, or to the fact that the increasing amount of small degradation products increase the solvent viscosity and slow the enzyme down, leading to a more concentrated degradation. Both of these effects represent a diffusion limitation.

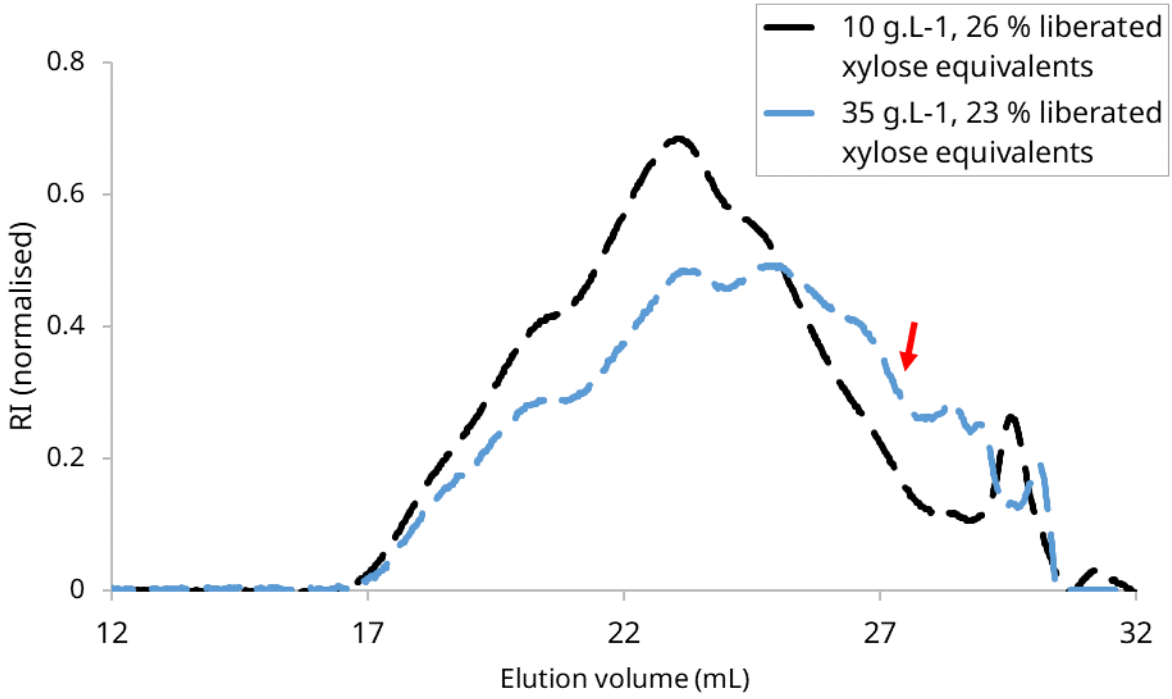

Figure 31: Refractive index plotted against elution volume for 10 g.L^{-1} AX after 1 h of degradation and 26 % liberated xylose units (black dashed line) and for 35 g.L^{-1} AX after 24 h and 23 % liberated xylose (blue dashed lines).

In addition to these qualitative observations, we can quantify the evolution of the average size of the polymer chains over the course of the degradation using the number or mass average molecular mass. For the number average molecular mass M_n, the different molecular masses M_i of the molecules of the same mass is multiplied by their number and summoned, then divided by the total number of molecules:

$$M_n = \frac{\sum_i N_i M_i}{\sum_i N_i}$$

The mass average molecular mass M_w is calculated by multiplying the molecular mass of all molecules of the same mass as well as their number with their mass again:

$$M_w = \frac{\sum_i N_i M_i M_i}{\sum_i N_i M_i}$$

This means that large molecules will have a larger contribution to the molecular mass.

Figure 32 shows the evolution of the normalised number average molecular mass M_n in function of the degradation progress (liberated xylose equivalents or number of catalytic events), and not in function of degradation time to consider the different temperatures used for the reactions. We can see that M_n evolves similarly for the three different concentrations and decreases over more than two decades. However, the masses found for the final degradation products of 5 and 10 g.L^{-1} were smaller than the mass of xylobiose, the theoretical final product (concerned masses are marked with a large red circle in Figure 32). This means that the number of small molecules might be overestimated, or their masses underestimated, during the automatic data analysis.

After an initial, fast decrease, the evolution slowed down. In literature, this type of behaviour is seen for complex substrates, where the enzyme first degrades all easy-access parts before the hydrolysis becomes more stagnant [112].

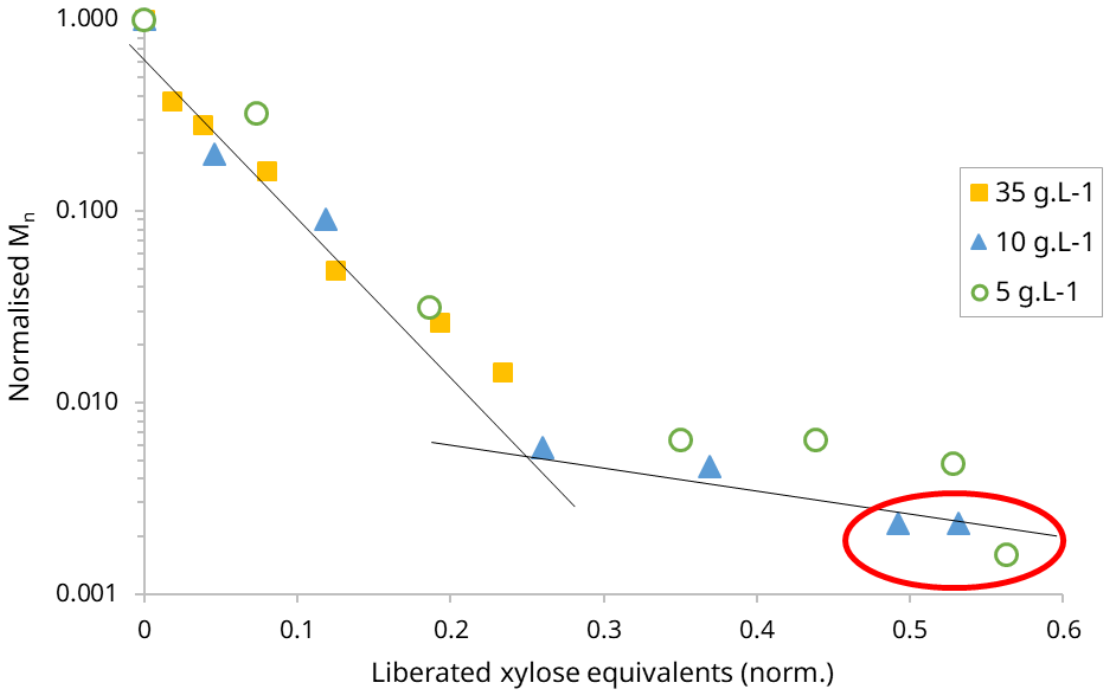

Figure 32: Evolution of the normalised number average molecular mass of AX solutions over the course of enzymatic degradation. The progress of the reaction is not represented by the reaction time but by the number of liberated xylose equivalents. M_n is normalised by $M_{n,0}$ and in logarithmic scale. The large red circle marks molecular masses that are smaller than the mass of the final theoretical reaction product xylobiose. The black lines serve as guide for the eye.

The evolution of the normalised mass average molecular mass can be seen in Figure 33. Over the course of the degradation, M_w decreased 5-fold for 35 g.L^{-1} AX and close to 10-fold for 5 and 10 g.L^{-1}. The evolution here was slower and steadier than for M_n. For 35 g.L^{-1} (yellow squares), the slope appeared steeper and M_w shifting towards smaller masses faster than for the other polymer concentrations. This could confirm what was qualitatively observed for the evolution of the refractive index in Figure 31, and suggest a diffusion limitation of the reaction and the consequent creation of smaller degradation products. To further evaluate this hypothesis, HPLC and mass spectrometry could give a precise molecular mass for small oligosaccharides and longer ones respectively.

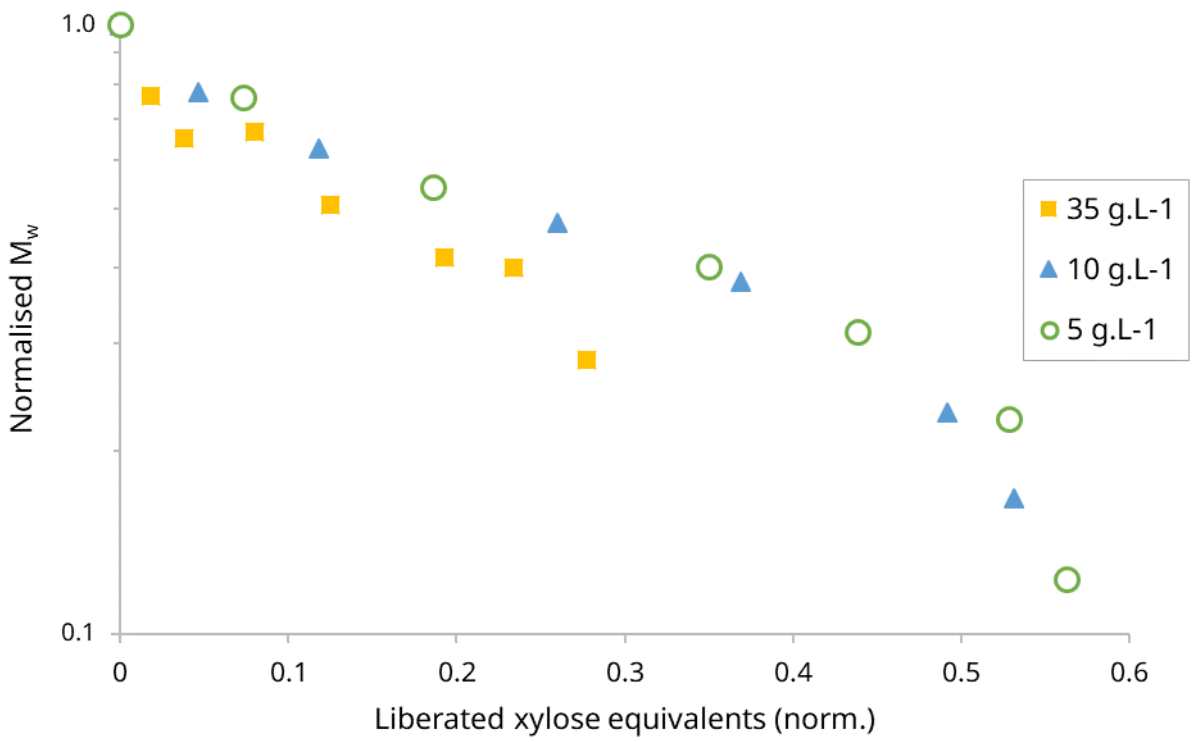

Figure 33: Evolution of the mass average molecular weight of AX solutions over the course of enzymatic degradation. The progress of the reaction is not represented by the reaction time but by the number of liberated xylose equivalents. M_w is normalised by $M_{w,0}$ and in logarithmic scale.

In the context of the characterisation of the initial reaction rate of the enzyme (section a), we have already evoked the work of Cheng *et al.* and Tayal *et al.* on the degradation of guar [6], [113]. They studied the enzymatic degradation of the polymer and used the evolution of the number average molecular mass to calculate the number of catalytic events over time (reaction rate). Using this method, they found that high polymer concentrations led to a decrease of the reaction rate caused by diffusion limitation. In our case, we did not see this decrease when we determined the reaction rate using the direct measurement of the number of catalytic events (Figure 32). Given the fact that we have measured the evolution of the number average molecular mass as well, it would be interesting to follow the method of Cheng *et al.* that is based on the work of Tayal *et al.* [113] to compare the results of this indirect method to the results of the previous direct method.

The first step is to determine the total number of hydrolysable bonds in an average polymer chain. Due to the activity of the enzyme, this concerns only the xylose-xylose bonds of the polymer backbone. However due to its specificity, the enzyme cannot hydrolyse all of these bonds, but only the ones that have unsubstituted neighbouring sugars. This number is difficult to determine, therefore we first used the total number of bonds which can be calculated by using either the number or the mass average molecular mass of a chain M at time t and divide it by the mass of one backbone element minus 1 (the terminal backbone element forms no further bond). On average, every xylose monomer carries 0.61 arabinose units, therefore the mass of one backbone element is the mass of 1.61 xylose monomers m_{xylose} (xylose and arabinose have both a mass of 150 Da). Consequently, the number of hydrolysable bonds per chain is

$$\frac{M(t)}{1.61 m_{xylose}} - 1$$

For the total number of remaining hydrolysable links L in the system at time t, it is multiplied with the initial molar concentration of chains:

$$L(t) = N(0) * \left(\frac{M(t)}{1.61 m_{xylose}} - 1\right)$$

With our direct method in section a, we did not measure the number of remaining links $L(t)$, but the number of cleaved links, so $L(0) - L(t)$, and divided by the total number of links $L(0)$. Therefore, we need to consider:

$$\frac{L(0) - L(t)}{L(0)} = 1 - \frac{N(0) * \left(\frac{M(t)}{1.61 m_{xylose}} - 1\right)}{N(0) * \left(\frac{M(0)}{1.61 m_{xylose}} - 1\right)}$$

$$= \frac{M(0) - M(t)}{M(0) - 1.61 m_{xylose}} \quad (Equ. 14)$$

We plot the previously determined evolution of the hydrolysed links (=liberated xylose equivalents) in function of Equation 14 for both mass and number average molecular mass in Figure 34, to compare the number of catalytic events determined by the two different methods. If both methods gave the same result, they would align on a straight line of slope 1 (black line). We can see that using the number average molecular mass (empty symbols) gives results that are very different to the previous results from xylose equivalents. The results from the weight average molecular mass (full symbols) are more comparable, though there is a factor 2.

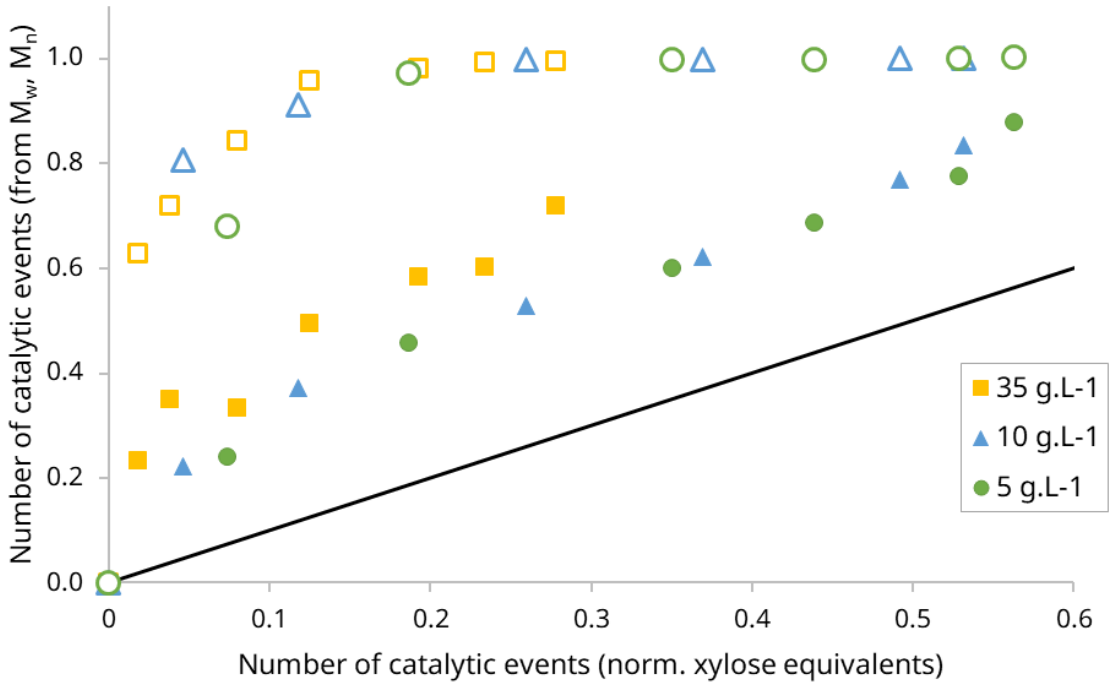

Figure 34: Number of catalytic events calculated using Equation X as a function of liberated xylose equivalents. Empty symbols use the number average molecular mass for Equation 14, full symbols the mass average molecular mass. Black line has a slope of 1 and serves as a guide for the eye for a perfect correlation between the two methods.

In their study, Tayal *et al.* further found that the evolution of cleavable links and therefore the evolution of the molecular mass over time correspond to a transition of zero-order kinetics to first-order kinetics. For this, we plot the evolution of the molecular mass as $\frac{1}{M(t)} - \frac{1}{M(0)}$ over time. Due to the findings in Figure 34, we considered only the mass average molecular mass here.

Figure 35 shows the results for the three polymer concentrations. Like in the study of Tayal *et al.*, we can see two different kinetic regimes marked by two different slopes (black lines): An initial increase at maximum rate and high concentrations of cleavable bonds (zero-order kinetics), followed by a decrease for smaller concentrations (first-order kinetics). The two different slopes can be linked to the catalytic properties of the enzyme. However, the quantification of this link is difficult and deserves an in-depth analysis and understanding of the necessary equations and hypothesis.

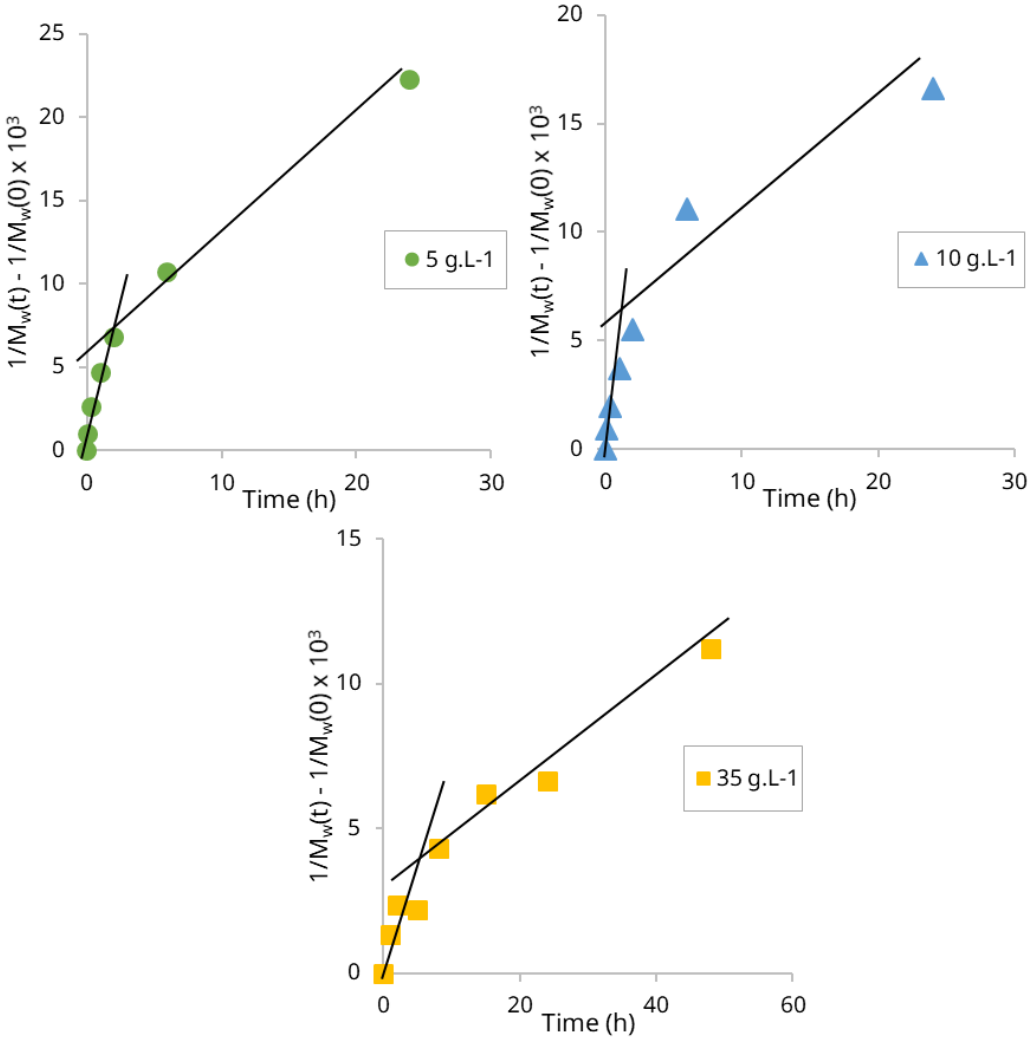

Figure 35: Inverse of the mass average molecular mass as a function of degradation time for 5, 10 and 35 g.L^{-1} AX respectively. The evolution can be divided into two regimes by a change in the slope (see black lines to guide the eye).

As an important note, it seems to us that the calculations of enzyme activities performed in the work of Prud'homme *et al.* may be incorrect due to some misleading hypotheses about the order of the reaction and the way the effective activity must be calculated in that case. Additionally, they did not consider the specificity of the enzyme. Malgas *et al.* have found that this mannanase is less active on higher galactose substituted guar, which indicates that substitutions impact its activity and the number of accessible and thus cleavable bonds [114]. All of this needs a more detailed examination at a later time, but that somewhat calls into question their results (Figure 12 of this manuscript), with this strong decrease of the 'effective' activity of the enzymes in concentrated gels.

v. Conclusion

In this chapter, we studied the enzymatic hydrolysis of the wheat arabinoxylan polysaccharide, a polymeric substrate, in homogeneous conditions. The aim was to see if, and how, the concentration of the polymeric substrate impacts the enzymatic activity. Possible effects could be **(1) a slower reaction rate**, because the polymer chains obstruct the diffusion of the enzyme and limit the access to its target sites. At longer times, the diffusion of the enzyme could also be slowed down due to the increasing concentration of small, molecular degradation products that increase the viscosity of the solvent. The presence of the polymer chains could also lead to a confinement of the enzyme and a reduction of its radius of activity. If the enzyme spent more time in one place, the polymer chains in close proximity could be more thoroughly hydrolysed, which would lead to **(2) the early appearance of smaller degradation products**.

To determine the impact of the polymer concentration on the reaction rate **(1)**, we first measured the initial reaction rate for substrate concentrations up to 50 $g.L^{-1}$ by dosing the number of catalytic events. Using this direct and common method, we found that the results followed the Michaelis-Menten model with no deviation. In a polymer solution of 50 $g.L^{-1}$, the chains form a mesh with an average mesh size of 15 nm, which is big enough to let the enzyme (6 nm) pass. This could explain why we did not see a diffusion limitation at short times (15 min). It would be interesting to measure the initial reaction rate for even higher substrate concentrations, where the mesh size is as large as the enzyme. Such polymer solutions are however very difficult to handle because of their high viscosity. To see whether there was an effect on the reaction rate at longer times, we dosed the number of catalytic events over 24 to 48 h for solutions of 5, 10 and 35 $g.L^{-1}$. Here, we saw a potential effect of the polymer concentration on the degradation yield: While the solutions at 5 and 10 $g.L^{-1}$ AX reached a plateau that indicated the theoretical end of the reaction (50 % of possible bonds hydrolysed), the 35 $g.L^{-1}$ solution appeared to stagnate at a lower level, even though the enzyme remained active.

Yet, it is not possible to conclude: Due to a lower temperature for this degradation, the reaction did not reach a plateau yet, so we could only estimate the final yield. This should be repeated, using the same temperature as the other reactions.

In addition to these experiments, we used SEC-MALS to determine the size of the degradation products **(2)**. Qualitatively, we saw a difference in the evolution of the refractive index between the concentrations. Interestingly, comparable levels of deconstruction, the spectrum of the 35 $g.L^{-1}$ sample showed more small molecules than the one of 10 $g.L^{-1}$. This could indicate diffusion limitation that caused the creation of smaller degradation products. Quantitatively, we looked at the evolution of the number and mass average molecular weight in function of the degradation progress. While M_n evolved similarly for all three concentrations, M_w showed a faster decrease to smaller masses for the highest polymer concentration. This corroborates what we qualitatively saw in the RI spectra, and suggests an impact of the polymer concentration on the size of the degradation products.

Overall, while no impact on the reaction rate was found, this work shows that the hydrolysis of the polysaccharide leads to smaller degradation products at high concentrations. These findings are relevant for process applications, since here the concentrations of polymer are usually high.

vi. Supporting Information

Enzyme production

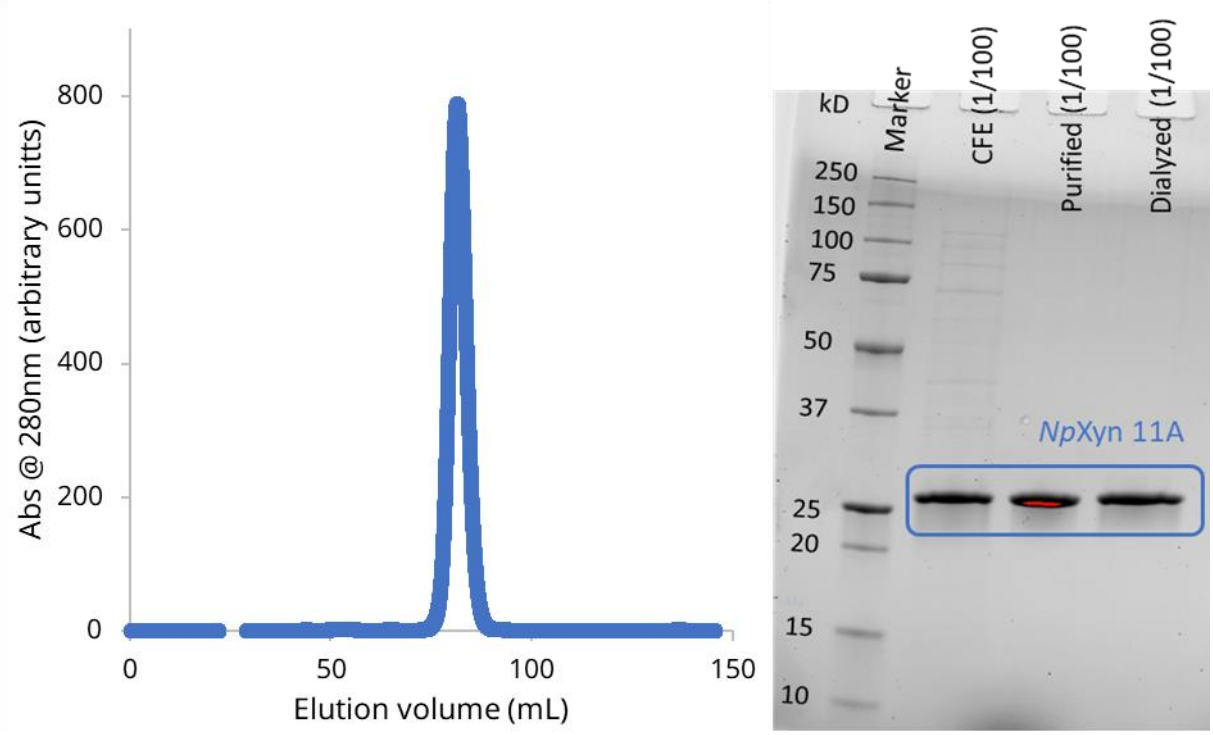

Figure SI.1: Gel filtration of the purified, dialyzed NpXyn 11A enzyme (left-hand side) and gel electrophoresis result (right hand side) with the molecular marker, the cell-free extract (dilution 1/100), the purified (1/100) and the final dialyzed enzyme (1/100), showing the band of NpXyn 11A at the expected size of 26 kDa.

Evolution of the light scattering intensity

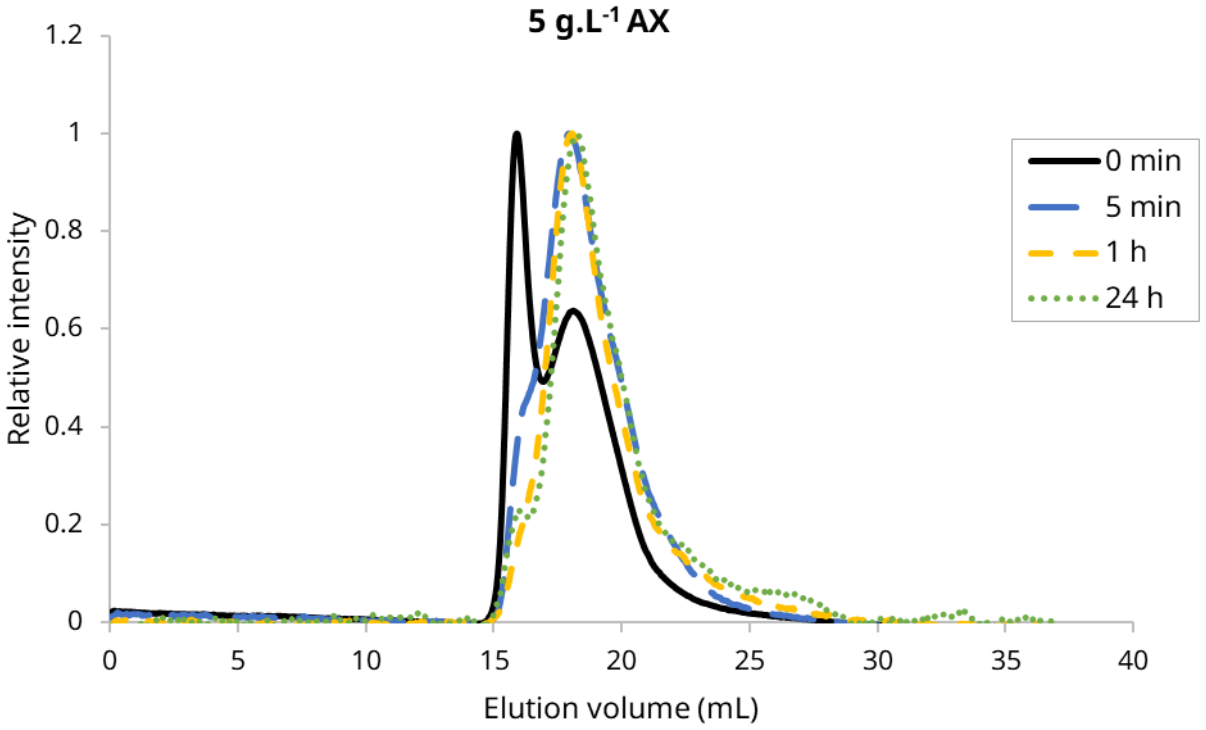

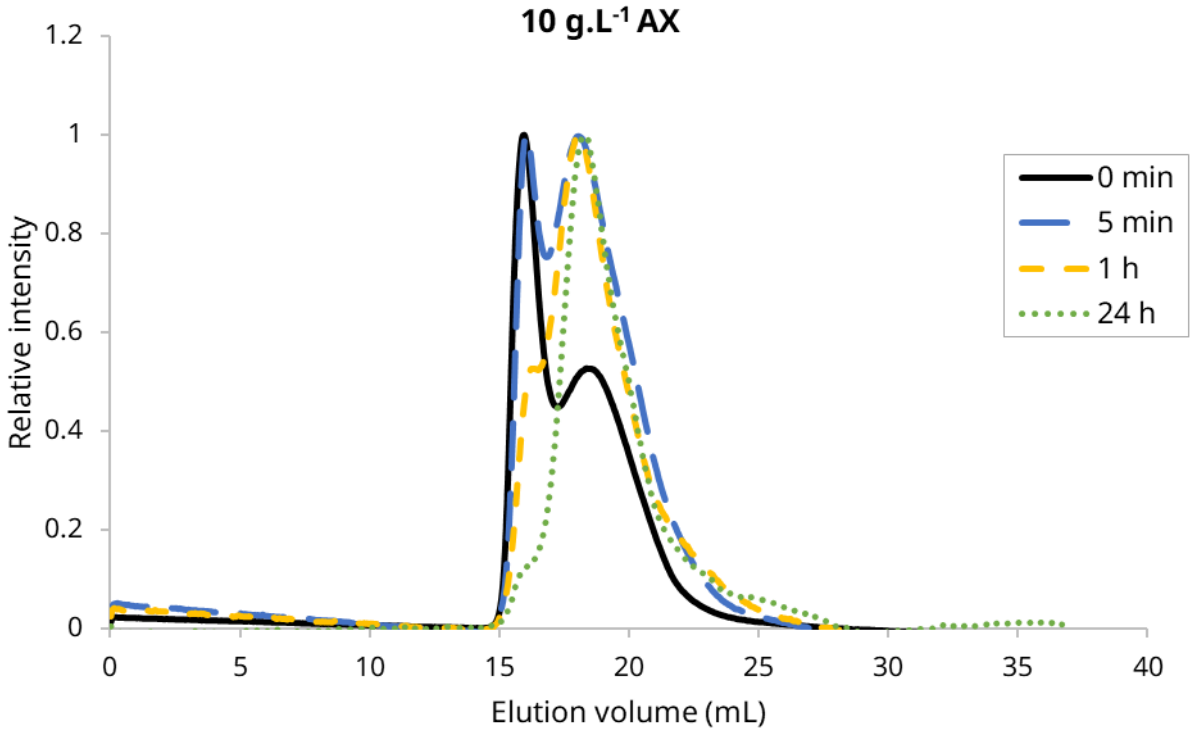

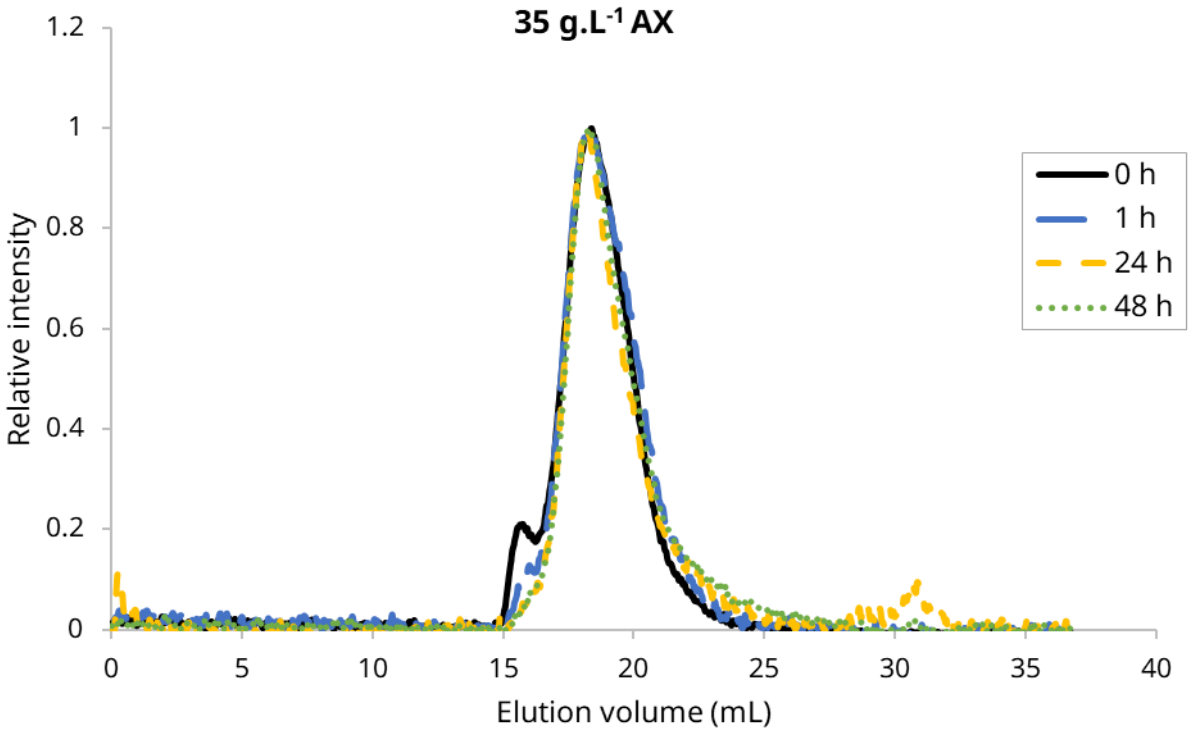

Evolution of the differential refractive index

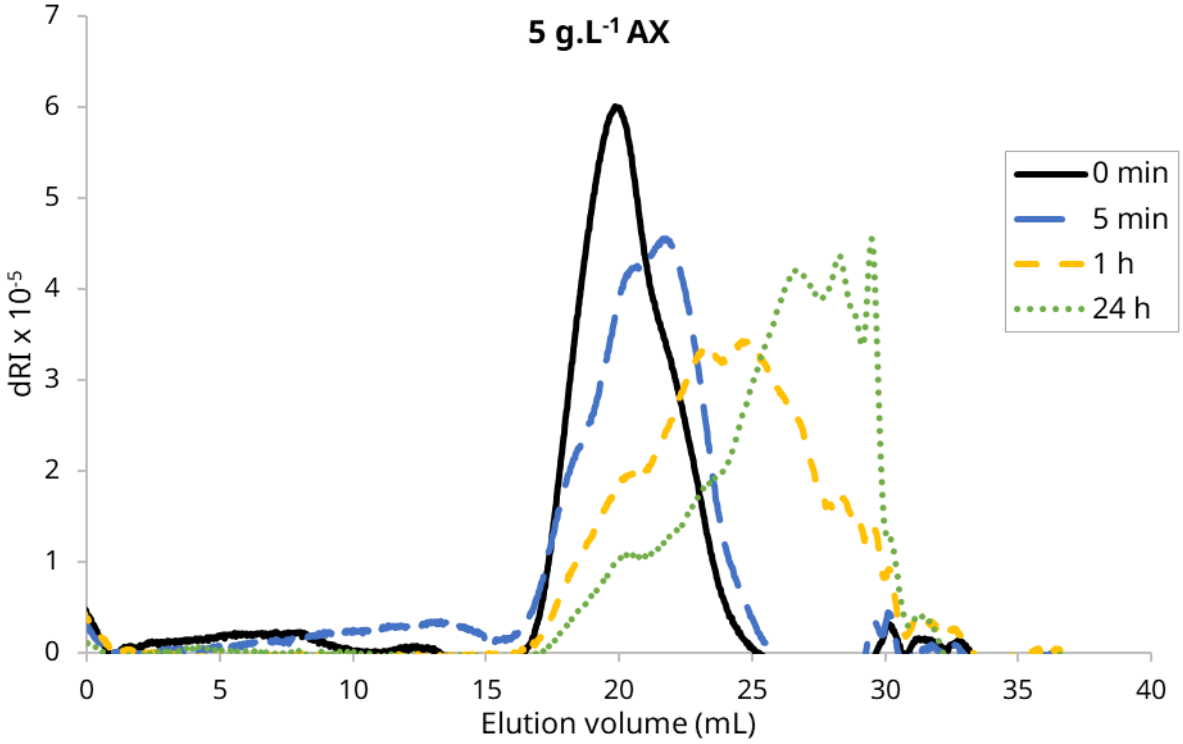

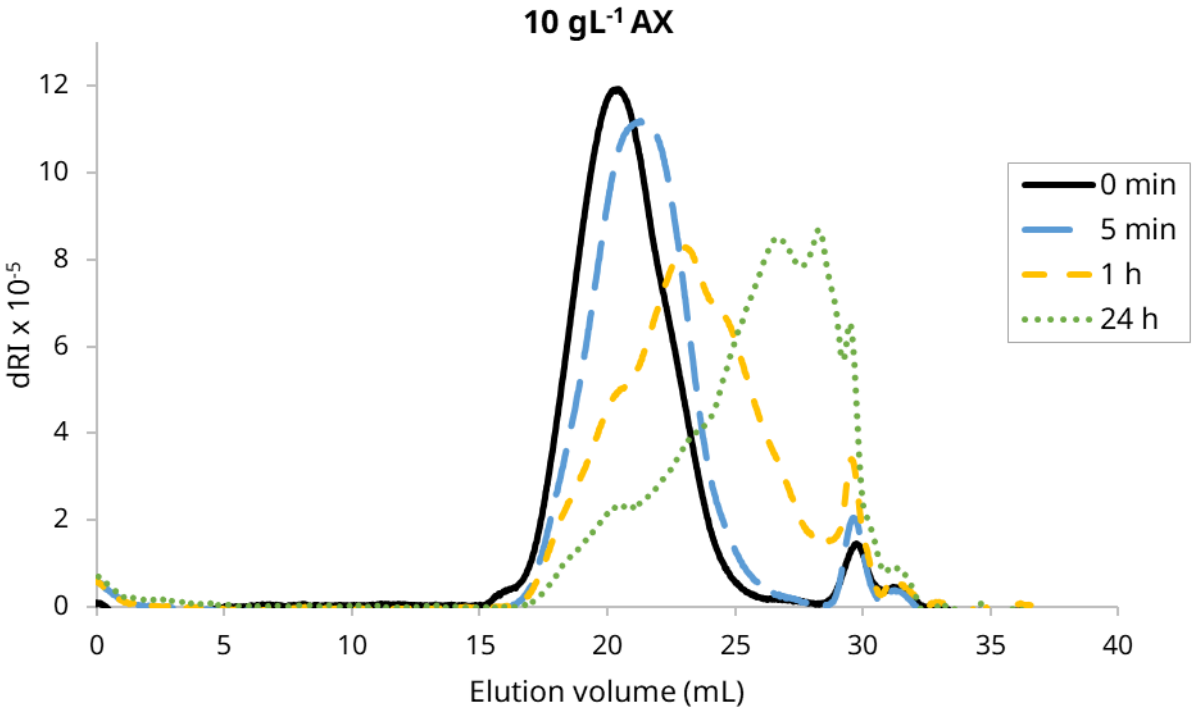
10 gL-1 AX
dRI x 10-5
Elution volume (mL)
0 min
5 min
1 h
24 h

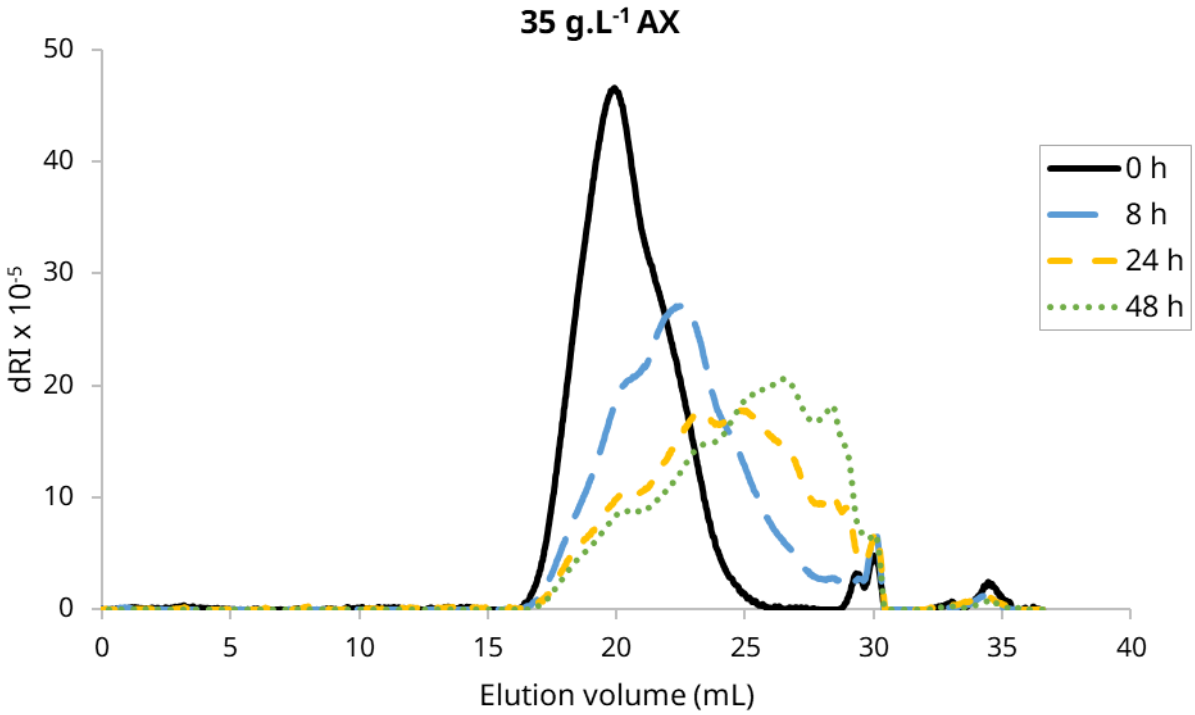
35 g.L-1 AX
dRI x 10-5
Elution volume (mL)
0 h
8 h
24 h
48 h

CHAPTER V

Enzyme Propagation and Diffusion in Dilute to Concentrated AX Solutions

i. Preamble

This chapter deals with the second major question of this PhD work, which is related to the propagation, i.e, the directional mobility of enzymes when they are confronted to a polymeric system that they can degrade. Our specific questions are:

1. What determines this mobility?

2. It there an effect of the enzymes' activity on their mobility?

3. How does the mobility changes with the concentration of polymer?

4. How do the experimental results compare with estimations made according to basic and more recent theories about diffusion of objects in polymer liquids?

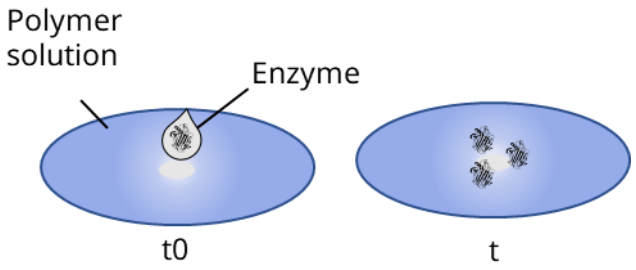

In contrast with the previous chapter, chapter V has been written as a first draft of an article. This leads to the repetition of some information, especially in the introduction.

ii. Introduction

Plant biomass plays a crucial role in the transition to a renewable economy, because its carbohydrates represent a promising source for sustainable carbon. These carbohydrates can be used by the biotechnology industry to produce bioplastics, biofuel and other platform molecules [1]. For this however, they first need to be broken down into basic sugars, for example using enzymes. Enzymatic degradation is both convenient and efficient, but it remains challenging to implement in industrial processes because of the recalcitrance of the plant biomass due to its structural and compositional complexity [3]. While there are some studies of the degradation of specific types of plant biomass that propose erosion-like or peel-off mechanisms [36], [42], [115], the general behaviour of an enzyme when confronted with a polymeric substrate is still poorly understood. In this respect, the propagation, or *directional mobility*, of the enzyme is one major question as it is a crucial factor in terms of degradation efficiency. Yet, this question is still clearly overlooked by the scientific community, with only a few articles that directly address it [11], [116]. At first sight, the mobility of an enzyme must be linked, as for any 'simple' particle, to their size and the porosity of the media [117]. In addition to this, the catalytic activity of the enzyme may also affect its mobility, because the cleaving of the polymer chains, and the consequent decrease in the effective viscosity of the medium, might facilitate its motion. Some more recent studies even found that the catalytic event leads to an enhanced diffusion of the enzyme in solutions of molecular substrates [7], [10], but with results and interpretations that are still the subject of some controversy.

The question that arises is – in the specific context of biomass valorisation and degradation - whether enzymes behave like simple nanoparticles and if, or to what extent, their activity impacts their mobility.

To study this question, we use a simplified experimental model system, for which we can control the principal characteristics and parameters. It consists of two components, a xylanase and a solution of its polymeric substrate. The polymer is a single purified plant polysaccharide, wheat arabinoxylan (AX), that we have characterised precisely in terms of network dimensional characteristics (submitted article *Arabinoxylan in Water Through SANS: Single Chain Conformation, Chain Overlap and Clustering*). AX is the main hemicellulose in grasses and is made up of a xylan backbone substituted by arabinose on the second and/ or third carbon. The fungal endo-xylanase from *Neocallimastix patriciarum* (*Np*Xyn 11A) hydrolyses the xylan backbone of the polysaccharide and is fluorescently labelled in order to follow its mobility.

For control experiments, we use the inactive version of *Np*Xyn 11A, which has the exact same size as the active one, but lacks one amino acid that is involved in the catalytic activity towards AX due to a mutation (E113A). Using a custom fluorescent microscopy set-up, we capture real-time images of the radial diffusion of the enzyme gradient in the polymer solution over time. These images are then analysed to examine the propagation front as a function of time, AX concentration and enzyme activity. We show that is also possible to extract the enzyme's effective diffusion coefficients from those experiments. The discussion is essentially based on this quantitative data, using simple or more complex theoretical framework and hypothesis.

iii. Materials and Methods

a. Polymer solution

Medium viscosity arabinoxylan (AX, Megazyme) solutions were prepared in two steps. First, a diluted stock solution at 1 $g.L^{-1}$ was prepared in 50 mM sodium phosphate buffer at pH 6, stirred and heated to approximately 90 °C and kept at this temperature for 2 h. This step ensures thorough hydration of the polymer and prevents the formation of strong aggregations. The second step is the concentration of this stock solution by removing water. For this, the solution was filtered through a membrane that retains and concentrates the polymer using centrifugal filter devices (Amicon® Ultra -15 3 kDa). Previous SANS and SEC-MALS analysis of the final polymer solutions indicate few to no initial aggregations using this preparation protocol (article: *Arabinoxylan in Water Through SANS: Single Chain Conformation, Chain Overlap and Clustering*, submitted on April 12th).

b. Enzyme labelling

The fungal endo xylanase *Np*Xyn 11A used in this study was produced using recombinant *Escherichia coli* cells. It was labelled at random lysine residues using tetramethyl rhodamine isothiocyanate (TRITC) mixed isomers (Sigma-Aldrich). For this, 1 mL enzyme solution was prepared at approximately 2 x 10^{-4} $mol.L^{-1}$ in 50 mM sodium phosphate buffer at pH 8.3. TRITC that had been dissolved in 25 µL DMSO (Sigma Aldrich) was rapidly added to the enzyme solution to obtain a final concentration of TRITC of 2 x 10^{-3} $mol.L^{-1}$, resulting in a 10-fold molar excess of fluorophore. Note that the fluorophore should not be stored in solution, as this leads to a considerable loss in reactivity. The labelling mixture was then first incubated at room temperature for 4 h and after that at 4 °C for another 20 h. Finally, unbound fluorophore was removed using Pierce™ Dye and Biotin Removal Spin Columns (ThermoFisher) according to the supplier's user guide.

Due to the remaining high quantity of free fluorophore molecules, the mixture was first passed through the 5 mL column and then through the 10 mL column (see SI for more information regarding the labelling protocol). The purification was verified by gel electrophoresis (see SI) and the labelled enzyme stored in 50 µL aliquots at -20 °C. The labelled active enzyme conserved approximately 80 % of its activity (see SI).

We measured the degree of labelling using absorbance measurements and mass spectrometry experiments. The results are quite different (see SI for details), but both indicate that 85-90 % of the enzymes carry an average of 1 to 3 fluorophore molecules.

c. Experimental set-up

The diffusion of the labelled enzyme was observed using a custom-built fluorescence microscope that is displayed in Figure 36. It is adapted to the fluorophore's excitation and emission maxima of 555 and 580 nm respectively. The light used to excite the fluorophore comes from a LED (530 nm, Edmund Optics) that is filtered through a 535 ± 43 nm excitation filter (OD6 Dia 50mm, Edmund Optics) and is situated underneath the sample. The emitted fluorescence is captured by a camera (Aca1920-40gm, Basler) above the sample that provides an observation field of 1920 x 1200 pixels with a pixel size of 5.86 μm^2 and 4095 grey levels (12-bit pixel depth). To ensure that the camera specifically detects the light emitted by the fluorophore, an emission filter (592 nm/43 nm OD6 Dia 25mm, Edmund Optics) as well as a dichroic filter are placed between the sample and the camera.

The chamber holding the sample consists of three components: bottom, middle and top layer (see Figure 36, components labelled A, B, C), which are deposited in a plastic tray. The bottom layer A is a circular quartz cell of 0.5 mm depth and 15mm inner width (124-0.5-40, Hellma). This cell is covered by the middle layer B, a circular optical glass (N-BK7) window with a diameter of 25 mm, a thickness of 1 mm and a 2 mm wide hole in the centre (Edmund Optics). The hole serves as a reservoir that allows the addition of the labelled enzyme to the polymer solution.

The top layer C has the same dimensions as the middle layer but without the centre hole. Grease (graisse universelle au lithium, 3-en-un) is used to seal the chamber.

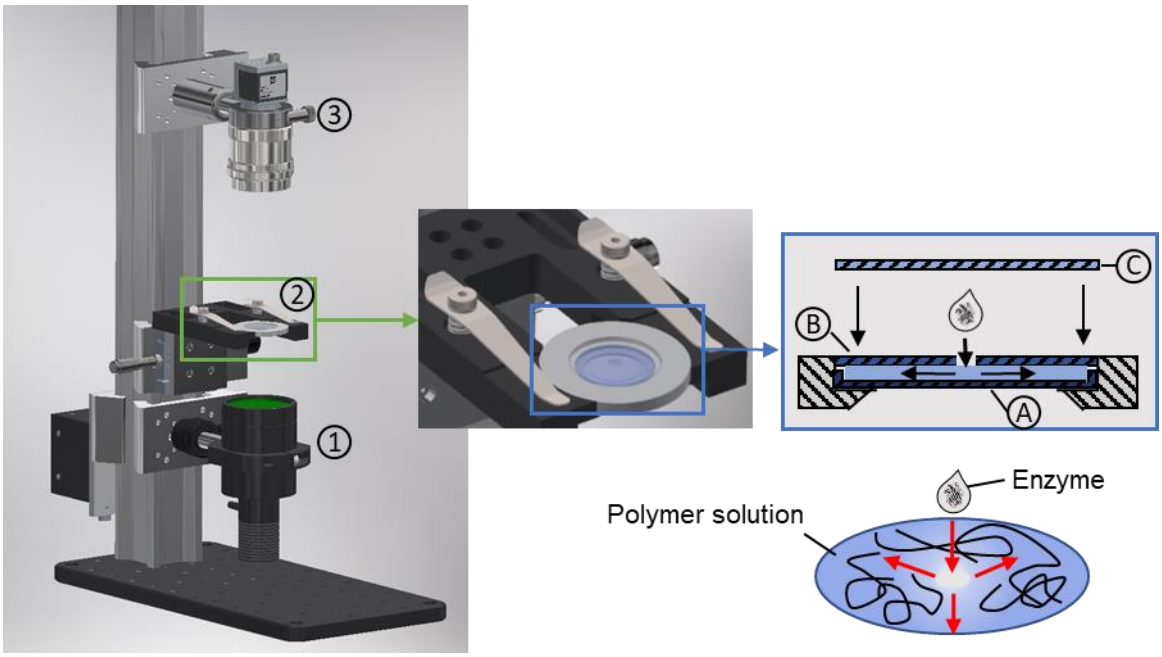

Figure 36: Experimental set-up. Left-hand side: Custom fluorescence microscope consisting of (1) a LED + excitation filter, (2) sample holder and (3) camera + emission filter. Middle: Sample holder. Right-hand side: The circular microscopy chamber made up of a bottom layer (A) holding the polymer solution (light blue layer), a middle layer with a hole for the deposit of the enzyme solution (B) and a top layer (C) to close the chamber.

d. Diffusion experiments

The diffusion experiments consisted of several steps. At first, images for the calibration and the image treatments were taken. Then, the different samples were prepared and their images taken over time.

Calibration of the enzyme concentration: 100 µL of labelled enzyme solutions at several concentrations were transferred into the bottom layer of the chamber and covered with the middle and top layer. The chamber was placed into the holder and for each concentration, a set of 50 images were taken. The exposure time of those images was adapted to the sample concentration to ensure a sufficient intensity and varied between 0.3 and 1 s.

In this time range, the acquired intensities are directly proportional to the exposure time. Therefore, the intensities at exposure times $t > 0.3$ s were divided by a factor $x/0.3$ to get equivalent values for $t = 0.3$ s. Then, we calculated the radial intensities following a protocol that is detailed below and that essentially involved a 'flat' image taken at 2 µmol.L^{-1} of labelled enzyme. This calibration enables the conversion of the intensities into an equivalent enzyme concentration (see SI).

Dark measurements: A set of 50 images at 0.3 s exposure time of the chamber filled with water without the LED were taken to quantify all parasitic light that is not due to fluorescence emission.

Flat measurements: In theory, a homogeneous fluorophore solution should result in a constant intensity over the whole available surface of the sample. However, there can be some heterogeneities that are caused by the light source. This type of heterogeneities was measured using a homogeneous solution of labelled enzymes at 2 µmol.L^{-1}.

Sample preparation for the diffusion experiments: 100 µL of AX solution were transferred into the quartz cell (bottom layer). The middle layer was slowly slid over the sample to avoid bubbles. Grease was added to the sample tray before placing the sample into it. Then, 3 µL of labelled enzyme solution were carefully deposited into the reservoir and the top layer slid on. More grease was added around the top layer at the

junction with the sample tray. Finally, the sample tray holding cell and sample was placed under the microscope.

Image acquisition settings: Due to the duration of the diffusion experiments, which ranged from several hours to 6 days, and the slow kinetics of the phenomenon, we chose to take images every 10 min for all experiments except for the diffusion in pure solvent (here every 5 min). The exposure time for all images was 0.3 s. To prevent the fluorophore from photodegradation, the sample was not continuously illuminated. Instead, we used light pulses of 0.5 s that were synchronised with the camera. A 'bleaching' experiment, that consisted in following the emitted intensity as a function of time with a continuous source, clearly indicated that there was no photodegradation over the total illumination times of all our experiments (results not shown).

f. Image treatment

The images obtained with our experimental set-up are 2-D views of the radial propagation of the enzymes from the centre of the chamber towards the *x* and *y* dimensions. However, diffusion also occurs in the *z*-direction, i.e., in the depth of the chamber. We made this depth as low as possible (0,5 mm) in order to neglect the diffusion in the *z*-direction. We provide in SI some COMSOL simulation results, that demonstrate that the diffusion in *z*-direction can be neglected and that the images can be safely considered as diffusion images over a 'flat' surface.

Because of the axisymmetric characteristic of the set-up geometry, the 2-D images were further treated to get the radially average 1-D intensity *I* as a function of the distance *r* from the centre of chamber. This was performed using a custom-made Python program given in SI that involved the following steps:

For one set of experiments, all images were first re-centred to assure correct pixel-by-pixel operations.

Then, every image was read, and their grey levels normalised pixel-by-pixel as follows:

$$Image_{normalised} = \frac{Image - Dark}{Flat - Dark} \quad (Equ. 15)$$

The subtraction of the dark image, which is the image without the light source, is a commonly used method that helps to account for any residual light [65]. The normalisation by the flat, which is an image of a homogeneous fluorophore solution, is used to correct any heterogeneities of the source.

Finally, circles with increasing radius and centred in the middle of the enzyme source are defined. The average intensity on each circle is calculated and attributed to its radius, generating a radial intensity profile *I(r)*.

Due to light reflection caused by the walls of the reservoir and the subsequent formation of a halo over a distance of about 0.5-0.7 mm from the reservoir wall, the intensities in and immediately around the reservoir were not considered. Note that the initial intensity profiles of all experiments were already a gradient of a given width. This is due to the temporal delay of several minutes between injecting and closing the chamber, which prevents the acquisition of the profile at time zero.

g. Determination of the diffusion coefficient

To quantify our results, and when all the criteria were met to make the calculation detailed below, we estimated a diffusion coefficient D that corresponds to a time t of the experience. For this, we use the numerical solution of Fick's second law of diffusion proposed by Crank for the radial diffusion of a localised source [118]:

$$c(i,t+1) = c(i,t) + \frac{D\Delta t}{\Delta r^2 * 2i}[(2i+1) * c(i+1,t) - 4i * c(i,t) + (2i-1) * c(i-1,t)] \quad (Equ. 16)$$

For $i \neq 0$, and i representing the position in radial space (r = i Δr), and c the concentration of the enzyme.

This equation is particularly adapted to our experiments, because it allows the reconstruction of a concentration gradient at time $t + 1$ based on the gradient at time t, whatever this time is, and so without the knowledge of the exact concentration profile at t = 0. Note that here, we use the model the other way around, meaning we estimated an effective diffusion coefficient D at time t based on two experimental concentration gradients at time t and t + 1, i.e., t + Δt.

To implement this solution, two experimental concentration profiles, that are as close in time as possible while still being distinct, were chosen. Then, the chamber diameter R was divided into equal intervals Δr. The size of Δr was chosen with consideration of the stability condition $2D\Delta t \leq (\Delta r)^2$, which ensures that the error of the calculation is small. Each space interval was numbered from 1 to $i_{\max}$, so that r equals $i\Delta r$ and R= $i_{max}\Delta r$. The estimation of D at a given time t then consisted in varying D to fit the model to two experimental concentration profiles at t and t + Δt.

We simply used the solver implemented in Microsoft Excel for that purpose. For each diffusion experiment, this calculation was performed for 10 sets of profiles in a time range between a minimal and maximal critical time, below and above which the Crank model cannot be used, respectively.

Indeed, at the beginning of the experiment, we observe a moment of stabilisation of the halo around the reservoir, which corresponds to the emptying of the reservoir. The minimal critical time t_{min} corresponds to the end of this stabilisation phase, and is determined using the integral of the fluorescence intensity between the spatial limit of the halo and the edge of the sample cell (see the next section). In addition, the equation of Crank is for an infinite milieu, while our geometry is limited in space. So, the second critical time t_{max} is defined, where t corresponds to the arrival of the fluorescence at the edge of our sample cell.

iv. Results and Discussion

In the following, we will look at the diffusion of the labelled enzyme in AX solutions of 16, 35, 50 and 90 $g.L^{-1}$ prepared by centrifugation. At first, we use the data of one experiment at 35 $g.L^{-1}$ AX with an inactive enzyme for illustrating all the different steps of the image treatment and analysis. Then, we will move on to the diffusion of the inactive enzyme and the evolution of the diffusion coefficient as a function of the polymer concentration. Then finally, we will examine the results of the diffusion of the active enzyme.

a. Typical workflow for image treatment and analysis

Image acquisition: Figure 37 displays the raw microscopy images of the diffusion of labelled inactive enzyme in a solution of 35 $g.L^{-1}$ AX taken by the microscope. Over time, the enzyme (bright colour) radially spread out of the reservoir (red circle) and diffused. The images were taken at regular intervals (6/h) with an exposure time of 0.3 s.

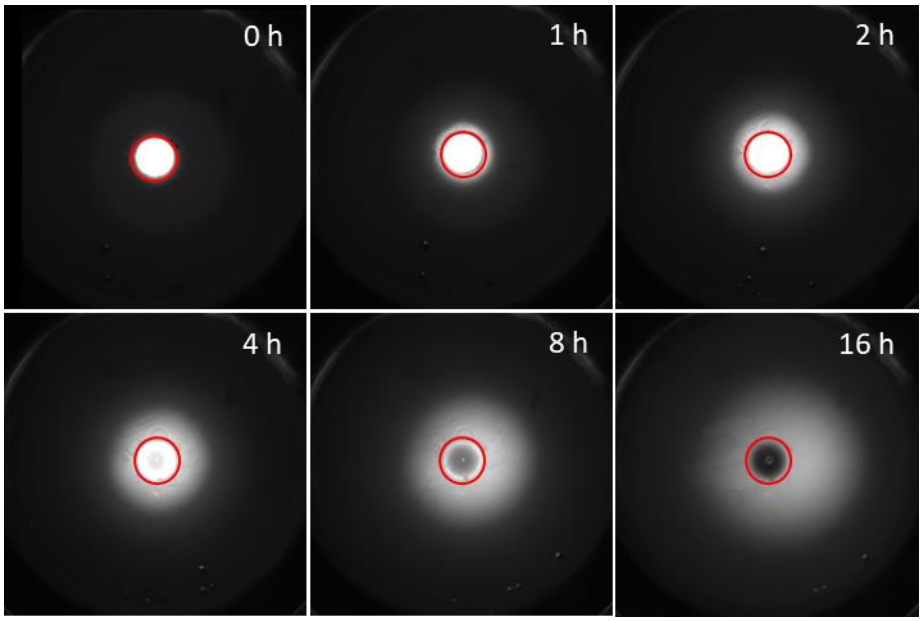

Figure 37: Fluorescent microscopy images of the labelled inactive enzyme (bright colour) diffusing in 35 $g.L^{-1}$ AX over time. The starting point is the reservoir (red circle). Image scale 15 x 15 mm.

Radial intensity gradients: Using the acquired raw microscopy images and the image treatment with Python (see Materials and Methods section e), we obtain a radial intensity profile for each picture (see Figure 38). We can see that the intensity close to the reservoir (small r) decreased as the labelled enzyme migrated away. This in turn led to an increase in intensity close to the edge of the sample (large r), flattening the profiles over time. Here, the total duration of the experiment is 70 h, a time at which the enzyme concentration becomes quasi-homogeneous in the whole chamber.

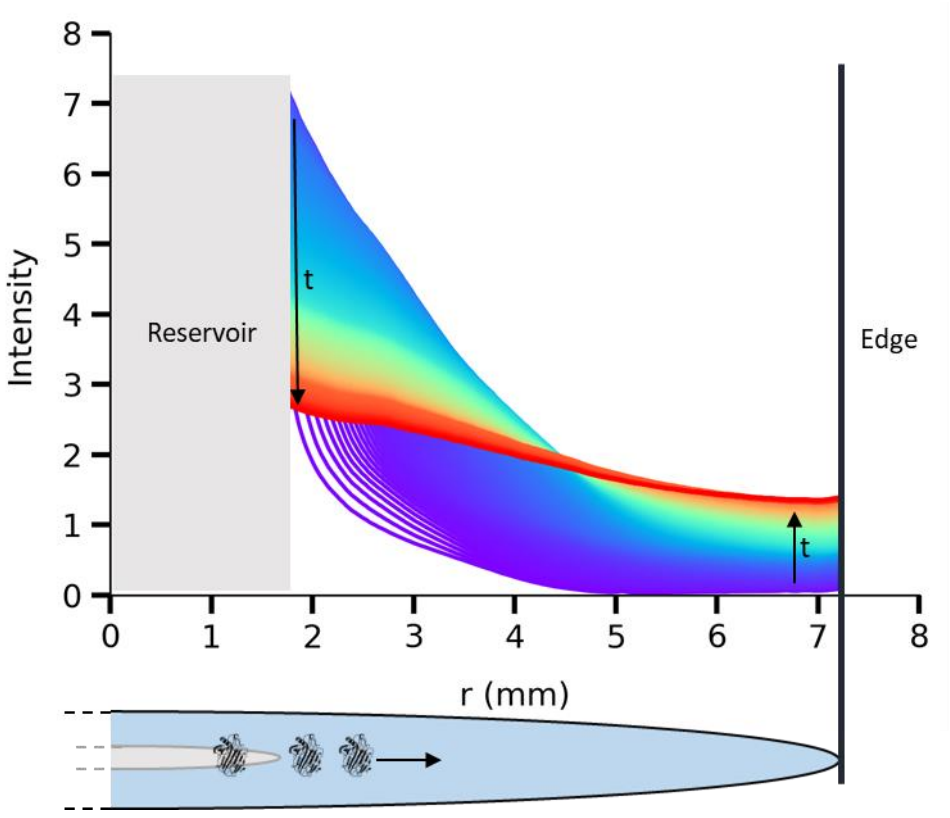

Figure 38: Radial intensity profiles of the diffusion of the labelled inactive enzyme in 35 g.L^{-1} AX over a duration of 70 h (purple/blue to red, see black arrows). The schema below the graph displays one half of the circular microscopy chamber with the half reservoir (grey colour) and polymer solution (blue colour). The enzymes (black icons) propagate from the reservoir towards the edge of the sample (black arrow).

Determination of the diffusion coefficient: Several radial profiles between the critical times t_{min} of 13 h and t_{max} of 24 h were chosen as described (Materials and Methods section f). Then, the profiles were reconstructed using the analytical solution by Crank with a time-step of 2 to 4 h and a Δr of 0.8 mm. Using Excel solver, the reconstructed profile was fitted to the experimental one by adjusting the diffusion coefficient of each selected time. Figure 39 displays the fit for two profiles. Due to the Δr of 0.8 mm, there is no fit for the first and last 0.8 mm of the profile. In this case we found a stable average diffusion coefficient of 2.20 $\pm$ 0.12 x 10^{-11} $m^2.s^{-1}$ with a good fit.

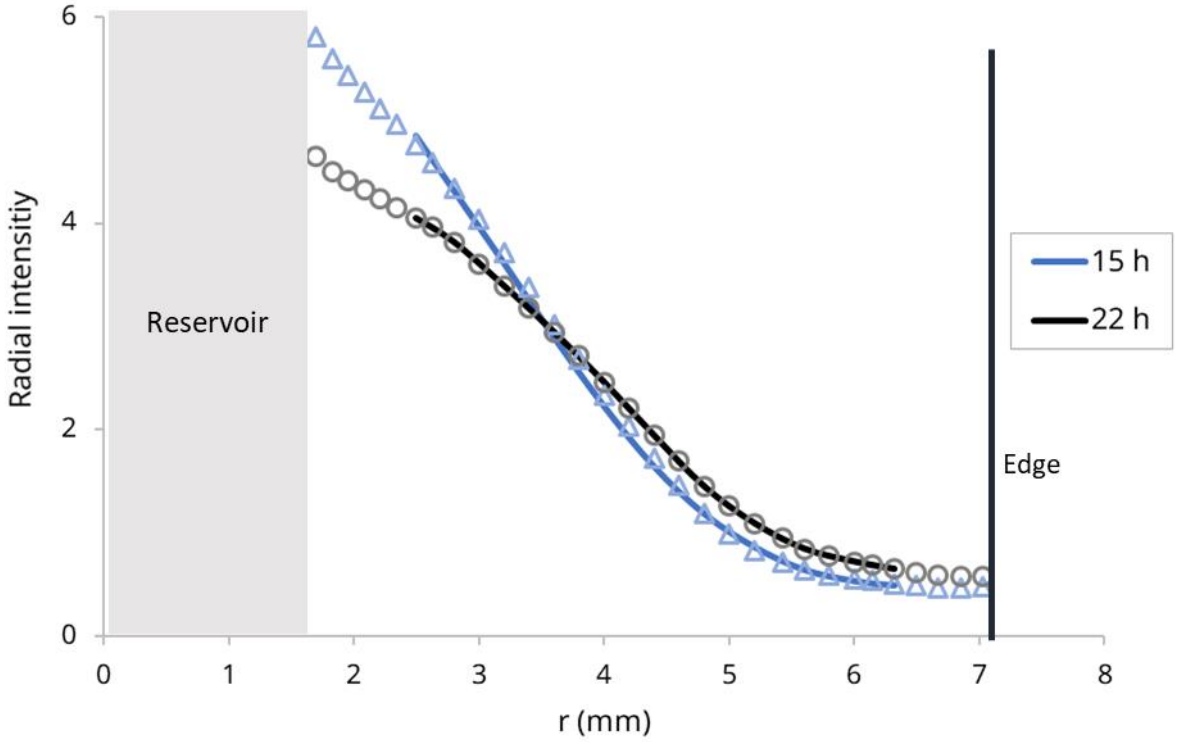

Figure 39: Fitted normalized intensity profiles of the diffusion of the inactive enzyme in 35 g.L^{-1} AX at two different times. The experimental data is represented by open symbols, the fit using Crank's equation by full lines.

b. Diffusion of the inactive enzyme

As a reference, we first measured the effective diffusion coefficient of the enzyme in pure solvent to determine D_0. The execution of this measurement was very challenging due to the low viscosity of the solution. The measurement was performed several times for the inactive as well as the active enzyme, and resulted in an average effective diffusion coefficient of $2.00 \pm 0.73 \times 10^{-10}$ $m^2.s^{-1}$. This value is higher than the theoretical diffusion coefficient of a particle the size of the enzyme (r = 3 nm) according to the Stokes-Einstein equation (Equ. 6, Chapter II), which is about 7.5×10^{-11} $m^2.s^{-1}$. This is a factor x ~2.7 in favour of the experimentally determined diffusion coefficient, meaning that the enzyme diffuses faster than expected. We do not have any explanation for this yet, but we were able to rule out some possible causes for this discrepancy, like evaporation, convection due to drying, and temperature changes. As all experiments were carried out under identical conditions, we decided to keep this value for D_0, and to rather discuss the evolution of the normalised diffusion coefficient D/D_0 as a function of AX concentration.

For all AX concentrations, the estimated diffusion coefficient remained stable in the observed window between t_{min} and t_{max}, which is what we expect for the diffusion of an object in a solution whose properties do not change over time. Therefore, we calculated an average value for each concentration. The results are displayed in Table 3 in terms of D and D/D_0, whereas Figure 40 focuses on the evolution of D/D_0 with AX concentration.

Table 3: Experimental values for the effective diffusion coefficient of the inactive enzyme in AX solutions.

AX concentration ($g.L^{-1}$)	Experimental diffusion coefficient D_{exp} ($m^{2}.s^{-1}$)	Normalised diffusion coefficient D_{exp}/D_0
0	$2.00 \pm 0.73 \times 10^{-10}$	1.00 ± 0.52
16	$2.16 \pm 0.04 \times 10^{-10}$	1.08 ± 0.40
35	$2.66 \pm 0.19 \times 10^{-11}$	0.13 ± 0.05
50	$2.36 \pm 0.86 \times 10^{-11}$	0.12 ± 0.06
90	$1.13 \pm 0.02 \times 10^{-11}$	0.06 ± 0.02

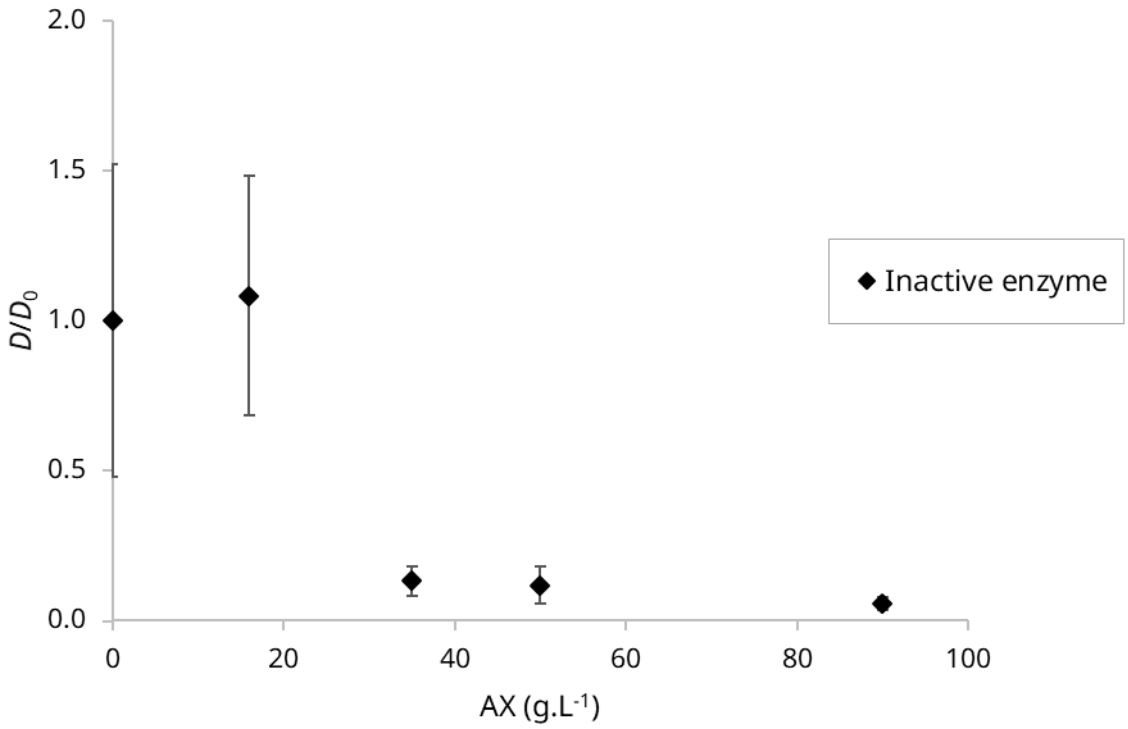

Figure 40: Evolution of the normalised diffusion coefficient of the inactive enzyme with polymer concentration. D_0 is the diffusion coefficient in pure solvent.

At 16 g.L^{-1} of AX, D/D_0, the viscosity of the solution remains low, and it is still challenging to measure an effective diffusion coefficient with good accuracy using our experimental setup; hence the large error bars for this point. Then, for C > 16 g.L^{-1}, we observe an important decrease in D with polymer concentration. This decline is better visualized in Figure 41, where D/D_0 is plotted in a log-log scale and shows a scaling power-law of about -1.69.

For discussing these results, let us first compare them to the evolution of D/D_0 for a tracer that would only follow the Stokes-Einstein equation (equ. 6 chapter II), that is repeated hereafter.

$$D_{SE} = \frac{k_B T}{6\pi\eta r}$$

Where k_B is the Boltzmann constant, η is the viscosity of the solution and r the radius of the particle.

In this simplistic view, the polymeric nature of the solution is not considered, and the tracer's diffusion (here the enzyme) is only determined by the effective viscosity of the solution. In that case, and because D is proportional to η^{-1}, one would have $D/D_0 = \eta_0/\eta$. Figure 41 shows that it is clearly not the case, with a diffusivity that is much less impacted by the AX concentration than it is for the viscosity of the solution. Still, in this framework of a simplified Stokes-Einstein explanation, our results suggest that the enzymes 'feel' an effective viscosity that is between the solvent and the solution viscosities, as it was already proposed in other studies [82], [83]. Such an effect would be explained by the large difference in dynamics between the enzymes and the polymer chains at small time and length: As the polymer network is quasi-static compared to the enzyme, the motion of the latter is mostly dictated by the viscosity of the solvent and only slightly affected by the obstacles that constitute the polymer chains.

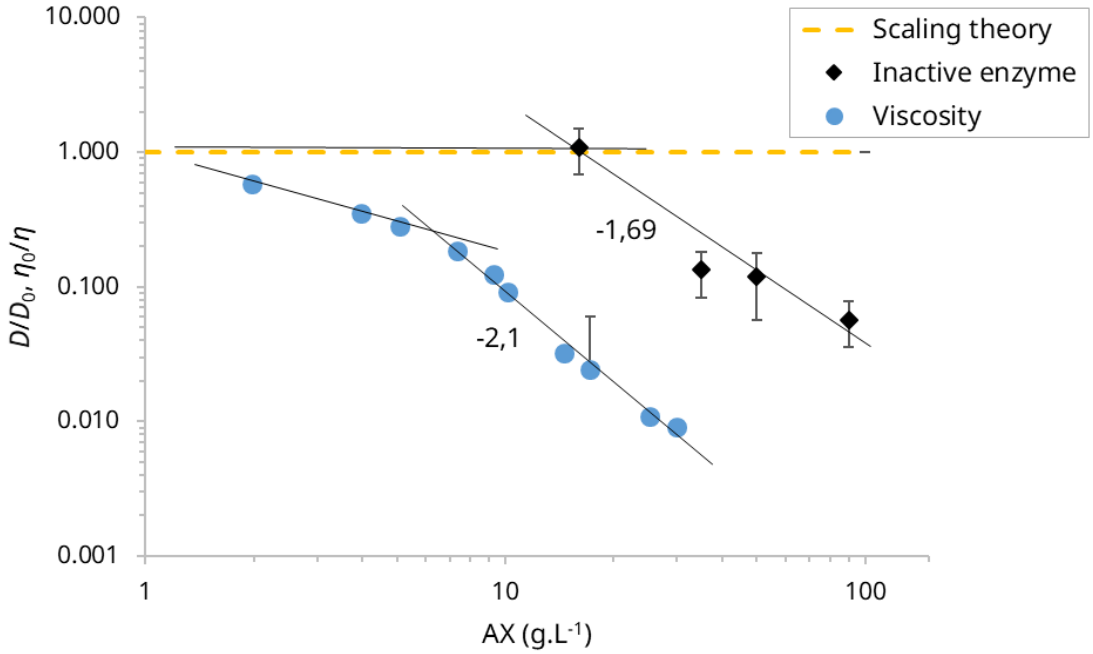

Figure 41: Evolutions of the normalised diffusion coefficient according to our experimental data (black diamonds), Stokes-Einstein theory (blue dots), and the scaling theory by Rubinstein et al. [117] (dashed yellow line). The values for the solution viscosity come from our submitted article "Arabinoxylan in Water Through SANS: Single Chain Conformation, Chain Overlap and Clustering". The full lines serve as a guide for the eye. Logarithmic scales.

The scaling theory for the diffusion of a tracer in polymer liquids, as proposed recently by the group of Rubinstein, is based on very similar considerations [117]. In addition, they specifically take into account the characteristic sizes of the system, i. e. the tracer size and the correlation length of the polymer solution. According to this theory, in the concentration regime where the particles are smaller than the correlation length of the solution, $D = D_0$, because the particles 'do not see' the polymer and thus move freely in between the chains. Knowing that the enzyme is about ~6 nm in size, and the correlation length of the solution is ~10 nm at 90 $g.L^{-1}$ AX (see our recently submitted article our article "*Arabinoxylan in Water Through SANS: Single Chain Conformation, Chain Overlap and Clustering*"), we should be in this regime (see dashed yellow line in Figure 41). In our case however, we observed this evolution only for polymer concentration up to 16 $g.L^{-1}$ followed by a decrease with a slope of -1.69.

So again here, it seems like we are in an intermediary situation where the enzyme motion is still affected by the presence of the polymer. This is reinforced by the slope of the diffusivity decay after 16 $g.L^{-1}$ (-1.69, Figure 41), which is very close to the one predicted by the theory of Rubinstein (-1.52). This slope is however predicted for a different concentration regime, where the correlation length of the polymer solution is equal or smaller than the size of the tracer, thus directly affecting its mobility. This suggests that, despite the fact that the enzymes are smaller than the mesh size of the polymer network, there must be some local effects that provoke a decrease in D that is similar to the one predicted by Rubinstein *et al.*

One reason for this 'premature' decrease of D/D_0 could be polymer-enzyme interactions. As the polymer concentration increases, so does the amount of possible binding sites and the probability of an encounter with an enzyme. While the enzyme is inactive, it could still interact with its substrate, because its active site remains correctly folded and able to accommodate the substrate, which would slow the diffusion down. Such interactions have been found and characterised for example for carbohydrate binding modules (CBMs) for instance. Carbohydrate binding modules can be part of multi-modular enzymes and increase their affinity towards the substrate. Paës *et al.*

studied the diffusion of different hemicellulose-active CBMs and found that the diffusion coefficient in presence of their target substrate indeed decreased [119].

In our case, the enzyme does not contain any CBM module. However, it was shown that its active site is able to recognise and accommodate up to six xylose residues, and that this rather elongated substrate binding cleft is important for the catalysis [100].

One possibility to determine the affinity of the inactive enzyme towards its substrate would be to measure the diffusion of the enzyme in a polymer solution with similar characteristics (correlation length) but that is clearly not recognised by the enzyme. Or, maybe simpler, measuring the diffusion of an inert tracer particle of the same size as the enzyme in AX solutions. These results would then allow to determine if there is any kind of affinity between the inactive enzyme and the substrate and to quantify this affinity.

In any case, the experiments performed using the inactive enzyme are crucial, in a sense that they are the best possible reference for the experiments performed with the active enzyme. The experiments using the active enzyme are the subject of the following section.

c. Active enzyme

The experimental diffusion coefficients and corresponding D/D_0 values for the active enzyme in AX solutions of the same concentration than in section b are given in Table 4 and Figure 42.

Table 4: Experimental values for the effective diffusion coefficient of the active enzyme in AX solutions.

AX concentration ($g.L^{-1}$)	Experimental diffusion coefficient D_{exp} ($m^2.s^{-1}$)	Normalised diffusion coefficient D_{exp}/D_0
0	$2.00 \pm 0.73 \times 10^{-10}$	1 ± 0.52
16	$2.7 \pm 0.43 \times 10^{-10}$	1.35 ± 0.54
35	$6.81 \pm 0.80 \times 10^{-11}$	0.34 ± 0.13
50	$3.71 \pm 0.97 \times 10^{-11}$	0.19 ± 0.08
90	$2.08 \pm 0.13 \times 10^{-11}$	0.10 ± 0.04

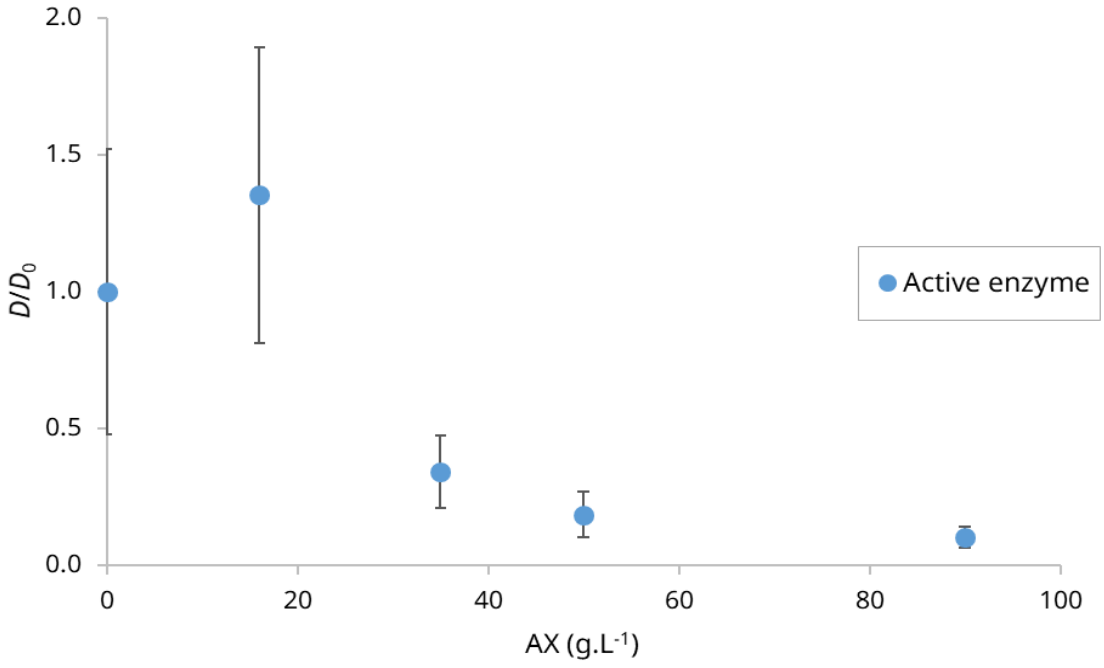

Figure 42: Evolution of the normalised diffusion coefficient of the active enzyme with polymer concentration. D_0 is the diffusion coefficient in pure solvent.

Quite importantly, and as for the inactive enzyme, we did not observe any variations in the estimated values of D between t_{min} and t_{max}. Therefore, the reported D values are the values averaged over this time range. This is illustrated in Figure 43, which displays the evolution of the estimated diffusion coefficients (black dots) and the integral of the intensity gradient (blue squares) for the diffusion of the active enzyme in 90 g.L^{-1} AX. The integral reached a plateau after 5 h, which marks t_{min} (red dashed line on the left), while the diffusion front reached the edge of the chamber at t_{max}. The diffusion coefficient calculated using the equation of Crank remained clearly stable between t_{min} and t_{max}.

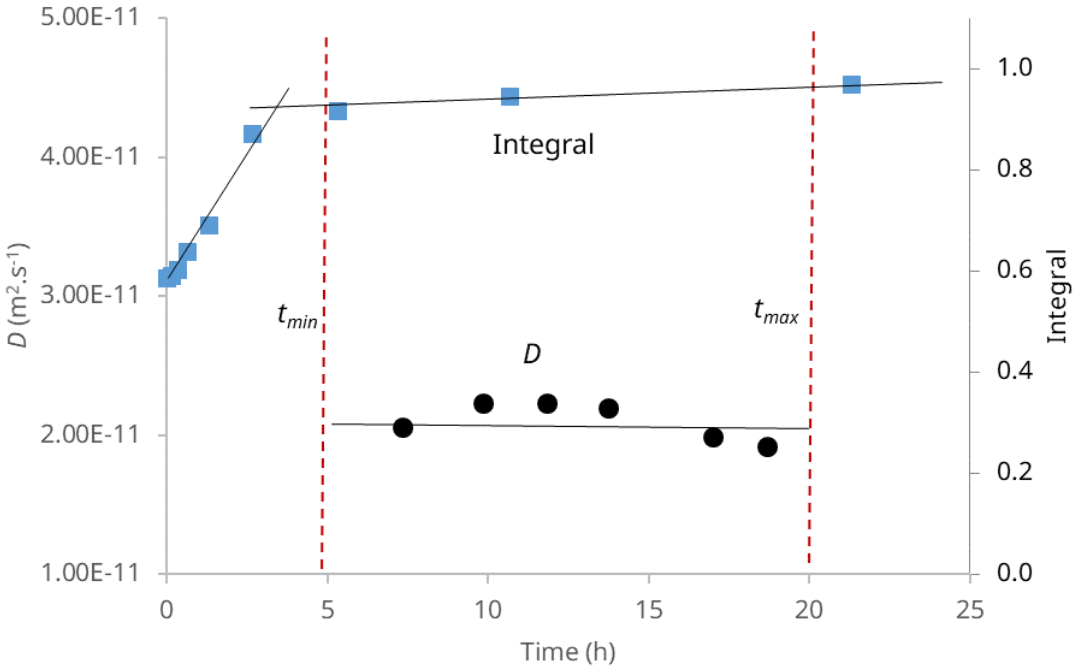

Figure 43: Evolution of the experimental diffusion coefficient (black dots) and intensity integral (blue squares) over time for the diffusion of the active enzyme in 90 g.L^{-1} AX. The dashed red lines mark the limits of the time window considered for the determination of D, t_{min} corresponds to the onset of the plateau of the integral.

One first interesting result is the value of D/D_0 at 16 g.L^{-1}, as it suggests that the active enzymes have a slightly larger mobility at 16 g.L^{-1} AX than in absence of the polymer. This is clearly reminiscent of the data of Granick et al. obtained in a rather comparable situation, and from which the authors concluded an enhanced diffusion of enzymes in presence of their substrate [8]. However, as already explained, the experiments at such low concentrations and viscosities are delicate to perform, which results in large error bars. Therefore, one has to be cautious in the interpretation of this first point at 16 g.L^{-1} AX. At C > 16 g.L^{-1}, we then observe a decrease in D/D_0 with the AX concentration, as it was the case with the inactive enzyme.

For comparison, we plotted them together in Figure 44. Like for the inactive enzyme, the relative diffusion for the active enzyme decreases as $\sim C^{-1.5}$ / $\sim C^{-1.7}$. However, and this is clearly the most important result of this work, the relative diffusion calculated for the active enzyme appears to be systematically larger that for the inactive one. On average, i.e., on the whole range of concentrations, the diffusion of the active enzymes is 1.8 ± 0.4 times faster than the diffusion of the inactive one.

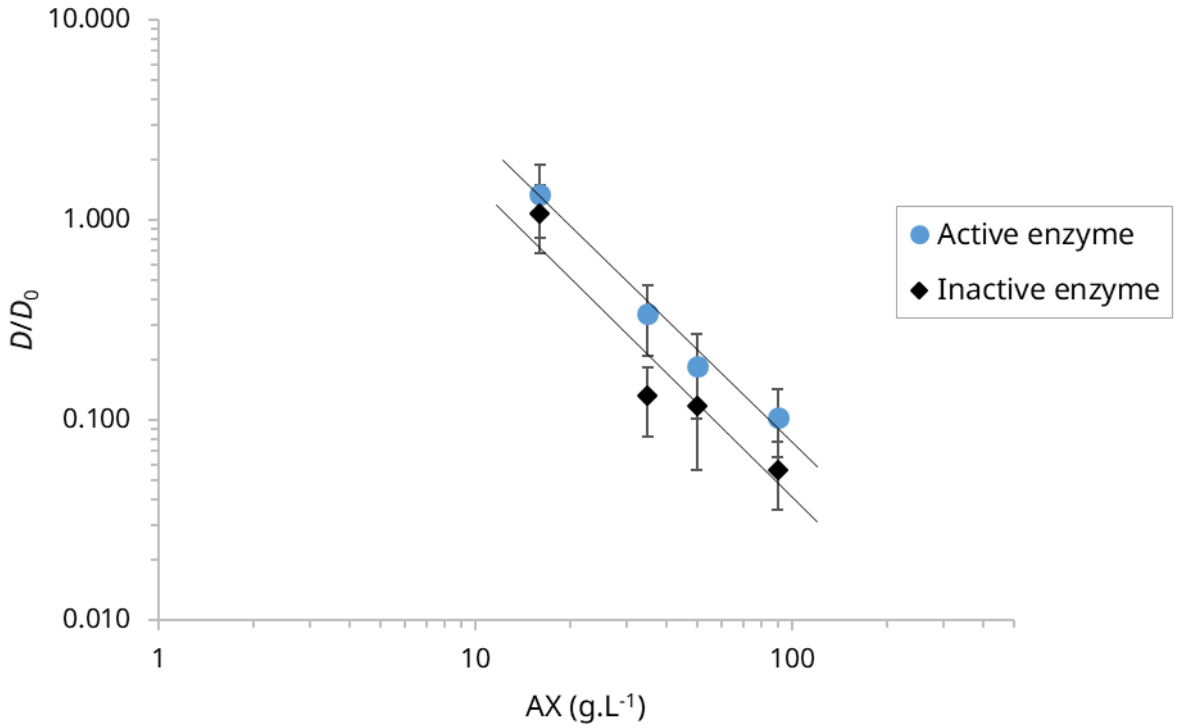

Figure 44: Evolution of the normalised diffusion coefficient of the active (blue dots) and inactive (black diamonds) enzyme as a function of polymer concentration. Lines serve as a guide for the eye. Logarithmic scales.

The impact of the activity on the enzyme mobility is also clearly visible qualitatively by looking at the evolution of the intensity gradients over the entire duration of the diffusion experiment. This is illustrated in Figure 45 for AX solutions at 50 $g.L^{-1}$. The black dashed and full lines correspond to times t where the intensity gradients are similar for both the active and inactive enzyme, respectively. To reach such gradients, the active enzymes needed $t \approx 1$ h of diffusion, while the inactive enzymes needed $t' \approx 4$ h. Then 4 hours later (t+4 h, t'+4 h, yellow colour), we can see that the gradients did not evolve in the same fashion: While the gradient of the active enzyme (dashed line) visibly flattened, the gradient of the inactive enzyme (full line) changed only slightly compared to time t'. This 'delay' between the active and inactive enzyme is also clearly visible when we look at the times needed to obtain a similar, near-flat gradient (green colour): t+70 h for the active enzyme (dashed line) t+140 h for the active enzyme (full green line).

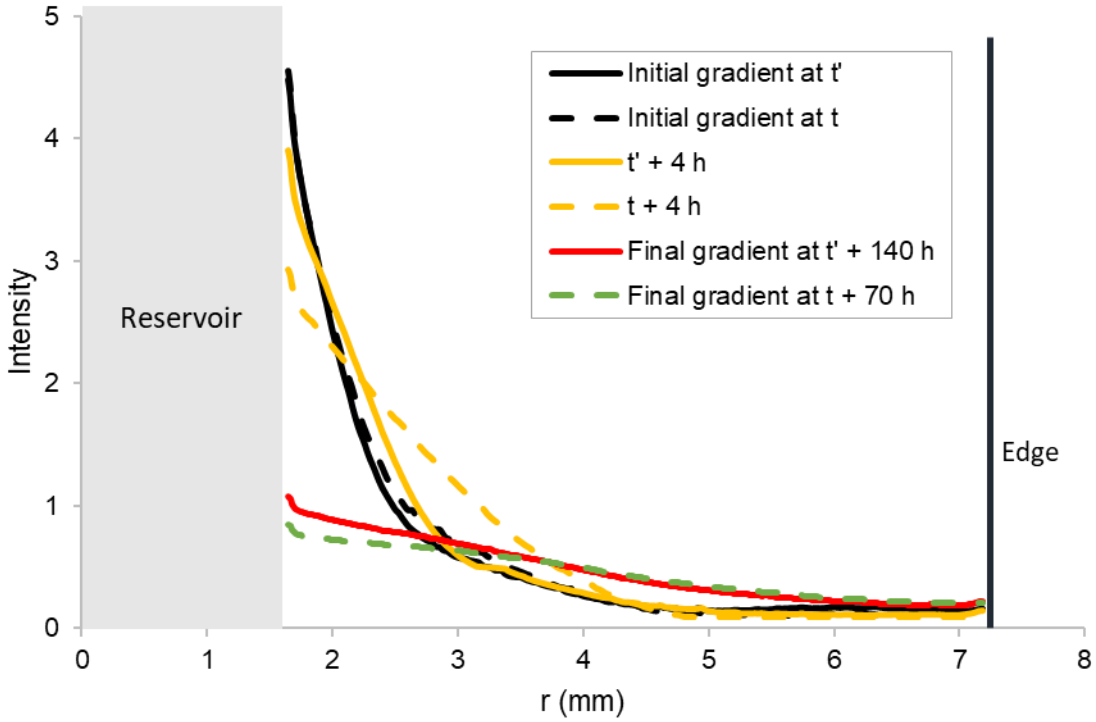

Figure 45: Intensity gradients at different times for the active (dashed lines) and inactive (full lines) enzyme in 50 g.L^{-1} AX. Time t and t' (black colour) represents the time where the gradient of the active and inactive enzyme was similar. For the active enzyme, t = 1 h, for the inactive enzyme, t' = 4 h. Time t, t' + 4 h (yellow colour) is the gradient for both enzymes 4 h later. The final gradients for both enzymes are at t = 70 h for the active enzyme (green colour) and t' = 140 h for the inactive enzyme (red colour).

These results were obtained at the end of the PhD and their interpretation remains a work in progress.

A first reflection concerns the fact that the effective diffusion coefficient of the active enzyme did not change over time. Due to its activity, the enzyme deconstructs the polymer over time, which should have an impact on its diffusion. The fact that D remains constant suggests that for the enzyme, its environment does not change, but remains constant and homogeneous in terms of diffusivity. This could be because the deconstruction of the polymer is 'instantaneous' as compared to the diffusion time of the enzyme. In other words, the diffusion would not be limited by the activity but only by the final products of the degradation. To test this hypothesis, one could follow the diffusion front of the active and non-active enzymes in a pre-digested polymer solution using our experimental set-up. Or we could measure the coefficient diffusion of the enzyme in fully deconstructed polymer solutions using other techniques such as FRAP. As FRAP measures the diffusion coefficient of a tracer in a solution where the tracer is homogeneously dispersed, it is adapted to the 'inert' situation that we evoke here where one does not expect any change in D with time and activity.

The second limiting case that could also explain our results is when the degradation is too slow in comparison to the diffusion of the enzyme. Then, the active enzyme is faster than the inactive enzyme only because its activity leads to an enhancement of its mobility. This could explain the similar evolution of D/D_0 with substrate concentration for both enzymes (Figure 44), as they both have the same dependence on the effective viscosity (similar slopes), and the active enzyme being on average 1.8 times faster would be the result of an enhancement of its mobility. Enhanced diffusion is a controversial phenomenon that can occur when an enzyme is in presence of its substrate [7], [10], [107]. In a recent and very extensive study, Granick *et al.* [8] linked this phenomenon to the free energy release rate of the catalytic reaction. Indeed, we found that the diffusion of the active enzyme in 16 $g.L^{-1}$ AX is faster than in the absence of AX (Figure 42), which supports the hypothesis of enhanced diffusion.

However, from previous degradation studies in homogeneous conditions (Chapter IV), we know that the deconstruction of the polymer is neither instantaneous

nor too slow, but happens on the same time-scale as the performed diffusion experiments. This means that over the time of the diffusion experiments, the deconstruction is in progress and its advancement is spatially heterogeneous, which adds a considerable complexity. Therefore, to understand the influence of activity on the mobility of the enzyme, it would be very valuable to know the state of the polymer and the evolution of its deconstruction over time. Some techniques that can be used to follow the evolution of the state of the polymer are nuclear magnetic resonance spectroscopy (NMR) and photon correlation imaging (PCI) (Chapter VI).

Conclusion

In this chapter, we studied the diffusion of active and inactive *Np*Xyn 11A in its polymeric substrate arabinoxylan, to determine if its activity impacts its mobility. For this, we used a custom fluorescent microscope and captured images of the directional diffusion of the enzyme gradient in the polymer solution over time. The polymer solutions were prepared in a way that ensured good hydration and their concentrations were above the overlap concentration to create a polymer mesh. The enzyme was labelled using a commercial fluorophore (TRITC). The acquired images were analysed using a custom Python program to get the radial 1-D intensity gradients. To quantify these results, we estimated a diffusion coefficient using a numerical solution of Fick's law of diffusion.

We found that the diffusion of the active and inactive enzyme in pure solvent was faster than the theoretical diffusion according to the Stokes-Einstein equation. Moreover, we found that D/D_0 for both active and inactive enzyme did neither evolve as predicted by the Stokes-Einstein relation with the inversed solution viscosity, nor as predicted by the scaling laws of Rubinstein *et al*. Instead, the diffusion was governed by an effective viscosity close to the viscosity of the solvent. With increasing polymer concentration, the normalised diffusion coefficient of the active and the inactive enzyme decreased. In the case of the inactive enzyme, the diffusion coefficient decreased approximately 20-fold and in the case of the active enzyme about 10-fold. Overall, the active enzyme diffused faster than the inactive enzyme in all studied polymer concentrations by an average of 1.8 times. While this clearly shows the link between the activity and the mobility of the enzyme, the nature of this link is not clear but needs to be further investigated.

v. Supporting information

Labelling protocol

The enzyme was covalently labelled with tetramethylrhodamine-5-(and-6)-isothiocyanate (TRITC, Sigma-Aldrich). It is a commonly used green fluorophore with a long-lasting signal. Its excitation and emission maximum are at 555 nm and 580 nm respectively. TRITC reacts covalently with primary amines of proteins (see Figure SI.1).

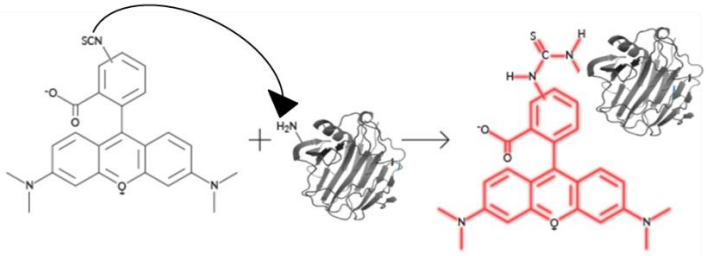

Figure SI.1: The thiocyanate group of the fluorophore reacts with accessible primary amine residues on the surface of the enzyme, creating a covalent bond (adapted from [120]).

*Np*Xyn11A has 12 lysines (K) that are possible target sites (see Figure SI.2). Using Pymol, 10 of those lysines were identified as accessible on the surface of the enzyme. While none of these lysines are directly part of the catalytic cleft or have a direct interaction with the substrate, some are located in delicate positions (K159, K43, K13) [100]. For all these reasons, a verification of the activity of the labelled enzyme is important.

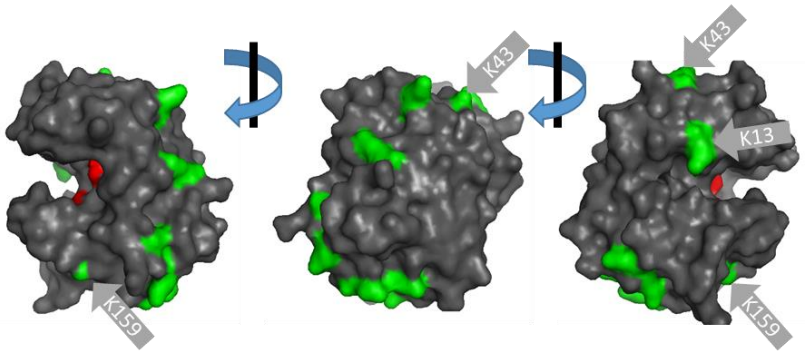

Figure SI.2: Three-dimensional surface structure of NpXyn11A visualised using Pymol. The catalytic site (red) is located within a cleft. Accessible lysine residues (K) are distributed over the enzyme's surface (green).

Instead of the 100 mM carbonate/bicarbonate buffer at pH 9 recommended in the labelling protocol by the supplier, a 50 mM sodium phosphate buffer at pH 8.3 was used to label the enzyme. Both buffers were approximately equal in terms of labelling efficiency, as both result in a DOL of 85 %. However, the buffer that was recommended by the supplier negatively affected enzymatic activity post-labelling more than the sodium phosphate buffer (see Figure SI.4). Another reason for the use of the sodium phosphate buffer is convenience. Given the fact that this is the enzymatic buffer in these experiments, no buffer exchange at the end of the purification is necessary.

Another change to the supplier's protocol was the time of incubation for the labelling reaction. Gel electrophoresis with samples taken at different times throughout the incubation reaction showed an increase of bound fluorophore over time (see Figure SI.3). Here, high labelling is desired, so the incubation time was adjusted to 20 h.

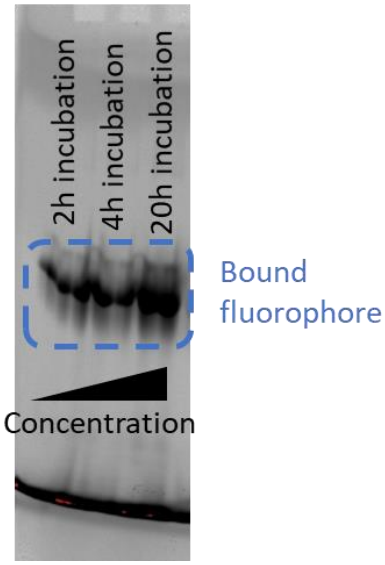

Figure SI.3: PAGE gel revealing the fluorophore. Over time, the band widens and the concentration of bound fluorophore increases (left to right).

To evaluate the efficiency of the labelling, the degree of labelling (DOL) was calculated following the ThermoScientific tech tip #31.It gives the ratio between the fluorophore (free and bound) and the protein within the sample and is determined using photo spectrometry.

At first, the concentration of protein is calculated. The absorbance of the sample is measured at 280 nm and at the wavelength of maximal absorbance for the fluorophore (for TRITC 548 nm). Because the fluorophore also absorbs at 280 nm, the absorbance of the labelling mix at 280 nm must be corrected using a corrective factor CF (for TRITC according to the supplier 0,34). The molar extinction coefficient of the protein at 280 nm is 61880 $M^{-1}.cm^{-1}$.

$$Protein\ concentration\ (M) = \frac{A_{280,labelling\ mix} - (A_{548,labelling\ mix} * CF)}{\varepsilon_{protein}}$$

Then, the ratio can be calculated as follows.

$$Fluorophore/Protein = \frac{A_{548,labelling\ mix}}{\varepsilon_{fluorophore} * protein\ concentration\ (M)}$$

The obtained DOL was between 85 and 90 %.

Additionally, the enzyme was analysed by mass spectrometry. This method allows to quantify not only the total amount of bound fluorophore per enzyme, but also the distribution of fluorophores (see Figure SI.4). The results indicated that most of the enzymes were labelled with one to a maximum of six fluorophore molecules, resulting in an average DOL of 2.8.

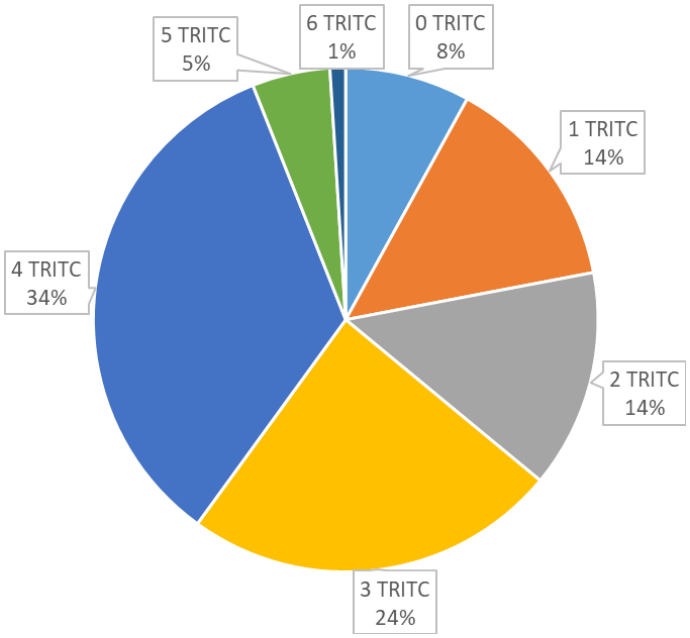

Figure SI.4: Distribution of the labelled fluorophore determined by mass spectrometry.

Post-labelling purification efficiency

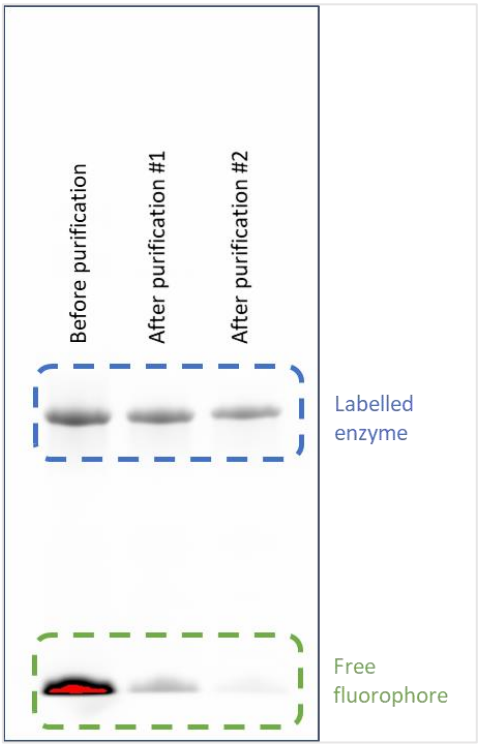

Figure SI.5: PAGE gel revealing the fluorophore of the labelling mix before purification, after purification using a 5 mL spin column and of the final solution (left to right). After purification, labelled enzyme yield is about 80 %.

Enzymatic activity post-labelling

Measurements: Enzymatic activity was measured using the dinitrosalicylic acid (DNS) assay. This assay is a colorimetric method that measures the absorbance of the product of the reaction between 3,5-dinitrosalicylic acid (DNS acid) and the aldehyde or ketone group of a reducing sugar. In the case of wheat arabinoxylan (WAX), a polysaccharide, the reaction partner of the DNS acid is the free aldehyde group belonging to the xylose unit at the reducing end of the chain. Using a standard curve of the sugar in question, the absorbance of the reaction product can be correlated to the concentration of the sugar. Here, xylose was used as a standard. The substrate was prepared at 1 % w/v in 50 mM sodium phosphate buffer at pH 6, heated to 95 °C and then stirred at room temperature for 10 min. The substrate was supplemented with 1 $g.L^{-1}$ BSA.

The enzymatic reactions were carried out in 1.5 mL Eppendorf tubes at 37 °C and 1200 rpm agitation (ThermoMixer© Eppendorf). Enzymatic concentration was 5 nM. Samples of 100 µL were taken at increasing intervals for a total of 15 min and mixed with 100 µL of DNS supplemented with 0.2 $g.L^{-1}$ xylose. All the samples including the standards were incubated at 95 °C for 10 min in a water bath. After cooling, deionized water was added to the samples to adjust the absorbance. 300 µL of all samples were displayed in a 96-wells plate and the absorbance was measured using a microplate spectrophotometer at 540 nm. A standard curve was measured using 0 to 5 $g.L^{-1}$ xylose.

Stability of the enzymatic activity post-labelling: To determine the impact of the fluorophore on the activity of the enzyme, the activities of the labelled enzymes were compared to those of a control group (see Figure SI.6). The enzymes of the control groups followed all the same steps of the labelling protocol but no fluorophore was added to them. This means that they underwent the same pH and temperature changes as the labelled enzymes. The results show that for both buffers, the presence of the fluorophore led to a decrease of the activity. This decrease however is larger for the enzymes in the buffer that was recommended by the supplier. This could be due to the higher pH of the recommended labelling buffer (100 mM carbonate/bicarbonate buffer pH 9), because optimal pH of *Np*Xyn 11A is 6 [111]. Therefore, the enzymatic buffer was chosen as it results in a better post-labelling activity.

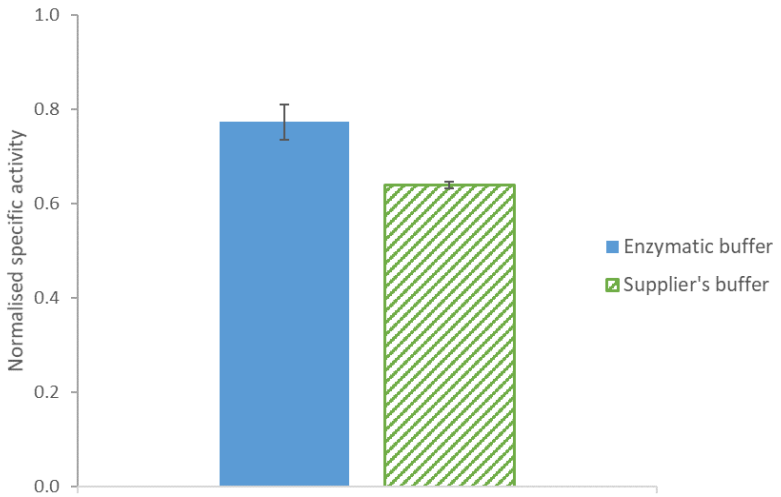

Figure SI.6: Specific activity of labelled NpXyn 11A in enzymatic buffer (50 mM sodium phosphate buffer pH 6) and the supplier's buffer (100 mM carbonate/bicarbonate pH 9. It was normalised by the specific activity of the control without TRITC.

Stability of the enzymatic activity over time: The enzymatic activity of the enzyme at room temperature as well as at different long-term storage temperatures was determined using the DNS method. The characterisation at room temperature indicates the stability of the enzymatic activity during the diffusion experiments, which are also performed at room temperature. The results show that the activity stayed stable for 72 h, which largely covers the time span of the diffusion experiments that was taken into account for their exploitation.

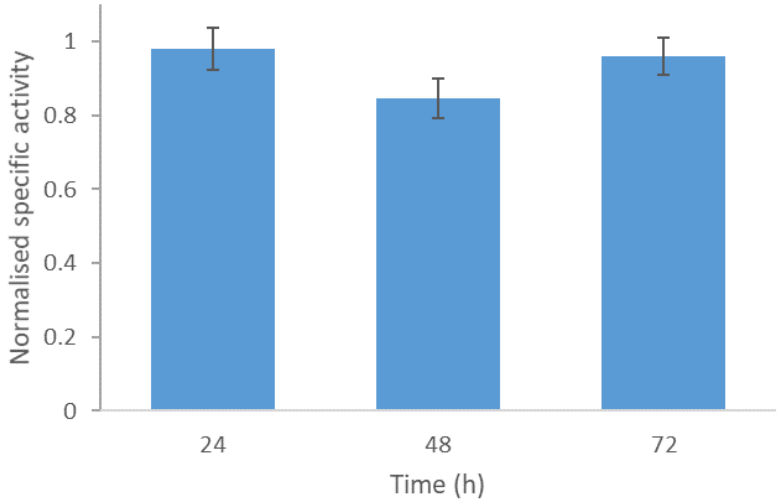

Figure SI.7: Specific activity of labelled NpXyn 11A at room temperature over time, normalised by the initial activity.

The characterisation of the activity of the enzyme stored at 6 and -20 °C was measured as well to ensure that it is preserved over the course of all diffusion experiments (see figure SI.8). The results indicate a good stability: after 7 months of storage, 75 % of the initial activity has been conserved. Consequently, the same batch of labelled enzyme could be used for all diffusion experiments. For this, the purified enzyme was stocked in small aliquots at -20 °C and thawed on ice before use.

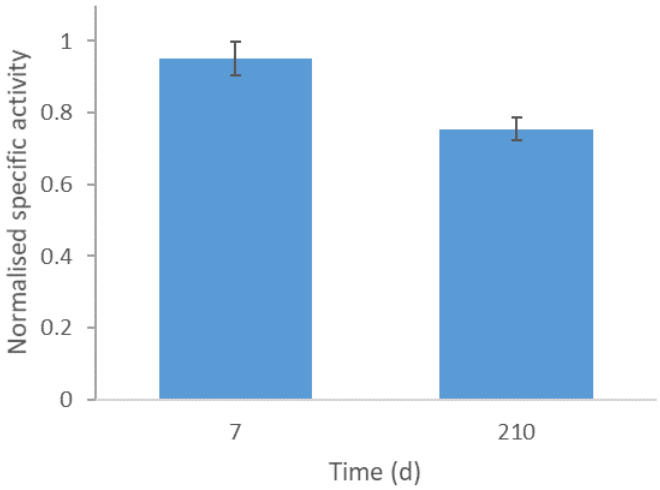

Figure SI.8: Specific activity of labelled NpXyn 11A at -20 °C over time, normalised by the initial activity.

Stability of the fluorescent intensity over time: Usually over time, fluorescence intensity decreases due to photooxidation of the fluorophore and other degradation processes. This is called bleaching. In some of the experiments here however, we observed an increase in fluorescence over time. This evolution of the intensity is clearly distinguishable from the evolution caused by the diffusion of the enzyme, because it leads to a homogeneous and global increase of the signal, as opposed to more local changes linked to diffusion. Data that was affected by this phenomenon was not taken into account. Even though the reason for this derivation is not yet clear, we found that the presence of the polymer limits this phenomenon.

Calibration labelled enzyme

For the calibration, enzyme concentrations between 1 and 10 µM were measured to cover the range of concentrations relevant for the experimental gradients. The obtained images were analysed and their radial profiles determined as detailed in the Materials and Methods section e. Then, for each measured concentration, an average intensity for 2 mm < r < 6 mm over 50 images was determined (see Figure SI.9).

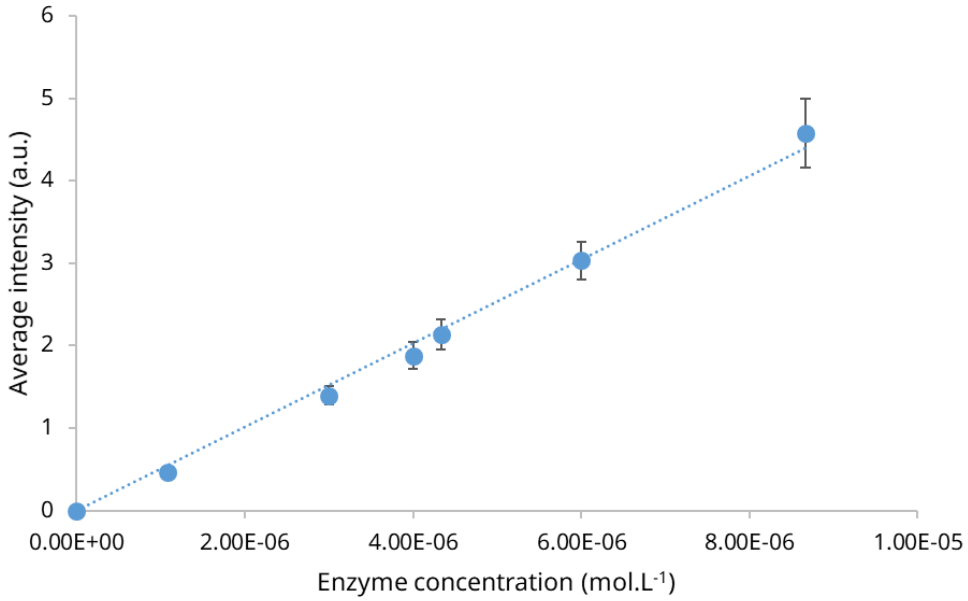

Figure SI.9: Calibration curve of the labelled enzyme (r^2 99.4 %).

Validation of 1 D diffusion using COMSOL

Our experimental set-up is adapted to the observation of radial, 1 dimensional diffusion. Nevertheless, it has to be verified whether the diffusion is purely radial and can be neglected in z. For this, we chose COMSOL to simulate the diffusion of an enzyme-sized particle in water ($D = 4.9 \times 10^{-11}$ $m^2.s^{-1}$) inside our device. Thanks to the symmetry of the device, we could use the 2D axisymmetric implementation in COMSOL and reduce the model size. Figure SI.10 shows the diffusion profiles at three different heights z (see inlet) inside the polymer layer for different times. We can see that the profiles for different z are different for $r < r_{reservoir}$, and become identical once we are

further from the reservoir and/or at longer time scales. From an experimental point of view, intensities at $r < r_{reservoir}$ and in close proximity were not taken into account anyways because of light reflection caused by the walls of the reservoir. Therefore, these limitations are not an issue and we can assume purely radial diffusion.

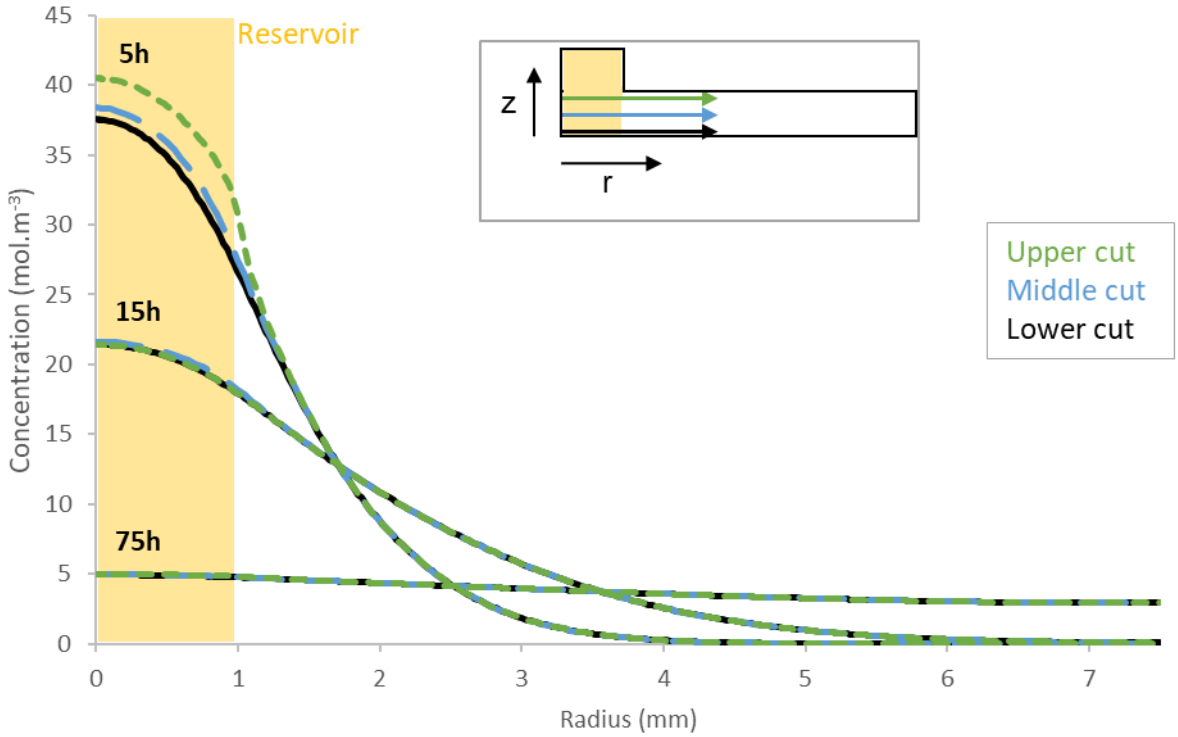

Figure SI.10: Results of the COMSOL simulation to investigate the diffusion in z-direction.

Image treatment/ python code

The diffusion of the enzyme is visualized by a camera that takes greyscale images. A grey scale image is made up of differently coloured pixels ranging from black to white. Each pixel represents an intensity value that is translated into its corresponding grey level. The number of grey levels is determined by the pixel depth of the image, e.g. a “12bit image” has 2^{12} (4096) different nuances. In this case, a pixel with an intensity of “0” is translated into black and a pixel with an intensity of “4095” is translated into white.

The intensity that is captured in one pixel comes from the cumulated light signal that reaches the camera. This signal can come from two different sources: 1) the studied object, here the fluorophore or 2) residual light from the background. Additionally, the intensity of the image is impacted by the light source that is never perfectly homogeneous and can distort the signal. Consequently, the signal from the studied object needs to be extracted from the total signal. This is done for each pixel and for each image, automated using Python.

Final commented code:

```
import numpy as np
import cv2
import glob, re
import csv
from PIL import Image


# definition of padding function to recenter the image
def add_padding(img, pad_l, pad_t, pad_r, pad_b):
    height, width = img.shape
    #Adding padding to the left side.
    pad_left = np.zeros((height, pad_l), dtype = int)
    img = np.concatenate((pad_left, img), axis = 1)

    #Adding padding to the top.
```

```
    pad_up = np.zeros((pad_t, pad_l + width))
    img = np.concatenate((pad_up, img), axis = 0)

    #Adding padding to the right.
    pad_right = np.zeros((height + pad_t, pad_r))
    img = np.concatenate((img, pad_right), axis = 1)

    #Adding padding to the bottom
    pad_bottom = np.zeros((pad_b, pad_l + width + pad_r))
    img = np.concatenate((img, pad_bottom), axis = 0)

    return img


# step 1: The dark : Image without LED (deconnected)
path = glob.glob(r'path to dark folder\*.tiff')
# empty matrix to store images
dark_total= np.empty([1000,1000])
# amount of images taken into account
nb_dark = 50

# loop to sum up all images, pixel by pixel, in matrix
# division by 16 because image is stored as 16bit
for image in path:
    dark = cv2.imread(image,-1)
    dark = np.array(dark)
    dark = dark/16.0
    dark_total = 1.0 * dark + dark_total

# dark matrix containing average value of each pixel
dark_moyen = (dark_total*0.6)/ nb_dark * 1.0

#########################################################################

## step 2: The flat : image of small concentration of fluorophore, same set-up as experiment
## same exposure time as experiment
path = glob.glob(r'path to flat folder\*.tiff')
```

```
# empty matrix to store images
flat_total= np.empty([1000,1000])
# amount of images taken into account
nb_flat = 50

# loop to sum up all images, pixel by pixel, in matrix
## padding function : determine x,y center using paint
## crop to resize image to 1000:1000,
for image in path:
    flat = cv2.imread(image,-1)
    padded_flat = add_padding(flat, 0, 0, 0, 0)
    padded_flat = np.round(padded_flat, decimals=0)
    padded_flat = padded_flat.astype(int)
    padded_flat = Image.fromarray(padded_flat)
    padded_flat = padded_flat.crop((0, 0, 1000, 1000))
    flat = np.array(padded_flat)
    flat = flat/16.0
    flat_total = 1.0 * flat + flat_total

# dark matrix containing average value of each pixel
flat_moyen = flat_total / nb_flat * 1.0

## subtract average dark and clip values < 0
flat_moyen = flat_moyen - dark_moyen
flat_moyen = flat_moyen.clip(min=0)

#########################################################################

# step 4: Diffusion images
path = glob.glob(r'path to diffusion experiment folder\*.tiff')
path.sort(key=lambda x:[int(c) if c.isdigit() else c for c in re.split(r'(\d+)', x)])

## count so we can see how far along the treatment is
## n goes into name of created txt file
count = 0
n = 1
```

```
## loop to read each image, pad and trim
## subtraction and normalisation of each image using dark and flat
## mask is superposed that groups pixels with same distance to center = same radius
## create list to stock radius, average intensity for each r, and stddev for each r
## loop over images to apply mask and extract average intensity and stddev for each r
## create txt file with that information
for image in path :
    diff = cv2.imread(image, -1)/16.0
    padded_diff = add_padding(diff, 0, 0, 0, 0)
    diff = np.round(padded_diff, decimals=0)
    diff = diff.astype(int)
    diff = Image.fromarray(diff)
    diff = diff.crop((0, 0, 1000, 1000))
    diff = np.array(diff)
    diff_final = diff - dark_moyen
    diff_final = diff_final / flat
    count += 1
    print(count)
    cen_x = 500
    cen_y = 500
    a = 1000
    b = 1000
    [X, Y] = np.meshgrid(np.arange(b) - cen_x, np.arange(a) - cen_y)
    R = np.sqrt(np.square(X) + np.square(Y))
    rad = np.arange(0, 450, 1)
    intensity = np.zeros(len(rad))
    standarddev = np.zeros(len(rad))
    index = 0
    bin_size2 = 1

    for i in rad:
        mask = (np.greater(R, i - bin_size2) & np.less(R, i + bin_size2))
        values = diff_final[mask]
        intensity[index] = np.mean(values)
        standarddev[index] = np.std(values)
        index += 1
```

```
    rad = rad *16 *0.001
    zip(rad, intensity, standarddev)
    with open('radial intensity and r in mm' + str(n) + '.txt','w+', newline='') as f:
        writer = csv.writer (f, delimiter='\t')
        writer.writerows(zip(rad, intensity, standarddev))
    n += 1

##########################################################################
##########################################################################
```

CHAPTER VI

Following the In-Situ Degradation of the Polymer: Preliminary Experiments

i. Preamble

In this chapter, we present some preliminary experiments where we followed the *in-situ* degradation of the polymer using two innovative techniques. By studying the evolution of the polymer and its structure over the course of its deconstruction, we gain a more global understanding of the action and the mobility of the enzyme. Our questions are:

1. Is it possible to 'see' the impact of the enzymatic deconstruction, i.e. is the change of the dynamics of the system induced by the enzymatic activity detectable using the technique?

2. Is it possible to add spatial resolution to the data, i.e. would it be possible to follow the progression of a degradation front?

ii. Nuclear magnetic resonance spectroscopy

Nuclear magnetic resonance spectroscopy is a powerful tool in the analysis of molecular structures. It can detect the magnetic resonance of certain nuclei such as protons when exposed to an external magnetic field. Depending on their surroundings, the nuclei will be more or less shielded from this field and the detected resonance will vary and give insights into their chemical environment [121]. Additionally, the width and intensity of the peaks of the spectrum contains information about the mobility of the proton. In the case of the (enzymatic) hydrolysis of a polymer, the chains become shorter and thus more mobile, which should in turn increase the mobility of the neighbouring protons and especially the water ones. These preliminary experiments as well as their analysis were possible thanks to Cyril Charlier and Guy Lippens from the NMR team of TBI.

a. Materials and methods

For proton NMR analysis, an AX stock solution at 9.1 $g.L^{-1}$ was prepared in D_2O using direct dissolution of the powder in 50 mM sodium phosphate buffer at pD 6 under agitation at 90 °C for 2 h. About 1 mL of this solution was transferred into a 5 mm NMR tube as an initial sample.

For a completely hydrolysed sample, 1 mL of this solution was transferred into a 1.5 mL Eppendorf tube and mixed with 1 µL of pre-diluted enzyme solution for a final enzyme concentration of 2.9×10^{-8} M. The enzyme was produced as described in chapter III and pre-diluted in the same D_2O buffer as the polymer. The mixture was incubated at 37 °C for 40 h under agitation. Then, the solution was transferred into an NMR tube.

Lastly, a sample under 'live' degradation was prepared by transferring 1 mL of the stock solution into an NMR tube. Just before the analysis, 1 µL of pre-diluted enzyme solution was carefully deposited on top of the AX solution in the tube. For the control experiment, 1 µL of buffer solution without any enzymes was used instead.

NMR analysis was performed in 5 mm tubes using a Bruker AVANCE NEO 800 MHz spectrometer at 37 °C. In addition to global spectra, spatially resolved proton mobility was acquired using 1D imaging in function of tube height z.

b. Results and discussion

As a first test, the intact (initial) and the degraded (final) AX solution was analysed to see whether there would be a detectible difference. Figure 46 displays a part of the resulting 1D ^{1}H spectra of the two samples. While the initial spectrum showed rather large peaks, the peaks of the final spectrum were higher and sharper. This evolution can be directly related to an increase in the mobility of the protons. The final spectrum also revealed a more detailed peak pattern. This could be due to the creation of new peaks corresponding to reaction products or simply to their revelation after being covered up by the initially wider peaks.

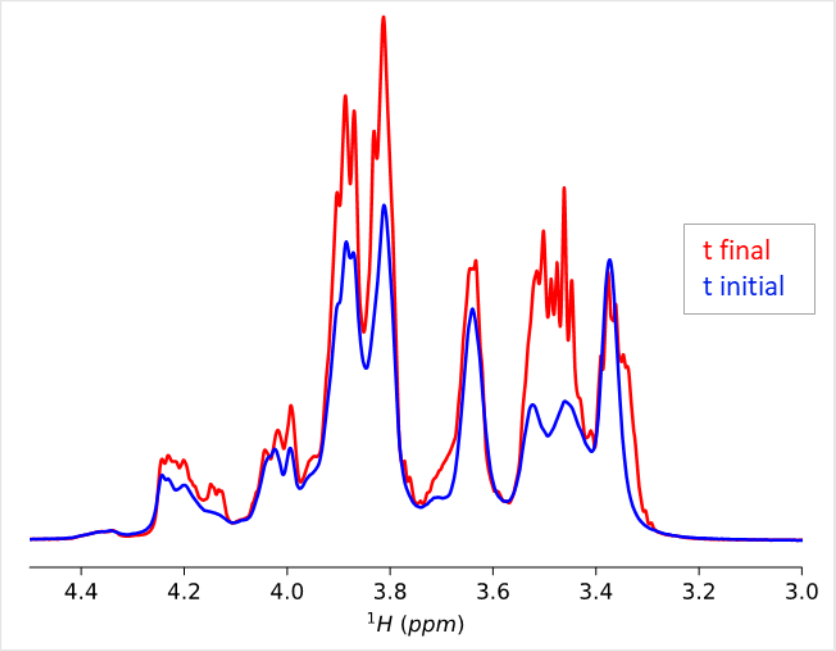

Figure 46: 1D ^1H spectra of 9 g.L^{-1} AX solutions before (blue) and after (red) enzymatic degradation at 47 °C for 40 h using an endo-xylanase. The reaction takes place in 50 mM sodium phosphate D_2O buffer at pD 6.

To get a more detailed look on the mobility of the water protons, their intensity over the height z of the tube was traced (see Figure 47). Again, the intensity and therefore the mobility of the protons increased after the degradation.

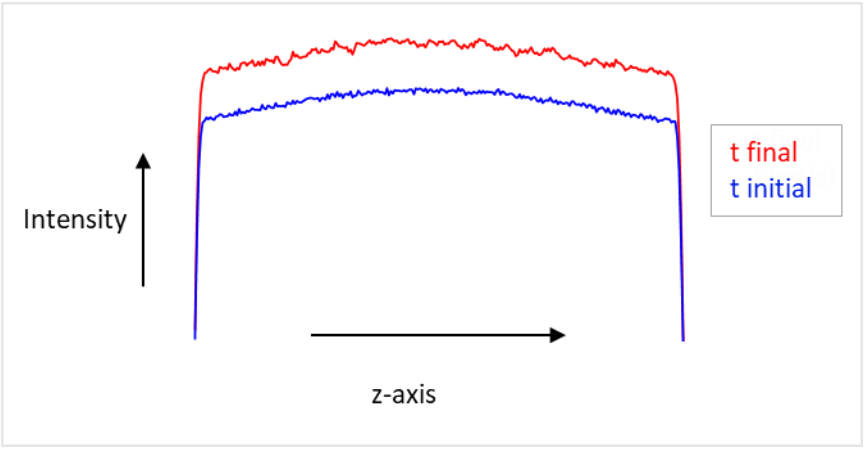

Figure 47: Intensity of the water peak of 9 g.L^{-1} AX solutions before (blue) and after (red) enzymatic degradation at 37 °C for 40 h using an endo-xylanase in function of sample height z.

In addition, the in-situ degradation of the polymer inside the NMR tube provides information about the evolution of the average proton mobility in function of time and might show the progression of a degradation front.

Figure 48 shows the evolution of the normalised integral of the peaks between 3.689 and 3.599 ppm as a function of degradation time. Just like before, the presence of the enzyme (full blue symbols) induces an increase in proton mobility and integral as a function of time. Without enzyme, the intensity remains constant (empty black symbols).

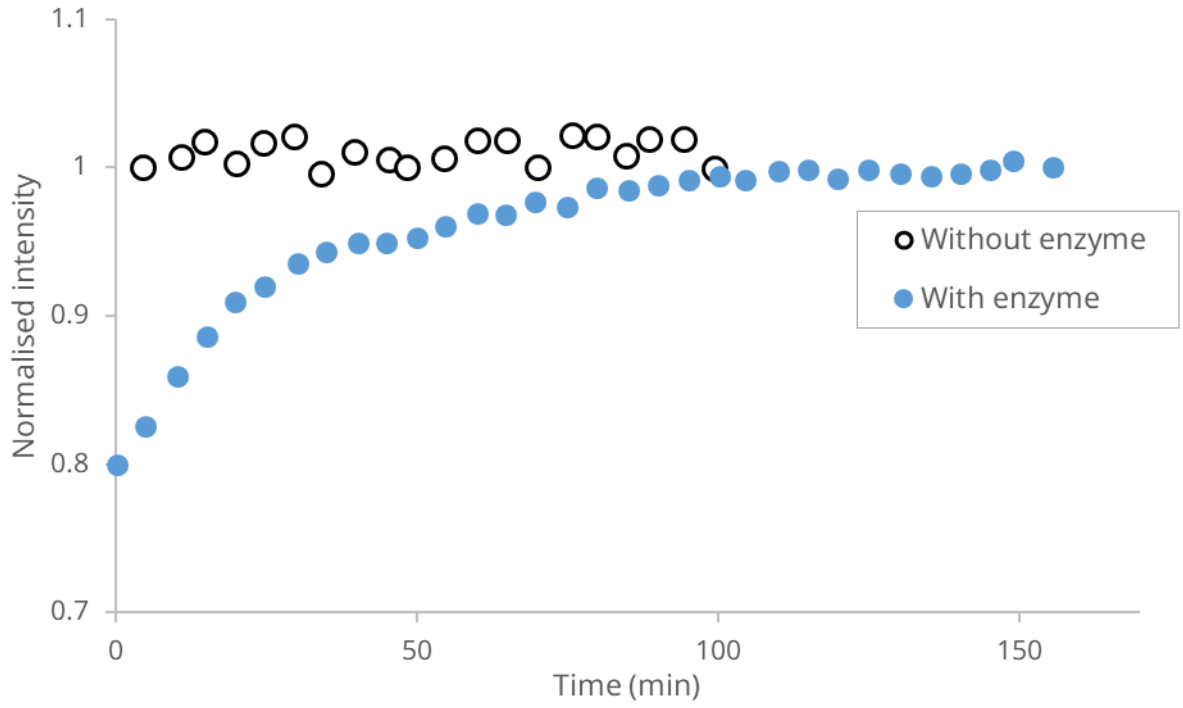

Figure 48: Evolution of the normalised integral over time (integration region: 3.689 – 3.599 ppm) of a 9 g.L^{-1} AX solution. Blue full symbols: AX that is being degraded by an enzyme gradient. Empty black symbols: control experiment without enzyme.

Looking at the spatial resolution of the intensity for the sample containing the enzyme, we can see that the intensity globally increases over time (see figure 49). Comparing the first two curves (0 and 10 min) after addition of the enzyme, there appears to be a small local shift in intensity where the curves separate and then meet again at smaller z. This shift might represent the degradation gradient of the polymer.

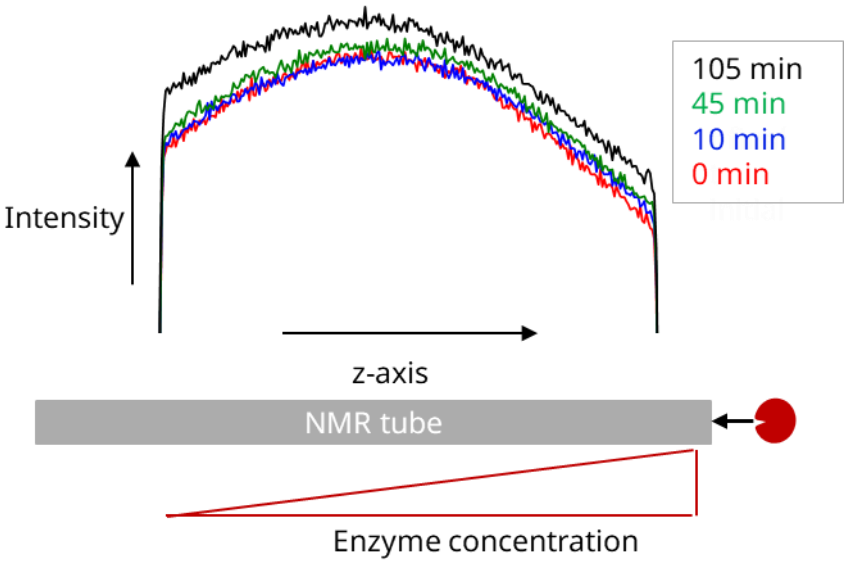

Figure 49: Intensity of the water peak of 9 g.L^{-1} AX solutions under enzymatic deconstruction as a function of sample height z for several degradation times (red to black).

c. Conclusion

With the help of ^{1}H NMR, it was possible to detect the homogeneous enzymatic hydrolysis of an arabinoxylan solution by following the evolution of proton mobility.

Using an enzyme gradient, preliminary results suggest that it could be possible to follow the degradation front caused by the migration of the enzymes towards the bottom of the tube in-situ. For this however, the concentration of polymer should exceed the concentration of 9 $g.L^{-1}$ that was tested here. A higher polymer concentration should ensure a stronger intensity gradient and therefore a more pronounced degradation front.

Moreover, ^{1}H NMR is not limited to observing only the effects of the enzyme's activity. In a study by Wisniewska *et al.*, this technique is used to measure the diffusion coefficient of surfactants inside a gel matrix. For this, the spatially resolved NMR signal of the molecule of interest is related to its concentration. The resulting concentration profiles over time is then used to calculate the diffusion coefficient [122]. Another study by Günther *et al.* used pulsed field gradients (PFG) NMR, where the detected NMR signal is susceptible to the diffusion of the molecule. If the observed nuclei move, their signal is attenuated, which can be quantified and a diffusion coefficient calculated [108]. In all of these cases, the native molecule is observed, no labelling is necessary, which is very promising.

iii. Photon Correlation Imaging

Photon correlation imagining (PCI) can be used to quantify the dynamics of polymer chains as well. For this, a transparent sample is illuminated using a light source and the scattered light is detected at 90° with a camera, resulting in a speckled image. As the scattering objects in the sample move, they cause local fluctuations of the intensity of this image over time, which represents the dynamics of the object and can be quantified [123].

The experiments were conducted and analysed with the help of Matteo Milani, Laurence Ramos and Luca Cipelletti from the soft matter team at the Charles Coulomb laboratory in Montpellier.

a. Materials and methods

An AX solution at 34 $g.L^{-1}$ was prepared using centrifugation as detailed in chapter II. The enzyme was produced as described in chapter II and diluted in 50 mM sodium phosphate buffer at pH 6. Samples were measure in NMR tubes.

At first, it was verified whether an intact and a fully degraded solution of 34 $g.L^{-1}$ AX present a detectible difference in dynamics. For the intact sample, 350µL of AX was transferred into an NMR tube and measured. For the degraded sample, 10 µL of diluted enzyme was added to 350 µL of AX at a final concentration of 1×10^{-7} M. The mixture was incubated at room temperature and measured after 15 and 90 min. This preliminary test was successful as two distinct dynamics could be detected.

Then, an *in-situ* homogeneous degradation was measured. For this, 350 µL AX and 10 µL of diluted enzyme for a final enzyme concentration of 1.2×10^{-9} M were mixed and immediately measured.

The next step was to try visualising the effects of an enzyme gradient, a heterogeneous degradation.

This sample was prepared by gently depositing 10 µL of enzyme on top of 350 µL AX in the NMR tube, for a final concentration of 1.2 x 10^{-9} M. Without mixing, the sample was immediately measured.

The PCI measurements were performed with a custom-built set-up that uses a laser (Verdi, 532 nm) to illuminate the sample and a camera (Basler, acA2000 340km) to capture the scattered light at a 90° angle.

b. Results and discussion

The results of the *in-situ* tracking of the enzymatic degradation of 34 g.L^{-1} AX are displayed in Figure 50. Over the course of 28 h, the decay time decreased, fastening the dynamics by almost a decade. The dynamics reached a plateau after approximately 20 h, indicating the end of the degradation. This length is in good agreement with viscosity and DNS measurements.

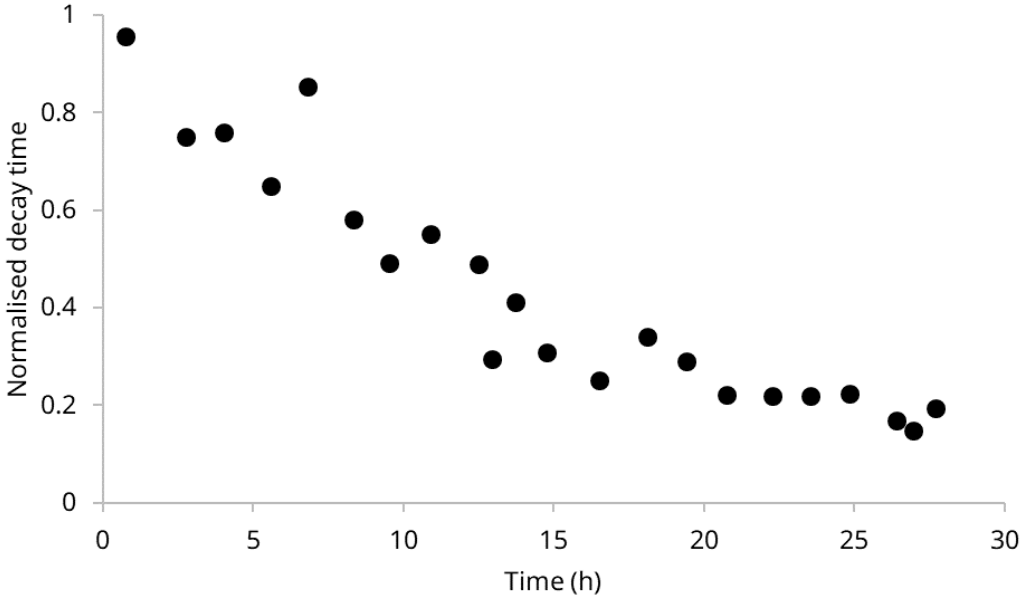

Figure 50: Evolution of the polymer dynamics of an in-situ degradation in homogeneous conditions over time. Polymer concentration of 34 g.L^{-1} and 1.2 nM of enzyme, incubated at 23 °C.

Figure 51 shows the results for the *in-situ* degradation using an enzyme gradient. For this, the decay time is plotted over the tube height for different degradation times. The 'zero' position was located 1 mm beneath the water/air interface. After the careful injection of the enzyme, the dynamics decreased rapidly, probably due to the fluctuations caused by the injection (times not shown). After 45 min, the dynamics stabilised and the decay time returned to the initial time that had previously been found for the homogeneous degradation. Later in time, we can see that the decay time globally decreased. However, this decrease was not always homogeneous in z, represented by the slope in some of the curves. These slopes could indicate the gradient in the dynamics, caused by the passage of the enzyme. The gradients appeared at about 4 h and faded at approximately 10 h after the injection, therefore the enzyme seemed to have passed through the observation window within this time range. After 10 h, the dynamics are homogeneous and their value is close to the one of the homogeneous solution after complete degradation.

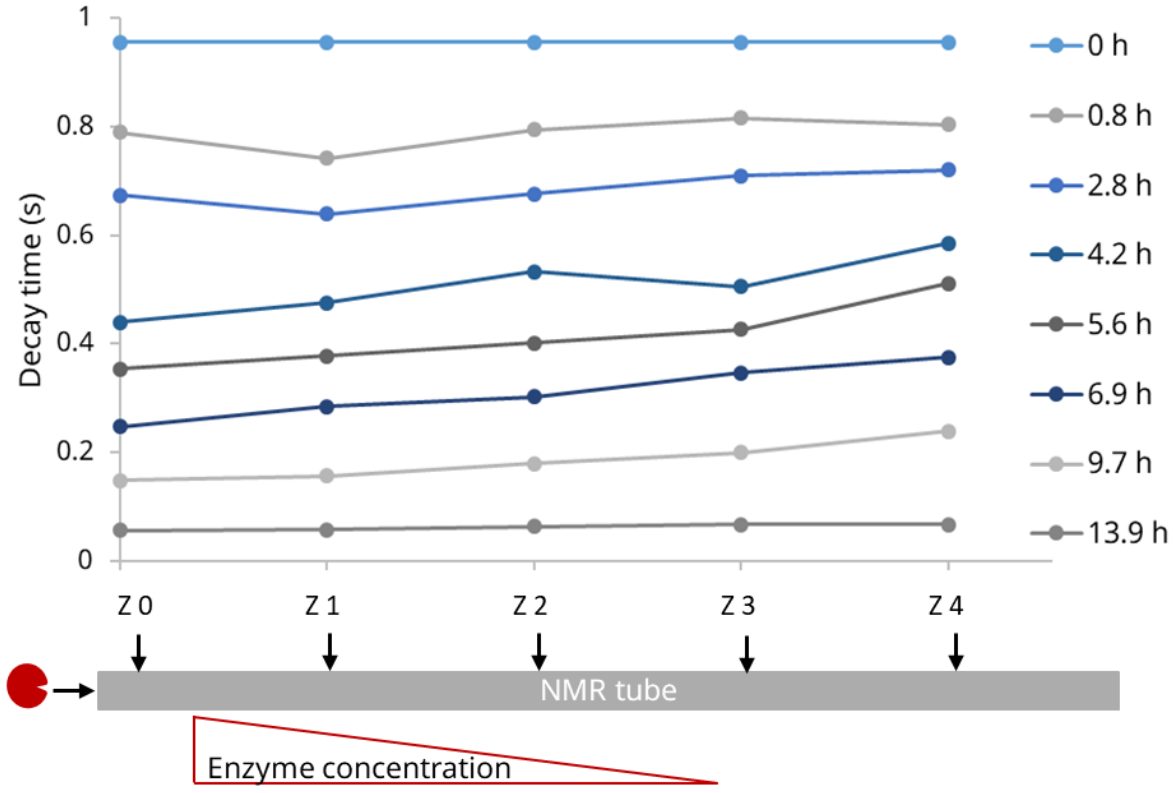

Figure 51: Evolution of the polymer dynamics an in-situ degradation using an enzyme gradient over time. Polymer concentration of 34 g.L^{-1} and 1.2 nM of enzyme, incubated at 23 °C. Position zero is located 1 mm beneath the surface of the solution.

c. Conclusion

We were able to detect and quantify the molecular dynamics of a polymer under enzymatic deconstruction using photon correlation imaging. First, the in-situ degradation of a homogenous enzyme-arabinoxylan solution was measured. Afterwards, enzyme solution was carefully deposited on top of a fresh polymer sample, to follow the effect of an enzyme gradient on the polymer dynamics. It was possible to observe a spatial gradient in dynamics that marked the passage of the enzyme front. It would be very interesting to repeat this experiment using a more concentrated polymer solution to create a more significant gradient. In addition, it is theoretically possible to detect fluorescence with the camera of the experimental set-up and therefore to follow the diffusion of the enzyme. This has not been tested yet however.

CHAPTER VII

General Conclusion and Perspectives

The general context of this PhD project is the valorisation of lignocellulosic plant biomass, which plays an important role in the transition towards a more sustainable economy. Before it can be valorised, the lignocellulose has to be deconstructed. This is very challenging due to its chemical and structural complexity. To address this complexity, the biomass undergoes a pre-treatment, after which the use of enzymes is very promising due to their specificity and 'soft' working conditions. However, the efficiency of the enzymatic deconstruction needs to be improved. For this, we proposed to better understand what happens during the enzymatic degradation of a concentrated polymeric substrate. How does the presence of the polymer impact the mobility of the enzyme, or its activity? And does the activity of the enzyme impact its mobility?

To investigate these questions, we chose to use a model system that considers the single factor of polymer concentration and study the activity and propagation of the enzyme. The model system consists of one lignocellulosic polymer, arabinoxylan, and one enzyme, a xylanase.

We began by thoroughly characterising arabinoxylan, in terms of single-chain and solution properties using SANS, rheology and SEC-MALS. This helped us identify a preparation protocol for the polymer solutions that favours good solubilisation even for high polymer concentrations. In addition, we were able to determine the general properties of the polymer such as the size, cross-section and stiffness of the chains. Most importantly, we were able to determine the onset of the formation of the network by the polymer chains, and the evolution of its mesh size with polymer concentration. The size of the mesh at different polymer concentrations determines the diffusivity of the polymer solution and is a crucial information to understand the environment of the enzyme.

Next, we characterised the second component, the enzyme, in terms of activity when confronted with the polymeric substrate under homogeneous conditions. The aim was to see if, and how, a high polymer concentration can affect enzymatic degradation. Here, we dosed the number of catalytic events using a colorimetric activity assay to obtain the initial reaction rate of the enzyme, and determined the size of the degradation products using SEC-MALS. The results of the activity assay did not show any diffusion limitation of the initial reaction rate for polymer concentrations up to

50 $g.L^{-1}$. The estimated mesh size for a polymer solution of 50 $g.L^{-1}$ is 2.5 times larger than the size of the enzyme, which could explain why we did not observe any diffusion limitation at very short times. Therefore, it would be interesting to add results for even higher polymer concentrations (90 $g.L^{-1}$ and higher). In addition, we might have seen an impact of the polymer concentration on the mode of action of the enzyme in terms of final degradation yield. However, this result needs to be verified, because it was obtained under different experimental conditions in terms of degradation temperature. Another possible effect on the mode of action of the enzyme concerns the size of the degradation products. Here, we saw some indications that a higher polymer concentration led to the formation of smaller degradation products due to diffusion limitation at intermediate times. These results should be confirmed by repetition and the use of still higher polymer concentrations.

Finally, we studied the propagation and diffusion of the active and inactive enzyme in their substrate to see how the polymer concentration impacts their mobility and what role their activity plays. For these experiments, we followed the diffusion of an enzyme gradient using a custom fluorescence microscope. The enzyme was labelled with a fluorophore using an optimised labelling protocol. Polymer solutions were prepared in a way that ensured good hydration, and their concentrations were above the overlap concentration to create a polymer mesh. We found that the evolution of the normalised diffusion coefficient of the active and inactive enzyme did neither follow the Stokes-Einstein relation, nor the scaling laws proposed by Rubinstein *et al.* (at least not in the same regime of concentration in the case of Rubinstein). We instead found that the enzymes diffuse like in a solution of an effective viscosity that is in-between the macroscopic viscosities of the solvent and polymer solutions This is something that has been observed in the case of the diffusion of inert tracers in polymer solutions, but that could also be due in some extent to possible attractive interactions between the enzyme and the polymer in our case. With increasing polymer concentration, the normalised diffusion coefficient of the active and the inactive enzyme decreased but not to the same extend: In the case of the inactive enzyme, the diffusion coefficient decreased approximately 20-fold and in the case of the active enzyme about 10-fold over the same range of concentration.

On average, the active enzyme diffused 1.8 times faster than the inactive enzyme. While this clearly shows the impact of the enzymatic activity on its mobility, the nature of this link is not clear yet but needs to be further investigated. To study the possibility of enhanced diffusion as a cause, this difference in the diffusion coefficients of the active and inactive enzyme has to be verified using another technique such as FRAP or FCS. In order to understand the role of the deconstruction of the polymer and the associated facilitation of the mobility of the enzyme, we need additional information concerning the state of the polymer. Our preliminary tests showed that it is possible to follow the evolution of the state of the polymer *in situ* over time using innovative techniques such as NMR and PCI. Here again, we used physics to study a biological system, another example of the great potential of an interdisciplinary approach for this subject.

Overall, we were able to gain some unique and fascinating insights into the activity and diffusion of enzymes in a concentrated polymeric substrate. For this, we used an original and multidisciplinary approach that combines biochemistry, physics and imaging. The main achievement of this PhD is the development of a novel, custom technique to follow and quantify the propagation and diffusion of the enzyme using fluorescence. This technique allowed us to shed new light on the complex link between enzymatic activity and mobility. Moreover, our methodology opens the door for future experiments involving different substrates and enzymes and to study other questions linked to enzymatic diffusion: Is the diffusion of an enzyme with a different activity, such as an arabinofuranosidase, impacted in the same way as the xylanase? How would modulating the affinity of the enzyme towards its substrate impact the diffusion? For this, carbohydrate binding moduls (CBMs), that are part of the multi-modular structure of some enzymes, could be used. The impact of synergies between different enzymes on their mobility is also an interesting question. Indeed, most processes rely on enzymatic cocktails, which are mixtures of different, complementary enzymes optimised for the degradation of complex substrates. The composition of these cocktails is selected based on their degradation efficiency, and our technique could be used to study the impact of this efficiency on the mobility of the enzymes. Moreover, an improved mobility could in return boost the degradation, because the enzymes need to be able to access their

targets to degrade them. In this respect, our technique could be used to screen enzymatic cocktails for optimal enzymatic mobility. As a result, our technique has the potential to improve the understanding and design of enzymatic reactions in industrial processes such as the deconstruction of lignocellulosic plant biomass.

References

[1] V. Menon et M. Rao, « Trends in bioconversion of lignocellulose: Biofuels, platform chemicals & biorefinery concept », *Prog. Energy Combust. Sci.*, vol. 38, n° 4, p. 522-550, août 2012, doi: 10.1016/j.pecs.2012.02.002.

[2] R. R. Philippini *et al.*, « Agroindustrial Byproducts for the Generation of Biobased Products: Alternatives for Sustainable Biorefineries », *Front. Energy Res.*, vol. 8, p. 152, juill. 2020, doi: 10.3389/fenrg.2020.00152.

[3] M. E. Himmel *et al.*, « Biomass Recalcitrance: Engineering Plants and Enzymes for Biofuels Production », *Science*, vol. 315, n° 5813, p. 804-807, févr. 2007, doi: 10.1126/science.1137016.

[4] T. Manavalan, A. Manavalan, et K. Heese, « Characterization of Lignocellulolytic Enzymes from White-Rot Fungi », *Curr. Microbiol.*, vol. 70, n° 4, p. 485-498, avr. 2015, doi: 10.1007/s00284-014-0743-0.

[5] S. Sun, S. Sun, X. Cao, et R. Sun, « The role of pretreatment in improving the enzymatic hydrolysis of lignocellulosic materials », *Bioresour. Technol.*, vol. 199, p. 49-58, janv. 2016, doi: 10.1016/j.biortech.2015.08.061.

[6] Y. Cheng et R. K. Prud'homme, « Enzymatic Degradation of Guar and Substituted Guar Galactomannans », *Biomacromolecules*, vol. 1, n° 4, p. 782-788, déc. 2000, doi: 10.1021/bm005616v.

[7] A.-Y. Jee, S. Dutta, Y.-K. Cho, T. Tlusty, et S. Granick, « Enzyme leaps fuel antichemotaxis », *Proc. Natl. Acad. Sci.*, vol. 115, n° 1, p. 14-18, janv. 2018, doi: 10.1073/pnas.1717844115.

[8] A.-Y. Jee, T. Tlusty, et S. Granick, « Master curve of boosted diffusion for 10 catalytic enzymes », *Proc. Natl. Acad. Sci.*, vol. 117, n° 47, p. 29435-29441, nov. 2020, doi: 10.1073/pnas.2019810117.

[9] M. Feng et M. K. Gilson, « Enhanced Diffusion and Chemotaxis of Enzymes », *Annu. Rev. Biophys.*, vol. 49, n° 1, p. 87-105, mai 2020, doi: 10.1146/annurev-biophys-121219-081535.

[10] H. S. Muddana, S. Sengupta, T. E. Mallouk, A. Sen, et P. J. Butler, « Substrate Catalysis Enhances Single-Enzyme Diffusion », *J. Am. Chem. Soc.*, vol. 132, n° 7, p. 2110-2111, févr. 2010, doi: 10.1021/ja908773a.

[11] E. Bonnin *et al.*, « Mobility of pectin methylesterase in pectin/cellulose gels is enhanced by the presence of cellulose and by its catalytic capacity », *Sci. Rep.*, vol. 9, n° 1, p. 12551, déc. 2019, doi: 10.1038/s41598-019-49108-x.

[12] M. J. Meents, Y. Watanabe, et A. L. Samuels, « The cell biology of secondary cell wall biosynthesis », *Ann. Bot.*, vol. 121, n° 6, p. 1107-1125, mai 2018, doi: 10.1093/aob/mcy005.

[13] A. Bjelić, B. Hočevar, M. Grilc, U. Novak, et B. Likozar, « A review of sustainable lignocellulose biorefining applying (natural) deep eutectic solvents (DESs) for separations, catalysis and enzymatic biotransformation processes », *Rev. Chem. Eng.*, vol. 38, n° 3, p. 243-272, avr. 2022, doi: 10.1515/revce-2019-0077.

[14] R. A. Burton, M. J. Gidley, et G. B. Fincher, « Heterogeneity in the chemistry, structure and function of plant cell walls », *Nat. Chem. Biol.*, vol. 6, n° 10, p. 724-732, oct. 2010, doi: 10.1038/nchembio.439.

[15] H. V. Scheller et P. Ulvskov, « Hemicelluloses », *Annu. Rev. Plant Biol.*, vol. 61, n° 1, p. 263-289, juin 2010, doi: 10.1146/annurev-arplant-042809-112315.

[16] P. McKendry, « Energy production from biomass (part 1): overview of biomass », *Bioresour. Technol.*, vol. 83, n° 1, p. 37-46, mai 2002, doi: 10.1016/S0960-8524(01)00118-3.

[17] T. J. Simmons *et al.*, « Folding of xylan onto cellulose fibrils in plant cell walls revealed by solid-state NMR », *Nat. Commun.*, vol. 7, n° 1, Art. n° 1, déc. 2016, doi: 10.1038/ncomms13902.

[18] Y. Pu, F. Hu, F. Huang, B. H. Davison, et A. J. Ragauskas, « Assessing the molecular structure basis for biomass recalcitrance during dilute acid and hydrothermal pretreatments », *Biotechnol. Biofuels*, vol. 6, n° 1, p. 15, janv. 2013, doi: 10.1186/1754-6834-6-15.

[19] J. H. Grabber, D. R. Mertens, H. Kim, C. Funk, F. Lu, et J. Ralph, « Cell wall fermentation kinetics are impacted more by lignin content and ferulate cross-linking than by lignin composition », *J. Sci. Food Agric.*, vol. 89, n° 1, p. 122-129, janv. 2009, doi: 10.1002/jsfa.3418.

[20] S. S. Hassan, G. A. Williams, et A. K. Jaiswal, « Moving towards the second generation of lignocellulosic biorefineries in the EU: Drivers, challenges, and opportunities », *Renew. Sustain. Energy Rev.*, vol. 101, p. 590-599, mars 2019, doi: 10.1016/j.rser.2018.11.041.

[21] S. Octave et D. Thomas, « Biorefinery: Toward an industrial metabolism », *Biochimie*, vol. 91, n° 6, p. 659-664, juin 2009, doi: 10.1016/j.biochi.2009.03.015.

[22] C. Dumon, L. Song, S. Bozonnet, R. Fauré, et M. J. O'Donohue, « Progress and future prospects for pentose-specific biocatalysts in biorefining », *Process Biochem.*, vol. 47, n° 3, p. 346-357, mars 2012, doi: 10.1016/j.procbio.2011.06.017.

[23] Y. Lin et S. Tanaka, « Ethanol fermentation from biomass resources: current state and prospects », *Appl. Microbiol. Biotechnol.*, vol. 69, n° 6, p. 627-642, févr. 2006, doi: 10.1007/s00253-005-0229-x.

[24] M. Brodin, M. Vallejos, M. T. Opedal, M. C. Area, et G. Chinga-Carrasco, « Lignocellulosics as sustainable resources for production of bioplastics – A review », *J. Clean. Prod.*, vol. 162, p. 646-664, sept. 2017, doi: 10.1016/j.jclepro.2017.05.209.

[25] T. Wuestenberg, *Cellulose and Cellulose Derivatives in the Food Industry: Fundamentals and Applications*. John Wiley & Sons, 2014.

[26] R. Rinaldi *et al.*, « Paving the Way for Lignin Valorisation: Recent Advances in Bioengineering, Biorefining and Catalysis », *Angew. Chem. Int. Ed.*, vol. 55, n° 29, p. 8164-8215, juill. 2016, doi: 10.1002/anie.201510351.

[27] P. Azadi, R. Carrasquillo-Flores, Y. J. Pagán-Torres, E. I. Gürbüz, R. Farnood, et J. A. Dumesic, « Catalytic conversion of biomass using solvents derived from lignin », *Green Chem.*, vol. 14, n° 6, p. 1573, 2012, doi: 10.1039/c2gc35203f.

[28] N. W. Dulie, B. Woldeyes, H. D. Demsash, et A. S. Jabasingh, « An Insight into the Valorization of Hemicellulose Fraction of Biomass into Furfural: Catalytic Conversion and Product Separation », *Waste Biomass Valorization*, vol. 12, n° 2, p. 531-552, févr. 2021, doi: 10.1007/s12649-020-00946-1.

[29] L. Chaa *et al.*, « Isolation, characterization and valorization of hemicelluloses from Aristida pungens leaves as biomaterial », *Carbohydr. Polym.*, vol. 74, n° 3, p. 597-602, nov. 2008, doi: 10.1016/j.carbpol.2008.04.017.

[30] A. N. Arzami, T. M. Ho, et K. S. Mikkonen, « Valorization of cereal by-product hemicelluloses: Fractionation and purity considerations », *Food Res. Int.*, vol. 151, p. 110818, janv. 2022, doi: 10.1016/j.foodres.2021.110818.

[31] O. B. Chukwuma, M. Rafatullah, H. A. Tajarudin, et N. Ismail, « Lignocellulolytic Enzymes in Biotechnological and Industrial Processes: A Review », *Sustainability*, vol. 12, n° 18, p. 7282, sept. 2020, doi: 10.3390/su12187282.

[32] V. Lombard, H. Golaconda Ramulu, E. Drula, P. M. Coutinho, et B. Henrissat, « The carbohydrate-active enzymes database (CAZy) in 2013 », *Nucleic Acids Res.*, vol. 42, n° D1, p. D490-D495, janv. 2014, doi: 10.1093/nar/gkt1178.

[33] J. S. Van Dyk et B. I. Pletschke, « A review of lignocellulose bioconversion using enzymatic hydrolysis and synergistic cooperation between enzymes—Factors affecting enzymes, conversion and synergy », *Biotechnol. Adv.*, vol. 30, n° 6, p. 1458-1480, nov. 2012, doi: 10.1016/j.biotechadv.2012.03.002.

[34] G. T. Beckham, Y. J. Bomble, E. A. Bayer, M. E. Himmel, et M. F. Crowley, « Applications of computational science for understanding enzymatic deconstruction of cellulose », *Curr. Opin. Biotechnol.*, vol. 22, n° 2, p. 231-238, avr. 2011, doi: 10.1016/j.copbio.2010.11.005.

[35] F. M. Medie, G. J. Davies, M. Drancourt, et B. Henrissat, « Genome analyses highlight the different biological roles of cellulases », *Nat. Rev. Microbiol.*, vol. 10, n° 3, p. 227-234, mars 2012, doi: 10.1038/nrmicro2729.

[36] K. Igarashi *et al.*, « Traffic Jams Reduce Hydrolytic Efficiency of Cellulase on Cellulose Surface », *Science*, vol. 333, n° 6047, p. 1279-1282, sept. 2011, doi: 10.1126/science.1208386.

[37] P. Biely, S. Singh, et V. Puchart, « Towards enzymatic breakdown of complex plant xylan structures: State of the art », *Biotechnol. Adv.*, vol. 34, n° 7, p. 1260-1274, nov. 2016, doi: 10.1016/j.biotechadv.2016.09.001.

[38] A. Hatakka, « Lignin-modifying enzymes fungi : production and role from selected white-rot in lignin degradation », 2002. /paper/Lignin-modifying-enzymes-fungi-%3A-production-and-in-Hatakka/1056c912ec454c7ca6b0c4325ba93ed018816640 (consulté le 27 mai 2020).

[39] M. Moon, J.-P. Lee, G. W. Park, J.-S. Lee, H. J. Park, et K. Min, « Lytic polysaccharide monooxygenase (LPMO)-derived saccharification of lignocellulosic biomass », *Bioresour. Technol.*, vol. 359, p. 127501, sept. 2022, doi: 10.1016/j.biortech.2022.127501.

[40] H.-T. Song *et al.*, « Synergistic effect of cellulase and xylanase during hydrolysis of natural lignocellulosic substrates », *Bioresour. Technol.*, vol. 219, p. 710-715, nov. 2016, doi: 10.1016/j.biortech.2016.08.035.

[41] L. Artzi, E. A. Bayer, et S. Moraïs, « Cellulosomes: bacterial nanomachines for dismantling plant polysaccharides », *Nat. Rev. Microbiol.*, vol. 15, n° 2, p. 83-95, févr. 2017, doi: 10.1038/nrmicro.2016.164.

[42] M. Eibinger, T. Ganner, H. Plank, et B. Nidetzky, « A Biological Nanomachine at Work: Watching the Cellulosome Degrade Crystalline Cellulose », *ACS Cent. Sci.*, vol. 6, n° 5, p. 739-746, mai 2020, doi: 10.1021/acscentsci.0c00050.

[43] C. Herve, A. Rogowski, A. W. Blake, S. E. Marcus, H. J. Gilbert, et J. P. Knox, « Carbohydrate-binding modules promote the enzymatic deconstruction of intact

plant cell walls by targeting and proximity effects », *Proc. Natl. Acad. Sci.*, vol. 107, n° 34, p. 15293-15298, août 2010, doi: 10.1073/pnas.1005732107.

[44] A. Labourel *et al.*, « The Mechanism by Which Arabinoxylanases Can Recognize Highly Decorated Xylans », *J. Biol. Chem.*, vol. 291, n° 42, p. 22149-22159, oct. 2016, doi: 10.1074/jbc.M116.743948.

[45] H. J. Gilbert, J. P. Knox, et A. B. Boraston, « Advances in understanding the molecular basis of plant cell wall polysaccharide recognition by carbohydrate-binding modules », *Curr. Opin. Struct. Biol.*, vol. 23, n° 5, p. 669-677, oct. 2013, doi: 10.1016/j.sbi.2013.05.005.

[46] F. Warnecke *et al.*, « Metagenomic and functional analysis of hindgut microbiota of a wood-feeding higher termite », *Nature*, vol. 450, n° 7169, Art. n° 7169, nov. 2007, doi: 10.1038/nature06269.

[47] G. Bastien *et al.*, « Mining for hemicellulases in the fungus-growing termite Pseudacanthotermes militaris using functional metagenomics », *Biotechnol. Biofuels*, vol. 6, n° 1, p. 78, 2013, doi: 10.1186/1754-6834-6-78.

[48] J. M. Brulc *et al.*, « Gene-centric metagenomics of the fiber-adherent bovine rumen microbiome reveals forage specific glycoside hydrolases », *Proc. Natl. Acad. Sci.*, vol. 106, n° 6, p. 1948-1953, févr. 2009, doi: 10.1073/pnas.0806191105.

[49] S. Voget, C. Leggewie, A. Uesbeck, C. Raasch, K.-E. Jaeger, et W. R. Streit, « Prospecting for Novel Biocatalysts in a Soil Metagenome », *Appl. Environ. Microbiol.*, vol. 69, n° 10, p. 6235-6242, oct. 2003, doi: 10.1128/AEM.69.10.6235-6242.2003.

[50] X. Xu, M. Liu, W. Huo, et X. Dai, « Obtaining a mutant of Bacillus amyloliquefaciens xylanase A with improved catalytic activity by directed evolution », *Enzyme Microb. Technol.*, vol. 86, p. 59-66, mai 2016, doi: 10.1016/j.enzmictec.2016.02.001.

[51] S. I. R. Damis, A. M. A. Murad, F. Diba Abu Bakar, S. A. Rashid, N. R. Jaafar, et R. Md. Illias, « Protein engineering of GH11 xylanase from Aspergillus fumigatus RT-1 for catalytic efficiency improvement on kenaf biomass hydrolysis », *Enzyme Microb. Technol.*, vol. 131, p. 109383, déc. 2019, doi: 10.1016/j.enzmictec.2019.109383.

[52] D. Chung *et al.*, « Glycosylation Is Vital for Industrial Performance of Hyperactive Cellulases », *ACS Sustain. Chem. Eng.*, vol. 7, n° 5, p. 4792-4800, mars 2019, doi: 10.1021/acssuschemeng.8b05049.

[53] R. Brunecky *et al.*, « Synthetic fungal multifunctional cellulases for enhanced biomass conversion », *Green Chem.*, vol. 22, n° 2, p. 478-489, 2020, doi: 10.1039/C9GC03062J.

[54] A. M. Lopes, E. X. Ferreira Filho, et L. R. S. Moreira, « An update on enzymatic cocktails for lignocellulose breakdown », *J. Appl. Microbiol.*, vol. 125, n° 3, p. 632-645, sept. 2018, doi: 10.1111/jam.13923.

[55] S. P. Gilmore, S. P. Lillington, C. H. Haitjema, R. de Groot, et M. A. O'Malley, « Designing chimeric enzymes inspired by fungal cellulosomes », *Synth. Syst. Biotechnol.*, vol. 5, n° 1, p. 23-32, mars 2020, doi: 10.1016/j.synbio.2020.01.003.

[56] Y. Amano, M. Shiroishi, K. Nisizawa, E. Hoshino, et T. Kanda, « Fine substrate specificities of four exo-type cellulases produced by Aspergillus niger, Trichoderma reesei, and Irpex lacteus on (1-->3), (1-->4)-beta-D-glucans and xyloglucan », *J.*

Biochem. (Tokyo), vol. 120, nº 6, p. 1123-1129, déc. 1996, doi: 10.1093/oxfordjournals.jbchem.a021531.

[57] L. A. M. Van Den Broek, R. M. Lloyd, G. Beldman, J. C. Verdoes, B. V. McCleary, et A. G. J. Voragen, « Cloning and characterization of arabinoxylan arabinofuranohydrolase-D3 (AXHd3) from Bifidobacterium adolescentis DSM20083 », *Appl. Microbiol. Biotechnol.*, vol. 67, nº 5, p. 641-647, juin 2005, doi: 10.1007/s00253-004-1850-9.

[58] D. Nurizzo, T. Nagy, H. J. Gilbert, et G. J. Davies, « The Structural Basis for Catalysis and Specificity of the Pseudomonas cellulosa α-Glucuronidase, GlcA67A », *Structure*, vol. 10, nº 4, p. 547-556, avr. 2002, doi: 10.1016/S0969-2126(02)00742-6.

[59] L. Michaelis et M. M. L. Menten, « The kinetics of invertin action: Translated by T.R.C. Boyde Submitted 4 February 1913 », *FEBS Lett.*, vol. 587, nº 17, p. 2712-2720, sept. 2013, doi: 10.1016/j.febslet.2013.07.015.

[60] « Michaelis-Menten-Kinetik », *MTA Dialog*. https://www.mta-dialog.de/artikel/michaelis-menten-kinetik.html (consulté le 3 juin 2020).

[61] S. Schläfle, T. Tervahartiala, T. Senn, et R. Kölling-Paternoga, « Quantitative and visual analysis of enzymatic lignocellulose degradation », *Biocatal. Agric. Biotechnol.*, vol. 11, p. 42-49, juill. 2017, doi: 10.1016/j.bcab.2017.06.002.

[62] L. Liu, C. Qian, L. Jiang, et H.-Q. Yu, « Direct Three-Dimensional Characterization and Multiscale Visualization of Wheat Straw Deconstruction by White Rot Fungus », *Environ. Sci. Technol.*, vol. 48, nº 16, p. 9819-9825, août 2014, doi: 10.1021/es5020983.

[63] I. Lee, B. R. Evans, et J. Woodward, « The mechanism of cellulase action on cotton fibers: evidence from atomic force microscopy », *Ultramicroscopy*, vol. 82, nº 1, p. 213-221, févr. 2000, doi: 10.1016/S0304-3991(99)00158-8.

[64] P. He, L. Chai, L. Li, L. Hao, L. Shao, et F. Lü, « In situ visualization of the change in lignocellulose biodegradability during extended anaerobic bacterial degradation », *RSC Adv.*, vol. 3, nº 29, p. 11759-11773, juill. 2013, doi: 10.1039/C3RA40654G.

[65] M.-F. Devaux *et al.*, « Synchrotron Time-Lapse Imaging of Lignocellulosic Biomass Hydrolysis: Tracking Enzyme Localization by Protein Autofluorescence and Biochemical Modification of Cell Walls by Microfluidic Infrared Microspectroscopy », *Front. Plant Sci.*, vol. 9, 2018, Consulté le: 22 avril 2023. [En ligne]. Disponible sur: https://www.frontiersin.org/articles/10.3389/fpls.2018.00200

[66] S. Blosse, A. Bouchoux, C. Y. Montanier, et P. Duru, « X-ray microtomography reveals the 3D enzymatic deconstruction pathway of raw lignocellulosic biomass », *Bioresour. Technol. Rep.*, vol. 21, p. 101351, févr. 2023, doi: 10.1016/j.biteb.2023.101351.

[67] C. Montanier *et al.*, « Evidence that family 35 carbohydrate binding modules display conserved specificity but divergent function », *Proc. Natl. Acad. Sci.*, vol. 106, nº 9, p. 3065-3070, mars 2009, doi: 10.1073/pnas.0808972106.

[68] H. E. Grethlein, « The Effect of Pore Size Distribution on the Rate of Enzymatic Hydrolysis of Cellulosic Substrates », *Bio/Technology*, vol. 3, nº 2, Art. nº 2, févr. 1985, doi: 10.1038/nbt0285-155.

[69] B. K. Behera, M. Arora, et D. K. Sharma, « Scanning electron microscopic (SEM) studies on structural architecture of lignocellulosic materials of Calotropis procera

during its processing for saccharification », *Bioresour. Technol.*, vol. 58, n° 3, p. 241-245, déc. 1996, doi: 10.1016/S0960-8524(96)00039-9.

[70] F. S. Steven, « Polymeric collagen fibrils: An example of substrate-mediated steric obstruction of enzymic digestion », *Biochim. Biophys. Acta BBA - Enzymol.*, vol. 452, n° 1, p. 151-160, nov. 1976, doi: 10.1016/0005-2744(76)90066-8.

[71] G. C. Fadda, D. Lairez, B. Arrio, J.-P. Carton, et V. Larreta-Garde, « Enzyme-Catalyzed Gel Proteolysis: An Anomalous Diffusion-Controlled Mechanism », *Biophys. J.*, vol. 85, n° 5, p. 2808-2817, nov. 2003, doi: 10.1016/S0006-3495(03)74704-3.

[72] S. C. Skaalure, U. Akalp, F. J. Vernerey, et S. J. Bryant, « Tuning Reaction and Diffusion Mediated Degradation of Enzyme-Sensitive Hydrogels », *Adv. Healthc. Mater.*, vol. 5, n° 4, p. 432-438, févr. 2016, doi: 10.1002/adhm.201500728.

[73] C. C. Hsieh, D. Cannella, H. Jørgensen, C. Felby, et L. G. Thygesen, « Cellulase Inhibition by High Concentrations of Monosaccharides », *J. Agric. Food Chem.*, vol. 62, n° 17, p. 3800-3805, avr. 2014, doi: 10.1021/jf5012962.

[74] T. van der Zwan, R. P. Chandra, et J. N. Saddler, « Laccase-mediated hydrophilization of lignin decreases unproductive enzyme binding but limits subsequent enzymatic hydrolysis at high substrate concentrations », *Bioresour. Technol.*, vol. 292, p. 121999, nov. 2019, doi: 10.1016/j.biortech.2019.121999.

[75] S. Bhagia, R. Kumar, et C. E. Wyman, « Effects of dilute acid and flowthrough pretreatments and BSA supplementation on enzymatic deconstruction of poplar by cellulase and xylanase », *Carbohydr. Polym.*, vol. 157, p. 1940-1948, févr. 2017, doi: 10.1016/j.carbpol.2016.11.085.

[76] J. K. Ko, E. Ximenes, Y. Kim, et M. R. Ladisch, « Adsorption of enzyme onto lignins of liquid hot water pretreated hardwoods », *Biotechnol. Bioeng.*, vol. 112, n° 3, p. 447-456, 2015, doi: 10.1002/bit.25359.

[77] P. Videcoq, K. Steenkeste, E. Bonnin, et C. Garnier, « A multi-scale study of enzyme diffusion in macromolecular solutions and physical gels of pectin polysaccharides », *Soft Matter*, vol. 9, n° 20, p. 5110, 2013, doi: 10.1039/c3sm00058c.

[78] H. C. Berg, *Random Walks in Biology*. Princeton University Press, 1993.

[79] A. Einstein, *Investigations on the Theory of the Brownian Movement*. Courier Corporation, 1956.

[80] A. Fick, « Ueber Diffusion », *Ann. Phys.*, vol. 170, n° 1, p. 59-86, 1855, doi: 10.1002/andp.18551700105.

[81] R. A. Omari, A. M. Aneese, C. A. Grabowski, et A. Mukhopadhyay, « Diffusion of Nanoparticles in Semidilute and Entangled Polymer Solutions », *J. Phys. Chem. B*, vol. 113, n° 25, p. 8449-8452, juin 2009, doi: 10.1021/jp9035088.

[82] K. K. Senanayake et A. Mukhopadhyay, « Nanoparticle Diffusion within Dilute and Semidilute Xanthan Solutions », *Langmuir*, vol. 35, n° 24, p. 7978-7984, juin 2019, doi: 10.1021/acs.langmuir.9b01029.

[83] D. N. Simavilla, V. Ramakrishnan, S. K. Smoukov, et D. C. Venerus, « Experimental investigation of anomalous molecular probe diffusion in entangled polymer melts », *Soft Matter*, vol. 18, n° 33, p. 6200-6208, août 2022, doi: 10.1039/D2SM00759B.

[84] L.-H. Cai, S. Panyukov, et M. Rubinstein, « Mobility of Nonsticky Nanoparticles in Polymer Liquids », *Macromolecules*, vol. 44, n° 19, p. 7853-7863, oct. 2011, doi: 10.1021/ma201583q.

[85] P. G. de Gennes, *Scaling Concepts in Polymer Physics*. Cornell University Press, 1979.

[86] M. Rubinstein et R. H. Colby, *Polymer Physics*. OUP Oxford, 2003.

[87] S. Sengupta *et al.*, « Enzyme Molecules as Nanomotors », *J. Am. Chem. Soc.*, vol. 135, nº 4, p. 1406-1414, janv. 2013, doi: 10.1021/ja3091615.

[88] C. Riedel *et al.*, « The heat released during catalytic turnover enhances the diffusion of an enzyme », *Nature*, vol. 517, nº 7533, p. 227-230, janv. 2015, doi: 10.1038/nature14043.

[89] X. Zhao, K. K. Dey, S. Jeganathan, P. J. Butler, U. M. Córdova-Figueroa, et A. Sen, « Enhanced Diffusion of Passive Tracers in Active Enzyme Solutions », *Nano Lett.*, vol. 17, nº 8, p. 4807-4812, août 2017, doi: 10.1021/acs.nanolett.7b01618.

[90] A.-Y. Jee, K. Chen, T. Tlusty, J. Zhao, et S. Granick, « Enhanced Diffusion and Oligomeric Enzyme Dissociation », *J. Am. Chem. Soc.*, vol. 141, nº 51, p. 20062-20068, déc. 2019, doi: 10.1021/jacs.9b06949.

[91] P. Illien, X. Zhao, K. K. Dey, P. J. Butler, A. Sen, et R. Golestanian, « Exothermicity Is Not a Necessary Condition for Enhanced Diffusion of Enzymes », *Nano Lett.*, vol. 17, nº 7, p. 4415-4420, juill. 2017, doi: 10.1021/acs.nanolett.7b01502.

[92] S. Ghosh, A. Somasundar, et A. Sen, « Enzymes as Active Matter », *Annu. Rev. Condens. Matter Phys.*, vol. 12, nº 1, p. 177-200, mars 2021, doi: 10.1146/annurev-conmatphys-061020-053036.

[93] C. Grootaert, J. A. Delcour, C. M. Courtin, W. F. Broekaert, W. Verstraete, et T. Van de Wiele, « Microbial metabolism and prebiotic potency of arabinoxylan oligosaccharides in the human intestine », *Trends Food Sci. Technol.*, vol. 18, nº 2, p. 64-71, févr. 2007, doi: 10.1016/j.tifs.2006.08.004.

[94] I. Egüés, A. M. Stepan, A. Eceiza, G. Toriz, P. Gatenholm, et J. Labidi, « Corncob arabinoxylan for new materials », *Carbohydr. Polym.*, vol. 102, p. 12-20, févr. 2014, doi: 10.1016/j.carbpol.2013.11.011.

[95] G. Niño-Medina, E. Carvajal-Millán, A. Rascon-Chu, J. A. Marquez-Escalante, V. Guerrero, et E. Salas-Muñoz, « Feruloylated arabinoxylans and arabinoxylan gels: structure, sources and applications », *Phytochem. Rev.*, vol. 9, nº 1, p. 111-120, mars 2010, doi: 10.1007/s11101-009-9147-3.

[96] D. Dodd et I. K. O. Cann, « Enzymatic deconstruction of xylan for biofuel production », *GCB Bioenergy*, vol. 1, nº 1, p. 2-17, 2009, doi: 10.1111/j.1757-1707.2009.01004.x.

[97] T. Köhnke, Å. Östlund, et H. Brelid, « Adsorption of Arabinoxylan on Cellulosic Surfaces: Influence of Degree of Substitution and Substitution Pattern on Adsorption Characteristics », *Biomacromolecules*, vol. 12, nº 7, p. 2633-2641, juill. 2011, doi: 10.1021/bm200437m.

[98] M. S. Kale, B. R. Hamaker, et O. H. Campanella, « Alkaline extraction conditions determine gelling properties of corn bran arabinoxylans », *Food Hydrocoll.*, vol. 31, nº 1, p. 121-126, mai 2013, doi: 10.1016/j.foodhyd.2012.09.011.

[99] R. P. D. Bank, « RCSB PDB - 2C1F: The structure of the family 11 xylanase from Neocallimastix patriciarum ». https://www.rcsb.org/structure/2C1F (consulté le 6 juin 2020).

[100] M. Vardakou *et al.*, « Understanding the Structural Basis for Substrate and Inhibitor Recognition in Eukaryotic GH11 Xylanases », *J. Mol. Biol.*, vol. 375, n° 5, p. 1293-1305, févr. 2008, doi: 10.1016/j.jmb.2007.11.007.

[101] C. Y. Montanier, M. Fanuel, H. Rogniaux, D. Ropartz, A.-M. Di Guilmi, et A. Bouchoux, « Changing surface grafting density has an effect on the activity of immobilized xylanase towards natural polysaccharides », *Sci. Rep.*, vol. 9, n° 1, p. 5763, déc. 2019, doi: 10.1038/s41598-019-42206-w.

[102] « Molecular Expressions Microscopy Primer: Specialized Microscopy Techniques - Fluorescence - Basic Concepts in Fluorescence ». https://micro.magnet.fsu.edu/primer/techniques/fluorescence/fluorescenceintro.html (consulté le 20 février 2023).

[103] D. Lleres, S. Swift, et A. Lamond, « Detecting Protein-Protein Interactions In Vivo with FRET using Multiphoton Fluorescence Lifetime Imaging Microscopy (FLIM) », *Curr. Protoc. Cytom. Editor. Board J Paul Robinson Manag. Ed. Al*, vol. Chapter 12, p. Unit12.10, nov. 2007, doi: 10.1002/0471142956.cy1210s42.

[104] K. A. Rose, M. Molaei, M. J. Boyle, D. Lee, J. C. Crocker, et R. J. Composto, « Particle tracking of nanoparticles in soft matter », *J. Appl. Phys.*, vol. 127, n° 19, p. 191101, mai 2020, doi: 10.1063/5.0003322.

[105] G. Tawil, F. Jamme, M. Réfrégiers, A. Viksø-Nielsen, P. Colonna, et A. Buléon, « In Situ Tracking of Enzymatic Breakdown of Starch Granules by Synchrotron UV Fluorescence Microscopy », *Anal. Chem.*, vol. 83, n° 3, p. 989-993, févr. 2011, doi: 10.1021/ac1027512.

[106] « Tetramethylrhodamine-5-(and-6)-Isothiocyanate (5(6)-TRITC), mixed isomers ». https://www.thermofisher.com/order/catalog/product/fr/fr/T490 (consulté le 22 février 2023).

[107] M. Xu, J. L. Ross, L. Valdez, et A. Sen, « Direct Single Molecule Imaging of Enhanced Enzyme Diffusion », *Phys. Rev. Lett.*, vol. 123, n° 12, p. 128101, sept. 2019, doi: 10.1103/PhysRevLett.123.128101.

[108] J.-P. Günther, G. Majer, et P. Fischer, « Absolute diffusion measurements of active enzyme solutions by NMR », *J. Chem. Phys.*, vol. 150, n° 12, p. 124201, mars 2019, doi: 10.1063/1.5086427.

[109] B. Srinivasan, « A guide to the Michaelis–Menten equation: steady state and beyond », *FEBS J.*, vol. 289, n° 20, p. 6086-6098, oct. 2022, doi: 10.1111/febs.16124.

[110] J. S. Luterbacher, D. Martin Alonso, et J. A. Dumesic, « Targeted chemical upgrading of lignocellulosic biomass to platform molecules », *Green Chem*, vol. 16, n° 12, p. 4816-4838, oct. 2014, doi: 10.1039/C4GC01160K.

[111] T. Enjalbert *et al.*, « Characterisation of the Effect of the Spatial Organisation of Hemicellulases on the Hydrolysis of Plant Biomass Polymer », *Int. J. Mol. Sci.*, vol. 21, n° 12, p. 4360, juin 2020, doi: 10.3390/ijms21124360.

[112] R. Du *et al.*, « Enzymatic hydrolysis of lignocellulose: SEC-MALLS analysis and reaction mechanism », *RSC Adv*, vol. 3, n° 6, p. 1871-1877, 2013, doi: 10.1039/C2RA21781C.

[113] A. Tayal, R. M. Kelly, et S. A. Khan, « Rheology and Molecular Weight Changes during Enzymatic Degradation of a Water-Soluble Polymer », *Macromolecules*, vol. 32, n° 2, p. 294-300, janv. 1999, doi: 10.1021/ma980773w.

[114] S. Malgas, S. J. van Dyk, et B. I. Pletschke, « β-Mannanase (Man26A) and α-galactosidase (Aga27A) synergism – A key factor for the hydrolysis of galactomannan substrates », *Enzyme Microb. Technol.*, vol. 70, p. 1-8, mars 2015, doi: 10.1016/j.enzmictec.2014.12.007.

[115] K. Zajki-Zechmeister, M. Eibinger, et B. Nidetzky, « Enzyme Synergy in Transient Clusters of Endo- and Exocellulase Enables a Multilayer Mode of Processive Depolymerization of Cellulose », *ACS Catal.*, vol. 12, n° 17, p. 10984-10994, sept. 2022, doi: 10.1021/acscatal.2c02377.

[116] S. Lalitha Sridhar et F. Vernerey, « Localized Enzymatic Degradation of Polymers: Physics and Scaling Laws », *Phys. Rev. Appl.*, vol. 9, n° 3, p. 031001, mars 2018, doi: 10.1103/PhysRevApplied.9.031001.

[117] L.-H. Cai, S. Panyukov, et M. Rubinstein, « Mobility of Nonsticky Nanoparticles in Polymer Liquids », *Macromolecules*, vol. 44, n° 19, p. 7853-7863, oct. 2011, doi: 10.1021/ma201583q.

[118] J. Crank, *The Mathematics of Diffusion*. Clarendon Press, 1979.

[119] G. Paës, L. von Schantz, et M. Ohlin, « Bioinspired assemblies of plant cell wall polymers unravel the affinity properties of carbohydrate-binding modules », *Soft Matter*, vol. 11, n° 33, p. 6586-6594, 2015, doi: 10.1039/C5SM01157D.

[120] « Fluorescent Probe Labeling Chemistry ». https://www.caymanchem.com/news/fluorescent-probe-labeling-chemistry (consulté le 15 mars 2023).

[121] « NMR Spectroscopy ». https://www2.chemistry.msu.edu/faculty/reusch/virttxtjml/spectrpy/nmr/nmr1.htm (consulté le 9 mars 2023).

[122] M. A. Wisniewska et J. G. Seland, « Investigating structure-dependent diffusion in hydrogels using spatially resolved NMR spectroscopy », *J. Colloid Interface Sci.*, vol. 533, p. 671-677, janv. 2019, doi: 10.1016/j.jcis.2018.08.112.

[123] H. M. van der Kooij, R. Fokkink, J. van der Gucht, et J. Sprakel, « Quantitative imaging of heterogeneous dynamics in drying and aging paints », *Sci. Rep.*, vol. 6, n° 1, p. 34383, déc. 2016, doi: 10.1038/srep34383.